# DISCO WHOLE BODY CLEARING AND IMAGING TO STUDY SYSTEMIC CHANGES IN NEURONAL PATHOLOGIES

Ruiyao Cai

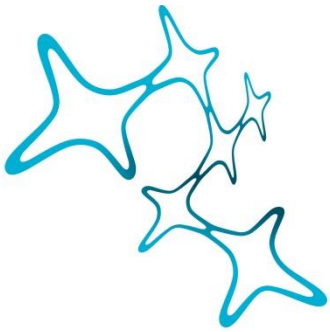

Graduate School of
Systemic Neurosciences

LMU Munich


Dissertation der
Graduate School of Systemic Neurosciences der
Ludwig-Maximilians-Universität München

13 März, 2019

Supervisor: Dr. Ali Ertürk
Second Reviewer: Prof. Dr. Nikolaus Plesnila

Date of Defense: 24 Juni, 2019

# Table of contents

# 1 List of abbreviations

| | |
|---|---|
| **3D** | 3-dimension, 3-dimentional |
| **3DISCO** | 3D imaging of solvent-cleared organs |
| **BABB** | 1:2 benzyl alcohol, benzyl benzoate |
| **BBB** | blood brain barrier |
| **CFP** | cerulean fluorescent protein |
| **CNS** | central nervous system |
| **CT** | computer tomography |
| **CUBIC** | clear, unobstructed brain imaging cocktails and computational analysis |
| **DBE** | dibenzyl-ether |
| **DCM** | dichloromethane |
| **DPE** | diphenyl-ether |
| **EAE** | experimental autoimmune encephalomyelitis |
| **ExM** | expansion microscopy |
| **GFP** | green fluorescent protein |
| **iDISCO** | immunolabeling-enabled three-dimensional imaging of solvent-cleared organs |
| **IHC** | immunohistochemistry |
| **IL** | interleukin |
| **MRI** | magnetic resonance imaging |
| **NIH** | National Institute of Health |
| **NO** | nitric oxide |
| **OPTIClear** | Optical Properties-adjusting Tissue-Clearing agent |
| **PACT** | passive clarity technique |
| **PARS** | perfusion-assisted agent release in situ |
| **PNS** | peripheral nervous system |
| **RI** | refractive index |
| **ROS** | reactive oxygen species |
| **SCI** | spinal cord injury |

| | |
|---|---|
| **SDS** | sodium dodecyl sulphate |
| **SeeDB** | See Deep Brain |
| **SHIELD** | stabilization to harsh conditions via intramolecular epoxide linkages to prevent degradation |
| **SMC** | short skull-meninges connection |
| **SWITCH** | system-wide control of interaction time and kinetics of chemicals |
| **TBI** | traumatic brain injury |
| **TDE** | 2,20-thiodiethanol |
| **TGF-β** | transforming growth factor beta |
| **THF** | tetrahydrofuran |
| **TNF-α** | tumor necrosis factor alpha |
| **UbasM** | Urea-Based Amino-Sugar Mixture |
| **uDISCO** | ultimate DISCO |
| **vDISCO** | nanobody(VHH)-boosted 3D imaging of solvent-cleared organs |
| **WHO** | World Health Organization |
| **YFP** | yellow fluorescent protein |

# 2 Abstract

The effects of most diseases are not confined to a particular body region. In fact, pathologies can affect multiple organs and whole organisms. Therefore, a systems biology approach could deliver new insights by studying diseases at a whole-body level. Tissue clearing methods started revolutionizing standard histology by making the samples transparent and allowing the 3-dimensional (3D) imaging and analysis of whole organs and organisms without sectioning. In this project we aimed to develop new tissue clearing methods that are able to clear whole mouse bodies in order to study pathological changes throughout the entire organism. We based our methods on organic solvents because, so far, they are the ones that can achieve the highest level of transparency. First, we developed ultimate DISCO (uDISCO), a protocol that is able to clear whole mice and to preserve the signal from endogenous fluorescent proteins up to months, by employing less reactive organic solvents. Moreover, uDISCO reduces the volume of the samples by up to 65%; therefore, it permitted the imaging of the whole mouse central nervous system (CNS) and whole-body at subcellular resolution for the first time using light-sheet microscopy. Nevertheless, owing to the fact that bones and hard tissues could not be efficiently cleared and that the organic solvents could eventually quench the endogenous fluorescent signal, the reliable detection and quantification of the biological fluorescent information in all body districts have still represented a challenge. To overcome these issues, we developed a second pipeline called (nanobody(VHH)-boosted 3D imaging of solvent-cleared organs) vDISCO, which exploits a pressure-driven, nanobody-based whole-body immunolabeling system to enhance the signal of fluorescent proteins, to preserve it for years and to image through dense and hard tissues such as bones and skin. vDISCO allowed us to image and quantify subcellular details in intact transparent mice. Using vDISCO, we reconstructed the first whole-body neuronal map in adult mice at subcellular resolution. Furthermore, we screened whole mice for changes caused by CNS damage and trauma and found degeneration of peripheral nerve terminals in the torso after traumatic brain injury and extensive multiple-organ inflammation after spinal cord injury. Moreover, using vDISCO we observed short vascular connections –named short skull-meninges connections (SMCs)–between skull marrow and brain meninges which were filled with immune cells upon stroke. The SMCs might represent a new route for immune cells to access into the brain. Taken together, our method represents a powerful tool to unbiasedly analyze effects of neuronal conditions in the whole organism.

# 3 Introduction

Nature follows a very strict rule: all organisms (from tiny bacteria to big mammals) are based on a hierarchical organization of their different parts and all organisms are made by different components that work in synchrony with each other. In particular, mammals including humans and mice — well known animal model in biomedical research[1]— are characterized by a high complexity in their structural and functional organization with a body composed of organs, which are made by tissues, which are in turn built out of cells that consist of organelles and so on. All these components are never completely isolated from each other, but they interact, they work in synergy and they communicate to each other to make complex living organisms possible.

This known concept justifies the need for studying complex organisms as whole entities and not simply as an assembly of many individual parts, especially when almost all diseases do not only affect the site where they arise but they can also cause undetected changes in other parts of the body and in some instances dramatically affect the entire organism. In previous decades, new research fields have appeared to target this need: there has been in fact an increased interest in systems biology which, through a holistic approach, has focused on studying complex interactions in a biological system in an unbiased manner[2]. However, the modeling and integration of the huge and complex data sets collected from whole organisms have to rely on computational and mathematical approaches to extract meaningful numerical datasets and information (e.g genomics and proteomics).

In the field of imaging, different approaches exist to acquire and analyze whole organisms at once. Computer Tomography (CT) and Magnetic Resonance Imaging (MRI) technologies allow the scanning of whole bodies of humans and other animals. Although they are powerful tools to study live phenomena by providing the gross anatomy, they lack subcellular resolution and therefore they can´t provide information at single cell level[3].

On the other hand, in order to investigate biological samples at a cellular and subcellular level, histological techniques were refined in the last century[4]. They traditionally rely on the cutting of the body parts of interest, which are subsequently sliced into thin sections (10-100µm). However, the histological procedures are not devoid of limitations:

- They do not allow the visualization of the organism as whole.
- They can lead to the loss of information and to the generation of errors, because the big picture has to be reconstructed from separate pieces.
- They can lead to bias in analysis, because the region of interest is predefined.

Moreover, the possibility to keep samples intact is especially advantageous when investigating highly complex phenomena such as global inflammation or microglia activation and especially when studying cells with long projections such as neurons. Ideally all the cellular structures of the neurons should be enclosed in the imaging volume to avoid the difficult reconstruction of their morphologies from fragments. Despite the efforts to overcome these limitations, the development of holistic 3D histology has been hindered by the natural opacity of mammalian tissues, which means that high-resolution imaging of the tissue can only be achieved for the first few hundred micrometers in depth[5]. However, the development of tissue clearing technologies has started paving the way to solve the problems of 2D histology, although many bottlenecks that prevent holistic 3D high resolution imaging and analysis still exist.

## 3.1 Tissue clearing technology

*Note: for the expanded version of the acronyms of the tissue clearing methods in this section, please see section 1 "List of abbreviations".*

The opacity of most of biological tissues, including the ones from mammals, is determined by the composition of the tissue itself. This is because the different components of the tissue (protein, lipids, water and so on) have different refractive indexes (RIs)[6,7]; therefore when light crosses these components with different RI, it will be scattered in different directions.

Tissue clearing technologies are methods that are able to render biological specimens transparent, by equalizing the RIs throughout the tissue and matching them with the RI of an immersion solution. The first translucent biological human samples had been achieved in 1911 by soaking the specimens in solutions with similar light refraction properties of the tissue[8]. However, at that time two main factors prevented the rise of 3D histology: the lack of modern fluorescent staining approaches to label the desired biological structures and the lack of advanced microscopy technologies. In 2007, Dodt *et al*. designed and built the first light-sheet fluorescence microscopes (ultramicroscopes), which, in combination with benzyl alcohol/benzyl benzoate (BABB) clearing, represented a big breakthrough because it was finally possible to quickly image relatively big cleared samples without sectioning[9].

Since then, many other clearing methods have been developed. Overall, there are currently three main groups, based on their principles to match the refractive index and to clear the tissue. Nevertheless, none of them so far allow a reliable detection of the fluorescence signal at a subcellular level for intact whole body analysis and quantification.

### 3.1.1 Tissue clearing types

**Organic-solvent-based clearing methods**

The first tissue clearing group is based on BABB clearing principles. It is characterized by the use of organic solvents which can achieve the highest grade of transparency, although at the cost of fast quenching the fluorescence signal[10,11]. Since the two main components that cause light scattering in the tissue are water and lipids (they have lower and higher RIs respectively, compared with the RI of the proteins), the methods from this group aim to dehydrate and delipidate the samples completely prior to RI matching. Different solvents have been used to achieve the dehydration, delipidation and RI matching: the first tests were performed with non-toxic alcohols (e.g. ethanol) as dehydrating reagent[9], although with the risk of completely quenching the transgenically expressed fluorescent protein signal [12]. One of the main methods of this group is represented by "*3D imaging of solvent-cleared organs*" (3DISCO). 3DISCO is an organic-solvent-based clearing method that is extremely reproducible and easy to perform; it produces very transparent samples and it has been widely used in biomedical research: for example to study stem cells[13], immune cells[14] and cancer cells[15] in thick tissues. In the 3DISCO method, tetrahydrofuran (THF) is used to remove the water, dichloromethane (DCM) to remove the lipids and dibenzyl-ether (DBE) replaced BABB to match the RI[12,16,17]. In Schwarz *et al*., *tert*-butanol replaced THF to remove water from the samples[18] and, according to the authors, improving the fluorescence signal retention. Some years later, different research groups combined 3DISCO with whole-mount and whole-organ labeling[19,20] including the one of Tessier-Lavigne that called its protocol "*immunolabeling-enabled three-dimensional imaging of solvent-cleared organs*" (iDISCO)[21]. Recently, iDISCO has been updated into iDISCO+ using methanol as dehydration agent, in order to reduce the size shrinkage effect caused by THF[22].

**Aqueous-based clearing methods**

The second group consists of aqueous-based clearing methods. In fact, these methods use hydrophilic reagents that are dissolved in water. The solutions can simply be with:

- High RI molecules (e.g. glycerol[23] or 2,20-thiodiethanol (TDE)[24-27]).
- High concentration of sugar (e.g fructose in SeeDB[28]) to increase the RI and match it to that of the tissue.
- A mixture of sugar and urea (e.g ScaleS[29] and FRUIT[30]).
- More complex chemical cocktails with both RI matching and delipidation properties: N-methylglucamine- TDE-Iohexol in OPTIClear[31] ,urea-xylitol-sodium deoxycholate in ClearSee[32],

urea-alcohols (e.g, glycerol in Scale[33]), urea-sucrose-1,3-Dimethyl-2-imidazolidinone in UbasM[34], or urea-aminoalcohol such as in CUBIC[35,36] and its derivatives[37-39].

**Hydrogel-based clearing methods**

The third group is based on the formation of a hydrogel scaffold in the tissue. CLARITY[40] is a clearing method that applies hydrogel-embedding fixation followed by delipidation with electrophoresis to clear the tissue. First, the tissue is stabilized by the induction of the endogenous proteins in the sample to form cross-links with acrylamide in order to form a hydrogel, then an electric field facilitates the removal of the lipids from the tissue via the strong detergent sodium dodecyl sulphate (SDS); in the end the tissue is immersed in the RI matching solution "Focus Clear" until transparency. In recent years, many other protocols have derived from the original CLARITY, including PACT and PARS[41] that exploit passive and perfusion delipidation respectively, and PACT-decal[42] and bone-CLARITY[43] that are both able to clear calcified tissues such as bones. Moreover, whole-mount labeling protocols were developed based on hydrogel formation, including SWITCH[44] and SHIELD[45] that allow multi-round protein labeling, and CLARITY coupled with RNA amplification/staining and imaging[46].

### 3.1.2 Signal stabilization and whole mount staining

The first applications of tissue clearing were based on the detection of endogenous florescent proteins, including green fluorescent protein (GFP) or yellow fluorescent protein (YFP) expressed by neurons of the central nervous system (CNS) in transgenic animals[9,33]. However, most of clearing protocols, especially the ones based on organic solvents, had the side effect of heavily quenching the fluorescence signal within few days[10,12], making the samples unusable for prolonged imaging. It has been shown that the fast quenching of the proteins depends on several factors such as the formation of peroxides, high clearing temperatures that can denaturate the GFP structure[47,48] and the removal of the proteins from their water environment[49]. Therefore, many efforts in protocol development aimed to preserve the fluorescent signal as long as possible[18,29,34,50,51] by increasing the pH of the clearing solutions[18,48,50,52,53], removing peroxides[12], adding substances able to stabilize protein conformation (e.g polyethylene glycol[50,54,55]) or reducing the clearing temperature[51,52]. On the other hand, the aqueous-based clearing methods have been shown to better preserve the fluorescence signal although being more time-consuming protocols and not efficient in reaching complete transparency of the samples[10]. Whole mount staining methods were introduced as a different solution for the fast quenching: for example in iDISCO and iDISCO+ the authors used antibodies conjugated to Alexa Fluor dyes that are more stable after solvent treatment and clearing. In this way they could perform repeated imaging for many months[21,22].

However, to this point, the whole mount staining protocols available in the literature were not able to achieve the labeling of samples bigger than single organs such as a mouse brain or kidney because one of the main limitations is the big size of the antibodies that prevents them to penetrate deep into the tissue[21].

### 3.1.3 Whole-body clearing

The possibility to clear whole organisms (such as entire mice) for unbiased studies of intact full bodies at subcellular resolution has been explored using perfusion systems to actively deliver the clearing agents into the body of the animals. In these protocols the removal of the skin remained a standard procedure in the pre-clearing step[36,39,41,42,50], since this organ acts as a barrier for penetration of chemicals and the optical properties of hair and strong melanin pigmentation cause additional problems during imaging[11,56,57]. This perfusion based strategy led to the publication of methods such as whole-body CUBIC[36], PARS[41,42] and PEGASOS[50]. In whole-body clearing the decolorization of the blood to remove the heme pigment in fundamental because this pigment is one of the most abundant in mammalian bodies and it can cause light absorption and strong autofluorescence[11,36]. In CUBIC and PEGASOS, heme is eluted from the body by the treatment with an aminoalcohol[35,36,39,50]; while in PARS, this is done by SDS[41,42]. These methods can achieve quite a high level of transparency[10], however the swelling of the samples after clearing or the lack of adequate imaging systems prevent the high resolution imaging of the intact body because the resulting whole body samples were too large to fit into conventional light-sheet microscopes. Recently, the group that developed CUBIC published a new method called CUBIC-cancer[39]. This updated CUBIC method is able to render the animals clear enough for light-sheet imaging of the entire body, although using a custom-made light-sheet microscope. CUBIC-cancer was used to detect cancer metastases in whole mouse bodies and in the related paper it was shown that despite the unbiased detection of cancer metastases in whole bodies, it was still necessary to apply confocal imaging on specific dissected organs of interest to obtain quantitative data (e.g number of metastases in specific organs). The main reason of this is because like all whole-body clearing and imaging methods published so far, CUBIC-cancer relies on the signal of transgenically expressed fluorescent proteins which emit light in the visible spectrum, range where muscles and other tissues such as bones have obstructive autofluorescence or can limit imaging penetration[6]. Moreover, fluorescent proteins are generally less bright than most of the synthetic fluorophores (e.g Alexa dyes) used for example in immunohistochemistry and their signal is further diminished by the clearing and imaging steps as mentioned before. Taken together, there are several factors that up to date prevent the reliable quantification of single cells in whole bodies.

Finally, all previous whole-body clearing protocols require the removal of the skin[36,39,41,42,50] and this means that the largest organ of a body is lost. This represents an important drawback because it has been shown that the skin has essential functions, beyond its main role of being merely a physical barrier against external

environment[58,59]. In fact, we can find many other functional elements such as nerve endings, immune cells, and vessels from the blood and lymphatic circulation in the skin. All these components, together with other organs contribute to the functionality of the skin[58,59].

### 3.1.4 Side technological applications

It is noteworthy that many of the clearing methods aforementioned paved the way for the development of protocols that could broaden the technical applications of tissue clearing beyond just making the sample transparent for deep tissue imaging. For example, the fact that the hydrogel based methods such as CLARITY and PACT could ratiometrically expand the size of the samples represented the groundwork for the field of expansion microscopy (ExM). In fact, in ExM[60] the creation within the specimen of a swellable superabsorbent nano-porous polymer network enables the sample to increase in size by the immersion in water. Therefore, the physical expansion corresponds to a physical magnification, giving the possibility for super-resolution microscopy: stained objects[42,61-63] that are closer than the diffraction limit in the untreated tissue can be optically resolved after expansion. Furthermore, the observation that some aqueous-based methods can also increase the size of the sample, led to the generation of further expansion protocols such as CUBIC-X[37].

## 3.2 CNS damage and injuries

Diseases involving the CNS (brain and the spinal cord) can lead to devastating effects and are a major cause of death and disability. Injuries to the CNS affect millions of people[64] worldwide and every year almost one million people experience a cerebral ischemia/stroke only in U.S[65]. Most people who survive from damage to the CNS will suffer from permanent neurological impairments.

The serious consequences of CNS damage result from the fact that the CNS is the organ assigned to control and to coordinate all other parts of the body. In fact, the CNS extends its reach to the rest of the body by connecting with the peripheral nervous system (PNS), which in turn innervates every single organ. It is therefore clear that the damage of one part of the CNS can have detrimental sequela, not only in the neuronal tissue itself but also in other tissues and in regions far from the damaged site, even out of the CNS. For example, it has been shown that CNS injury can trigger a systemic response via activation of the inflammatory components[66].

At the moment, the study of such an intricate complex neuronal network and how it affects the whole body represent a big challenge not only in neuroscience but also in other fields especially when all the organs are controlled by its activity. So far, the morphological investigation of all pathophysiological changes caused by

CNS diseases has been conducted by analyzing each single organ of interest separately, dissecting them out from the body. For example, the visualization of spine reduction after traumatic brain injury (TBI) was done by dissecting out the brain[67] or the analysis of the systemic immune cell activation after stroke was done dissecting out selected peripheral organs such as the femur bone or the aorta[68]. This focused approach makes difficult to discover unexpected effects in other parts of the body after CNS damage.

Therefore, a more global approach with the ability to capture the changes at a systemic level to obtain the whole view of the disease is needed.

Although whole-body imaging and scanning systems such as MRI or CT exist, none of them is able to provide information at single cell resolution.

### 3.2.1 Traumatic brain injury

Traumatic brain injury is defined as damage to the brain due to external mechanical forces that can include shockwaves[69], repetitive head hits in contact sports[70] or severe impacts in car accidents[71]. It is the leading cause of death and disability in high-income countries in people under 45 years old. In fact, millions of deaths and/or hospitalizations annually are directly attributable to TBI[64,72]. Until today, despite extensive research, there are no adequate therapeutic treatments available. The heterogeneity in trauma lesion as well as the complexity of subsequent pathophysiological events accounts for the failure of clinical trials[73,74]. Thus, TBI represents an overwhelming global health problem.

According to the American National Institute of Health (NIH), TBIs that are caused by a direct head trauma can include: concussion (also known as mild TBI), which is a temporary impairment of brain functions due to a trauma[75], and contusion, which is a moderate to severe TBI with bruise of the brain tissue and possibly skull fracture[76,77]. Brain contusion represents the type of TBI that is the most studied within animal models, because it is relatively easy to model[77].

The pathophysiology of TBI starts with its acute phase which consists of two stages. In the first phase, the brain tissue is immediately damaged, both physically and mechanically. This leads to primary acute effects such as: focal injury due to the mechanical impact, rupture of tissue which results into vascular damage and hemorrhages, death of glial limitans, generation of free radicals and axonal shearing[77-81]. These phenomena are followed by secondary acute effects that can evolve over minutes to months and are the results of specific molecular, metabolic and cellular events such as excitotoxicity[82], perturbation of the calcium homeostasis[83], increased generation of free radicals, increased peroxidation, mitochondrial dysfunction[84], ischemia, inflammation[85], infiltration of peripheral immune cells[86,87], apoptosis, diffuse axonal injury[88,89] and damage of the blood brain barrier (BBB)[80]. All these events can lead to neuronal, endothelial and glial cell death resulting

in white matter degeneration, tissue damage, brain atrophy and death[77,88,89]. For the TBI survivors, these events can lead to long-term symptoms, for instance clinical manifestations so far associated to neurodegenerative diseases[90]. In fact, considerable literature from human studies showed a strong association between TBI and the development and/or worsening of chronic focal and global impairments[91,92] including neurodegenerative diseases such as dementia[93,94], Parkinson´s disease[95], epilepsy[96], depression[90] as well as pathologies affecting the whole body such as progressive motor decline syndromes[97], hemidystonia[98] and peripheral neuropathies[99]. It is reasonable to hypothesize that all the events that occur during the acute phase of TBI can trigger prolonged tissue degeneration causing the long-lasting effects of TBI (chronic TBI) which can persist for years or decades[100].

However, although it has been already shown that the initial localized focal injury can affect the whole brain in terms of neurodegeneration and neuronal inflammation[67], little is known about the mechanisms that cause this phenomenon and how the focal damage can trigger changes in the rest of the body. In fact, up until now, it is still not clear whether peripheral neuronal connectivity is altered in remote body regions after TBI and in which locations such alterations might occur.

### 3.2.2 Spinal cord injury

Spinal cord injury (SCI) is the damage to the spinal cord caused by a trauma (e.g. a car accident) or from disease or degeneration (e.g. cancer). According to the World Health Organization (WHO), the annual global incidence is estimated 40 to 80 cases per million in the world population and up to 90% of these cases are the result of a trauma. The injury is characterized by a series of symptoms (loss of sensitivity, chronic pain, paralysis or bladder dysfunction) which depend on the severity and the location of the damage to the spinal cord. So far, research efforts were devoted in the direction of promoting axonal regeneration to re-establish the original neuronal network[101-104]. However, the treatment of spinal cord injury in clinic has been particularly difficult due to the inability of most of the damaged axons to regenerate[17] or the inability of neurons to be replaced in the CNS[105]. In fact, there is currently a lack of effective therapies for SCI condition[105].

As for TBI, the pathophysiology of SCI consists of two stages: the primary injury, which is characterized by the initial mechanical damage (immediate hemorrhage and cell death) and the secondary injury that lasts for weeks or months[106]. The secondary injury is characterized by biochemical, cellular, tissue and vascular changes that worsen the effects of the SCI even further[106]: energy failure[107], perturbation of ion homeostasis[108], excitotoxicity[109], edema[110], apoptosis[111,112], lipid peroxidation[113], oxidative stress[114], inflammation with release of cytokines[115,116], immune cell invasion[117] and vasospasm[118]. Among these events, it has been shown that the inflammatory response plays a main role in the secondary damage generally

worsening the outcome after SCI[119-124]. One of the main components of the inflammation is represented by immune cells, in particular macrophages/microglia[125]. In physiological and healthy conditions, these cells have been observed as peripheral macrophages in the meningeal spaces, in the perivascular compartment and in the choroid plexus, while as microglia inside the CNS tissue. Upon SCI, many studies reported that macrophages/microglia can detrimentally affect the injury outcome by secreting pro-inflammatory mediators including cytokines, tumor necrosis factor alpha (TNF-α), interleukin(IL)-1, reactive oxygen species (ROS), and nitric oxide (NO)[121,126-128], but also have a beneficial effect via production of anti-inflammatory cytokines such as IL-10, and transforming growth factor beta (TGF-β)[128,129]. However, the mechanisms underlying this dual role have not been completely elucidated yet. Owing to the importance of their role in SCI, extensive research has been conducted to influence the activity of these cell populations in order to develop effective therapeutic strategies to reduce the damage after SCI.

Besides the activation of resident microglia, an infiltration of peripheral macrophages attracted by chemokines into the CNS after SCI has been observed[130-132]. These infiltrating cells are actively involved in the progression of the injury together with the resident microglia cells[133]. As mentioned before, macrophages/microglia (which are the predominant immune cell population present in the spinal cord after injury[134]) can at the same time damage neurons and glia by secreting inflammatory molecules but also be essential for the reconstruction of the injured tissue, for example phagocytizing cellular debris and dead cells[133,134]. It has been speculated that the dichotomy of their role is due to the heterogeneity of the macrophage/microglia population[135,136]. For example, microglia might have unique functions versus the infiltrating macrophages[136]. Therefore, it would be important to distinguish the nature and different features of these cellular populations. However, the investigation of the infiltrating and resident immune cells has been mainly conducted *post-mortem* in isolated spinal cords that have been dissected out from the body[134,137-140]. Other techniques have been exploited for the same purpose: MRI has been used to indirectly follow the spatio-temporal course of macrophages invasion *in vivo* after nerve injury in a selected body area[141]; while intravital and 2-photon microscopy have been used after laminectomy to observe the infiltration event but only in small areas of the spinal cord[125,142]. Therefore, no study has ever shown the extent of inflammation in the body areas surrounding the injury site at single cell level and no study could in a global way monitor all the putative infiltrating routes, tracking each single cell that moves from the surrounding peripheral organs into the spinal cord.

Although TBI and SCI share extensive similarities in terms of neuroinflammatory response[143], in this project I have focused on the study of the inflammatory events after SCI.

### 3.2.3 Stroke

Stroke or cerebral ischemia is defined by the WHO[144] as "a clinical syndrome consisting of rapidly developing clinical signs of focal (or global in case of coma) disturbance of cerebral function lasting more than 24 hours or leading to death with no apparent cause other than a vascular origin". In other words, it is a medical condition where the insufficient blood supply in the brain results into tissue death. In ischemic stroke the neurological dysfunction is the visible result of the infarction of an area of the brain, caused by the narrowing or the occlusion of a brain artery. Ischemic stroke is considered as a medical urgency because it is the second leading cause of death and the main cause of long-term disability in the world[65]. As in TBI and SCI, the CNS tissue damage resulting from brain ischemia evolves in time and space through a complex series of ionic, biochemical and cellular pathophysiological events. The brain is an organ particularly vulnerable to ischemia, because it is characterized by a high intrinsic metabolic activity and a high demand of oxygen and glucose supply[145]. In case of ischemia, the reduced delivery of both oxygen and glucose causes the failure of ionic pumps and of reuptake mechanisms leading to the alteration of the ionic balance, excitotoxicity and spreading depression-like depolarizations[146]. Then, subsequent oxidative stress, necrosis, apoptosis and inflammatory processes lead to neuronal damage[147,148] and to the release of proinflammatory mediators (cytokines and chemokines) which attract and promote the trans-endothelial migration of peripheral leukocytes[149].

The stroke-induced inflammation plays an important role in stroke pathophysiology. It has been shown that the ischemic injury causes an acute (minutes to hours after stroke) and a prolonged (hours to days after stroke) inflammatory response, which consists of the activation of microglia in the acute phase and, as mentioned before, the recruitment of circulating leucocytes in the prolonged phase[150-154]. In rodent models, these recruited white blood cells are first represented by myeloid cells including neutrophils and macrophages that invade the brain parenchyma within hours to days, followed by infiltration of lymphocytes that occurs days to weeks after the initial injury[155-158]. Although the immediate inflammatory response tries to cope with the damage of the tissue by clearing dead cells and cellular debrids, the accumulation of immune cells including the infiltrating ones becomes quickly detrimental[154]. For example, these leucocytes can release pro-inflammatory mediators and different effector molecules such as proteases and prostaglandins, and ROS that can directly harm the cells, the vessels and the extracellular matrix further, eventually causing damage to the endothelial layer and an impairment of the BBB[159,160]. On the other hand, some sub-populations of the infiltrating leucocytes might play a protective role especially in the chronic phase (in rodents approx. two weeks after stroke) including $T_{reg}$ lymphocytes that can immunoregulate the inflammatory activity of T cells, secrete anti-inflammatory cytokines, suppress astrogliosis, prevent secondary infarcts and contribute to the neurological recovery[161,162].

Owing to the key roles that infiltrating immune cells play in stroke, there has been an increasing effort to understand the exact mechanisms that allow the circulating leucocytes to migrate into the ischemic brain. The trans-endothelium access across the impaired BBB represents the route that has been investigated the most[163,164]. However, other routes for other sub-populations of cells warrant investigation to elucidate their contribution to the stroke outcome. In particular, a better understanding of how these sub-populations access the CNS and interact with the brain microvasculature would likely lead to the development of more efficient immune interventions for patients affected by stroke[165].

In general, the studies of the infiltration of immune cells into the brain were mostly performed using standard immunohistochemistry (IHC) on *post-mortem* material, *in vivo* intravital microscopy and especially by *ex vivo* flow cytometry[158,166]. However, these methods have certain limitations: for example in flow cytometric analysis, the enzymatic digestion used to process the brain samples might change the surface antigens of the cells; while standard IHC requires the slicing of the tissue causing partial loss of 3D information and making the reconstruction of the entry routes for immune cells less accurate, more difficult and time consuming for large volumes. The usage of *in vivo* imaging techniques such as intravital microscopy has given important insight into the mechanisms behind the adhesion and the trans-endothelial migration of these cells, although it can only provide information about the surface of the brain. Positron emission tomography/single photon emission tomography and functional MRI on the other hand do not have the resolution power necessary to provide single cells information. Accordingly, there is a need for improved technologies to investigate these specific important aspects of stroke disease.

## 3.3 The brain lymphatic system as a route of immune cell trafficking

The lymphatic system is a vascular network connecting different organs which is critical for the body´s immune response and for coordinating the trafficking of antigens and immune cells[167]. In the past, it was thought that the brain was not reached by this network and that the only immune cells residing in the brain parenchyma in healthy conditions were the microglia. However, recent studies confirmed that the CNS is not devoid from this network and other papers even described how brain lymphatic vessels play an important role in CNS diseases[168]. But where are the brain lymphatic vessels located?

The meningeal compartments represent an important factor in the immune surveillance of the brain[169] because they are populated by a variety of immune cell types that can affect the CNS functions[170]; however, it was not clear how the immune components such as immune cells could enter and leave the CNS. Only recently it has

been discovered that the dural sinuses of the meninges are lined with lymphatic vessels, which carry fluid and leucocytes and are connected to the deep cervical lymph nodes[168]. It has been shown that these vessels can contribute to the drainage of the cerebrospinal fluid transporting leucocytes and soluble macromolecules together with the glymphatic system[171,172] and can be a route for immune cells to access the CNS[168] in health and disease. In fact, a recent study has reported that in mice affected by experimental autoimmune encephalomyelitis (EAE, a model for multiple sclerosis) the disruption of the meningeal lymphatic function could ameliorate the disease outcome. This has led to the hypothesis that this system can actively play a role in the activation of harmful 2D2 T cells that contribute to the pathogenesis of EAE[173]. Moreover, new studies have demonstrated that this lymphatic vasculature also works as a CNS-meninges drainage system for macromolecules such as amyloid-β and Tau[174]. Interestingly, they showed that the impairment of this system could cause the accumulation of these molecules in the brain[174,175] and consequently worsen the cognitive deficits in animal models of neurodegenerative diseases such as Alzheimer´s disease[175].

These important newly discovered functions of the meningeal lymphatic vessels highlight them as a promising delivery route and direct target for new therapeutics to control neuroinflammatory and neurodegenerative conditions. However, the study of these small structures has been difficult: they are located between the brain and the skull and thus easily destroyable during the dissection of the brain from the skull for histological processing. So far, the histological analysis of these vessels has only been possible by either sectioning the complete head[176] or removing the brain from the skull. In the latter case the meningeal membranes were carefully peeled out from the remaining bone or directly observed in the inner side of the skull[168,173]. However, all these strategies are very laborious and suffer from the limitations of classical histology, which are the sectioning of the region of interest or the disruption of the structures at the brain-meninges interface when the brain and meninges are separated. Therefore, new methods that can preserve the integrity of the brain in the skull and that are able to study meningeal lymphatic vessels embedded inside the head are needed.

# 4 Research Articles

## 4.1 Shrinkage-mediated imaging of entire organs and organisms using uDISCO

Tissue clearing methods, together with the invention of light-sheet microscopy, have contributed to the development of 3D-histology for the study of large transparent specimens. Nevertheless, there are still limitations that prevent the imaging of entire mammals such as rodents: (i) light-scattering in thick tissues, (ii) fast quenching of endogenous fluorescence signal and (iii) the size of the entire bodies that could not fit into the existing microscopes.

To overcome these limitations, we have developed a new tissue clearing method called uDISCO. Thanks to the introduction of new chemical reagents (*tert*-butanol to dehydrate, and Diphenyl-ether (DPE) to match the RI) that are chemically stable and less prone to create peroxides which are harmful to the endogenous fluorescent proteins, uDISCO can preserve the fluorescence signal of the endogenous fluorescent proteins up to months. Moreover, thanks to the ability of uDISCO to clear entire organs and rodent bodies reducing their size up to 65%, our method allows the imaging of whole bodies by light-sheet microscopy. With uDISCO, we imaged for the first time at subcellular resolution entire CNS and entire bodies from *Thy1*-GFPM mice, where motor and sensory neurons express GFP. Furthermore, we applied uDISCO to reconstruct the whole vasculature of the CNS from rats over 7 cm and we performed unbiased detection and screening of transplanted fluorescent stem cells in whole body of adult mice. We also showed that uDISCO is compatible with antibody and histological dye stainings of 1 mm thick tissue slices not only from fresh-fixed mouse brains but also from over-fixed human samples.

Taken together, uDISCO is a powerful method that can be applied for many biomedical inquires when the analysis of intact large organs and organisms is required.

*Contribution of R.C. to this work: equal contribution to the development of the method with C.P., in particular I performed: chemical screen and optimization of the best chemical cocktail for the protocol; characterization of the method: preservation of the fluorescent signal, comparison with other clearing methods, compatibility with histological staining, imaging depth, size change and ratio-metrical shrinkage evaluation; my shared first authors C.P., F.P.Q. and I contributed equally for the other aspects of the project: performing experiments, data analysis, interpretation of the results, writing the manuscript (please see section 12 for further details)*

# Shrinkage-mediated imaging of entire organs and organisms using uDISCO

Chenchen Pan[1,2,6], Ruiyao Cai[1,2,6], Francesca Paola Quacquarelli[1,6], Alireza Ghasemigharagoz[1], Athanasios Lourbopoulos[1], Paweł Matryba[1,5], Nikolaus Plesnila[1–3], Martin Dichgans[1–4], Farida Hellal[1,3] & Ali Ertürk[1–3]

**Recent tissue-clearing approaches have become important alternatives to standard histology approaches. However, light scattering in thick tissues and the size restrictions on samples that can be imaged with standard light-sheet microscopy pose limitations for analyzing large samples such as an entire rodent body. We developed 'ultimate DISCO' (uDISCO) clearing to overcome these limitations in volumetric imaging. uDISCO preserves fluorescent proteins over months and renders intact organs and rodent bodies transparent while reducing their size up to 65%. We used uDISCO to image neuronal connections and vasculature from head to toe over 7 cm and to perform unbiased screening of transplanted stem cells within the entire body of adult mice. uDISCO is compatible with diverse labeling methods and archival human tissue, and it can readily be used in various biomedical applications to study organization of large organ systems throughout entire organisms.**



Until recently, histological techniques relied on sectioning to observe nonsuperficial cellular structures deep in tissues. However, investigation of complex cells with large projections, such as those in the nervous system, is best performed in intact tissue. While recently developed tissue-clearing methods have overcome obstacles imposed by light scattering[1–10], the difficulties associated with specimen size remain to be addressed. Available clearing methods either increase or do not change the volume of tissues, with the exception of organic-solvent-based methods such as 3D imaging of solvent-cleared organs (3DISCO), which causes a substantial volumetric reduction instead[5,6,11].

When combined with tissue clearing, light-sheet microscopy produces micrometer-resolution image volumes of large specimens within minutes. However, several limitations still exist. Photons traveling through samples (cleared or uncleared) are absorbed or scattered by interaction with the tissue, resulting in attenuation of both excitation and emission light[12,13]. Relatively thick light sheets (thickness ≥ 4 µm) are used to image volumes larger than a few hundred micrometers[14]. These light sheets are generated by cylindrical lenses and have Gaussian profiles; thinnest widths, which provide the best resolution, occur only at the beam waist. Thus, the volume of sample that can be imaged at the highest resolution is limited to the central region of the light sheet. Finally, both small imaging chambers and the short working distance (WD ≤8 mm) of high numerical aperture (NA ≥ 0.9) objectives pose additional challenges. Thus, 3D reconstruction of neuronal connections over 5–8 mm (the approximate size of a mouse brain) has remained a challenging task.

Organic-solvent-based clearing methods, such as 3DISCO, achieve the highest level of transparency and size reduction among all clearing approaches[11,15]. 3DISCO has been used to study immune cells[16], stem cells[17], cancer cells[18], and transdifferentiating lung cells[19]; and it has been combined with deep-tissue antibody labeling and automated activity mapping[20–22]. However, 3DISCO quickly quenches endogenously expressed fluorescent proteins (with a half-life of a few days)[6], which has limited the applicability of 3DISCO. Here, we developed uDISCO, a method that revealed and preserved the signal of endogenous fluorescence over months while retaining the advantageous size reduction. Thus, uDISCO allows subcellular imaging of 2× to 3× larger volumes in a single scan and avoids or reduces artifacts of physical sectioning and mosaic imaging. Using uDISCO, we imaged entire bodies of adult rodents to determine long-distance neuronal and vascular projections and spatial information on stem cell transplants (which have previously been difficult to study) at single-cell resolution.

## RESULTS

### uDISCO preserves endogenous signal and reduces volume by 65%

We reasoned that 3DISCO-induced shrinkage could be promising for imaging whole rodent bodies. However, 3DISCO resulted in a fast decline of endogenous fluorescence signal during whole-body clearing, where longer treatments with clearing solutions are required (**Supplementary Figs. 1** and **2**). To overcome this, we searched for organic compounds that preserved fluorescence while providing a potent tissue-clearing effect. Our screen

[1]Institute for Stroke and Dementia Research, Klinikum der Universität München, Ludwig Maximilians University of Munich (LMU), Munich, Germany. [2]Graduate School of Systemic Neurosciences (GSN), Munich, Germany. [3]Munich Cluster for Systems Neurology (SyNergy), Munich, Germany. [4]German Center for Neurodegenerative Diseases (DZNE, Munich), Munich, Germany. [5]Current address: Department of Molecular and Cellular Neurobiology, Nencki Institute of Experimental Biology of Polish Academy of Sciences, Warsaw, Poland. [6]These authors contributed equally to this work. Correspondence should be addressed to A.E. (ali.ertuerk@med.uni-muenchen.de).

RECEIVED 1 MARCH; ACCEPTED 26 JULY; PUBLISHED ONLINE 22 AUGUST 2016; DOI:10.1038/NMETH.3964

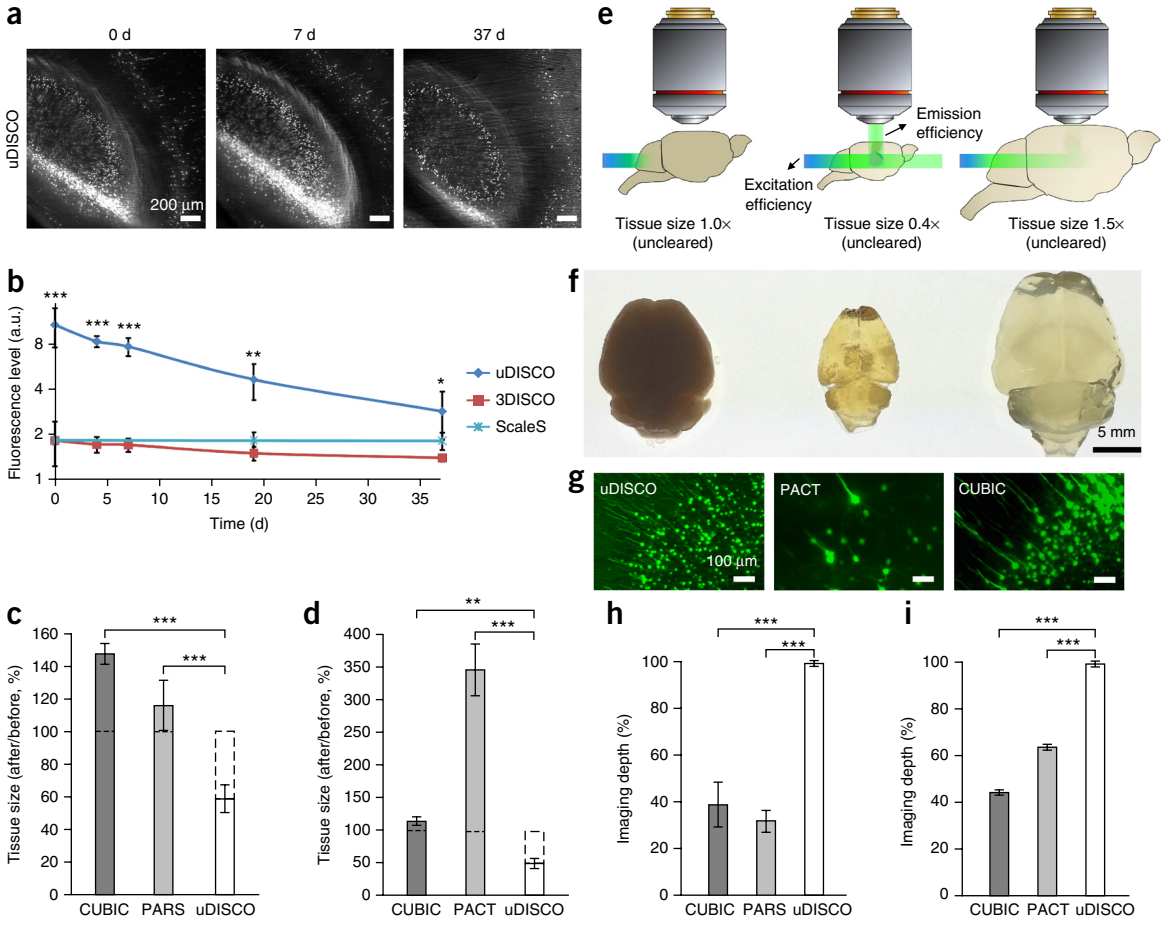


**Figure 1** | Development and principles of uDISCO. (**a**) Preservation of GFP (*Thy1*–GFP-M brain) after uDISCO, assessed by light-sheet microscopy. (**b**) Fluorescence-level quantifications in the GFP-M brains after uDISCO, ScaleS, and 3DISCO over time ($n$ = 3, 3, and 4 mice, respectively; a.u., arbitrary unit). (**c**) Volume changes of 4-month-old GFP-M mice after CUBIC, PARS, and uDISCO whole-body clearing ($n$ = 5, 3, and 7 mice, respectively). (**d**) Volume changes of dissected brains from 6-month-old mice after CUBIC, PACT, and uDISCO passive clearing ($n$ = 4, 4, and 3 mice, respectively). (**e**) Illustration of the advantages and disadvantages of tissue shrinkage versus expansion during imaging. (**f**) Mouse brains (GFP-M, 4 months old): uncleared (left), after uDISCO (middle), and after CUBIC (right) whole-body clearing. (**g**) Light-sheet microscopy imaging of cortical neurons in GFP-M brains with shrinkage (uDISCO) and expansion (PACT and CUBIC) after clearing. (**h**) Imaging depth quantifications on brains after CUBIC, PARS, and uDISCO whole-body clearing ($n$ = 4, 4, and 3 mice, respectively). (**i**) Imaging depth quantifications on brains after CUBIC, PACT, and uDISCO passive clearing of dissected brains ($n$ = 4, 3, and 3 mice (6 months old), respectively). All values are mean ± s.d.; statistical significance in **b**–**d**, **h**, and **i** (*, $P < 0.05$; **, $P < 0.01$; and ***, $P < 0.001$) was assessed by one-way ANOVA followed by Dunnett's *post hoc* test.

resulted in a tissue-clearing method (uDISCO) based on diphenyl ether (DPE), an organic solvent with a refractive index of 1.579 (**Supplementary Fig. 3**). uDISCO reveals fluorescence notably better and maintains it several weeks longer within *Thy1*–GFP-M mouse brains (expressing GFP in a sparse neuronal population[23]) compared with 3DISCO and water-based ScaleS protocols (**Fig. 1a**,**b**, **Supplementary Figs. 4**–**6**, and **Supplementary Video 1**). As DPE has a melting point of 26 °C, we mixed it with benzyl alcohol (−15 °C melting point) and benzyl benzoate (18 °C melting point) to obtain a mixture that is liquid at room temperature, which we named BABB-D (**Supplementary Table 1** and **Supplementary Protocol**). Additionally, uDISCO utilizes both the antioxidant α-tocopherol (Vitamin E) to scavenge peroxides and *tert*-butanol[24], a dehydrating reagent that is more stable than tetrahydrofuran (THF) used in 3DISCO. With the resulting protocol, the fine structures of labeled neurons in the lipid-dense brain and spinal cord can be detected over weeks to months.

uDISCO effectively cleared internal organs (**Supplementary Fig. 7**) and hard tissues, including calcified bones (**Supplementary Figs. 8**–**10**; **Supplementary Videos 2** and **3**), without any additional treatment, such as decalcification with EDTA[25]. Bones are heavily mineralized, allowing only minimal exchange of clearing solutions. Therefore, bone clearing requires clearing solutions with similar refractive index (RI) to reduce the clearing duration and light scattering. The RI of bones has been estimated as 1.555–1.564 (refs. 26 and 27), which is very similar to the RI of BABB-D, the final clearing agent in uDISCO.

We measured the size-reduction capability of uDISCO compared with existing whole-body clearing techniques. We found that whole-body clearing by uDISCO reduced the volume of mice (~42%), while both CUBIC (clear, unobstructed brain imaging cocktails and computational analysis) and PARS (perfusion-assisted agent release *in situ*) whole-body clearing methods enlarged it (**Fig. 1c** and **Supplementary Fig. 11**). We also tested the size reduction on dissected organs and found that uDISCO

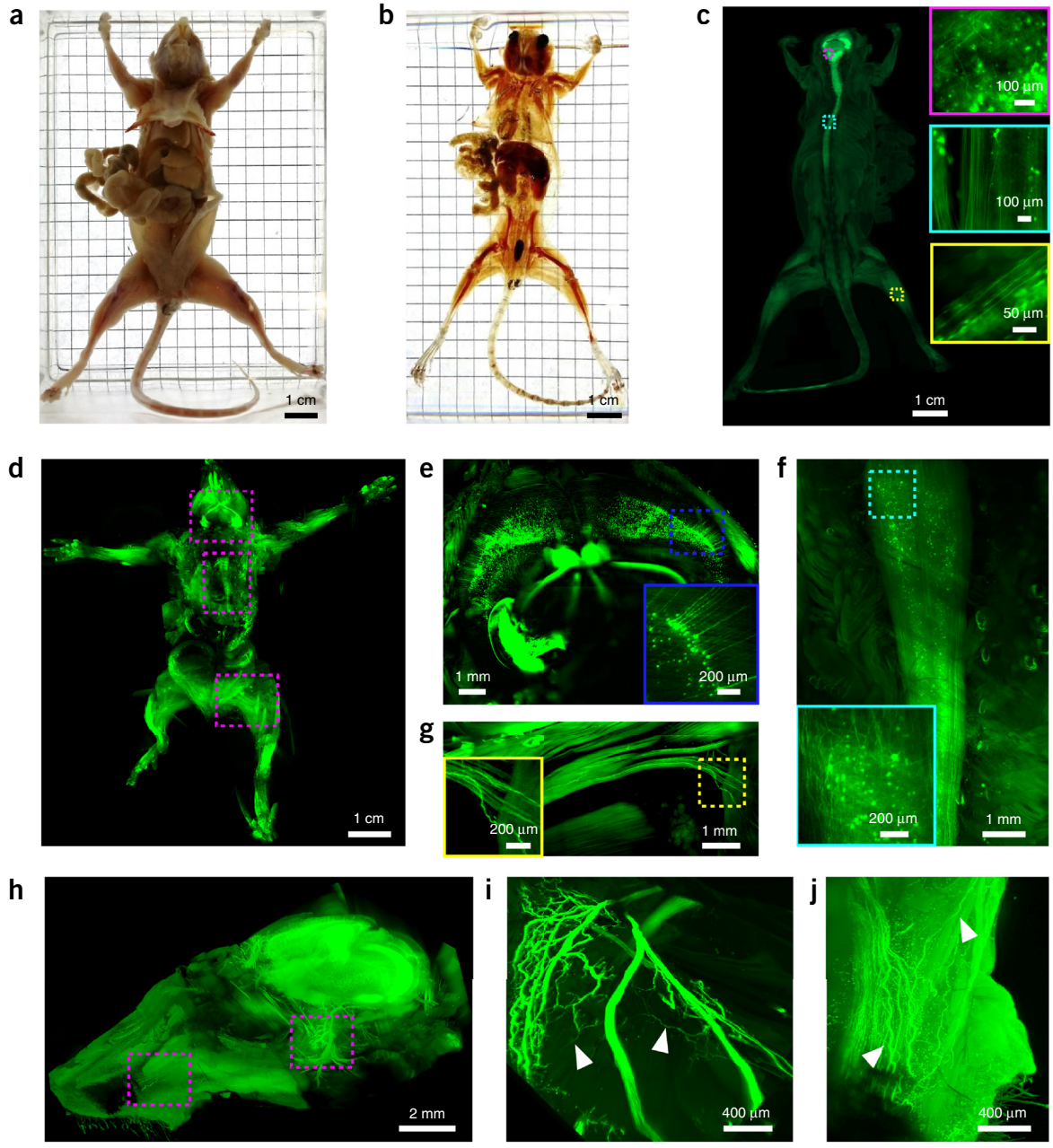


**Figure 2** | Whole-body clearing and imaging of adult mouse with uDISCO. (**a**–**c**) Adult GFP-M mouse (3 months old) was transcardially perfused (**a**), cleared with uDISCO (**b**) and imaged by fluorescence stereomicroscope at cellular resolution (**c**). Insets show higher-magnification images of the brain (magenta rectangle), spinal cord (cyan rectangle), and sciatic nerve (yellow rectangle). (**d**) Whole-body light-sheet imaging of intact GFP-M mouse (4 weeks old). (**e**–**g**) High-magnification images of the boxed regions in **d**. Colored rectangles show high-magnification images from the indicated regions in the brain (**e**), spinal cord (**f**), and sciatic nerve (**g**). (**h**) 3D visualization of the intact head from *Thy1*-YFP-H mouse (4 months old) after whole-body uDISCO clearing, indicating the detailed structure of optic nerve (**i**) and nerves at the base of the whiskers (**j**). The arrowheads in **i** and **j** mark some of the individual axons. The composites in **c**, **d**, and **h** were obtained via tile imaging.

reduced the size of adult mouse brains up to 55%, in contrast to CUBIC and PACT (passive CLARITY technique), both of which enlarged mouse brains (**Fig. 1d** and **Supplementary Fig. 11**). This size reduction, together with uDISCO's preservation of fluorescent proteins, resulted in a substantial advantage for imaging larger volumes compared with other tissue-clearing methods (**Fig. 1e**,**f**). Using light-sheet microscopy, we found that the maximum portion of a cleared tissue that can be imaged at once increased 2× to 4× with uDISCO compared with PARS or PACT and CUBIC (**Fig. 1g**–**i**).

To test whether the shrinkage was isotropic, we compared images before and after clearing. We found that brain tissues such as the cortex and hippocampal layers shrank homogenously, ~30% in each dimension at macroscopic scale (**Supplementary Fig. 12**). In addition, the shrinkage of different cell types (neurons, glia, etc.) and vasculature in the same brain region was homogenous in all dimensions (**Supplementary Fig. 13**). Finally, we found that individual cell and vascular morphologies were preserved in brain tissue after uDISCO clearing (**Supplementary Fig. 14**).

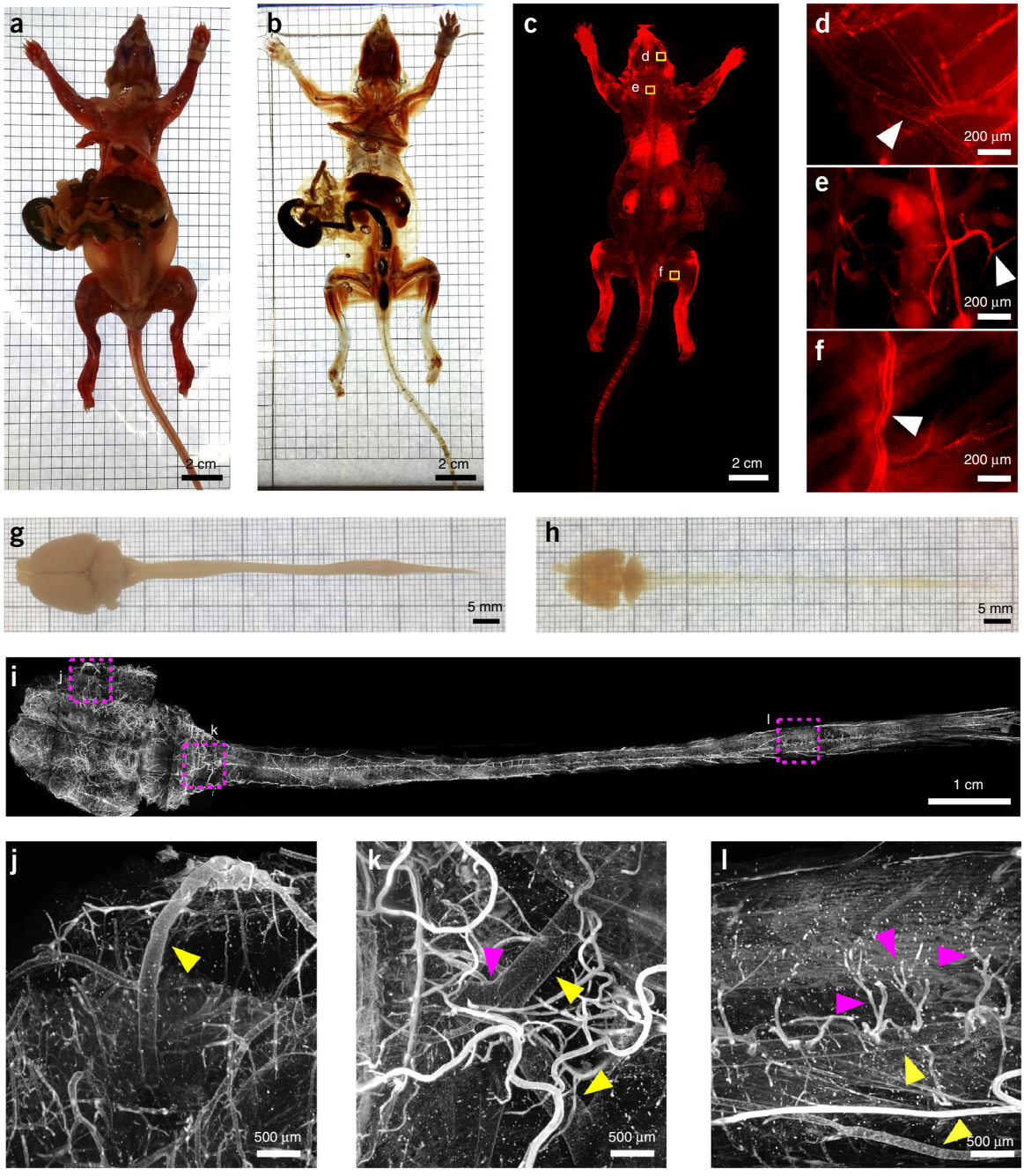


**Figure 3** | Whole-body clearing and imaging of rats with uDISCO. (**a**–**c**) A young adult female rat (4 weeks old) was injected with Texas Red Dextran to label the vasculature. The rat was transcardially perfused (**a**), cleared with uDISCO (**b**) 20 min after the dextran injection, and imaged with a fluorescence stereomicroscope (**c**). (**d**–**f**) High-magnification images of the boxed regions in **c**, such as the brain (**d**), spinal cord (**e**), and hindlimb (**f**). (**g**–**i**) Adult rat (10 weeks old) CNS (brain and spinal cord) before (**g**) and after (**h**) uDISCO clearing. (**i**–**l**) 3D visualization of vasculature via light-sheet imaging throughout the entire CNS from the adult rat (**i**). The vasculature in the cortex (**j**) (yellow arrowhead shows the right middle cerebral artery), brainstem (**k**) (yellow arrowheads show the two vertebral arteries, and purple arrowhead shows the basilar artery), and lumbar spinal cord (**l**) (yellow arrowheads show the spinal vessels, and purple arrowheads show their small s ulcal branches) are shown. The composites in **c** and **i** were obtained via tile imaging.

### uDISCO enables micrometer-resolution whole-body imaging

We used uDISCO on whole rodent bodies for system-level interrogation. We cleared the whole body of an adult *Thy1*–GFP-M mouse within 3–4 d (**Fig. 2a**,**b**; 3-month-old mouse; the skin was removed before clearing). We first imaged the whole transparent mouse with a standard fluorescence stereomicroscope (**Fig. 2c**; the skull and vertebra were removed for epifluorescence imaging). We readily identified the individual neurons and their extensions throughout the brain, spinal cord, and limbs in the intact mouse (**Fig. 2c**). To accommodate the entire transparent mouse into the imaging chamber of a standard light-sheet microscope, we constructed sample holders to keep the cleared specimens in place within the imaging chamber for automated tile scans without obstructing the excitation light

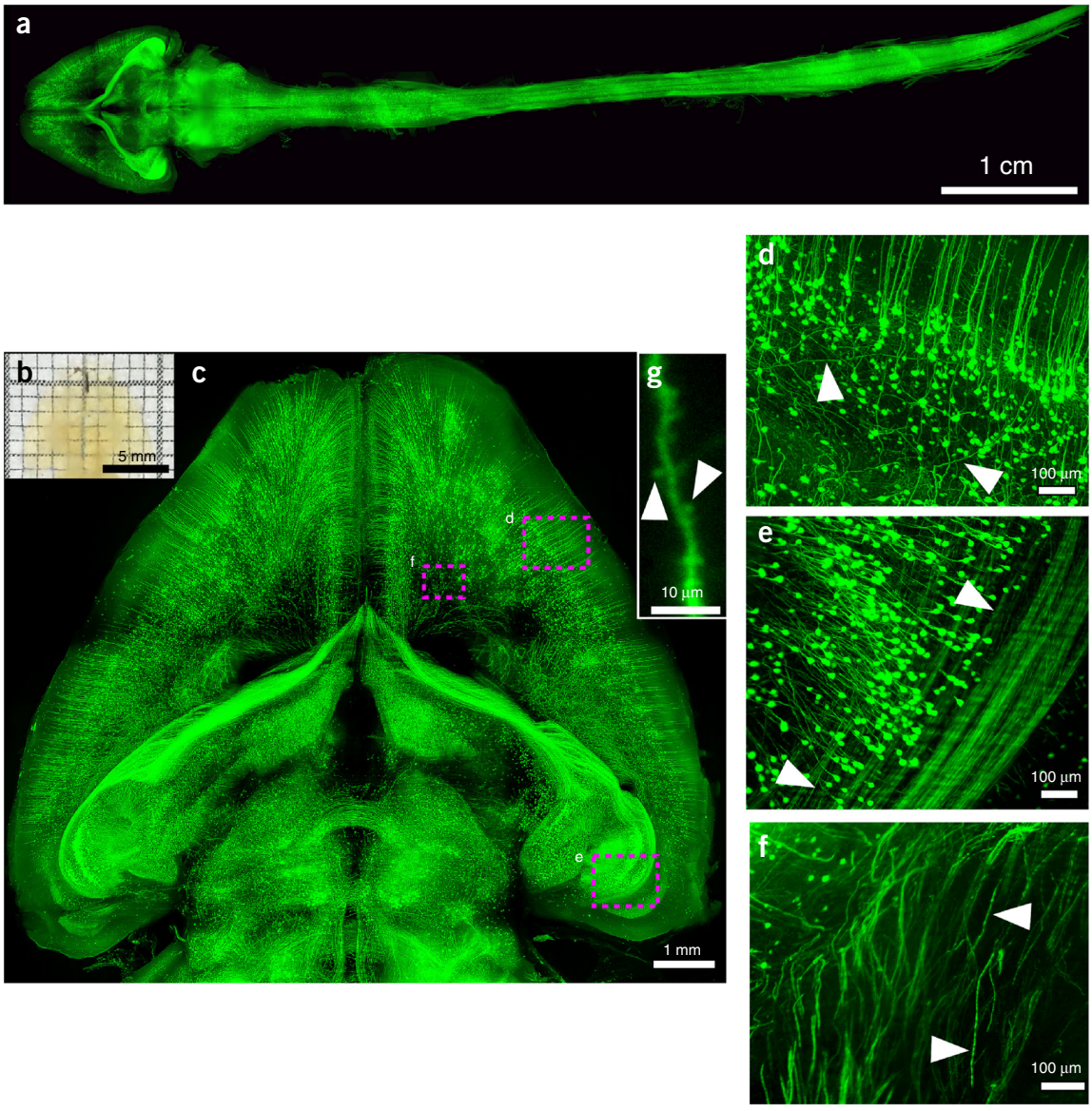


**Figure 4** | Projections throughout the entire adult mouse CNS (whole brain and spinal cord). (**a**) The intact CNS from a GFP-M mouse (4 months old) after uDISCO clearing and light-sheet microscopy imaging. (**b**) Image of the brain in **a** showing the transparency after uDISCO. (**c**) Details of neuronal structures in the entire brain in **a**. (**d**–**f**) High-magnification images of boxed regions in **c**, showing the neuronal structures at subcellular resolution in the cortex (**d**), in the hippocampus (**e**), and projecting to the midbrain (**f**). (**g**) After uDISCO, imaging of dendritic spines with light-sheet microscopy. The composites in **a** and **c** were obtained via tile imaging.

(**Supplementary Figs. 15** and **16**). Upon shrinkage, the width of the largest body region (torso) was reduced from 2.24 ± 0.052 cm to 2.0 ± 0.048 cm (mean ± s.e.m., $n$ = 7 mice), allowing us to complete 10-mm depth scans from dorsal and ventral sides of the mouse (**Supplementary Fig. 17**). Subsequently, we imaged the entire transparent mouse using light-sheet microscopy to detect neuronal structures throughout the intact mouse body at ~0.5- to 2-µm lateral and ~4-µm axial resolution (**Fig. 2d**). Subcellular details of neuronal projections in the whole body were visible throughout the animal with light-sheet microscopy (**Fig. 2e**–**g**). In addition, large body regions such as the head, torso, and whole limbs could be studied in detail. For example, when we imaged the entire head from an adult *Thy1*–YFP-H mouse[23], we observed the projections of optic nerves and innervation of whiskers (**Fig. 2h**–**j**).

uDISCO is also applicable to larger rodents. Rats (*Rattus norvegicus*) are valuable experimental models in toxicology and neurological studies because, compared with those of mice, rat physiology and behavior more closely resemble those of humans. uDISCO successfully cleared whole rats (**Fig. 3a**,**b** and **Supplementary Fig. 18**). We could observe the details of Texas Red–dextran-labeled vasculature in the brain, brainstem, and limbs using a standard fluorescence stereomicroscope in the intact 4-week-old rats (**Fig. 3c**–**f**). In addition, uDISCO achieved uniform clearing and over 60% tissue shrinkage of the intact central nervous system (CNS) in adult rats (10 weeks old, $n$ = 4 rats; **Fig. 3g**,**h**). Subsequently, we obtained light-sheet microscopy images of the vasculature in the intact CNS over 13 cm (**Fig. 3i** and **Supplementary Video 4**). We identified vascular structures such as the right middle cerebral artery (**Fig. 3j**); the two vertebral

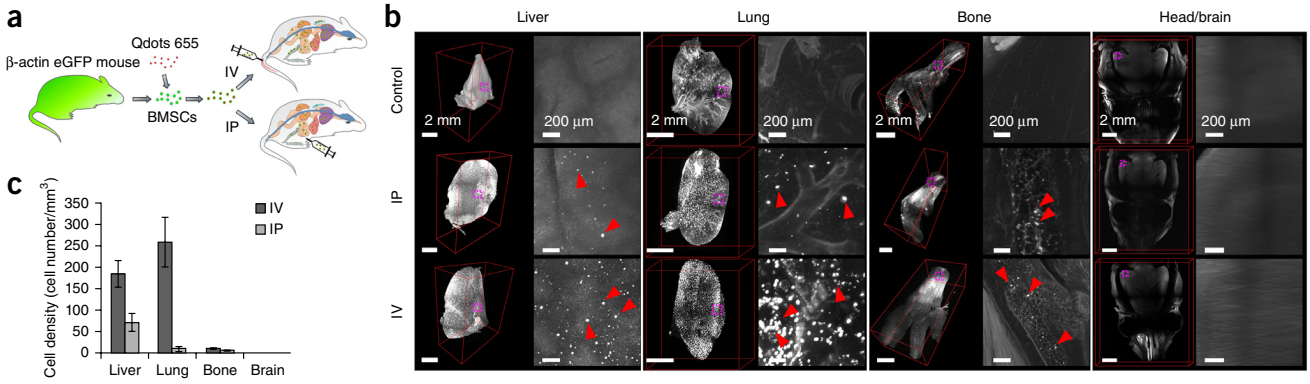


**Figure 5** | Distribution of mouse BMSCs after transplantation. (**a**) Illustration of the experimental design. (**b**) Images of liver, lung, limb, and head (brain) from host mice in control, IP, and IV groups assessed by light-sheet imaging. The composites of individual organs were obtained via tile imaging. The background autofluorescence signal outlines the overall morphology of the organs. Some Qdots-positive BMSCs are indicated by red arrowheads. (**c**) Quantification of BMSCs in different organs. Values are mean ± s.e.m.; $n = 3$ mice for each group (control, IP, and IV).

arteries, which merge to form the basilar artery (**Fig. 3k**); and the spinal vessels and their small sulcal branches (**Fig. 3l**).

### uDISCO allows tracing of the intact central nervous system

Since we could image the intact CNS of rodents with light-sheet microscopy at subcellular resolution, we used uDISCO to trace neuronal structures from head to toe in the entire CNS (brain and spinal cord) of 3- to 5-month-old *Thy1*–GFP-M adult mice. We could trace individual axons in the intact CNS over several centimeters in these scans (**Fig. 4a**; **Supplementary Videos 5** and **6**). Focusing on the brain, we observed the details of neuronal structures in the cortex, the hippocampus, and fine axonal projections to the midbrain (**Fig. 4b–f** and **Supplementary Video 7**). PACT[1] and CUBIC[8] reported visualization of dendritic spines using confocal or two-photon microscopy. For the first time for an organic-solvent-based clearing method in intact adult mouse brain, uDISCO achieved dendritic-spine resolution using light-sheet microscopy (**Fig. 4g** and **Supplementary Video 8**).

### uDISCO allows interrogation of BMSCs in the entire mouse

Bone marrow stem cells (BMSCs) are widely used for neuroprotection, regeneration, immunomodulation, and localized drug delivery studies[28,29]. So far, assessment of their distribution and densities has relied on methods such as histology, bioluminescence, or radiolabeling[30]. These approaches are time consuming and lack the sensitivity to detect sparsely localized cells or unexpected sites of grafting[31]. We used uDISCO whole-body clearing for an unbiased screen of transplanted syngeneic mouse BMSCs in the entire body at single-cell resolution. We collected BMSCs from β-actin EGFP mice as described previously[32] and labeled them with quantum dots (Qdots) (**Supplementary Fig. 19**). Cells easily incorporate Qdots, which do not interfere with cell functionality or migration capacities and therefore Qdots are widely used for cell tracking[33]. Subsequently, we injected the cells either intravenously (IV) or intraperitoneally (IP) into host C57BL/6N mice (**Fig. 5a**). Control animals were injected with vehicle (PBS) only. At 3 h after injection, we euthanized the animals for whole-body clearing. We first imaged whole mouse bodies using a fluorescence stereomicroscope to determine sites of grafted BMSCs (**Supplementary Fig. 20**). Subsequently, we performed high-resolution light-sheet microscopy on body parts and organs that hosted BMSCs. As expected, the majority of BMSCs were trapped in the first-passage, low-flow organs such as the lungs, liver, and spleen after IV injection (**Fig. 5b,c**, **Supplementary Figs. 20–22**, and **Supplementary Video 9**)[31,34]. Moreover, we detected sparsely distributed BSMCs in organs such as kidneys, bone marrow, and intestines (**Fig. 5b,c**; **Supplementary Figs. 21** and **22**). The localizations in bone marrow and intestines are of high interest because they were previously difficult to investigate despite their importance for hematopoietic cell populations or immune reactions[31]. As reported[35], we did not observe any BMSCs in the intact healthy CNS (**Fig. 5b,c**). Overall, our data demonstrate that uDISCO whole-body clearing can be used to study density and distribution of fluorescently labeled transplanted cells throughout the entire host body at single-cell resolution in an unbiased way, combining both high speed and resolution for transplantation studies.

### uDISCO is compatible with virus labeling and immunostaining

Most animal models used in the laboratory, as well as human clinical samples, do not express fluorescent proteins. Hence, we sought to test alternative methods to label tissues for uDISCO. To this end, we used adeno-associated virus (AVV) tracing to label neurons in the CNS of mice. We transduced the right motor cortex of mice with AAV2–Syn–EGFP and the left motor cortex with AAV2–Syn–RFP (**Fig. 6a**). 4 weeks after transduction, we performed whole-body uDISCO clearing. Fluorescence expression of the virally delivered proteins was detectable in the brain and throughout the intact spinal cord (**Fig. 6b–f** and **Supplementary Fig. 23**). The pyramidal decussation of descending motor axons was clearly visible (**Fig. 6c**). We detected both bundles of axons as well as individual axons in the brain and spinal cord over several centimeters (**Fig. 6d–f**).

Antibody staining is a valuable approach for labeling molecules of interest without the need for fluorescent tagging. Deep-tissue antibody-labeling methods[20,21] were recently combined with 3DISCO. To test these methods with uDISCO, we cut 1-mm-thick tissue sections of mouse brains and labeled them with antibodies against glial fibrillary acidic protein (GFAP) and ionized calcium binding adaptor molecule 1 (Iba1) as well as with a DNA-specific dye (**Fig. 6g**). After uDISCO, the slices shrank more than 60% in volume. We found that the signals from GFAP (astrocytes), Iba1 (microglia and macrophages), and TO-PRO-3 (DNA dye) were visible

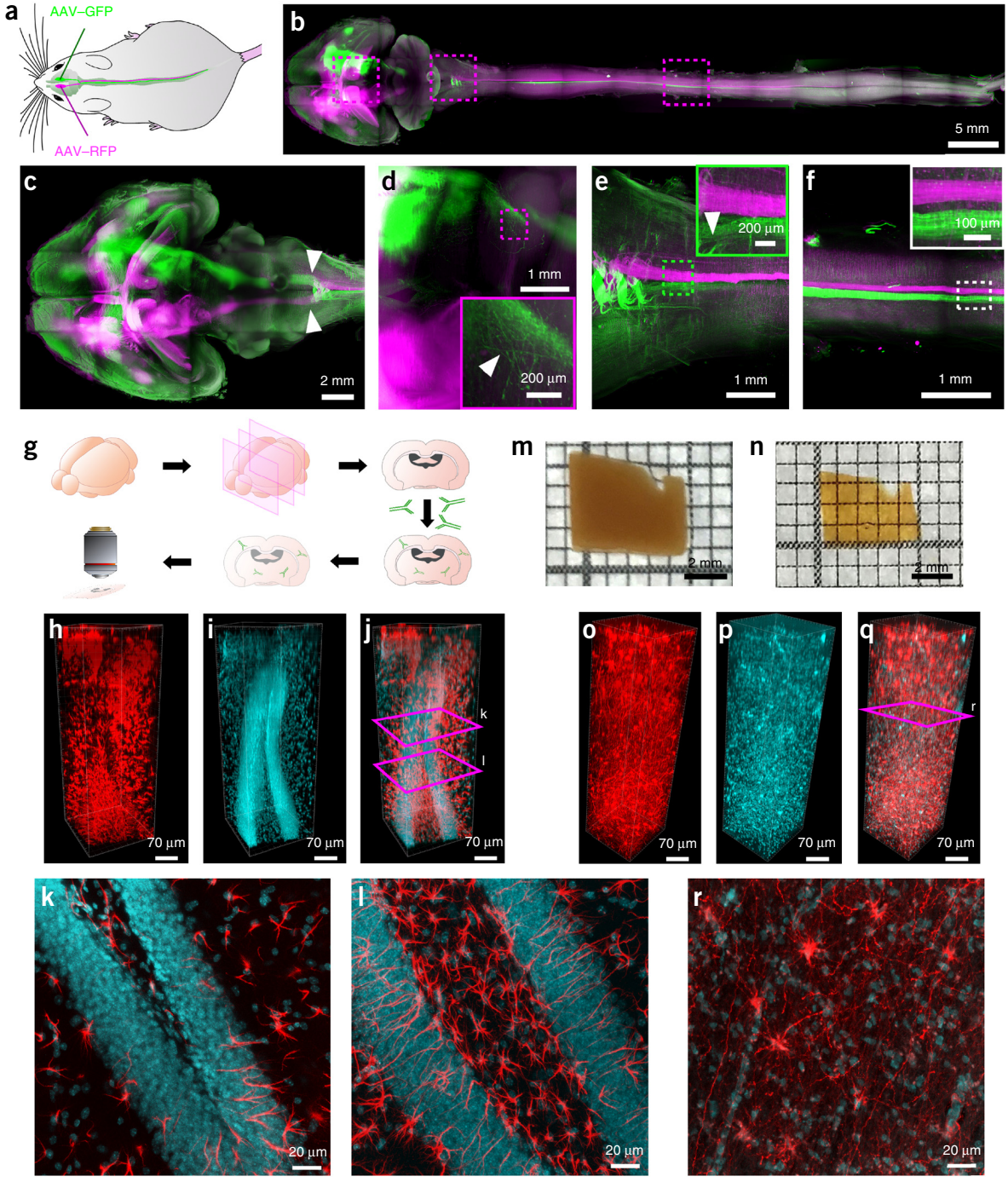


**Figure 6** | uDISCO is compatible with AVV neuron tracing and immunolabeling. (**a**) Experimental design for AAV–Syn–RFP and AAV–Syn–GFP injections. (**b**,**c**) Maximum-intensity projections of the entire brain (**b**,**c**) and CNS (**b**) after whole-body uDISCO clearing. Arrowheads in **c** indicate decussation of the descending motor axons. (**d**–**f**) Details of neuronal extensions of boxed regions in (**b**): the thalamus and midbrain (**d**), cervical (**e**), and thoracic (**f**) spinal cord regions. Colored rectangles show the enlarged views from the respective images. (**g**) Immunolabeling workflow. (**h**–**l**) GFAP and TO-PRO-3 labeling of coronal sections. 3D reconstructions show labeling of astrocytes (**h**) and cell nuclei (**i**) stained by GFAP antibody and TO-PRO-3, respectively. (**j**) Merged image of **h** and **i**. (**k**,**l**) Maximum-intensity projections of the *z*-positions marked by purple boxes in **j**; nuclei are shown in cyan and astrocytes in red. (**m**,**n**) 14-month fixed human tissue before (**m**) and after (**n**) uDISCO. (**o**–**r**) GFAP and TO-PRO-3 labeling of 14-month fixed human cortical tissue. Astrocytes (**o**) and nuclei (**p**) are labeled. (**q**) Merged image of **o** and **p**. (**r**) Maximum-intensity projection of the *z*-position marked by the purple box in **q**; nuclei are shown in cyan and astrocytes in red. All values are mean ± s.d. The composites in **b** and **c** were obtained via tile imaging.

throughout the tissue, indicating compatibility of uDISCO with deep-tissue labeling (**Fig. 6h–l** and **Supplementary Fig. 24**).

Human clinical tissue samples are typically stored in 4% formalin over extended periods of time. To determine whether uDISCO could be applied to such specimens, we immunostained 1-mm-thick human samples (archived for either 1 month or 14 months) for GFAP and TO-PRO-3 or Iba1 and TO-PRO-3. We measured shrinkage of 52% and 46% in samples stored for 1 month or 14 months,

respectively (**Fig. 6m**,**n**). uDISCO allowed successful clearing, signal preservation, and imaging of human tissues stored in formalin more than a year (**Fig. 6o–r** and **Supplementary Fig. 25**), although the image quality was better for shorter storage periods (**Supplementary Fig. 25i**). Importantly, the combination of uDISCO and deep-tissue antibody labeling did not require additional antigen retrieval steps. Overall, these results demonstrate that uDISCO is a versatile method that can be used to clear and image different types of tissues with various labeling methods.

## DISCUSSION

uDISCO achieved whole-body clearing and imaging because of sample-size reduction and preservation of fluorescent proteins. Another major advantage of organic-solvent-based clearing methods is the easy handling of cleared tissues; specimens become hard because of dehydration, yet are flexible enough for versatile positioning of long samples, such as the entire spinal cord of adult rats. In contrast, concentrated glycerol and sugar solutions used in various clearing methods are difficult to work with because of their high viscosity, the resulting gel-like texture of the cleared tissue, and the air bubbles generated during the refractive-index matching procedures and imaging[11].

Recently, tissue expansion was used to obtain super-resolution images of small volumes (expansion microscopy)[36–38]. Treweek *et al.*[25,39] used a similar concept (expansion (e) PACT) for high-resolution imaging. While expansion provides more resolution, tissue shrinkage, in theory, decreases resolution (30% in one dimension for uDISCO). However, uDISCO resulted in high-quality images (**Supplementary Fig. 26**), allowing the visualization of dendritic spines and individual axons over several centimeters in the intact CNS of adult mice. This high image quality could result from a larger proportion of shrunken samples (compared with nonshrinking samples) fitting into the optimal imaging region of the light sheet. Hence, shrinkage allows imaging of 2× to 3× larger volumes in the same setup without apparent loss of resolution. Importantly, uDISCO did not alter the structural integrity of the brain either at macroscopic (e.g., cortex and hippocampus structures) or microscopic scales (e.g., individual cells). However, isotropic shrinkage remains to be confirmed for other tissues such as muscle or fat. In addition, uDISCO can be combined with microscopy techniques that deliver even higher resolution and/or faster scanning, such as confocal, two-photon, and lattice light-sheet microscopy[40]. We demonstrated that high numerical aperture (NA), long working distance objectives such as Zeiss CLARITY 20× and Olympus 25× are compatible with uDISCO (**Supplementary Fig. 27**).

Acute injuries in the CNS might affect not only the injury site but also uninjured distal parts of the CNS[41,42]. Thus, repair strategies after CNS traumas need to be evaluated throughout the entire CNS. The uDISCO approach enables the assessment of long-range axonal projections and individual cells throughout entire organisms. Hence, this approach can help to reduce (1) the bias of analyzing only selected organs; (2) the time needed to prepare and screen individual organs and body parts of a complete mouse[43]; and (3) by generating whole mouse atlases and databases it can reduce the resources and number of animals needed in experimental research.

Whole-body clearing of diverse tissues, and the compatibility of this method with different imaging techniques, may have broad applications in the biomedical sciences. Whole-body clearing approaches could facilitate the assessment of neurodegeneration in diseases that affect both the central and peripheral nerves such as in amyotrophic lateral sclerosis (ALS), inflammation that may extend from gut to brain, stem cell transplantation studies, or even 3D mapping of the cellular structures in larger brain volumes, possibly even the whole human brain.

## METHODS

Methods and any associated references are available in the online version of the paper.

*Note: Any Supplementary Information and Source Data files are available in the online version of the paper.*


### ACKNOWLEDGMENTS

This work was supported by the Vascular Dementia Research Foundation, Synergy Excellence Cluster Munich (SyNergy), ERA-Net Neuron (01EW1501A to A.E. and N.P.), and the European Union's Horizon 2020 research and innovation programme (grant agreement no. 666881, SVDs@target, M.D.). A.L. and N.P. were supported by a Marie Curie Intra European Fellowship grant (FP7-PEOPLE-2013-IEF, project no. 625970). We thank M. Hübener and F. Voss (Max Planck Institute of Neurobiology, Munich) for providing mice; D. Trauner and O. Thorn-Seshold for helpful discussions; A. Weingart for illustrations; and C. Hojer, S. Tappan and T. Misgeld for critical reading of the manuscript. C.P. and R.C. are members of the Graduate School of Systemic Neurosciences (GSN), Ludwig Maximilian University of Munich. Human tissues were provided by the brain bank of the Institute of Anatomy, University of Leipzig.


### AUTHOR CONTRIBUTIONS

A.E. designed and led all aspects of the project. C.P., R.C., and F.P.Q. performed most of the experiments. A.G. performed the image rendering and developed algorithms for data analysis. C.P., R.C., F.P.Q., and A.G. analyzed the data. A.L. interpreted data and performed the BMSC cultures, characterization, and transplantations; F.H. performed virus tracing; P.M. assisted first-clearing experiments; N.P. and M.D. supervised A.L. and F.H., respectively. A.E., C.P., R.C., F.P.Q., and A.G. wrote the paper. All authors edited the paper.

### COMPETING FINANCIAL INTERESTS

The authors declare no competing financial interests.




1. Yang, B. *et al.* Single-cell phenotyping within transparent intact tissue through whole-body clearing. *Cell* **158**, 945–958 (2014).
2. Hama, H. *et al.* ScaleS: an optical clearing palette for biological imaging. *Nat. Neurosci.* **18**, 1518–1529 (2015).
3. Chung, K. *et al.* Structural and molecular interrogation of intact biological systems. *Nature* **497**, 332–337 (2013).
4. Tainaka, K. *et al.* Whole-body imaging with single-cell resolution by tissue decolorization. *Cell* **159**, 911–924 (2014).
5. Ertürk, A. *et al.* Three-dimensional imaging of the unsectioned adult spinal cord to assess axon regeneration and glial responses after injury. *Nat. Med.* **18**, 166–171 (2011).
6. Ertürk, A. *et al.* Three-dimensional imaging of solvent-cleared organs using 3DISCO. *Nat. Protoc.* **7**, 1983–1995 (2012).
7. Kuwajima, T. *et al.* ClearT: a detergent- and solvent-free clearing method for neuronal and non-neuronal tissue. *Development* **140**, 1364–1368 (2013).
8. Susaki, E.A. *et al.* Whole-brain imaging with single-cell resolution using chemical cocktails and computational analysis. *Cell* **157**, 726–739 (2014).
9. Ke, M.T., Fujimoto, S. & Imai, T. SeeDB: a simple and morphology-preserving optical clearing agent for neuronal circuit reconstruction. *Nat. Neurosci.* **16**, 1154–1161 (2013).
10. Susaki, E.A. *et al.* Advanced CUBIC protocols for whole-brain and whole-body clearing and imaging. *Nat. Protoc.* **10**, 1709–1727 (2015).
11. Richardson, D.S. & Lichtman, J.W. Clarifying tissue clearing. *Cell* **162**, 246–257 (2015).
12. Tuchin, V.V. Tissue optics and photonics: light-tissue interaction. *Journal of Biomedical Photonics & Engineering* **1**, 98–134 (2015).
13. Lichtman, J.W. & Conchello, J.A. Fluorescence microscopy. *Nat. Methods* **2**, 910–919 (2005).

14. Dodt, H.U. *et al.* Ultramicroscopy: three-dimensional visualization of neuronal networks in the whole mouse brain. *Nat. Methods* **4**, 331–336 (2007).
15. Susaki, E.A. & Ueda, H.R. Whole-body and whole-organ clearing and imaging techniques with single-cell resolution: toward organism-level systems biology in mammals. *Cell Chem. Biol.* **23**, 137–157 (2016).
16. Liu, Z. *et al.* Immune homeostasis enforced by co-localized effector and regulatory T cells. *Nature* **528**, 225–230 (2015).
17. Espinosa-Medina, I. *et al.* Neurodevelopment. Parasympathetic ganglia derive from Schwann cell precursors. *Science* **345**, 87–90 (2014).
18. Oshimori, N., Oristian, D. & Fuchs, E. TGF-β promotes heterogeneity and drug resistance in squamous cell carcinoma. *Cell* **160**, 963–976 (2015).
19. Lafkas, D. *et al.* Therapeutic antibodies reveal Notch control of transdifferentiation in the adult lung. *Nature* **528**, 127–131 (2015).
20. Renier, N. *et al.* iDISCO: a simple, rapid method to immunolabel large tissue samples for volume imaging. *Cell* **159**, 896–910 (2014).
21. Belle, M. *et al.* A simple method for 3D analysis of immunolabeled axonal tracts in a transparent nervous system. *Cell Rep.* **9**, 1191–1201 (2014).
22. Renier, N. *et al.* Mapping of brain activity by automated volume analysis of immediate early genes. *Cell* **165**, 1789–1802 (2016).
23. Feng, G. *et al.* Imaging neuronal subsets in transgenic mice expressing multiple spectral variants of GFP. *Neuron* **28**, 41–51 (2000).
24. Schwarz, M.K. *et al.* Fluorescent-protein stabilization and high-resolution imaging of cleared, intact mouse brains. *PLoS One* **10**, e0124650 (2015).
25. Treweek, J.B. *et al.* Whole-body tissue stabilization and selective extractions via tissue-hydrogel hybrids for high-resolution intact circuit mapping and phenotyping. *Nat. Protoc.* **10**, 1860–1896 (2015).
26. Ascenzi, A. & Fabry, C. Technique for dissection and measurement of refractive index of osteones. *J. Biophys. Biochem. Cytol.* **6**, 139–142 (1959).
27. Genina, E.A., Bashkatov, A.N. & Tuchin, V.V. Optical clearing of cranial bone. *Adv. Opt. Technol.* **2008**, 1–8 (2008).
28. De Miguel, M.P. *et al.* Immunosuppressive properties of mesenchymal stem cells: advances and applications. *Curr. Mol. Med.* **12**, 574–591 (2012).
29. D'souza, N. *et al.* Mesenchymal stem/stromal cells as a delivery platform in cell and gene therapies. *BMC Med.* **13**, 186 (2015).
30. Guenoun, J. *et al.* *In vivo* quantitative assessment of cell viability of gadolinium or iron-labeled cells using MRI and bioluminescence imaging. *Contrast Media Mol. Imaging* **8**, 165–174 (2013).
31. Leibacher, J. & Henschler, R. Biodistribution, migration and homing of systemically applied mesenchymal stem/stromal cells. *Stem Cell Res. Ther.* **7**, 7 (2016).
32. Nemeth, K., Mayer, B., Sworder, B.J., Kuznetsov, S.A. & Mezey, E. A practical guide to culturing mouse and human bone marrow stromal cells. *Curr. Protoc. Immunol.* **102**, Unit 22F.12 (2013).
33. Rosen, A.B. *et al.* Finding fluorescent needles in the cardiac haystack: tracking human mesenchymal stem cells labeled with quantum dots for quantitative *in vivo* three-dimensional fluorescence analysis. *Stem Cells* **25**, 2128–2138 (2007).
34. Goldmacher, G.V. *et al.* Tracking transplanted bone marrow stem cells and their effects in the rat MCAO stroke model. *PLoS One* **8**, e60049 (2013).
35. Detante, O. *et al.* Intravenous administration of 99mTc-HMPAO-labeled human mesenchymal stem cells after stroke: *in vivo* imaging and biodistribution. *Cell Transplant.* **18**, 1369–1379 (2009).
36. Chen, F., Tillberg, P.W. & Boyden, E.S. Optical imaging. Expansion microscopy. *Science* **347**, 543–548 (2015).
37. Chozinski, T.J. *et al.* Expansion microscopy with conventional antibodies and fluorescent proteins. *Nat. Methods* **13**, 485–488 (2016).
38. Chen, F. *et al.* Nanoscale imaging of RNA with expansion microscopy. *Nat. Methods* **13**, 679–684 (2016).
39. Treweek, J.B. & Gradinaru, V. Extracting structural and functional features of widely distributed biological circuits with single cell resolution via tissue clearing and delivery vectors. *Curr. Opin. Biotechnol.* **40**, 193–207 (2016).
40. Chen, B.C. *et al.* Lattice light-sheet microscopy: imaging molecules to embryos at high spatiotemporal resolution. *Science* **346**, 1257998 (2014).
41. Bareyre, F.M. *et al.* The injured spinal cord spontaneously forms a new intraspinal circuit in adult rats. *Nat. Neurosci.* **7**, 269–277 (2004).
42. Wahl, A.S. *et al.* Neuronal repair. Asynchronous therapy restores motor control by rewiring of the rat corticospinal tract after stroke. *Science* **344**, 1250–1255 (2014).
43. Reinhardt, R.L., Khoruts, A., Merica, R., Zell, T. & Jenkins, M.K. Visualizing the generation of memory CD4 T cells in the whole body. *Nature* **410**, 101–105 (2001).

## ONLINE METHODS

A step-by-step protocol for uDISCO is available as **Supplementary Protocol** (and ref. 44).

**Animals.** We used the following animals in the study: 1- to 6-months-old, mixed gender 27 (15 male and 12 female) C57BL/6N (Charles Rivers Laboratories), 57 (28 male and 29 female) *Thy1*–GFP mice (line GFP-M), 5 (2 male and 3 female) *Thy1*–YFP mice (line YFP-H)[23], 32 (13 male and 19 female) CX3CR1–GFP mice (B6.129P-Cx3cr1tm1Litt/J, Jackson Laboratory strain code: 005582), 6 (3 male and 3 female) β-actin EGFP mice (C57BL/6-Tg(CAG–EGFP); 131Osb/LeySopJ, Jackson Laboratory strain code: 006567), and four rats (4 female) (CD IGS Rat strain 001). Sample sizes were chosen based on preliminary experiments. Sample sizes are specified in figure legends. The animals used in this study were selected for each experiment based on their genetic background (wild type or fluorescent transgenes), and animals that resulted fluorescent-protein negative by genotyping were excluded from the study. Within each strain, animals were randomly selected; different stages of experiments (clearing, imaging, and data analysis) were carried out by different operators. Animals were housed in our animal facility under a 12/12 h light/dark cycle and were provided food and water ad libitum. Experiments were conducted according to institutional guidelines of the Ludwig Maximilian University of Munich after approval of the Ethical Review Board of the Government of Upper Bavaria (Regierung von Oberbayern, Munich, Germany). All data are reported according to the ARRIVE criteria[45].

**Human tissue.** Human tissues used for this study were obtained from five donors of 64–89 years old (1 male and 4 females). Human tissue donors gave their informed and written consent to the donation of their bodies for teaching and research purposes regulated by the Saxonian Death and Funeral Act of 1994 (third section, paragraph 18 item 8).

**Perfusion and tissue preparation.** Animals were deeply anesthetized by intraperitoneal injection with the triple combination of midazolam/medetomidine/fentanyl (MMF) (1 ml per 100 g of body mass for mice) before intracardial perfusion. Subsequently, animals were perfused transcardially (100–125 mm Hg pressure on Leica perfusion one system) with heparinized 0.1 M PBS (10 U/ml of heparin, Ratiopharm) for 5–10 min at room temperature until the blood was washed out and with 4% paraformaldehyde in 0.1 M PBS (pH 7.4; Morphisto, 11762.01000) for 20 min using 100–125 mm Hg pressure. The dissected tissue samples (whole brain, spinal cord, whole brain with the spinal cord, and femurs) were postfixed in 4% paraformaldehyde for 1–2 d at 4 °C. Then, tissues were washed once in PBS for 5 min; meninges were removed; and bent samples, such as spinal cords, were kept straight for the clearing procedure.

For cut bone clearing, femurs dissected from CX3CR1–GFP mice were fixed in cold 4% PFA for 24 h. Afterwards, the bones were washed with PBS and incubated in 30% sucrose PBS solution overnight at 4 °C. For longitudinal dissection, a Leica cryostat (Leica, CM3050S) was used to cut the bones embedded in optimum cutting temperature (O.C.T.) formulation (SAKURA, 4583). The section thickness was set at 30 µm, and the serial sectioning was performed until the entire bone marrow appeared. The remaining intact half bones were collected and washed with PBS to remove OCT and then processed for immunostaining and respective clearing[46].

For whole-body clearing, after the mouse body was well perfused and fixed, the skin was separated from the body while avoiding adhesion of pelage. The skull and vertebra were carefully opened, avoiding any damage such as puncturing and squeezing of the tissue. Whole-body tissue clearing was started immediately.

**Immunostaining.** The following antibodies and dyes were used in this study: Iba1 (Wako, 019-19741, dilution 1:350), GFAP (Dako, Z033401-2, dilution 1:350), Collagen 4 (SouthernBiotech, 1340-01, dilution 1:650), AlexaFluor 647 conjugated anti-GFP rabbit polyclonal antibody (Life Technology, A31852, dilution 1:500), TO-PRO-3 iodide (642/661) (Life Technologies, T3605, dilution 1:500), AlexaFluor 568 goat anti-rabbit IgG (H+L) (Life Technologies, A-11036, dilution 8 µg/mL), AlexaFluor 647 goat anti-rabbit IgG (H+L) (Life Technologies, A-21245, dilution 8 µg/mL), and Cy3 AffiniPure donkey anti-goat IgG (H+L) (Jackson, 705-165-147, dilution 1:300).

For immunostaining, the tissues (mouse brains or human tissue) were cut into 1 mm slices using a vibratome (Leica, VT1200S). Mouse sections were immunostained using iDISCO[20] or Belle *et al.*[21] protocols. We used the following iDISCO protocol. The sections were initially pretreated: first, they were washed in 0.1 M PBS for 50 min two times, then they were incubated in 50% and 80% methanol (in 0.1 M PBS) for 50 min at each step and then in 100% methanol for 1 h two times. Sections were bleached with ice-cold 5% $H_2O_2$ (Sigma, D216763) and 20% DMSO (Sigma D8418)/methanol (AppliChem, 141091.1211) at 4 °C overnight. After bleaching, sections were washed in methanol for 45 min three times; then in 20% DMSO/methanol for 45 min two times; then in 80% and 50% methanol for 45 min each step; then in 0.1 M PBS for 45 min two times; and finally in PBS/0.2% Triton X-100 (Sigma, T8787) for 45 min two times. For the immunostaining step, pretreated sections were incubated in PBS–0.2% Triton X-100–20% DMSO–0.3 M glycine (Sigma, G8898) at 37 °C overnight, then blocked in PBS–0.2% Triton X-100–10% DMSO–6% goat serum at 37 °C for 1 d, washed in PBS–0.2% Tween-20 (Sigma, P9416) with 10 mg/ml heparin (PTwH) overnight and then incubated with primary antibody dilutions in PTwH–5% DMSO–3% goat serum at 37 °C with gentle shaking on an oscillator for 6–8 d, refreshing the primary antibodies once after 3–4 d. Sections were then washed for 1 h with PTwH four times and then incubated with secondary antibodies diluted in PTwH–3% goat serum at 37 C° with gentle shaking on an oscillator for 3–4 d, refreshing once after 2 d. Sections were finally washed in PTwH 30 min five times and incubated with TO-PRO-3 iodide (642w/661) (dilution 1:750) in PTwH for 5 h at room temperature with gentle oscillation, washed again for 1 h four times with PTwH, and stored at 4 °C in 0.1 M PBS until clearing.

Human sections were immunostained using a modification of the protocol from Belle *et al.*[21]; briefly, 1 mm thick brain sections were incubated on a rocker (IKA, 2D digital) at room temperature in PBSGT solution, which consists of 0.1 M PBS with 0.2% porcine skin gelatin (Sigma, G2500), 0.5% Triton X-100, and 0.05% sodium azide (Sigma, 71290) for 24 h. Next, PBSGT was exchanged with PBSGT + 1% goat serum containing the primary antibodies and left in incubation at 37 °C with gentle shaking on





doi:10.1038/nmeth.3964

an oscillator (IKA, MS 3 basic) for 8–9 d. The primary antibodies were refreshed once after 4–5 d. Then, samples were washed for 30 min with PBSGT five times at room temperature and incubated with secondary antibodies, diluted in PBSGT + 1% goat serum at 37 °C with gentle shaking on an oscillator for 4–5 d. The secondary antibody was refreshed once after 2 d. Finally, samples were washed for 30 min three times with PBSGT, incubated with TO-PRO-3 in PBSGT for 5 h at room temperature with gentle oscillation, washed again for 1 h four times with PBSGT and stored at 4 °C in 0.1 M PBS until clearing.

For cut bone immunostaining, collected half bones were pretreated with 5 d of PBSGT incubation at room temperature. Then, the tissue was incubated in PBSGT with 1% goat serum and AlexaFluor 647 conjugated anti-GFP antibody (dilution 1:500) at 37 °C for 10 d, refreshing once after 5 d, and finally washed five times with PBSGT for 10 min.

**Preparation of uDISCO solutions.** Dehydrating solutions were prepared by mixing *tert*-butanol (Sigma, 360538) and distilled water in the following concentrations: 30 vol% *tert*-butanol, 50 vol% *tert*-butanol, 70 vol% *tert*-butanol, 80 vol% *tert*-butanol, 90 vol% *tert*-butanol, 96 vol% *tert*-butanol. Pure (100%) *tert*-butanol has a melting point between 23 °C and 26 °C; therefore. we recommend keeping it above the melting temperature before use. Delipidation solution dichloromethane (DCM) (Sigma, 270997) was used as a pure solution. Three refractive index matching solutions were used: BABB-D4, prepared by mixing BABB (benzyl alcohol + benzyl benzoate 1:2, Sigma, 24122 and W213802) with diphenyl ether (DPE) (Alfa Aesar, A15791) at a ratio of 4:1 and adding 0.4% vol DL-alpha-tocopherol (Vitamin E) (Alfa Aesar, A17039); BABB-D10, prepared by mixing BABB with DPE at a ratio of 10:1 and adding 0.4% vol vitamin E; BABB-D15, prepared by mixing BABB with DPE at a ratio of 15:1 and adding 0.4% vol vitamin E. In passive clearing, BABB-D4 preserved the fluorescence signal better, while BABB-D15 gave better transparency. BABB-D10 was used for whole-body tissue clearing. The ratio of DPE to BABB can be adjusted to achieve either better preservation of fluorescence or more tissue transparency.

**uDISCO passive clearing procedure.** All incubation steps were performed in a fume hood with gentle rotation or shaking using 5 ml tubes (Eppendorf, 0030 119.401) for whole mouse brain or smaller samples, or steps were performed using glass chambers (Omnilab, 5163279) for bigger samples such as rat tissues or whole brain and spinal cord. The samples were covered with aluminum foil to keep them in dark.

The clearing consisted of serial incubations of the fixed samples in 5–80 ml of 30 vol%, 50 vol%, 70 vol%, 80 vol%, 90 vol%, 96 vol% and 100% *tert*-butanol at 34–35 °C to dehydrate the tissue, followed by immersion in DCM for 45–60 min at room temperature to remove the lipids. Eventually, they were incubated in BABB-D at room temperature for at least 2 h until samples became transparent. The requirement of DCM step and the incubation time of each step in tert-butanol solutions depended on sample size. For instance, small tissues such as mouse spinal cord or 1-mm-thick coronal slices did not need DCM step and required short incubation times (2–4 h) per each *tert*-butanol step compared with thicker or mineralized tissues such as whole brain and intact bones (12 h). Details of each protocol are showed in **Supplementary Table 1**. Samples could be stored in BABB-D at room temperature in dark for weeks.

All other clearing methods, including PACT, CUBIC, 3DISCO, 1-propanol BABB, ScaleS, SeeDB and Murray's clear (**Fig. 1**; **Supplementary Figs. 5**,**6**, and **9**–**11**), the clearing protocols were performed following the original publications[1,2,6,9,10,14,24,25,47].

**uDISCO whole-body clearing procedure.** We established a transcardial circulatory system comprised of a peristaltic pump (Gilson, Peristaltic Pump MINIPULS 3; **Supplementary Fig. 28**; see also the step-by-step protocol of uDISCO in **Supplementary Protocol**). In principle, two channels from the pump were required for circulation. The first channel pumped the clearing solution through the mouse body, and the second channel collected the solution exiting the mouse body and recirculated it back to the original bottle. Since clearing solutions are corrosive, Viton reference tubing was chosen (Gilson, F1817745) because it is resistant to clearing chemicals. First, the reference tubing was set up following the instructions, and each end of the tubing was connected to a tubing connector (Omnilab, 5434482). Next, the tubing connectors were linked with additional PVC tubing (Omnilab, 5437920). For the outflow tubing of the first channel, which injected the solution into the heart, the head part cut from a 1 ml syringe (Braun, 9166017V) was inserted as the connector of the perfusion needle and fixed with a mouse transcardiac perfusion needle (Leica, 39471024). Meanwhile, the inflow tubing of the second channel, which recirculated solution, was fixed to the glass chamber containing the mouse body. Eventually, the inflow tubing of the first channel was kept below the surface of the solution, and the circulation was started until air bubbles were pushed out from the tubing system.

All clearing steps should be performed in a fume hood. First, the mouse body was put in a glass chamber, and the perfusion needle was set into the heart through the same pinhole made during tissue preparation in the perfusion setup. Next, the chamber was covered with aluminum foil, and the transcardial circulation was started. Each gradient of dehydration solution was circulated at 8–10 ml/min for 10–12 h. As the melting point of *tert*-butanol is 23 to 26 °C (close to room temperature), a heating plate with 35–40 °C was used for the two rounds of 100% *tert*-butanol circulation to prevent the solution from solidification. The final step of tissue clearing could normally be achieved by circulating BABB-D10 with the same injection rate for 6–12 h. The transparency of the mouse body was checked by eye during clearing. Bubbles were carefully prevented from forming, especially in the first channel, at every step. For rat whole-body clearing, a thicker perfusion needle (Leica, 39471022) without rubber head was used, and each step of circulation was prolonged to 24 h with a flowing rate of 15–20 ml/min. A passive incubation step of DCM for 6–8 h with gentle shaking was included before performing BABB-D10 circulation. **Supplementary Table 1** summarizes the incubation times and temperatures of each clearing solution for whole-body clearing.

As a final note, the amount of solutions for circulation depends on the capacity of the clearing chamber. For mice whole-body clearing, if the maximum volume of the glass chamber is 400 ml, 300 ml of volume of solution was used for circulation. For rat whole-body clearing, a 1,000 ml capacity glass chamber with 800 ml working clearing solution would be sufficient.

PARS and CUBIC whole-body clearing methods (**Fig. 1** and **Supplementary Fig. 11**) were performed following the original papers[10,25].

**Vasculature labeling with Texas Red Dextran.** Texas Red Dextran (70,000 MW, Lysine Fixable, Invitrogen) was diluted in saline with a concentration of 15 mg/ml for mouse (0.1 ml per animal) and 8 mg/ml for rat (1 ml per animal). A pulled tubing (nonsterile polythene tubing, ID 0.86 mm, OD 1.27 mm, Harvard Apparatus) was attached to the syringe needle to achieve sharp ending thinner than femoral vein. For dextran injection, animals were anesthetized (MMF triple combination, 8 ml/kg, i.p.) and placed ventral side up. The right femoral vein was identified and exposed by surgical dissection in the inguinal region. The sharp ending of the tubing was inserted into the venous sinus of femoral vein, and the dextran was injected at a rate of 0.3–0.4 ml/min. After injection, the tubing was retreated and the wound was sealed by surgical suture. Then, the animals were placed in a warm cage for 15–20 min before proceeding with the standard perfusion and tissue preparation procedure. We experienced that skipping heparin in the prewashing step of the perfusion (and using only 0.1 M PBS instead) resulted in better labeling of the vasculature.

**Neuronal tracing by AAV virus.** AAVs expressed EGFP (AAV2–Syn–EGFP) and RFP (AAV2–Syn–RFP) under the promoter of human Synapsin (Vector Core, University of North Carolina). The final titers were around $2\times10^9$ GC (Genome Copy) per µl. For the virus injection, 3- to 4-month-old female C57BL/6N mice were anesthetized (MMF triple combination, 8 ml/kg, i.p.) and placed in a stereotaxic frame. To expose the motor cortex targeted for tracing axons into spinal cords, two cranial windows on each side of the skull were created within the area: 1.0 mm and 2.0 mm lateral; 0.5 mm anterior and 1.5 mm posterior to bregma. AAVs were injected into the cortex using a custom-established injector fixed with a pulled glass pipette. First, ten independent injection sites were targeted with the following coordinates: 1.2 mm and 1.8 mm lateral; 1.0 mm deep; 0.3 mm anterior to bregma, 0.1 mm, 0.5 mm, 0.9 mm, and 1.3 mm posterior to bregma. Next, 400 nl virus was injected at a rate of approximately 200 nl/min for every injection site. The glass pipette was kept *in situ* for 1 min before moving to the next site. After finishing all the injections, the cranial windows were covered by absorbable gelatin sponge (GELITA-SPON, GS-110), and the incision was closed by wound clips (CellPoint Scientific, part no. 203-1000). The animal was placed in a warm cage for waking up and then transferred into a regular keeping room. Carprofen (0.2 ml per injection, 1 mg/ml, i.p.) was given 3 times per d for 3 d. The animal survived for 4 weeks post virus injection before performing uDISCO.

**Culture and characterization of mouse BMSCs.** Mouse BMSCs were collected and cultured from β-actin EGFP mice as described previously[32,48]. Briefly, femur and tibia from 8- to 12-week-old mice (4–5 mice per culture) were removed under sterile conditions, and bone marrow was flushed out using a 20 gauge needle syringe. After mechanical dissociation with repeated flow of the bone marrow through needles of progressively smaller diameter, the cell suspension was filtered through a sterile 40 µm nylon cell strainer mesh. Cells were resuspended in a final density of $20 \times 10^6$ cells per ml of medium and were plated in T25 flasks (5 ml per flask) at 37 °C with 5% $CO_2$. Culture medium was composed of aMEM, 10% lot-selected mesenchymal-stem-cell-qualified fetal bovine serum (FBS), 1% L-glutamine, 1% penicillin–streptomycin, and medium was stored at 4 °C for 1–3 weeks until usage. The medium was changed on day 2 (half of medium) and day 7 (complete change), followed by a complete change of medium every 3–5 d. Cells were passaged for the first time when 70–80% confluent using 0.05% trypsin–EDTA, and they were split at a 1:3 ratio.

Characterization of mix BMSCs was done with flow cytometry (FACS) and differentiation assays on passage 3. For FACS analysis the following primary antibodies were used in two different staining panels: CD11b-eFluor450 (eBiosciences 48-0112, clone M1/70, dilution 1:400), CD45.2-PE (eBiosciences 12-0454, clone 104, dilution 1:400), CD34-eFluor450 (eBiosciences 48-0341, clone RAM34, dilution 1:100), Sca1-APC (eBiosciences 17-5981, clone D7, dilution 1:200), CD29-PE (eBiosciences 12-0291, clone HMb1-1, dilution 1:200), and CD44-APC (eBiosciences 17-0441, clone IM7, dilution 1:200). Briefly, cells were harvested by trypsinization with 0.05% trypsin, washed with ice-cold PBS, centrifuged at 1,500 r.p.m. for 8 min at 4 °C, resuspended at a concentration of $1–5 \times 10^6$ cells/ml, and stained with the primary antibodies for 45 min at 4 °C in the dark. Following washing with ice-cold PBS three times, cells were immediately read at a flow cytometer (BD Biosciences, FACS Verse). Unstained cells and cells stained with the corresponding isotypic controls were used as negative controls for FSC, SSC, and autofluorescence adjustments.

Osteogenic and adipogenic differentiation capacity of BMSCs was tested on cells of passage 3 as previously detailed[47]. Bone mineralization and fat droplets after osteo- and adipo-differentiation were detected using alizarin red and oil red O staining assays, respectively, according to standard protocols. Chondrogenic differentiation capacity of mBMSCs was studied using the StemPro chondrogenesis differentiation kit (Gibco A10071-01) according to manufacturer instructions; proteoglycans produced by chondrocytes were stained with 1% alcian blue solution according to a standard protocol. Characterization of the transplanted EGFP+ mBMSCs is shown in **Supplementary Fig. 19**. Approximately 30% of the transplanted cells were EGFP+, and 60% were loaded with quantum dots.

**Labeling of cells with Qdots.** The EGFP+ BMSCs were cultured for 30–45 d until reaching passage 4 or 5. 1 d before transplantation, EGFP+ BMSCs were labeled with fluorescent carboxyl quantum dot nanoparticles (Qtracker Qdots, Invitrogen, emission at 655 nm or 800 nm). The nanoparticles were aseptically reconstituted according to manufacturer's instructions (20 µl of component A and 20 µl of B), allowed to sit at room temperature for 5 min, vortexed for 30 s, mixed with full BMSC medium up to a volume of 400 µl, and then added to the flasks (200 µl per 1 T75 flask with confluent BMSCs). Labeling of the EGFP+ BMSCs with Qdots 655 was checked 24 h later with microscopy and FACS analysis before transplantation. The efficiency of the labeling and the presence of any remaining free Qdots was also checked by sequential transferring of the Qdots-containing medium to a new flask with BMSCs, which did not produce any further cell labeling.

**Transplantation procedures.** Transplantation of the EGFP+ BMSCs, EGFP+/Qdot-labeled BMSCs, or vehicle (PBS) was





doi:10.1038/nmeth.3964

performed via tail vein intravenous (IV) or intraperitoneal (IP) injections. The injections were performed in C57BL/6N mice. All animals were food-starved overnight before the transplantation to clear the intestines for visualization.

For IV transplantation, animals were shortly anesthetized with 2% isoflurane. To achieve maximum vein dilation for successful infusion, the tail was shortly dipped and gently massaged in warm water (35–38 °C, for 10 s) and was then immediately placed for 5 min between a prewarmed (38 °C) heating pad and warm wet gauzes. The suspension of $1 \times 10^6$ BMSCs in 300 µl was injected IV at once using a 30-gauge needle attached to a 1 ml syringe. The injection caused a short heart arrest (approximately 10 s) in some animals that recovered either spontaneously or after short thoracic massaging. For IP transplantations, animals were briefly (30–60 s) anesthetized with isoflurane just before the injection and then received IP injection of $1 \times 10^6$ BMSCs in 300µl of PBS at once. Following successful injections, animals recovered from anesthesia in a heat chamber (set at 30–31 °C) for approximately 30 min before returning to their home cage. The control animals were injected with PBS. 3 h after injection, we euthanized the animals for uDISCO.

**Imaging setup, light-sheet microscopy.** We used LaVision BioTec Ultramicroscope II light-sheet microscope (**Supplementary Table 2**). The axial resolution of the Ultramicroscope is 4 µm, and the lateral resolution is 0.5–2 µm, depending on the objective used (details are in **Supplementary Table 2**). We used exposure times of 250 ms to 50 ms, laser power of 1 to 3mW (25% to 70% of the power level at a given wavelength, mostly centered around 470 nm, 545 nm, or 640 nm), distributed across a Gaussian light sheet of variable width and NA; according to the manufacturer specifications, the light sheet has a thickness of 4.5 µm at its waist at 488 nm. A typical width spanning between 0.5 mm and 0.3 mm was chosen to adjust the illumination extent to the field of view of the objective used. The excitation branch of the imaging setup was used as provided, without further calibration. The microscope features a zoom body (Olympus revolving zoom unit U-TV, 1×, 2×, and 4×) equipped with an automated filter box for 25 mm mounted filters. An enhanced fluorescence acquisition branch consists of refractive-index-corrected long working distance objectives (Clear4brain, Munich): Olympus 2×/0.15 NA (WD 10 mm), Olympus 4×/0.28 NA (WD 10 mm) and Olympus 20×/0.45 NA (WD 5 mm). Making use of the entire scanning area, defined by the built-in scanner capabilities, we acquired tile scans to cover the entire specimens.

**Imaging setup, laser-scanning confocal microscopy.** Cleared specimens such as brain slices or whole organs were incubated in BABB-D solution for a minimum of 2 h. Samples were mounted on histological glasses using transparent silicone gel (OBI, 4799656): a pool on glass was created with the glass as the bottom surface and silicone as walls, then samples were put into the pool filled with BABB-D. Eventually, glass coverslips were used to seal the pool, creating a closed chamber to prevent leakage of BABB-D.

Regions of brain slices were imaged with an inverted laser-scanning confocal microscopy system (Zeiss, LSM 880) using a 25× water-immersion long working distance objective lens (Leica, 0.95 NA, WD = 2.5 mm) mounted on a custom mounting thread. The *z*-step size was 3–5 µm, and whole stacks of the slices were acquired (**Supplementary Table 2**).

**Imaging setup, fluorescence stereomicroscopy.** Cleared and uncleared specimens such as brain slices, whole bodies, or organs were immersed either in BABB-D or in PBS, respectively, and imaged with Zeiss AxioZoom EMS3/SyCoP3 fluorescence stereomicroscope using a 1× long working distance air objective lens (Plan Z 1×, 0.25 NA, WD = 56 mm; **Supplementary Table 2**).

**Image processing.** Processing and 3D rendering was executed by HP workstation with 8 core Xeon processor, 196 GB RAM, and Nvidia Quadro k5000 graphics card. We used Imaris, Amira, and Fiji (ImageJ2) for 3D and 2D image visualization. Stitching of tile scans was done via Fiji's stitching plugin[49]. Stitched images were saved in tiff format to enable fast processing using different software. We removed acquisition errors using Fiji's TrakEM2 plugin and Imglib2 (ref. 50) library.

Image processing consists of three main steps: error correction, image quality enhancement, and quantification.

*Error correction*. (e.g., **Fig. 3j**) Errors in image acquisition and following steps may occur for various reasons, such as physical interference with the microscope during image acquisition or miscalibration of a dynamic plate of the microscope, resulting in unwanted shifting of tiles or drifting effects between different slices of the same image series.

*Quality enhancement*. (e.g., **Fig. 5b**) We used filtering techniques (such as Gaussian, median, and anisotropic diffusion filtering) in the spatial domain for noise reduction. Morphological filters were used to correct the artifacts based on their shapes. Owing to the big size of data sets, filtering in the frequency domain is not feasible. Image intensity manipulation and equalization employed local (CLAHE in Fiji) and pseudo flat-field correction in Fiji (**Supplementary Video 1**).

*Quantification*. (e.g., **Fig. 5c**) To quantify the density of Qdot-positive BMSCs, we developed a simple workflow based on Fiji (**Supplementary Figure 29**).

**Quantifications.** *Normalized fluorescence signal profile plots and total signal intensity.*

Normalized signal profiles demonstrate the quality of the signal over the background, which defines the ability to trace the individual cellular structures in the scans (e.g., axon tracing in **Supplementary Video 6**). We calculated the total signal intensity to compare the remaining fluorescence signal after each clearing method. We presented details of these calculations with example images in **Supplementary Figure 30**.

For normalized signal profile measurement, a straight line was drawn across the specific area, which includes signal and background, and plotted via Fiji's 'plot profile' option. To calculate the mean background intensity, we chose another line adjacent to the profile line with no intersection to any specific signal. Subsequently, the profile plot was normalized by dividing the profile data over the calculated mean background intensity. Normalized profile of each sample was shown in the representative line chart (**Supplementary Figs. 2**,**5**,**6** and **10**).

For total signal intensity quantification, we selected a rectangular area covering the signal (several cellular structures), and measured the integrated density as the representative of the total signal

intensity of selected area. To calculate the mean background, a straight line was drawn across the area. Eventually, the total sum of the signal intensity in the sample area was determined as:

$$\text{Sum of background intensity} = \text{Number of background pixels} + \text{Mean background value}$$

$$\text{Sum signal intensity} = \text{Total sum of intensity of the area} - \text{Sum of background intensity}$$

We calculated the average total signal intensity by dividing the sum of the signal intensity over the pixel number of the rectangular selection (**Supplementary Figs. 2**,**5**,**6**,**9** and **10**).

*Signal-to-noise ratio (SNR).* A small part of the image was selected, and pixels belonging to a specific signal were separated from the background by thresholding the input image, *f*, and applying the binary image as the mask to the same image.

$$f(n,m) = S(o,p) + X(i,j)$$

$$o \neq i, p \neq j$$

*S* is the image that contains only the specific signal, and *X* is the background image. SNR was calculated based on Jahr *et al.*[51]

$$\text{SNR} = \text{Mean}(S)/\text{Std}(X)$$

*Peak signal-to-noise ratio* (PSNR). PSNR was calculated as previously described[52]. In brief, we used a mean square error (MSE) calculation between the sample image and a reference image. We took the average intensity of the background pixels as the reference image without the noise. Then, we calculated the MSE and PSNR as:

$$MSE = \frac{1}{N * M} \sum_{i=0}^{N-1} \sum_{j=0}^{M-1} [X(i,j) - Y(i,j)]^2$$

*Y* is the reference image with $N \times M$ dimension.

$$PSNR = 20 * \log_{10}\left(\frac{MAX}{\sqrt{MSE}}\right)$$

*MAX* represents the maximum intensity of the input image *f* in the selected neighborhood.

*RMSE calculation.* The root mean square (RMS) of the morphology deformation error at single-cell scale was used as a quantification factor for isotropy. RMSE calculation includes three steps: 1) Postclearing and preclearing images of a single cell were registered by similarity transformation in Fiji's TrakEM2 plugin. To achieve perfect overlay, output images from step 1 were registered with nonrigid transformations using Fiji's bUnwrapj plugin[53]. 2) The deformation parameter for preclearing image pixels was masked with a skeletonized preclearing image to remove irrelevant deformation parameters. 3) RMS of the deformation error with respect to the distance from the center of the cell or vessel (constant point) was calculated[37].

*Fluorescence level.* Fluorescence level quantification was expressed as a signal-to-background ratio and was calculated using Fiji at the following timepoints after clearing: 0, 4, 7, 19, and 37 d (**Fig. 1b**). From each brain scan, a *z*-projection of three consecutive images in Tiff format was made at the same anatomic region for all the samples. The mean value of the background for each *z*-projection was obtained by averaging the background values of 15–20 regions from equally sized areas of the projection without signal. To calculate the mean value of the signal of each *z*-projection, we used the threshold function of the software; the threshold was adjusted to consider the fluorescence signal visible in the projection. After adjusting the threshold, only the sharp signal from specific cellular structures was analyzed per each *z*-projection. To this end, we used Fiji's "analyze particles" to measure the signal intensity only of particles sized between 10 and 150 pixels (visible fluorescent cells), and we calculated the mean value from all the particles. Next, this value was divided by the mean value of the background of the respective projection, obtaining the fluorescence level on the background.

*Imaging depth quantification.* To assess the imaging depth between different clearing methods (CUBIC, PARS, PACT, and uDISCO), the tile scans of three whole brains per clearing method were taken with a light-sheet microscope with 4 µm *z* step (in **Fig. 1h**,**i**, and **Supplementary Fig. 11**). 3D reconstructions at the same anatomic level (from the surface of the brain to the center of the brain, including the region of the hippocampus) of each sample were shown in the coronal view using Imaris. Next, the images of the 3D reconstructions were analyzed in Fiji. Using the scale bar provided by Imaris, the distance of imaging depth was measured from the surface (where the signal was sharp) to the inner part of the brain until the last identifiable signal over the background coming from cell body or cellular structure (e.g., axons or dendrites) was detected.

**Statistical analysis.** Data are presented as mean ± s.d. in **Figures 1b–d**,**h**,**i**;**3i**;**6h**,**n** and in **Supplementary Figures 4**,**7b**,**8c**,**11b**,**12e**,**13s**,**25i**,**26**. Data are presented as mean ± s.e.m. in **Figure 5c** and in **Supplementary Figures 2c**,**5h**,**6h**,**9g**,**10h**. The data distribution in each experiment was checked for normality using Shapiro–Wilk test in IBM SPSS statistics software. *P* values were calculated using unpaired *t*-test to compare data between two groups (**Supplementary Figs. 2c**,**4**,**8c**,**25i**). One-way ANOVA was used to compare more than two groups of data (**Fig. 1b–d**,**h**,**i**; and **Supplementary Figs. 5h**,**6h**,**9g**,**10h**,**11b**,**12e**,**13s**); if ANOVA was significant, it was followed by *post hoc* Dunnett's test for multiple comparisons (**Figs. 1b–d**,**h**,**i** and **Supplementary Figs. 5h**,**6h**,**9g**,**10h**,**11b**).


44. Pan, C., Cai, R., Quacquarelli, F.P., Ghasemi, A. & Ertürk, A. Whole organ and organism tissue clearing by uDISCO. *Protocol Exchange* http://dx.doi.org/10.1038/protex.2016.055 (2016).
45. Kilkenny, C., Browne, W.J., Cuthill, I.C., Emerson, M. & Altman, D.G. Improving bioscience research reporting: the ARRIVE guidelines for reporting animal research. *PLoS Biol.* **8**, e1000412 (2010).
46. Acar, M. *et al.* Deep imaging of bone marrow shows non-dividing stem cells are mainly perisinusoidal. *Nature* **526**, 126–130 (2015).
47. Ertürk, A., Lafkas, D. & Chalouni, C. Imaging cleared intact biological systems at a cellular level by 3DISCO. *J. Vis. Exp.* **89**, e51382 (2014).
48. Zacharaki, D. *et al.* Characterization of *in vitro* expanded bone marrow-derived mesenchymal stem cells isolated from experimental autoimmune encephalomyelitis mice. *J. Mol. Neurosci.* **51**, 282–297 (2013).
49. Preibisch, S., Saalfeld, S. & Tomancak, P. Globally optimal stitching of tiled 3D microscopic image acquisitions. *Bioinformatics* **25**, 1463–1465 (2009).
50. Pietzsch, T., Preibisch, S., Tomancák, P. & Saalfeld, S. ImgLib2–generic image processing in Java. *Bioinformatics* **28**, 3009–3011 (2012).
51. Jahr, W., Schmid, B., Schmied, C., Fahrbach, F.O. & Huisken, J. Hyperspectral light sheet microscopy. *Nat. Commun.* **6**, 7990 (2015).
52. Gonzalez, R. *Digital Image Processing* 3rd edn. (India, Pearson Prentice Hall, 2006).
53. Arganda-Carreras, I. *et al.* Consistent and elastic registration of histological sections using vector-spline regularization. in *Computer Vision Approaches to Medical Image Analysis* (eds. Beichel, R.R. & Sonka, M.) 85–95 (Springer, 2006).






doi:10.1038/nmeth.3964

**Supplementary Figure 1: Whole-body clearing and imaging of adult mice with 3DISCO**

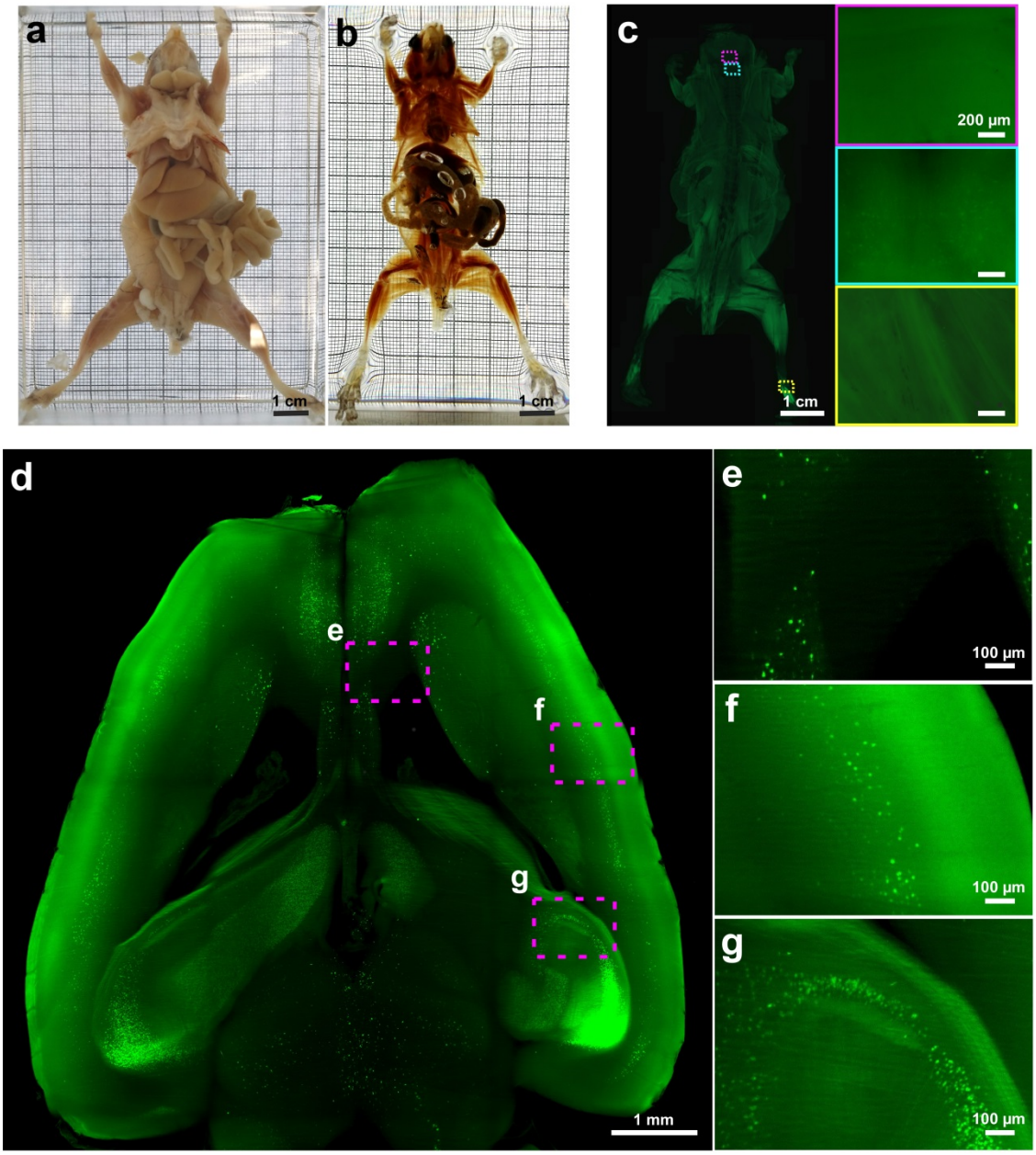


Whole-bodies of adult GFP-M mice (3 months old) were cleared with 3DISCO (same protocol as used in uDISCO). Before (**a**) and after (**b**) 3DISCO whole-body clearing images of a representative mouse body. 3DISCO whole-body clearing provided a comparable optical transparency to uDISCO (see Fig. 2b). (**c-g**) In contrast, preservation of endogenous GFP signal was weak after 3DISCO whole-body clearing. (**c**) Fluorescence stereomicroscope acquisition could not detect any identifiable neuronal structures unlike the uDISCO sample (see Fig. 2c). (**d-g**) Light-sheet microscopy of entire GFP-M mouse brain after 3DISCO whole-body clearing. While a weak GFP signal remained in some cell bodies, neuronal projections were completely undetectable due to diminished signal after 3DISCO whole-body clearing (see Fig. 4c-f).

**Supplementary Figure 2: Fluorescence signal quality comparison after whole body uDISCO and 3DISCO clearing**

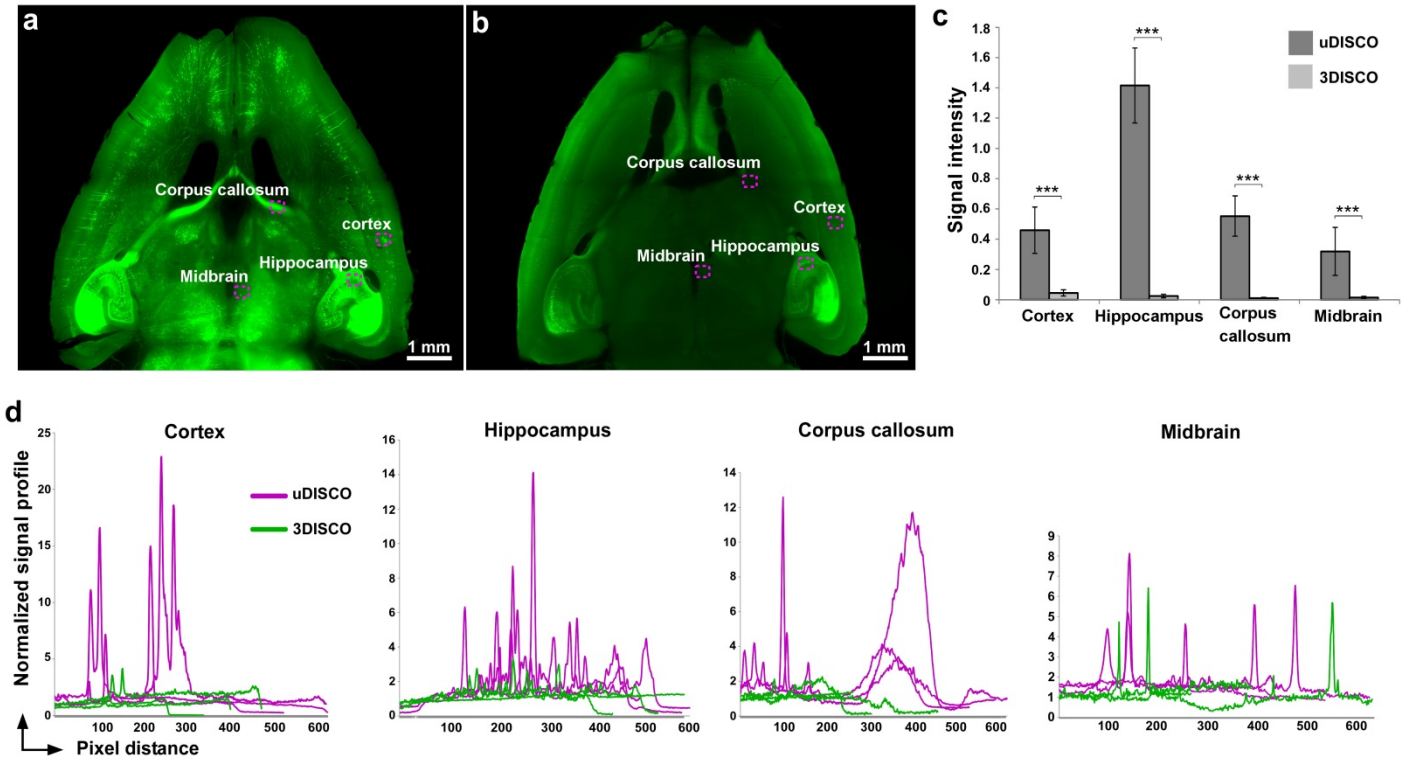


Representative light-sheet microscopy images of GFP-M brains at 2.5 mm depth from the dorsal surface after whole-body uDISCO (**a**) or 3DISCO (**b**) clearing. (**c**) Signal intensity (calculations are explained in Methods and Supplementary Fig. 30) comparison after whole-body uDISCO and 3DISCO clearing. Statistical significance (***$P < 0.001$) was assessed by unpaired *t*-test at each brain region. Values are mean ± s.e.m.; n=3 brains for each group (3 months old GFP-M mice). (**d**) Normalized signal profiles (calculations are explained in Methods and Supplementary Fig. 30) after whole body uDISCO and 3DISCO clearing at different depths (distance from brain surface) to compare the fluorescence signal: cortex (0.5 mm), hippocampus (1.2 mm), corpus callosum (2.5 mm) and midbrain (4.0 mm); n=3 brains for each group plotted (each magenta or green line profile represents one brain).

**Supplementary Figure 3: The details of chemicals used in 3DISCO and uDISCO**

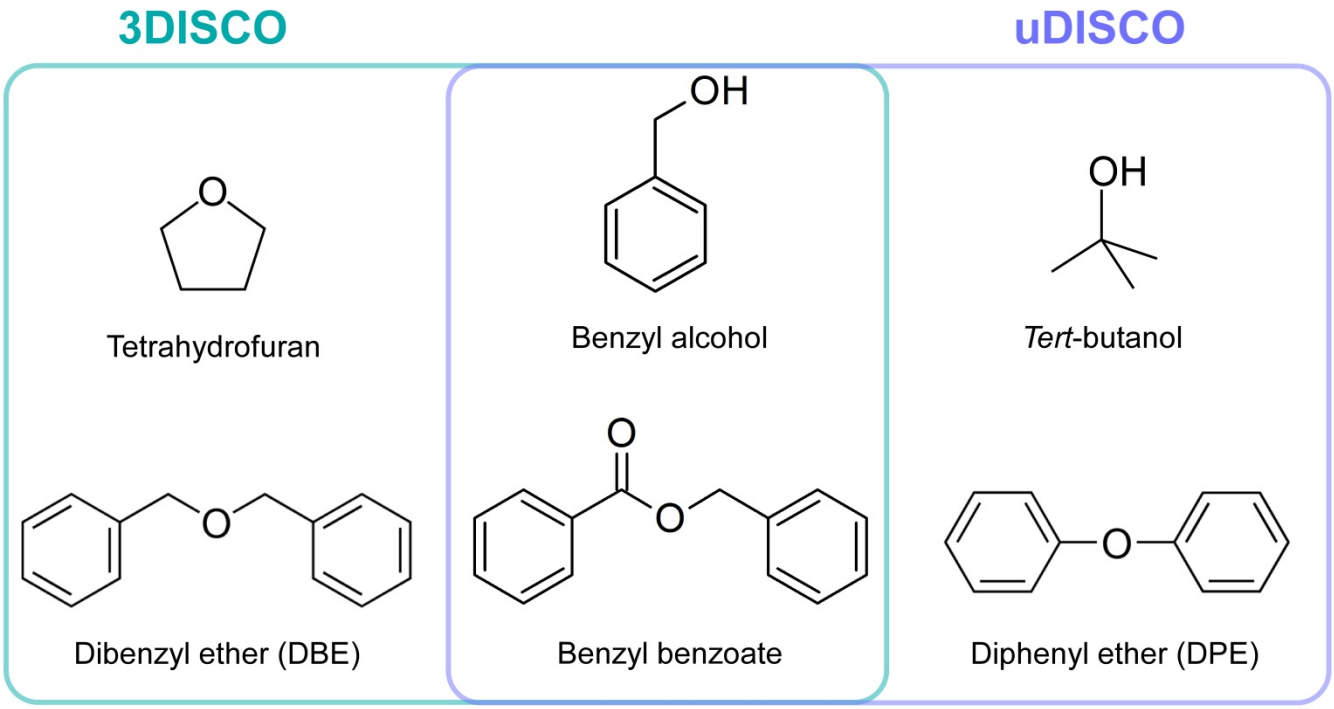


Tetrahydrofuran (THF) used in dehydration step of 3DISCO has an ether functionality, which is prone to oxidation and further reactions. In contrast, *tert*-butanol used in uDISCO is a tertiary alcohol and more stable to oxidation and less reactive. 3DISCO utilizes dibenzyl ether (DBE) or BABB (benzyl alcohol and benzyl benzoate) in refractive index matching step. Both of these chemicals have reactive benzylic C-H and C-O bonds, hence, they can form peroxidase and quench the fluorescence signal. To reduce chemical interactions that could diminish the endogenous fluorescence signal in uDISCO, 1) we performed refractive index matching in the presence of diphenyl ether (DPE): DPE does not have reactive benzylic C-H and C-O bonds, therefore, it is less prone to radical and other oxidative reactions; 2) we used antioxidant vitamin E to scavenge further the peroxides that can destroy the fluorescent proteins.

**Supplementary Figure 4: Endogenous fluorescent signal stabilization in uDISCO**

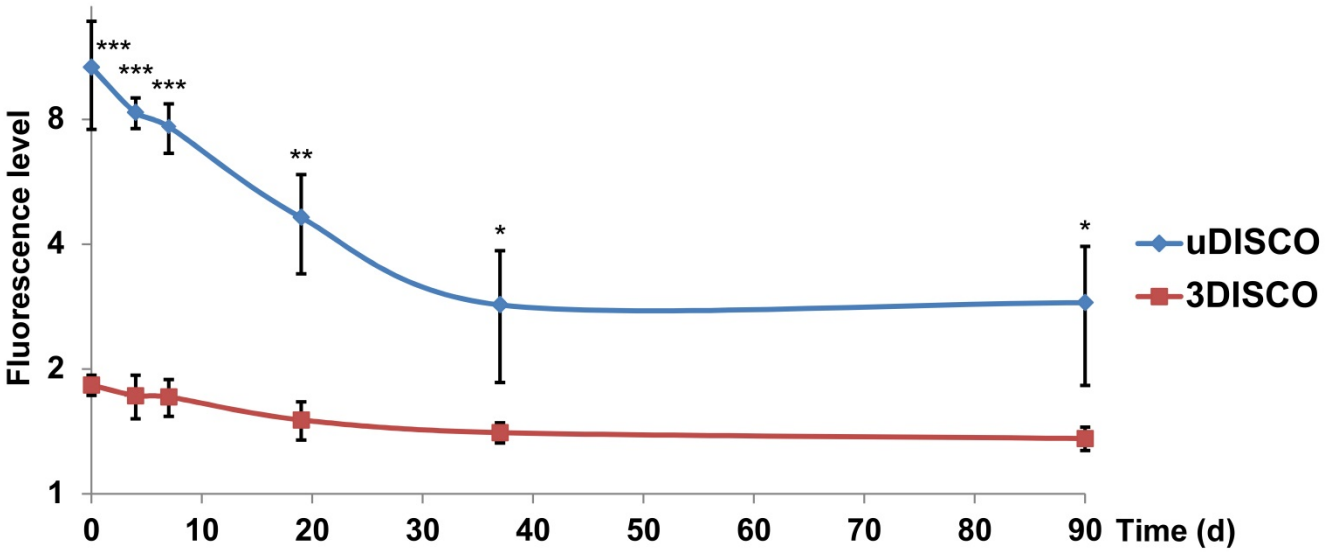


We measured the fluorescence signal of the same uDISCO and 3DISCO samples presented in Fig. 1b, 3 months after the clearing. We observed some decrease in signal level within the first few weeks (most probably due to the further dehydration of tissues in final clearing solutions), which got stabilized after about a month. At all-time points the level of fluorescence after uDISCO was higher compared with the level of fluorescence after 3DISCO. Values are mean ± s.d.; n=3 and 4 mice for uDISCO and 3DISCO, respectively. Statistical significance (*$P$ < 0.05, **$P$ < 0.01, ***$P$ < 0.001) was assessed by unpaired $t$-test.

**Supplementary Figure 5: Fluorescence signal quality comparison after uDISCO, 3DISCO, 1-proponal BABB, PACT, CUBIC, ScaleS and SeeDB clearing in *Thy1*-GFP-M mice**

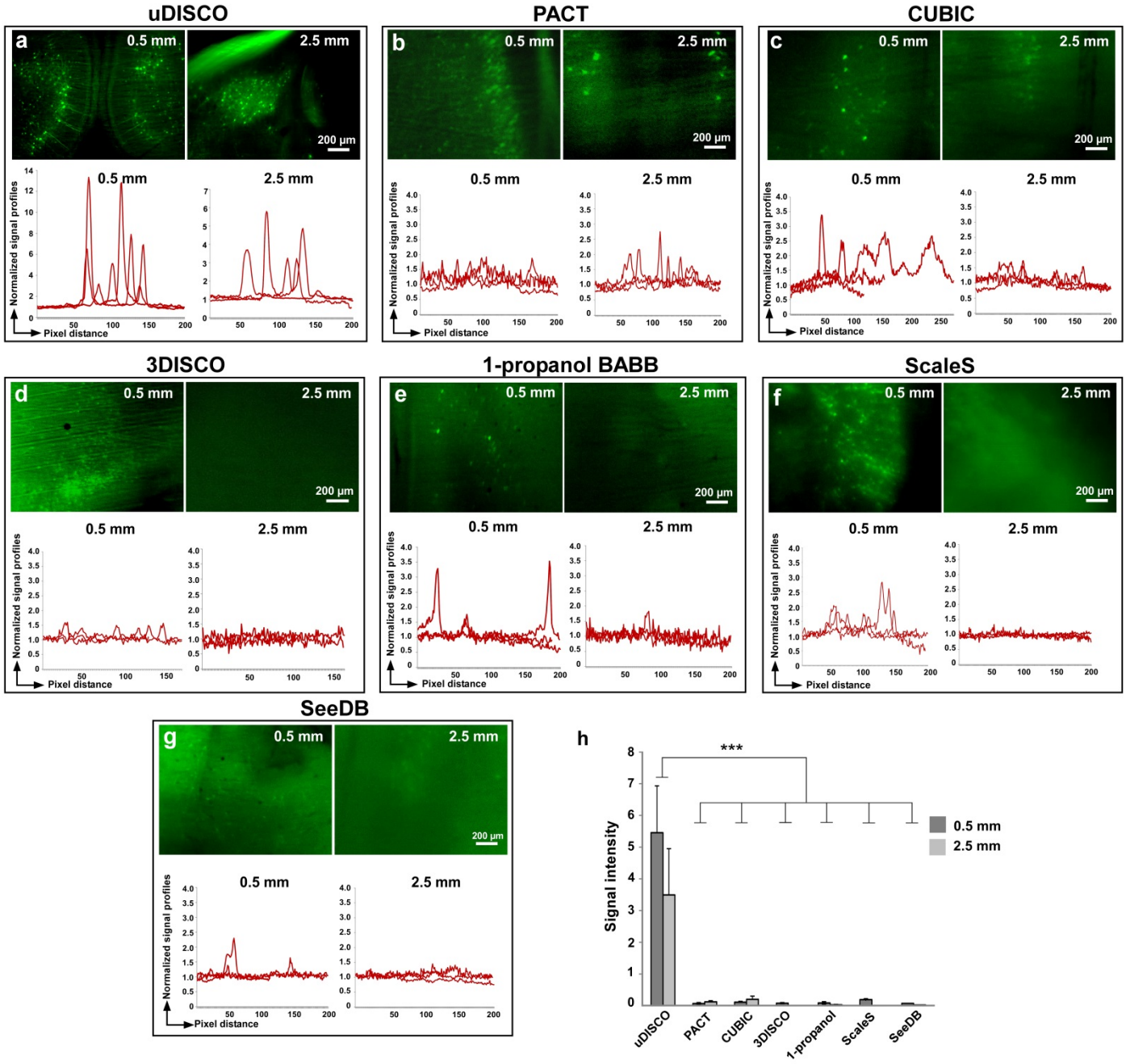


Representative images of normalized signal profiles at 0.5 mm and 2.5 mm depth from the dorsal surface after uDISCO (**a**), PACT (**b**), CUBIC (**c**), 3DISCO (**d**), 1-proponal BABB (**e**), ScaleS (**f**) and SeeDB (**g**) clearing of GFP-M brains. Normalized signal profile for each sample demonstrates the dynamic range of the obtained signal, which is the primary parameter for the tracing of imaged structures (separation of specific signal from the background). (**h**) Quantification of total signal intensity on specific cellular structures (cell bodies) at different depths (0.5 mm and 2.5 mm) of the samples after respective clearing (see the Methods and Supplementary Fig. 30). uDISCO cleared brains resulted in greater signal intensity compared with other methods. Statistical significance (***$P < 0.001$) was assessed by one-way ANOVA followed by Dunnet's post-hoc test. Values are mean ± s.e.m.; n=3 brains for each group (3 months old GFP-M mice).

**Supplementary Figure 6: Fluorescence signal quality comparison after uDISCO, 3DISCO, 1-proponal-BABB, PACT, CUBIC, ScaleS and SeeDB clearing in CX3CR1-GFP mice**

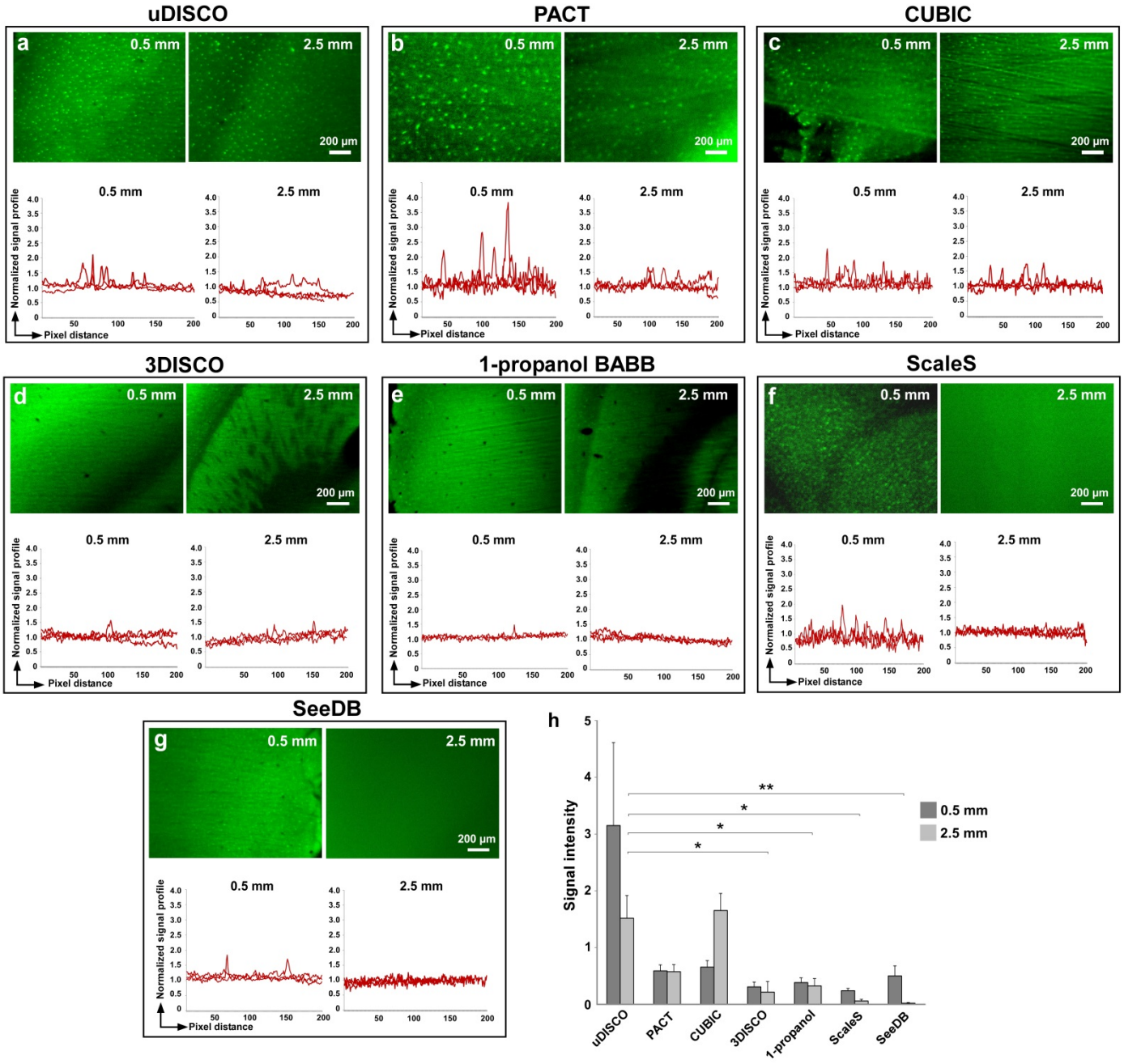


Representative images and normalized signal profiles at 0.5 mm and 2.5 mm depth from the dorsal surface after uDISCO (**a**), PACT (**b**), CUBIC (**c**), 3DISCO (**d**), 1-propanol BABB (**e**), ScaleS (**f**) and SeeDB (**g**) clearing of CX3CR1-GFP brains. In all cases, regions at the same depth and anatomical locations were quantified. Note that tissue shrinkage by uDISCO allowed visualization of larger volumes with the same imaging parameters, while tissue expansion e.g. by PACT allowed visualization of more details as cells appear larger. (**h**) Signal intensity quantifications at different depths of the samples after respective clearing. While uDISCO showed comparable results to PACT and CUBIC clearing, it has outperformed 3DISCO, 1-propanol BABB, Sca*l*eS and SeeDB at deeper brain regions (2.5 mm depth). Statistical significance (*$P < 0.05$, **$P < 0.01$) was assessed by one-way ANOVA followed by Dunnett's post-hoc test. Values are mean ± s.e.m.; n=6 brains for uDISCO group, n=3 brains for each other group (3 months old CX3CR1-GFP mice). See also Supplementary Video 1.

**Supplementary Figure 7: Clearing performance of uDISCO for dissected organs and shrinkage quantifications**

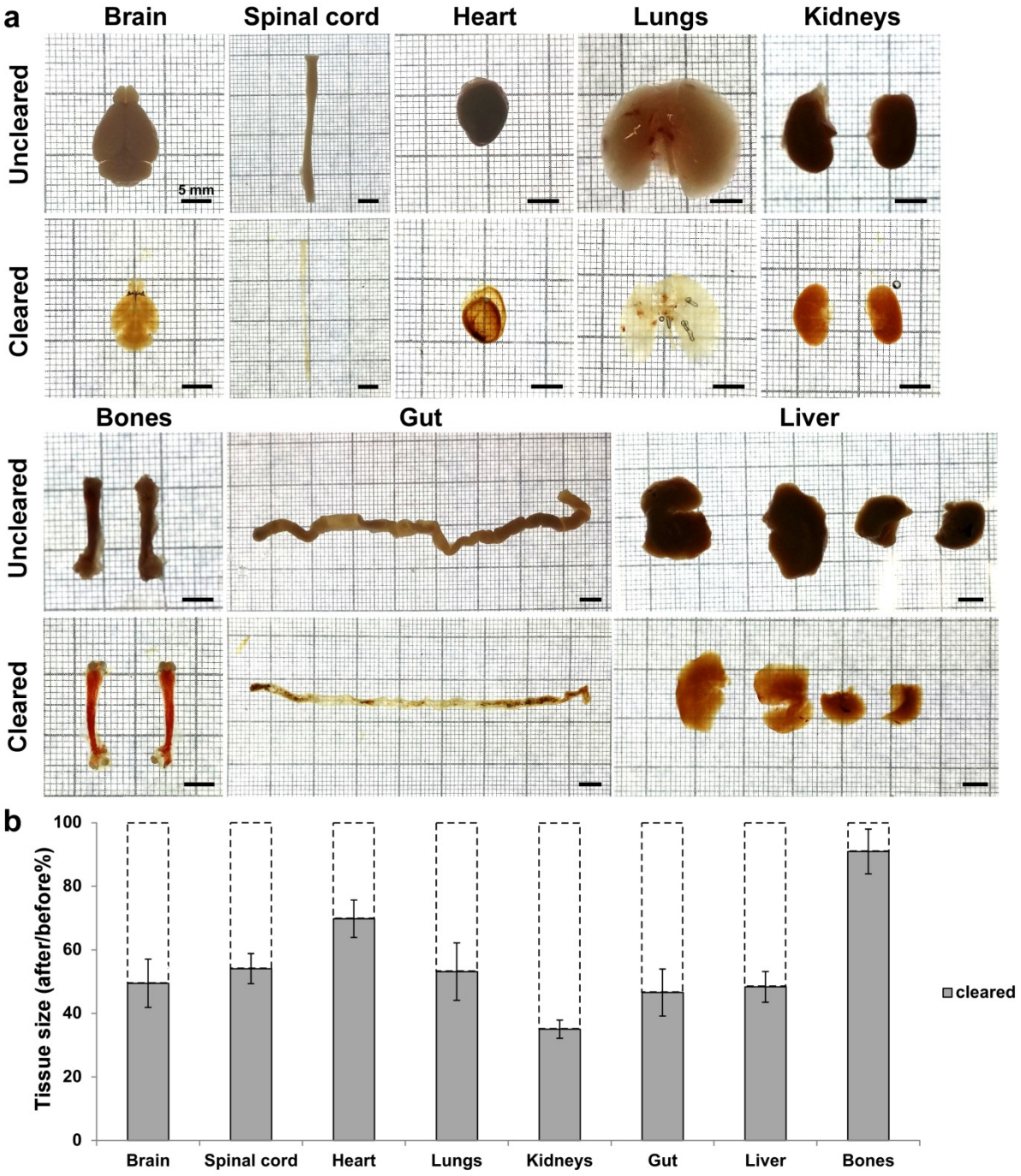


(**a**) Individual organs before and after uDISCO clearing. They became optically transparent after uDISCO clearing. The redness after the clearing is due to the residual blood, which did not impede the imaging of fluorescent structures as shown in Fig. 5 and Supplementary Fig. 22. (**b**) Volume quantifications of individual organs, showing that brain, spinal cord, heart, lungs, kidneys, gut, liver and bones shrank in average 50.54%, 45.92%, 30.22%, 46.85%, 64.94%, 53.44%, 51.76% and 8.08%, respectively. Values are mean ± s.d.; n=4 mice (5 months old) for each organ.

**Supplementary Figure 8: uDISCO clearing resulted in similar shrinkage of hard bone and bone marrow**

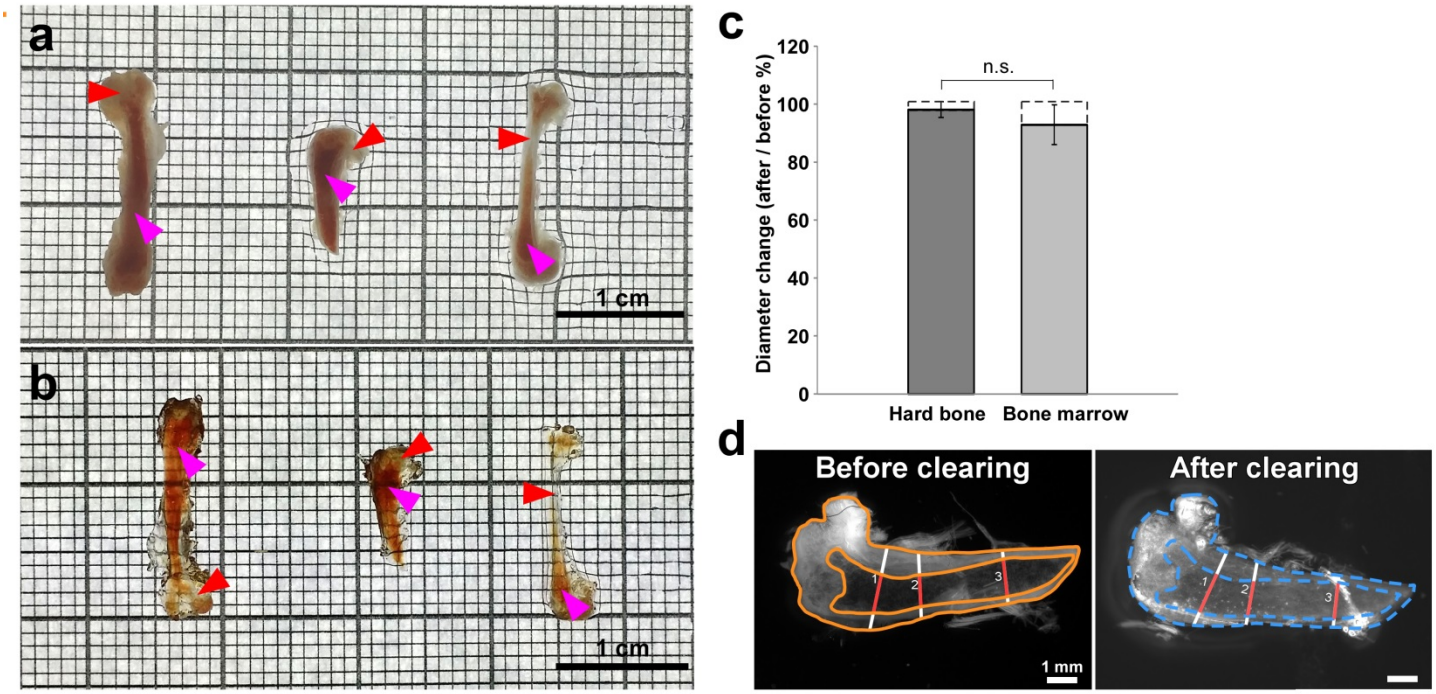


(**a**) Femurs from 6 months old CX3CR1-GFP mice were cut into half for visualization of hard bone (red arrowheads) and bone marrow regions (purple arrowheads). (**b**) Same bones are shown after uDISCO clearing. (**c**) Quantification of diameter change before and after uDISCO clearing: the shrinkage rate was slightly higher for bone marrow regions, even though it did not reach statistical significance (unpaired *t*-test, n.s. = $P > 0.05$). Values are mean ± s.d.; n=3 bones. (**d**) Illustration of how the quantification is performed: 1) the bone images before and after clearing were overlapped with each other, 2) 3 lines were drawn at different positions along the bone, and 3) the diameter change of the same hard bone (white line) and bone marrow (red line) regions were calculated at these three different axes using ImageJ.

**Supplementary Figure 9: Different clearing protocols on intact bones: assessment of endogenous GFP signal in CX3CR1-GFP mice**

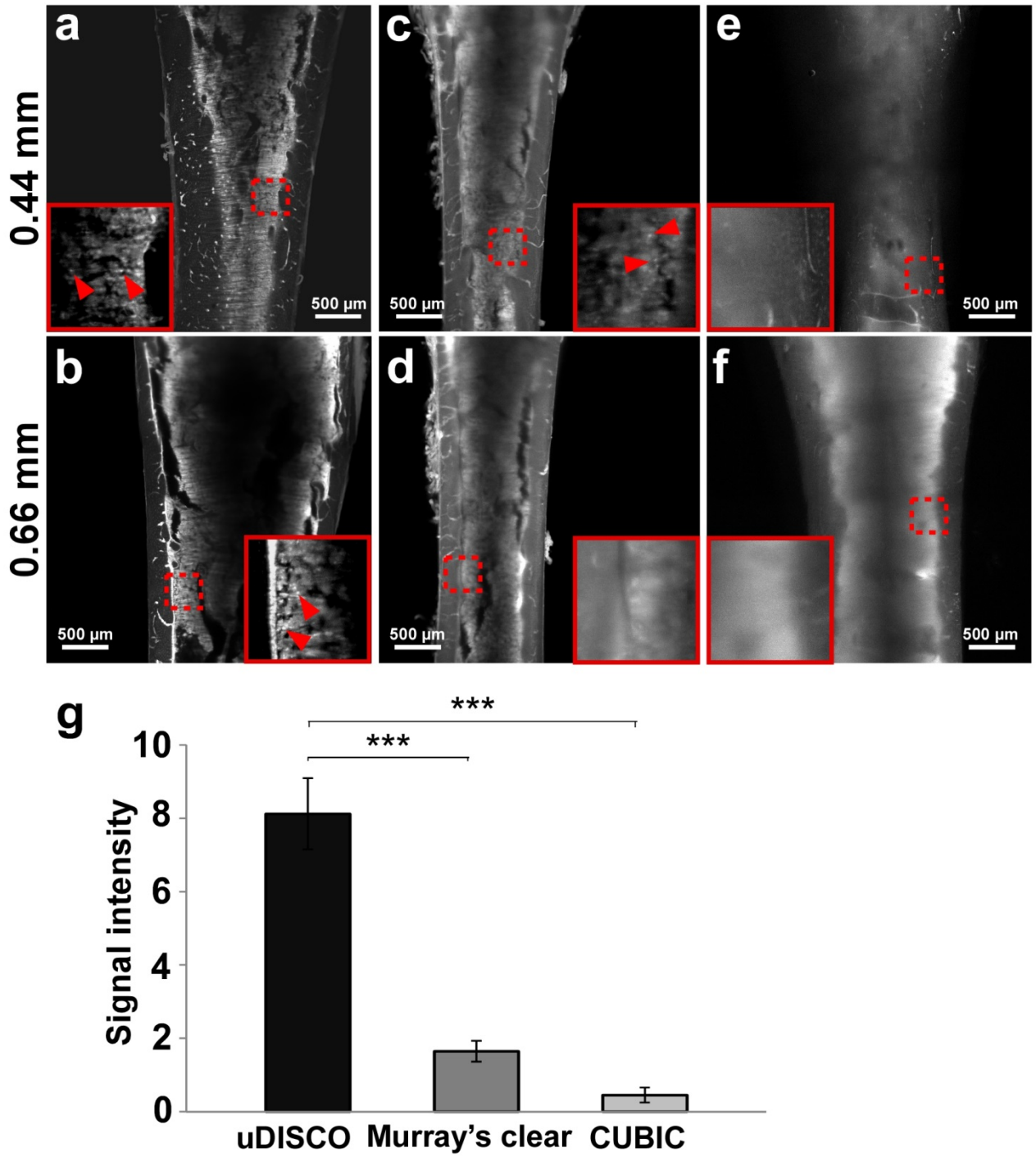


The bones from CX3CR1-GFP transgenic mice were cleared by uDISCO, Murray's clear and CUBIC methods. Maximum intensity projections at 0.4 mm and 0.66 mm depth from the bone surface for uDISCO (**a,b**), Murray's clear (**c,d**), and CUBIC (**e,f**) protocols are shown. (**g**) Quantification of total signal intensity through the bones; statistical significance (***$P < 0.001$) was assessed by one-way ANOVA followed by Dunnett's post-hoc test; values are mean ± s.e.m.; n=8 ROI in uDISCO bones, n=5 ROI in Murray's clear and CUBIC bones (5 months old CX3CR1-GFP mice).

**Supplementary Figure 10: Test of IHC with different bone clearing protocols**

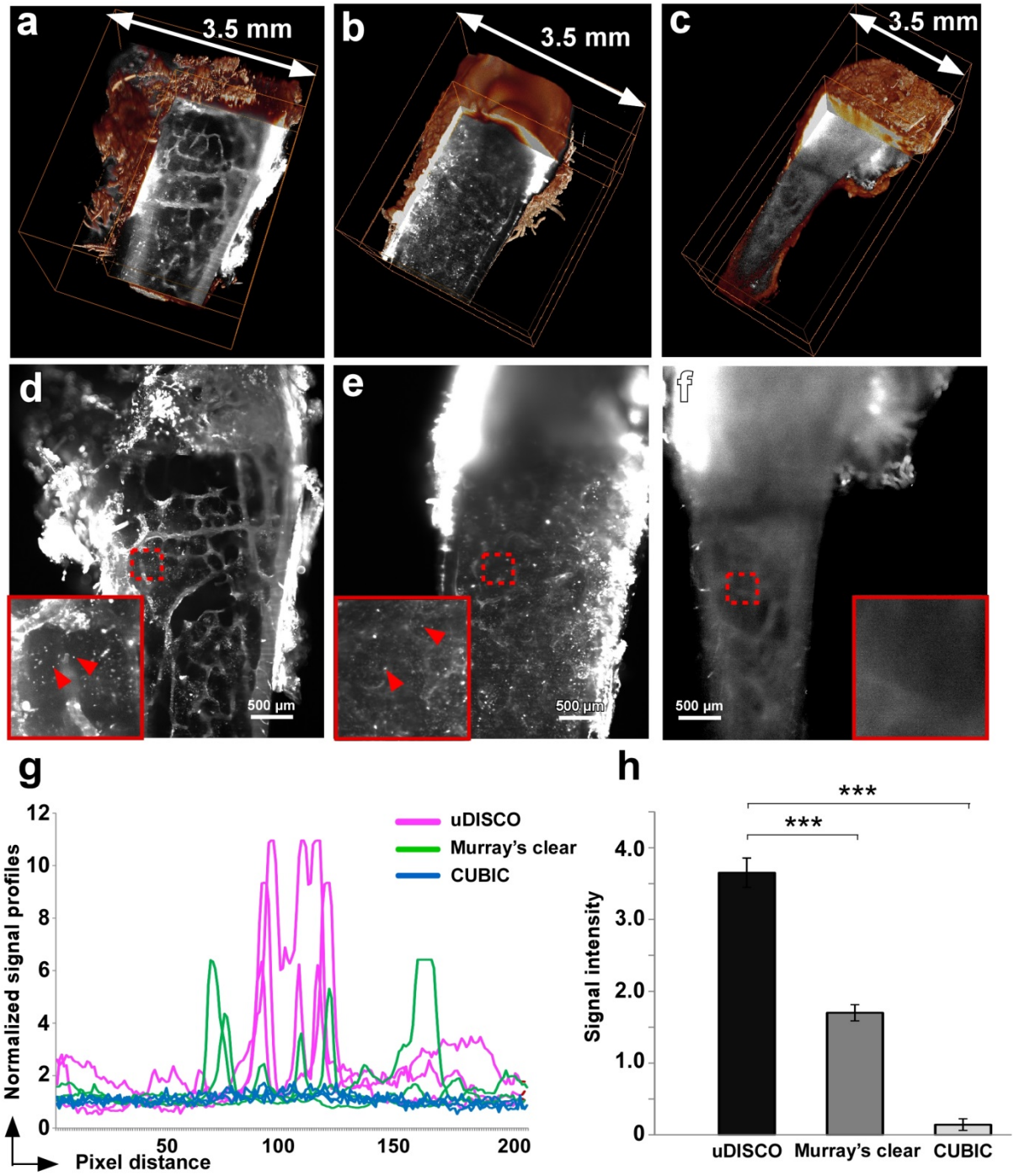


3D reconstruction of CX3CR1-GFP mice bones after (**a**) uDISCO, (**b**) Murray's clear and (**c**) CUBIC clearing. The bones were immunolabeled with AlexaFluor-647 conjugated anti-GFP rabbit polyclonal antibody before clearing. (**d-f**) Projections at 0.66 mm depth (~half-way through the cut bone) showing the signal quality after respective clearing. (**g**) Normalized signal profile plots of AlexaFluor-647 positive cells in uDISCO (magenta line), Murray's clear (green line) and CUBIC (blue line) cleared cut bones. (**h**) Quantification of signal intensity of antibody labeling in the bones after respective clearing. Statistical significance (***$P$ < 0.001) was assessed by one-way ANOVA followed by Dunnett's post-hoc test. Values are mean ± s.e.m.; n=8 ROI in uDISCO and Murray's clear cut bones; n=5 ROI in CUBIC cut bone (5 months old CX3CR1-GFP mice).

**Supplementary Figure 11: CUBIC PARS/PACT uDISCO size and imaging comparison**

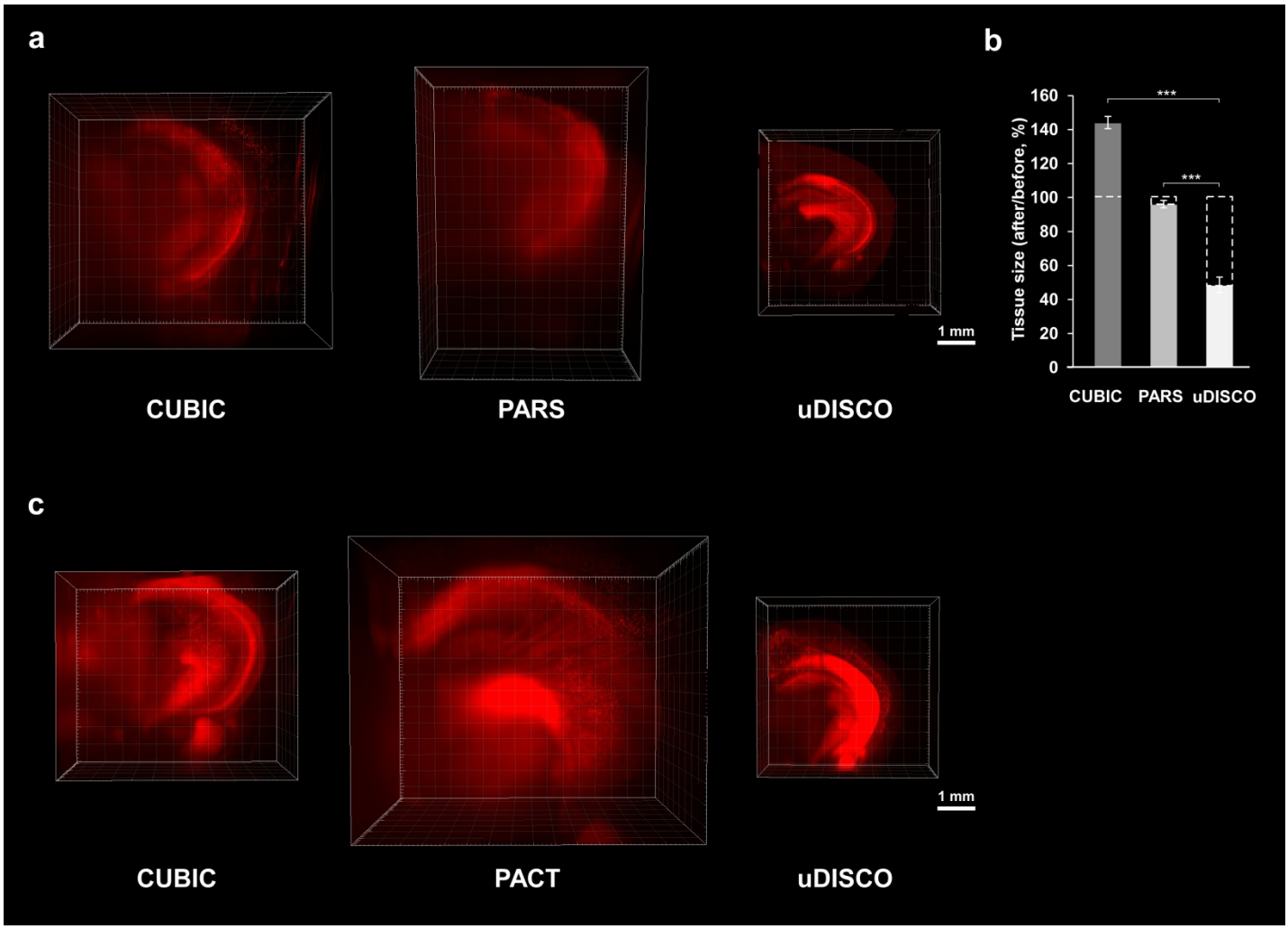


(**a**) 3D reconstruction of brains after CUBIC, PARS and uDISCO whole-body clearing. Imaging depth quantifications on brains in (a) are shown in Fig. 1h. (**b**) Volume changes of brains of 4 months old GFP-M mice after CUBIC, PARS and uDISCO whole-body tissue clearing methods. The final brain volume after uDISCO was significantly lower than after CUBIC and PARS whole-body clearing. Statistical significance (***$P < 0.001$) was assessed by one-way ANOVA followed by Dunnett's post-hoc test. Values are mean ± s.d.; n=4, 3, 3 GFP-M mice for CUBIC, PARS and uDISCO, respectively. (**c**) 3D reconstruction of brains after CUBIC, PACT and uDISCO passive tissue clearing of dissected brains. Imaging depth quantifications on brains in (c) are shown in Fig. 1i. With the same imaging settings at a single scan, more neurons can be imaged with uDISCO (owing to shrinkage) while more detailed structures of individual neurons can be resolved by PACT and CUBIC (owing to expansion) (see also Fig. 1g).

**Supplementary Figure 12: Comparison of gross tissue structures before and after uDISCO clearing**

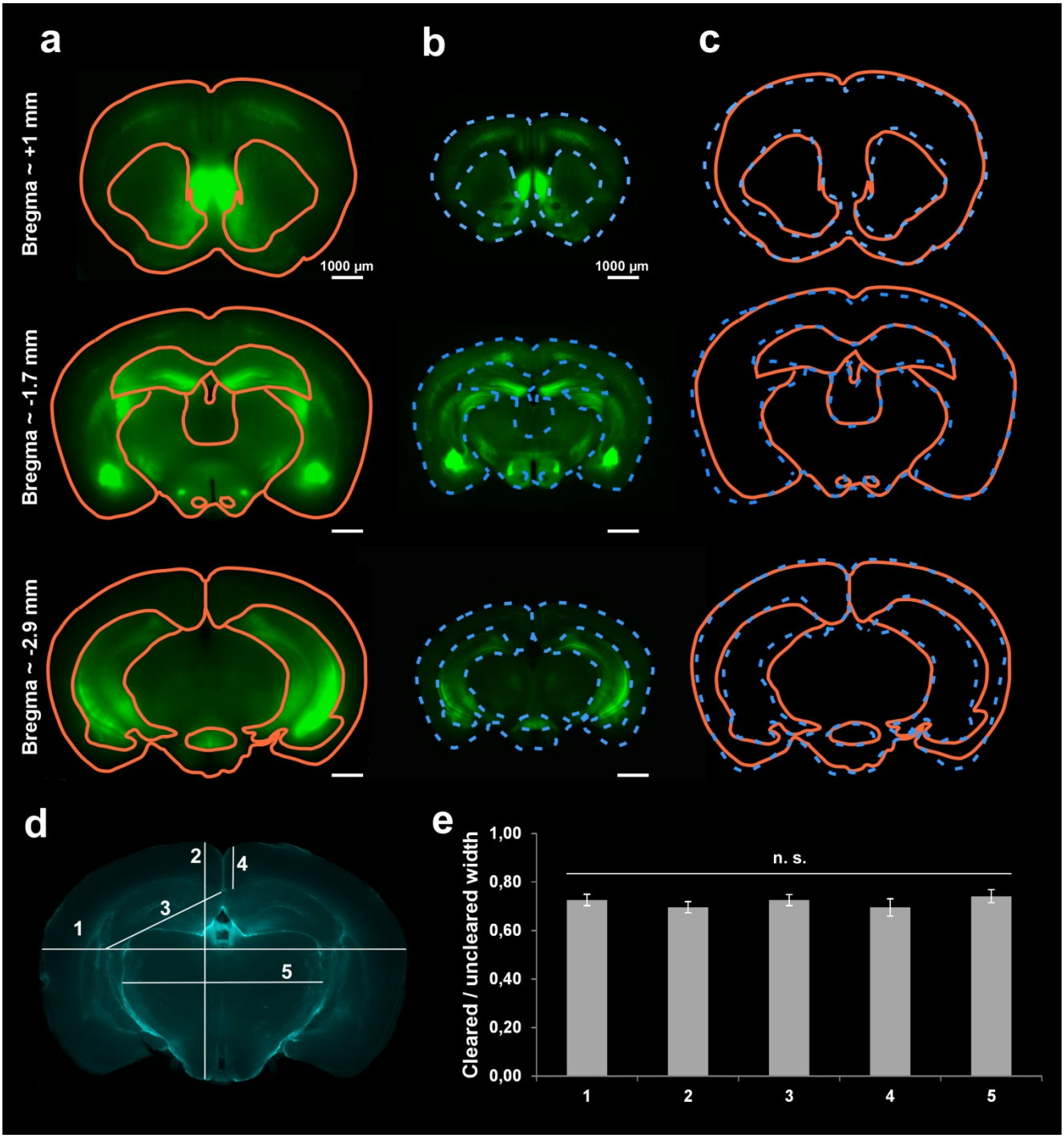


1 mm coronal brains slices from GFP-M mice (5 months old) at different levels were imaged with a fluorescence stereomicroscope before (**a**) and after (**b**) uDISCO clearing. The borders of main structures before and after clearing are highlighted in orange and blue, respectively. (**c**) The overlay of borders by ratio-metric enlargement of shrunken tissue shows a substantial overlap. (**d**) To quantify the proportions of size change on same the slice, we assessed the width of different brain regions (indicated by numbered lines) before and after clearing. (**e**) The quantifications showed that different tissue regions shrank at a similar rate (~30%) in length after clearing (one-way ANOVA, n.s. = $P > 0.05$). Values are mean ± s.d.; n=4, 4, 3, 4, 4 for regions 1, 2, 3, 4, 5, respectively.

**Supplementary Figure 13: Microscale changes of different cells and tissues before and after uDISCO clearing**

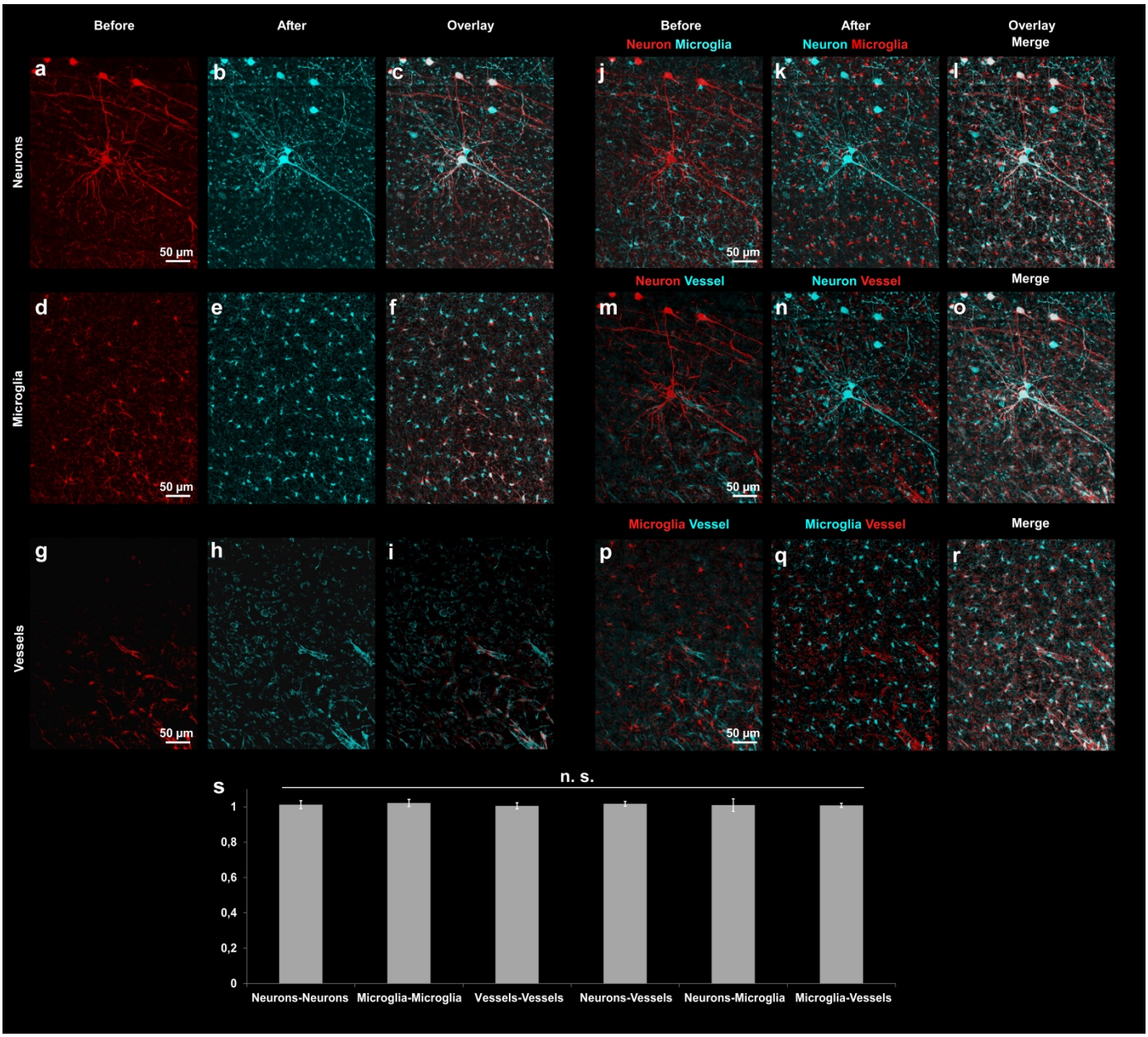


To assess the uniformity of shrinkage on different types of cells and tissues, we measured shrinkage of neurons, microglia and vessels with respect to each other. To this end, we immunolabeled 1 mm thick GFP-M brain slices (from 2 months old mice) with Iba1 (microglia) and Collagen4 (vessels) and acquired confocal images before and after uDISCO clearing. (**a-i**) Single channel views from the same tissue location containing neurons (**a-c**), microglia (**d-f**) and vessels (**g-i**). Overlay channels show a substantial overlap of before and after images. (**j-r**) Double channel views from the same tissue location demonstrating neurons-microglia (**j-l**), neurons-vessels (**m-o**) and microglia-vessels (**p-r**) together. To simplify the interpretation of overlay channels, we used only two colors (red and cyan) and swapped the colors before and after clearing channels, resulting in white color for overlay of tissue components. (**s**) The distances between neurons-neurons, microglia-microglia, vessels-vessels, neurons-microglia, neurons-vessels and microglia-vessels were measured before and after uDISCO and normalized to the rate of gross shrinkage of the slice (n=7 per each tissue structure/cell type from at least 3 different slices). The quantification showed that the relative distances between the structures and cells were not significantly changed after clearing (one-way ANOVA, n.s. = $P > 0.05$). Values are mean ± s.d.

**Supplementary Figure 14: Comparison of single cells and vessels before and after uDISCO clearing**

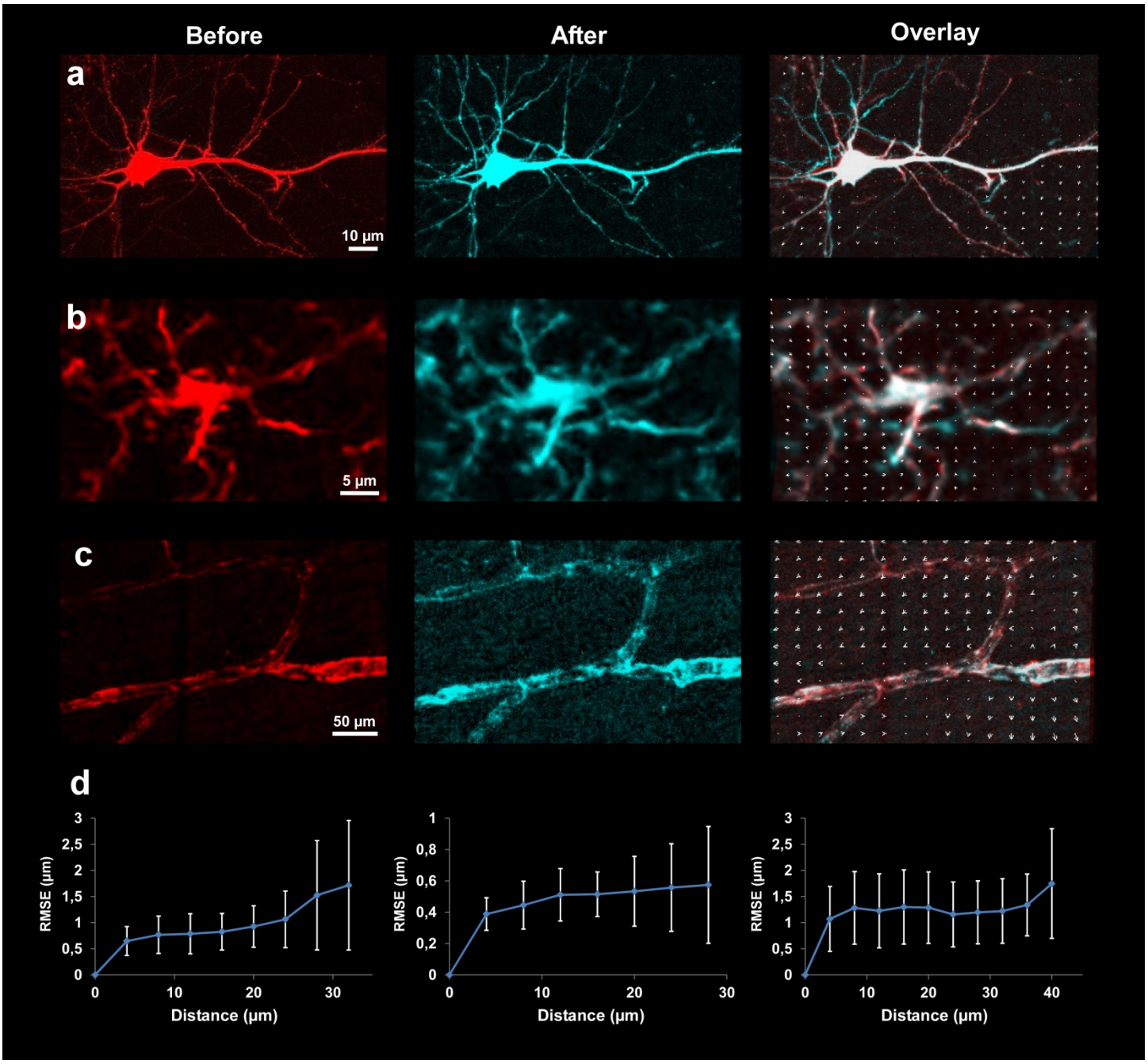


Confocal images of 1 mm coronal brains slices from GFP-M mouse (2 months old) before and after uDISCO clearing, showing individual neurons (**a**), Iba1 stained microglia (**b**), and Collagen4 stained vessels (**c**). The overlay after ratiometric enlargement of shrunken cells and vessels shows a substantial overlap suggesting that individual cell morphology is preserved after uDISCO clearing. Note that more structures are visible after clearing (cyan in "after" and "overlay" images). (**d**) Quantifications of RMSE to evaluate the degree of morphological deformations for neurons (left), microglia (middle) and vessels (right). After defining a center of a cell or a structure as the constant point, displacements of cellular and vascular structures before and after clearing have been plotted with regular intervals from the center point. The degree and direction of regional deformations are shown with arrows in overlay images ($n \geq 6$ cells from at least 3 different slices and $n \geq 3$ vessel structures from at least 3 different slices). Values are mean ± s.e.m.

**Supplementary Figure 15: Details of light-sheet microscope and sample holders for whole mouse body imaging**

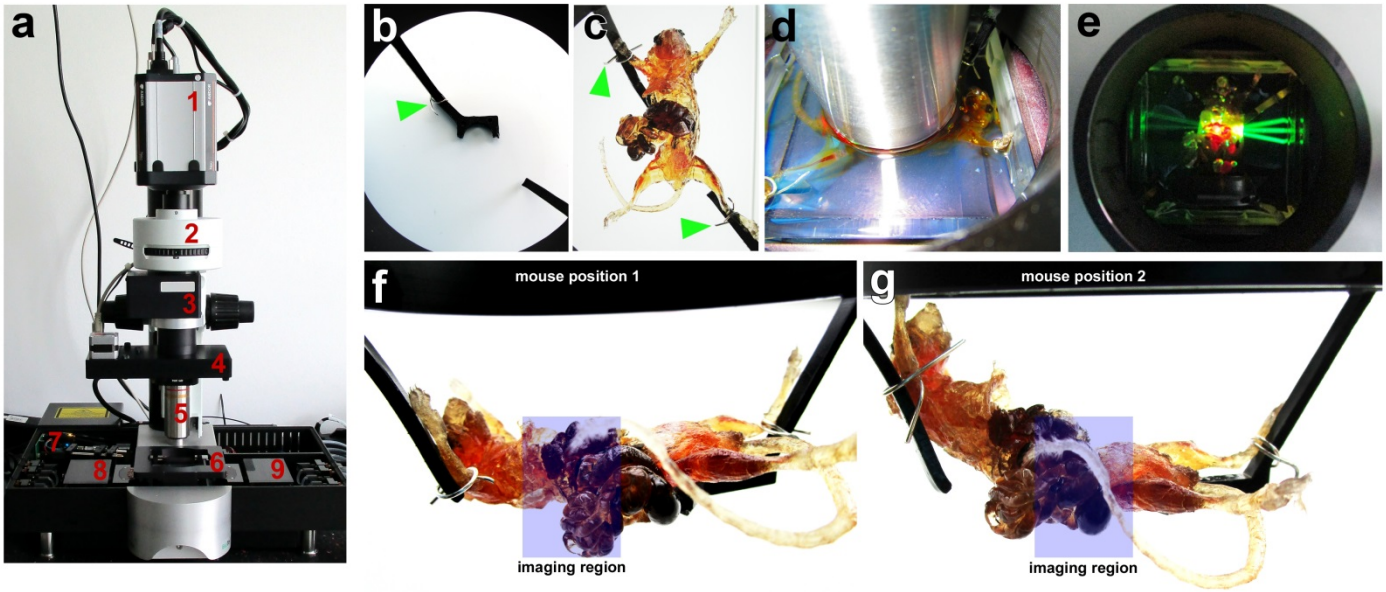


(**a**) LaVision Biotec light-sheet ultramicroscope featuring: (1) Andor Neo 5.5 sCMOS camera; (2) Olympus U-TVCAC revolving zoom unit enabling 1x, 2x, 4x additional magnification with a fourth slot for a shutter plate; (3) LaVision autofocusing unit for automatic focus correction at different wavelengths; (4) filter box with 8 slots for 25 mm mounted filters; (5) BABB corrected Olympus objective; (6) imaging chamber, where LaVision Biotec suspension trays for sample holders are placed; (7) fiber coupled laser outlet for supercontinuum laser (SuperK EXTREME EXW 9 - 450-1000); (8-9) beam profile generation units. (**b**) Half of the central part of the commercial sample holder suspension (LaVision Biotec) is cut to make space, which allows flexible positioning of the mouse body at the center of the imaging beam. Silver plated copper wires are used to secure the mouse (**c**) to the branches of the suspension by its fore- and hind-limb (green arrowheads). (**d**) View of cleared adult mouse body immersed in the imaging chamber. Note that there is a large space left from the sleek immersion objective (Olympus air immersion corrected for RI 1.56), which facilitates the repositioning of the mouse in the chamber. (**e**) Demonstration of laser light sheets crossing the cleared mouse body. After imaging a region (**f**), the mouse is repositioned (**g**) so that next body part is now in the center of imaging area (purple rectangles).

**Supplementary Figure 16: Details of customized sample holders for individual brain and other organs**

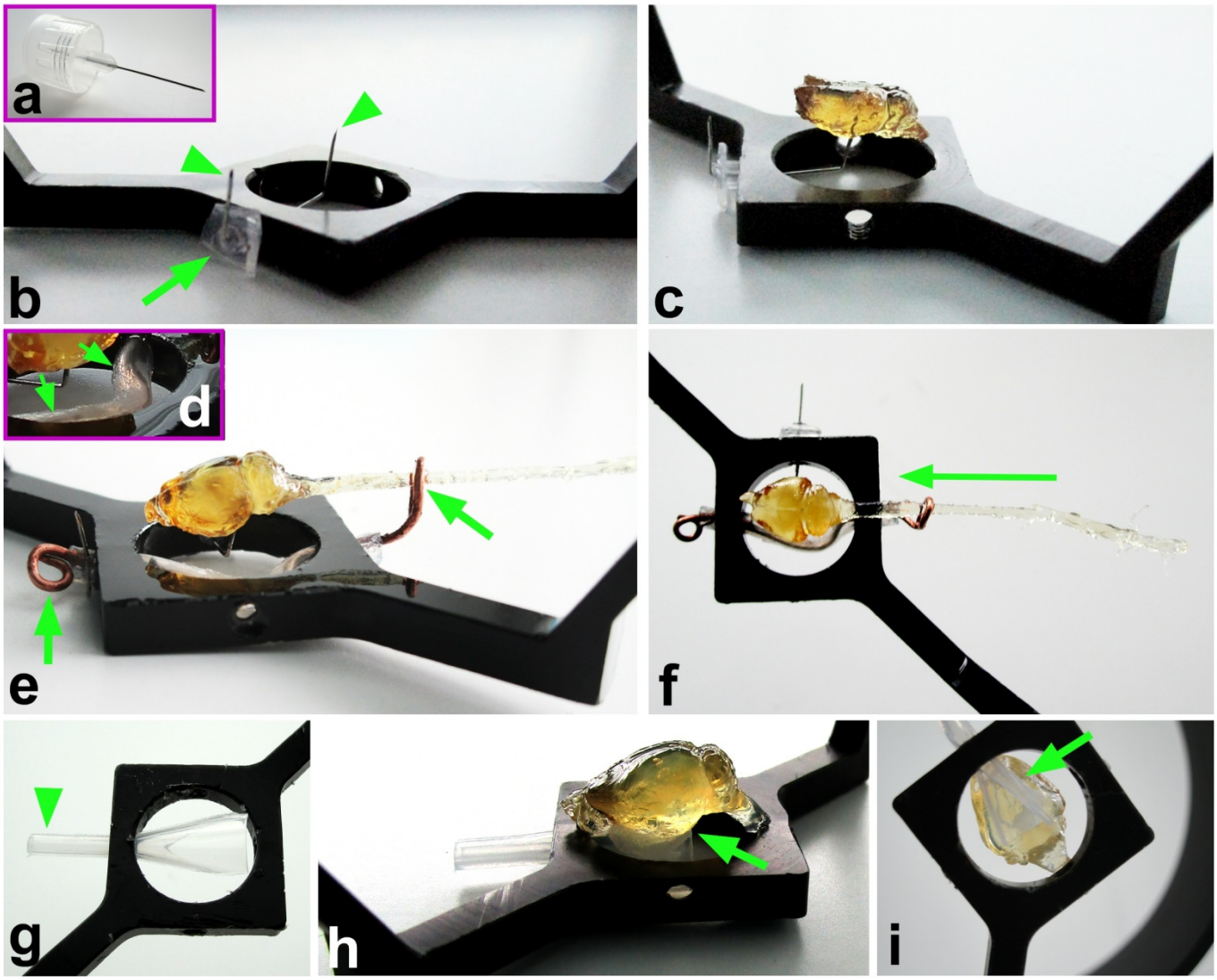


(**a**) To allow maximum flexibility, we used 0.33 mm thick fine needles (BD Micro-Fine Ultra, 325118) in combination with commercially available sample suspension (Lavision Biotec). The plastic cup is trimmed (**b**, arrow) to avoid contact with the bottom of the imaging chamber. The needle is inserted into the hole of sample holder and bent as shown (**b**, arrowheads). (**c**) An example of an uDISCO-cleared brain secured to the fine needle: the resinous consistency of uDISCO cleared brains allows a clean piercing that is not visible in the sample once imaged, owing to the multiple sheets coming from different angles and compensating for cast shadows. (**d-f**) Variation of customized sample holders for long specimens, such as entire CNS (brain and spinal cord together). To this end, in addition to the fine needle holding the brain, we used a cooper wire to stabilize the long spinal cord. The copper wire is prepared as follows: first, we inserted it into a Pasteur pipette tube (**d**, arrowheads) and into the hole of suspension. Finally, we looped the ends as shown (e, arrows). The brain is imaged first while the spinal cord lies in a loop of the wire to keep it at a suitable height. After imaging, the sample is swept along its axis (**f**, arrow), so that a different part of the unsectioned CNS can be imaged, until completion. (**g-i**) Customized sample holders for specimen clarified with water-based clearing methods. If the samples have jelly-like textures, they cannot be held in place with fine needles. Instead, we trimmed a plastic Pasteur pipette as shown (**g**, arrowhead) and glued the specimens on top (**h,i**, arrows). A mounted CUBIC brain is shown from the side (**h**) and bottom (**i**).

**Supplementary Figure 17: 10 mm depth z-scan across rodent body parts after uDISCO clearing**

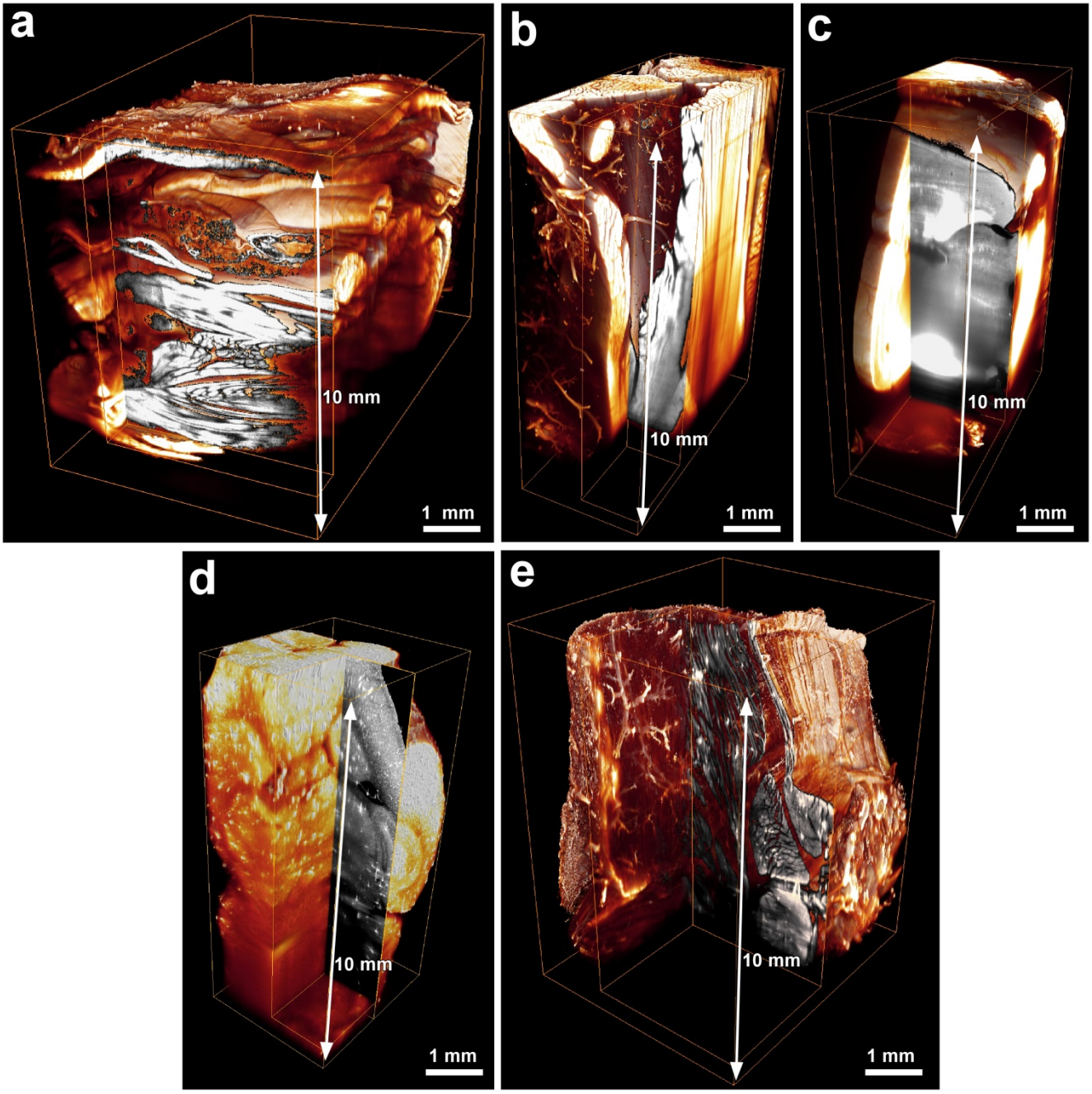


3D Volren surface reconstructions (red-orange) of 10 mm z-scans obtained by light-sheet microscopy. An ortho-slice (black-white) is shown in the corner-cut view (Amira software) to demonstrate the details throughout the scans. (**a-c**) Different body parts of the whole-body light-sheet microscopy scanned mouse in Fig. 2d: the pelvic area (**a**), hindlimb (**b**) and the head (**c**); voxel size: 1.625 x 1.625 x 6 µm. (**d**) A 10 mm z-scan through vasculature labeled (FITC-lectin) mouse brain; voxel size: 1.625 x 1.625 x 4 $\mu m^3$. (**e**) 10 mm z-scan through the shoulder of a vasculature labeled (Texas Red) adult rat. Vessels and fine structure are well defined.

**Supplementary Figure 18: Rat organs after uDISCO clearing**

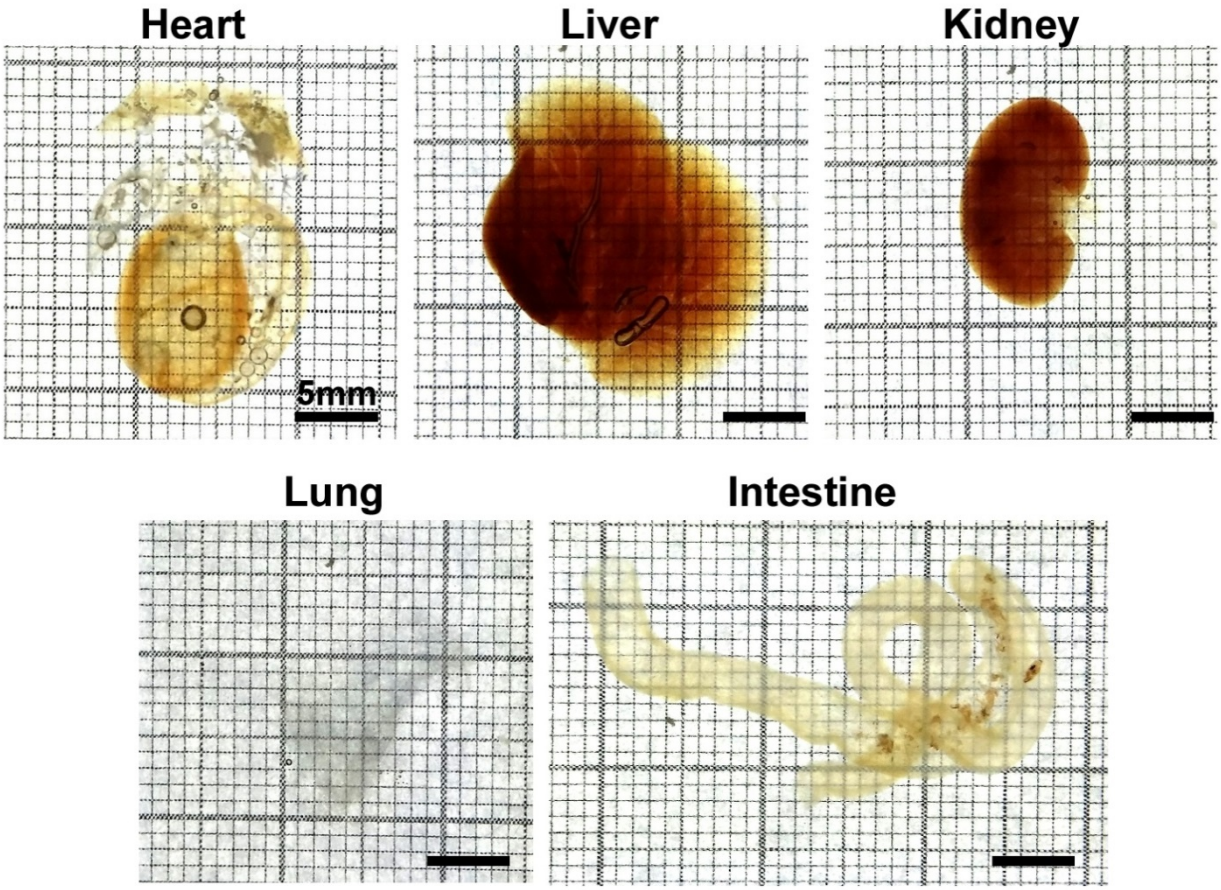


Grid images of individual organs from rat after whole-body uDISCO clearing, showing that the heart, liver, kidney, lung and intestine were rendered optically transparent. The redness after the clearing in liver and kidney images is due to the residual blood.

**Supplementary Figure 19: BMSCs characterization**

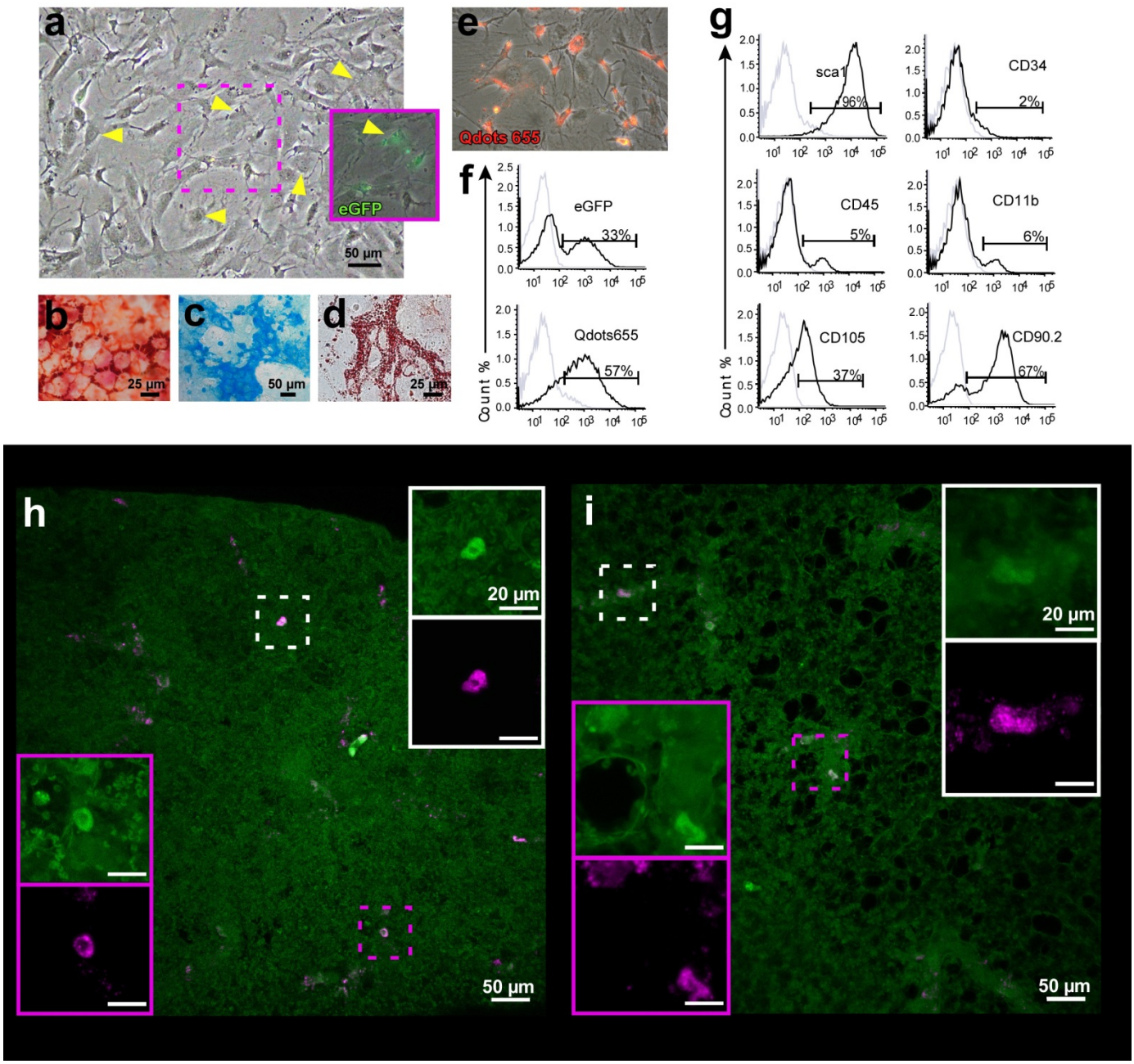


Characterization of β-actin EGFP BMSCs loaded with Qdots. (**a**) Representative picture of BMSCs (passage 4-5) that were harvested for IV transplantation (arrowheads mark some of the BMSCs). The purple insert shows the EGFP+ cells (superimposed image of wide-field and GFP channels). (**b-d**) The osteogenic (**b**), chondrogenic (**c**) and adipogenic (**d**) potential of the BMSCs confirms their mesenchymal origin. (**e**) BMSCs loaded with Qdots, shown as red cytoplasmic aggregates (superimposed image of wide-field and Qdot channels). (**f**) FACS characterization of the EGFP+ and Qdot+ BMSCs before their harvest for transplantation. (**g**) BMSCs were sca1+, CD34-, CD45- and CD11b- while expressing medium levels of CD105 and CD90.2 as characterized by FACS; the population only contained a small fracture of CD11b+ and CD45+ monocytes, as expected. (**h,i**) Colocalization of GFP and Qdot signals in cleared lungs from animals injected with BMSCs, imaged by confocal microscopy. White and magenta rectangles show high-magnification single channel images (EGFP (green), Qdot (magenta)) of dashed marked regions in the same images.

**Supplementary Figure 20: Whole-body clearing and imaging of mouse after BMSCs transplantation**

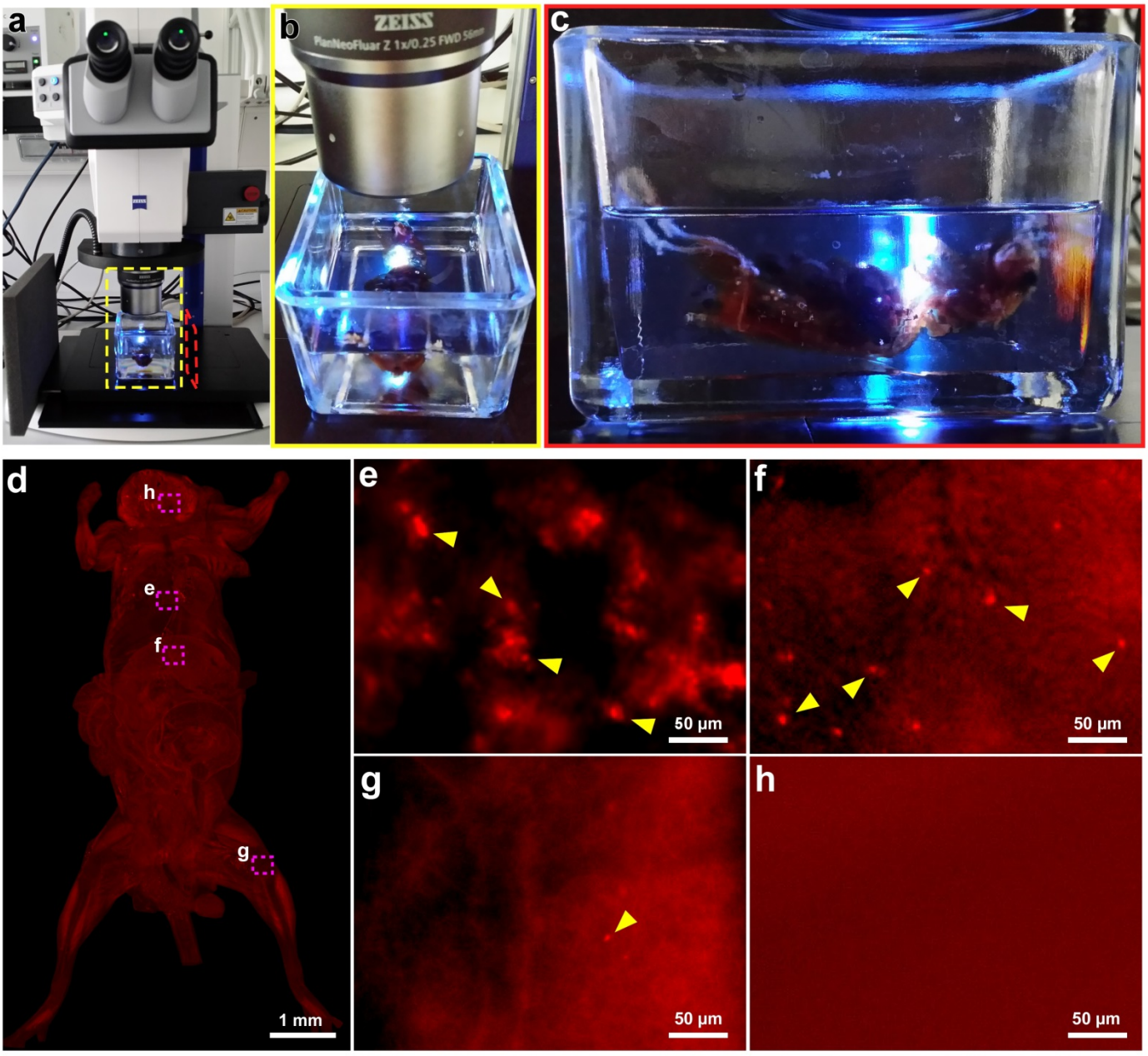


BMSCs were collected and labeled with Qdots, then transplanted into 2 months old C57BL/6N mice through IV injection. The mice were transcardially perfused and cleared with uDISCO. The intact mouse bodies could readily be screened by fluorescent stereomicroscope (**a-c**). (**d**) Whole-body stereomicroscope imaging of intact host mouse body. The individual cells were identifiable throughout the body, e.g. in the lung (**e**), liver (**f**) and bone marrow (**g**). No BMSCs were detected in the brain as expected (**h**).

**Supplementary Figure 21: 3D reconstruction of internal organs from intact mouse transplanted with Qdot labeled BMSCs**

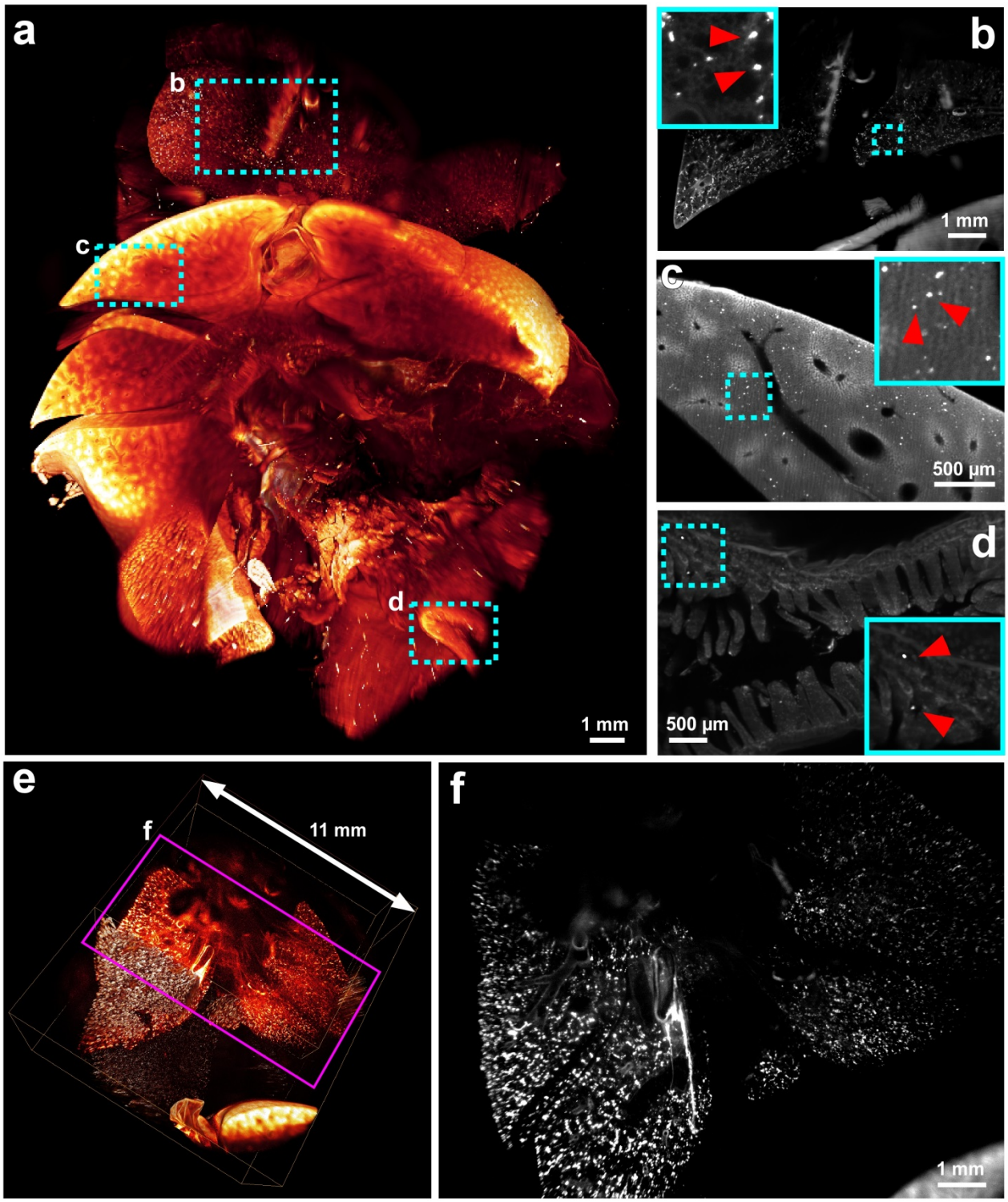


Light-sheet microscopy images from intact mice, which were transplanted with Qdot loaded BMSCs. (**a**) Lungs, liver layers, right kidney and part of the intestine shown in 3D surface rendering view. (**b-d**) The projection images of regions marked in (a): lung (**b**), upper liver layer (**c**) and intestine (**d**). (**e**) 3D surface reconstruction of lungs from another mouse. (**f**) The projection image of region marked in (e).

**Supplementary Figure 22: Distribution of mouse BMSCs in kidney, spleen and intestine**

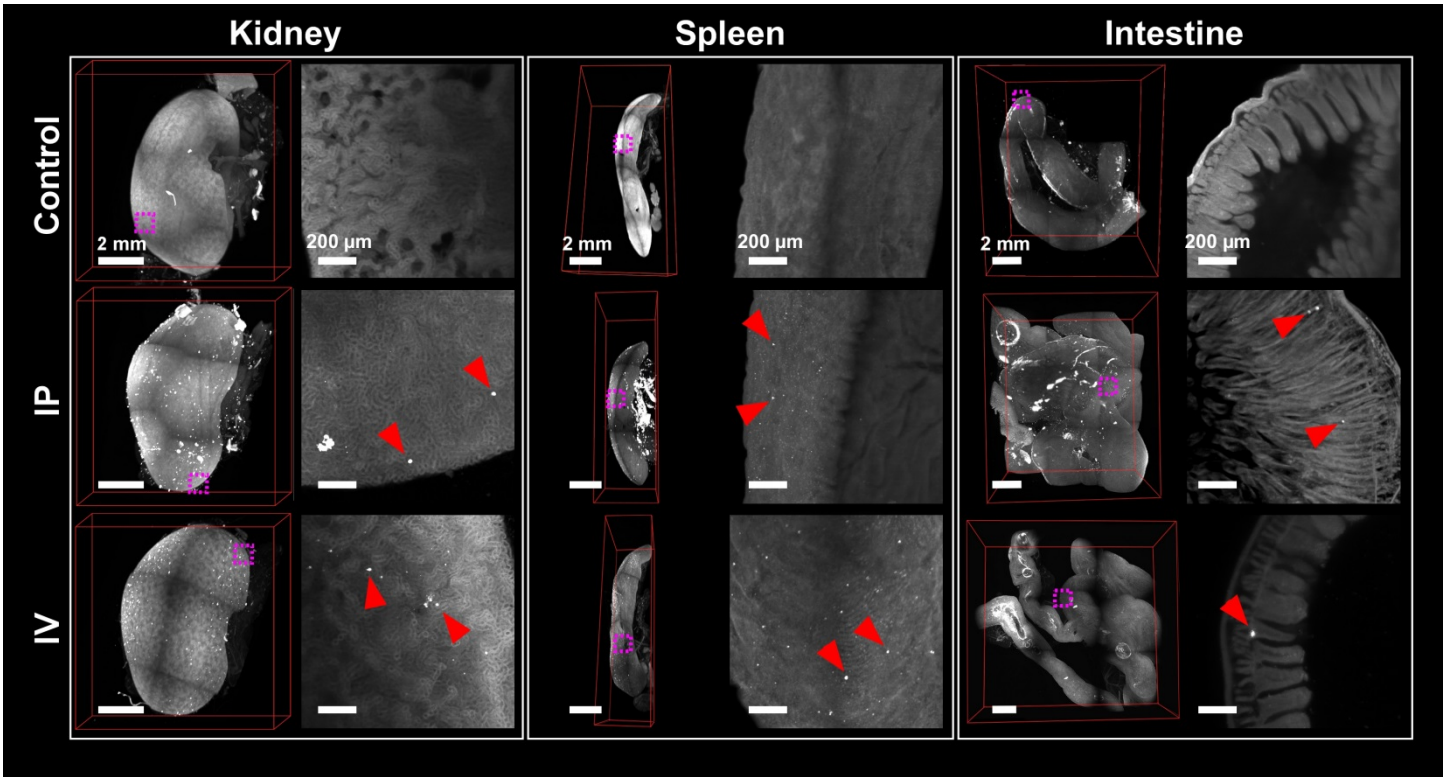


Images of kidney, spleen and intestine from host mice in control, IP and IV groups. We found a sparse distribution of Qdot positive BMSCs throughout the kidney, spleen and intestine in both IP and IV groups

**Supplementary Figure 23: AVV tracing of whole adult mouse CNS**

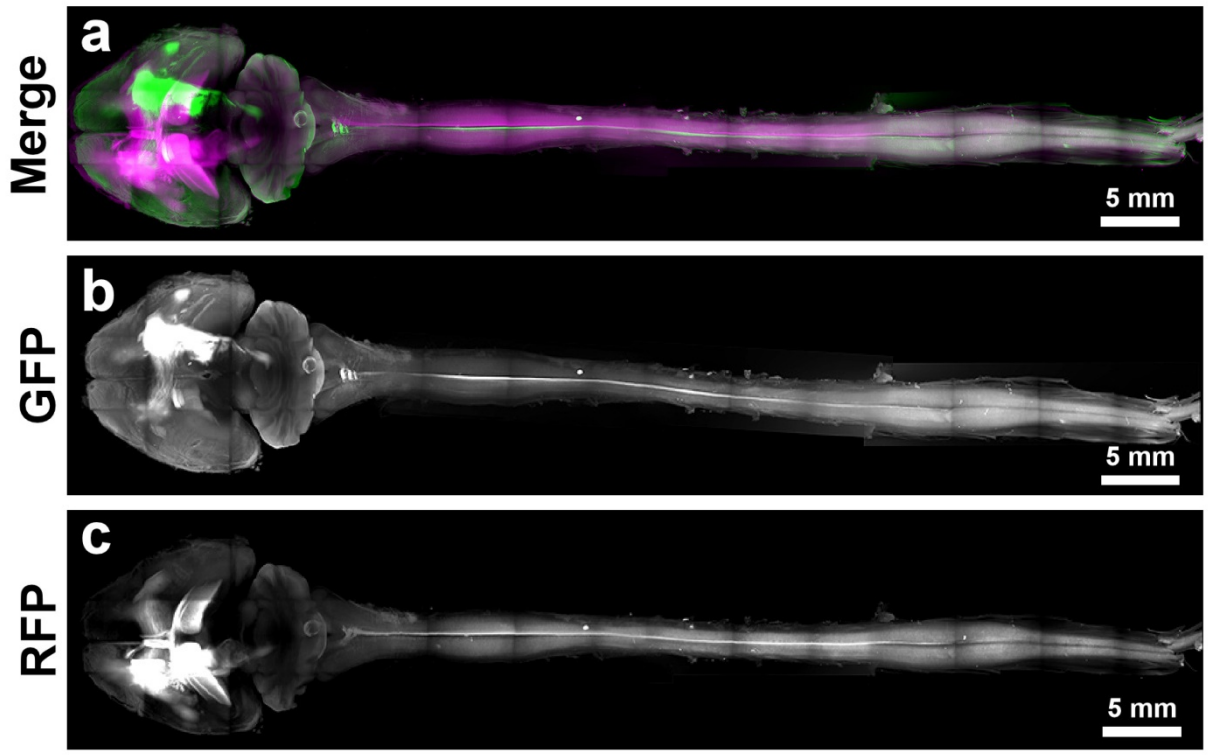


Individual channels of traced adult mouse CNS (**a**) shown in Fig. 6. AAV-syn-GFP signal in the entire CNS is shown in (**b**), AAV-syn-RFP signal in (**c**).

**Supplementary Figure 24: Microglia/macrophage IHC on mouse brain**

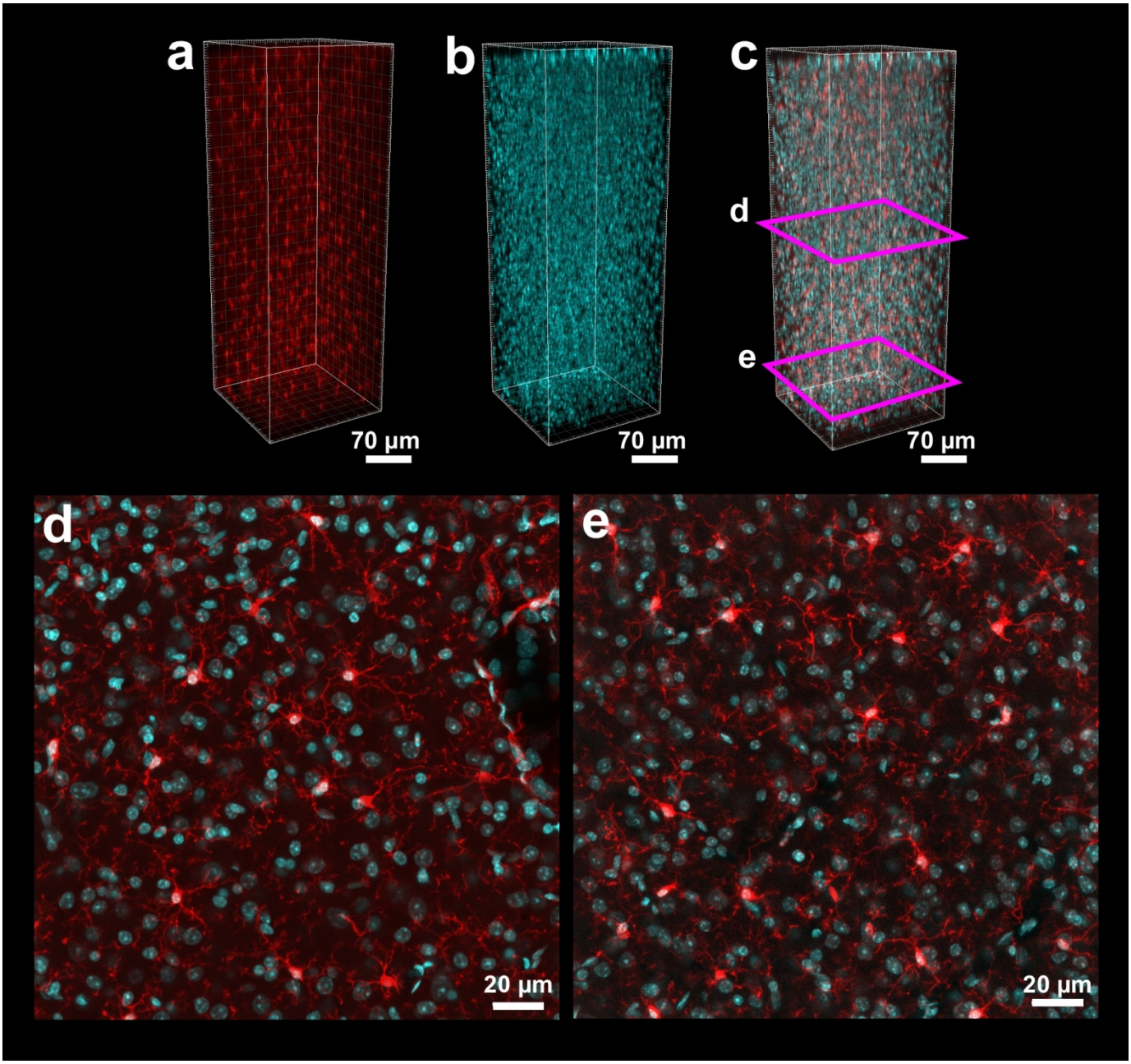


Iba1 and TO-PRO-3 labeling of coronal sections from the cortex of 4 months old mouse brain. (**a-c**) 3D reconstructions showing the homogeneous labeling of microglia and cell nuclei stained with Iba1 antibody (**a**) and TO-PRO-3 (**b**) and their merge (**c**). (**d,e**) Maximum intensity projections of the z-positions marked by purple boxes in (c); microglia are shown in red and TO-PRO-3 staining in cyan.

**Supplementary Figure 25: Microglia/macrophage IHC on short and long-term formalin-fixed human clinical tissue slices**

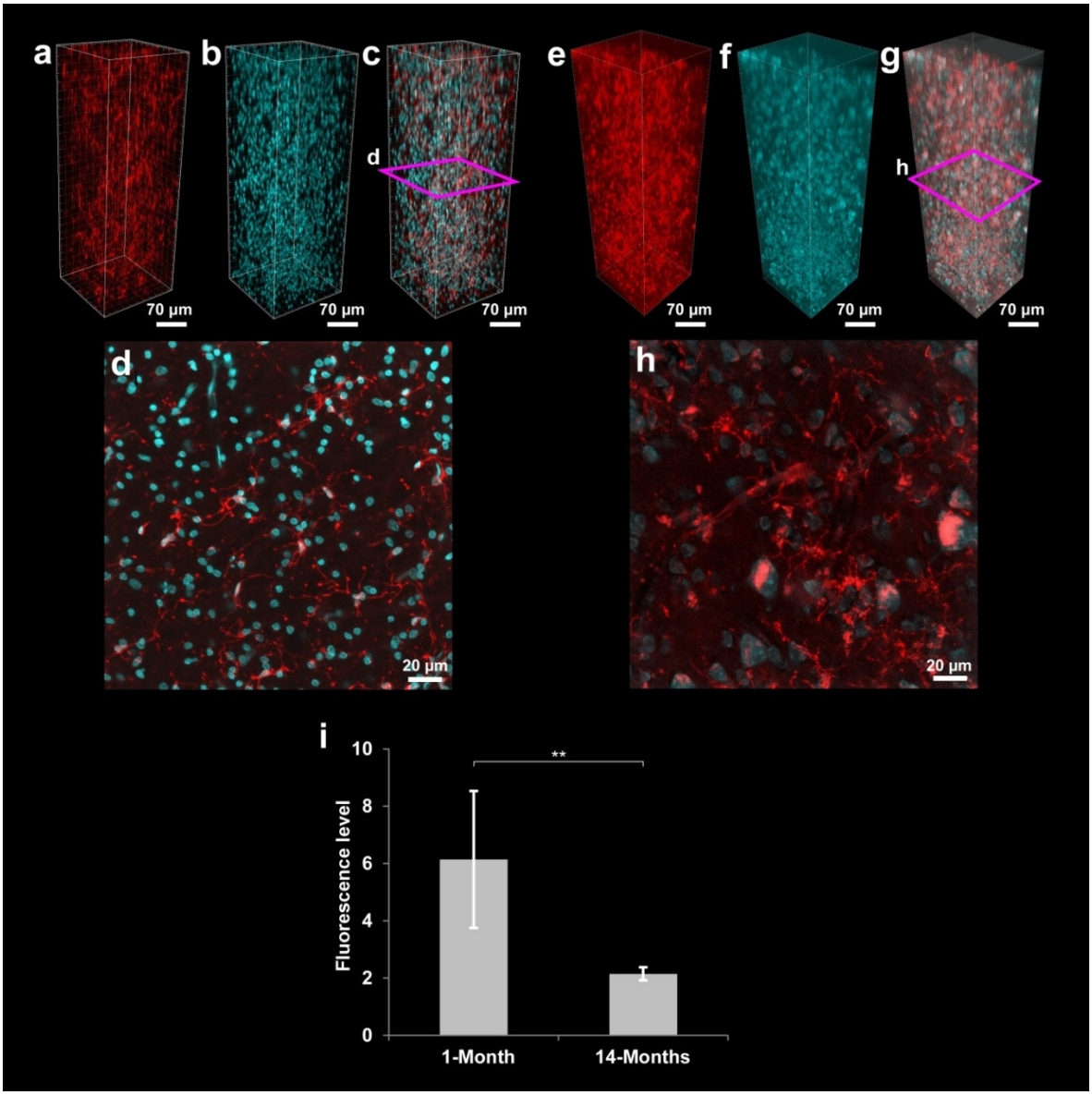


Iba1 and TO-PRO-3 labeling of short-term (1-month) (**a-d**) and long-term (14-months) stored (**e-h**) clinical cortical tissue samples of human brains. 3D reconstructions showing the homogeneous labeling of microglia (Iba1) (**a,e**) and cell nuclei (TO-PRO-3) (**b,f**) and their merge (**c,g**) throughout the 1 mm human tissue samples stored short-term (**a-c**) or long-term (**e-g**). (**d,h**) Maximum intensity projections of the z-position marked by the purple box in (c,g), respectively. Nuclei are shown in cyan, microglia and their processes are in red. All the images were taken by confocal microscopy with 3-4 µm z-steps. (**i**) Fluorescence level quantification. Antibody (microglia) and dye (cell nuclei) labelings were complete and specific on both short-term and long-term stored human clinical tissue samples even though the fluorescence level was significantly lower in long-term stored tissues, mostly owing to the increased background in long-term storage. Note that the 1-month fixed sample was obtained from an individual without any obvious brain pathology reported vs. the 14-months fixed sample from an individual who suffers from obesity. Values are mean ± s.d.; n=6, 4 slices for short-term fixed samples and long-term fixed samples, respectively. Statistical significance (**$P < 0.01$) was assessed by unpaired *t*-test.

**Supplementary Figure 26: SNR and PSNR in uDISCO cleared samples**

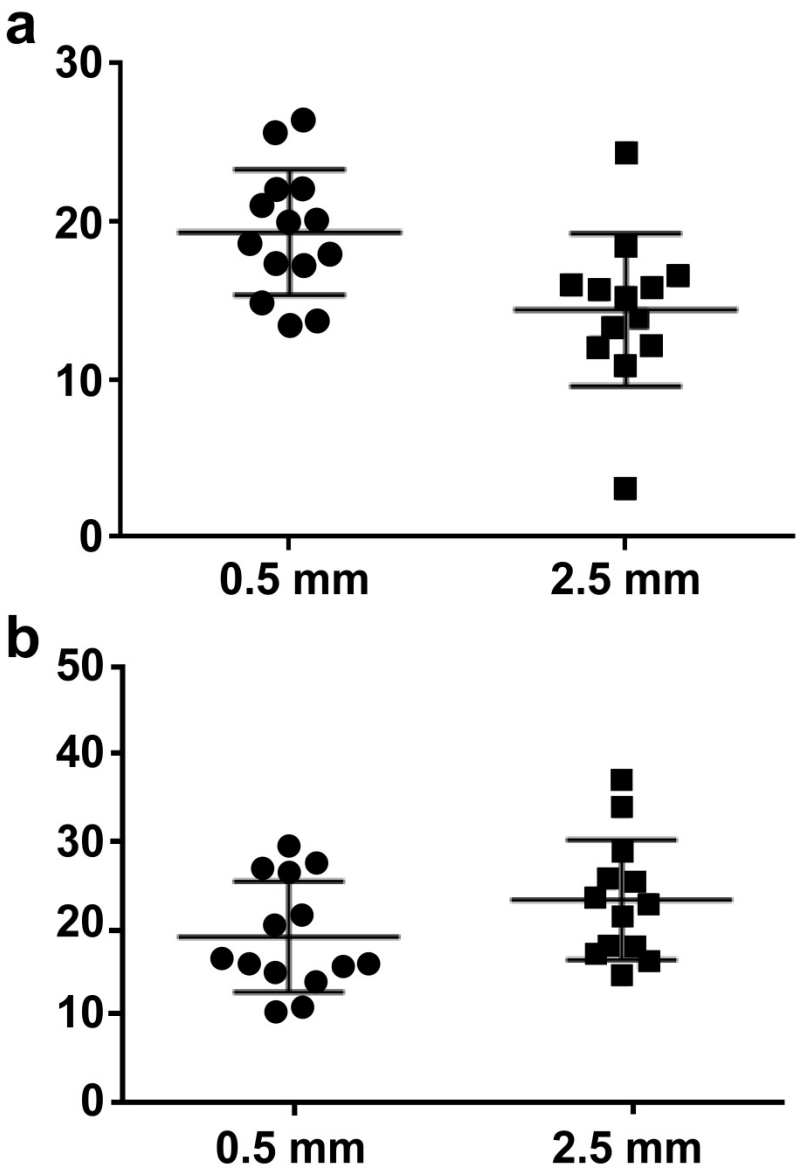


Signal-to-noise ratio (SNR) (**a**) and peak signal-to-noise ratio (PSNR) (**b**) range at different depths for uDISCO clearing as assessed on 3 months old GFP-M mice. Lines represent mean ± s.d.; n=3 brains for each group. The exact formulas and more details are given in the Methods part.

**Supplementary Figure 27: Different objectives in BABB-D**

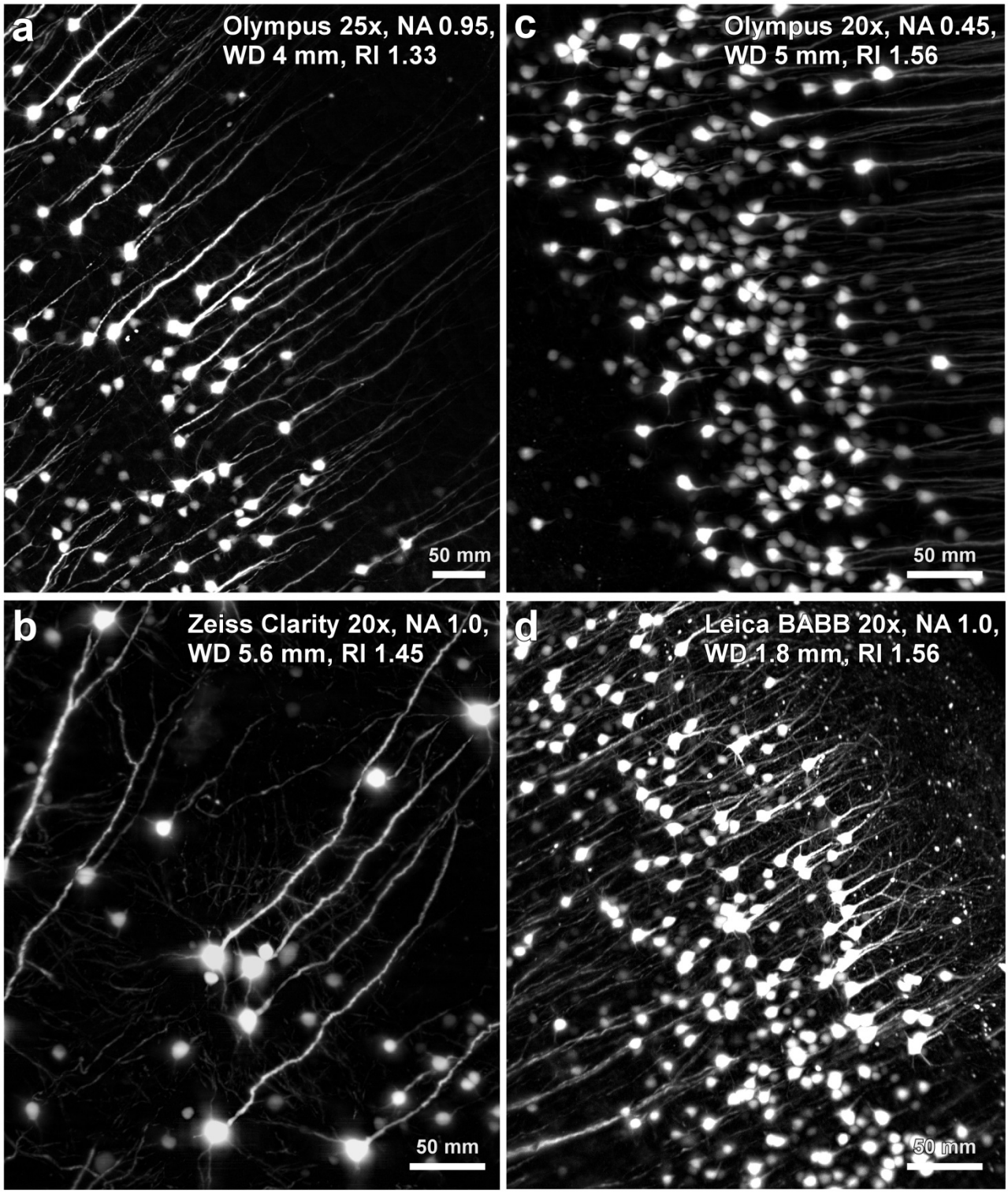


The quality comparison of four commercially available objectives (as indicated in the respective images) in BABB-D (RI 1.56) after uDISCO clearing of GFP-M brains. All images were generated using light-sheet microscopy at 1.5 mm depth from the cortex surface. It is worth mentioning that the water (**a**) and CLARITY (**b**) corrected objectives (therefore not corrected for BABB-D refractive index) generated comparable quality images to BABB corrected objectives (**c,d**). NA = numerical aperture, WD = working distance, RI = refractive index.

**Supplementary Figure 28: The transcardiac circulatory system for uDISCO whole body tissue clearing**

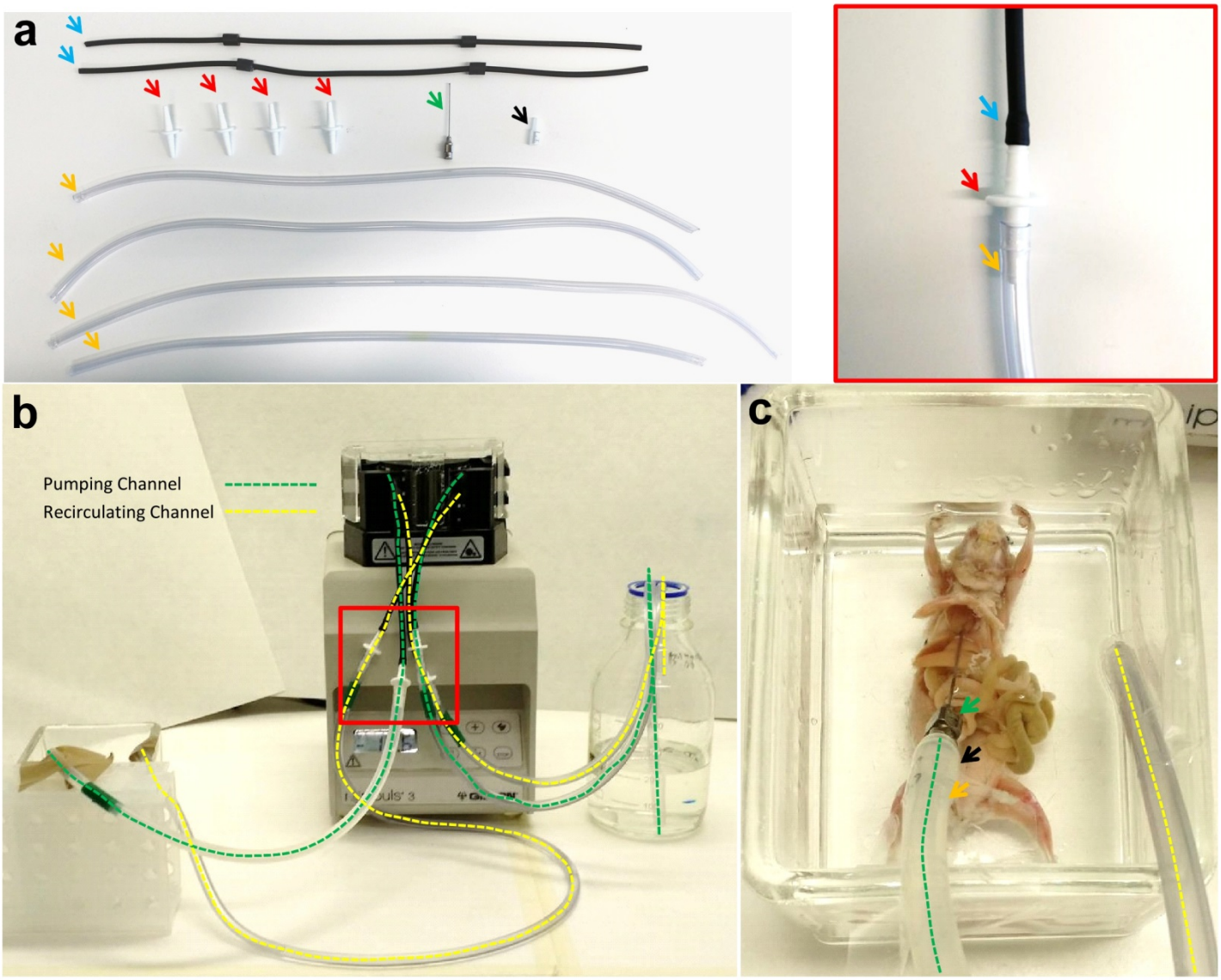


(**a**) Components of the circulation loop: 2x Viton reference tubing (Gilson, F1817745) (blue arrow), 4x tubing connectors (Omnilab, 5434482) (red arrow), 4x PVC tubing for extension (Omnilab, 5437920) (orange arrow), 1x transcardiac perfusion needle (Leica, 39471024) (green arrow), 1x needle connector cut from 1 ml syringe (Braun, 9166017V) (black arrow). The red box shows the connection of each Viton tubing ending indicated in (b). (**b**) A completed setup of the transcardiac circulatory system. Green dash highlights the first channel for pumping the clearing solution through whole mouse body. The yellow dash shows the second channel for collecting and recirculating the solution back to the original bottle. (**c**) Insert the cutting connector (black arrow) into the outflow tubing of the pumping channel (orange arrow) and fix it with a transcardiac perfusion needle (green arrow). After pushing the air bubble out of the tubing system, the animal is placed in the glass clearing chamber and the perfusion needle is inserted into the left ventricle of the heart.

**Supplementary Figure 29: Workflow for cell counting**

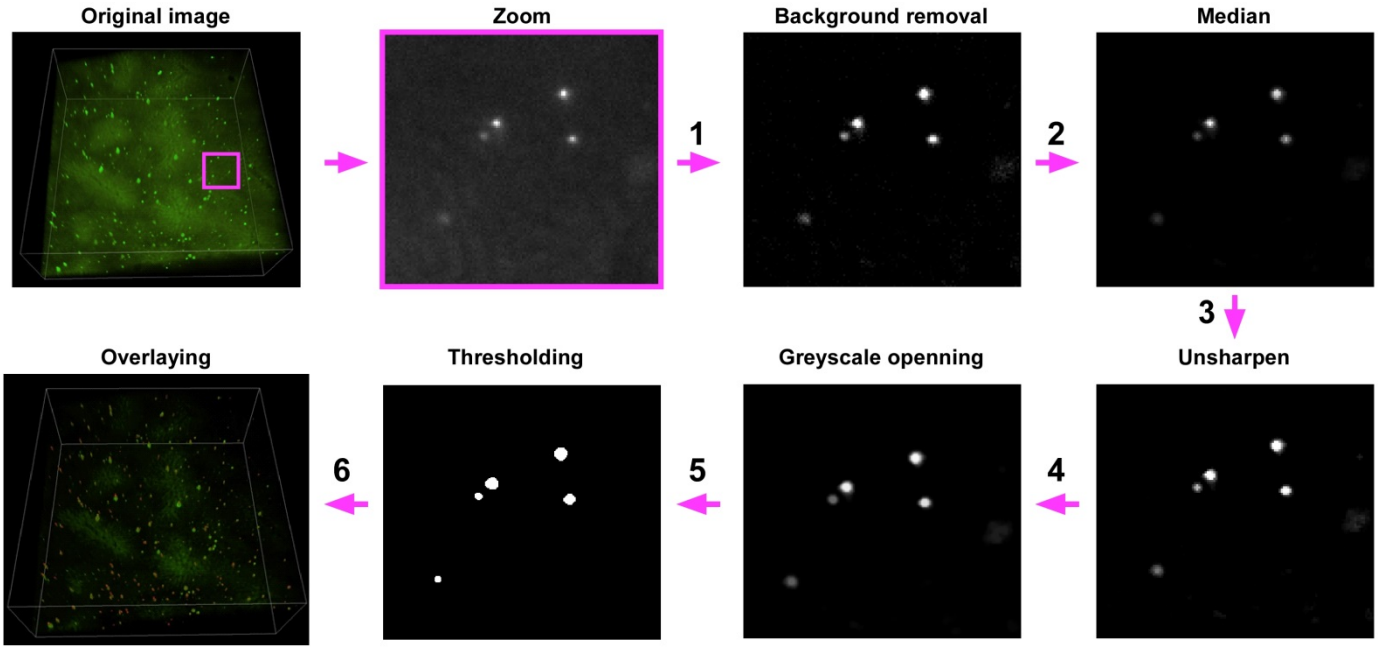


To count the number of bone marrow stem cells (BMSCs), we used publicly available ImageJ and its plugins as detailed below. Here we showed each step of the analysis on a sample image (a single optical section from a liver scan at 1.62 x1.62 x 12 µm voxel size). 1) To improve the background, we used convoluted median background subtraction option in BioVoxxel plugin. This plugin works fast, and removes the background smoothly in our samples because of low artifacts. 2) Median filtering was performed to remove artifacts coming from background subtraction. In this filtering, the radius is equal to the smallest object to be maintained (4 µm in our example). 3) Unsharpen mask was used when the signal-to-background ratio was lower than 2. In this mask, R stands for the average radius of the cells (6 um in our example). 4) To remove all the artifacts smaller than the cells, we used Grayscale opening morphological filter option in MorpholibJ plugin. In this filter, R is the radius of the biggest object to be removed (3 µm in our example) and disk option was used as structuring elements. 5) To decrease complexity of the quantification, we converted processed images to binary images by thresholding. To perform automatic thresholding, we used Otsu Limited function in DeadEasy plugin, which can perform multi-level thresholding. In addition, watershed can be used to separate the connected cells in densely labeled samples (this step was not performed in the example above because of sparse distribution). 6) Finally, detected cells were overlaid with the original data to check accuracy of the cell detection.

**Supplementary Figure 30: Methods for normalized signal profile and intensity quantifications**

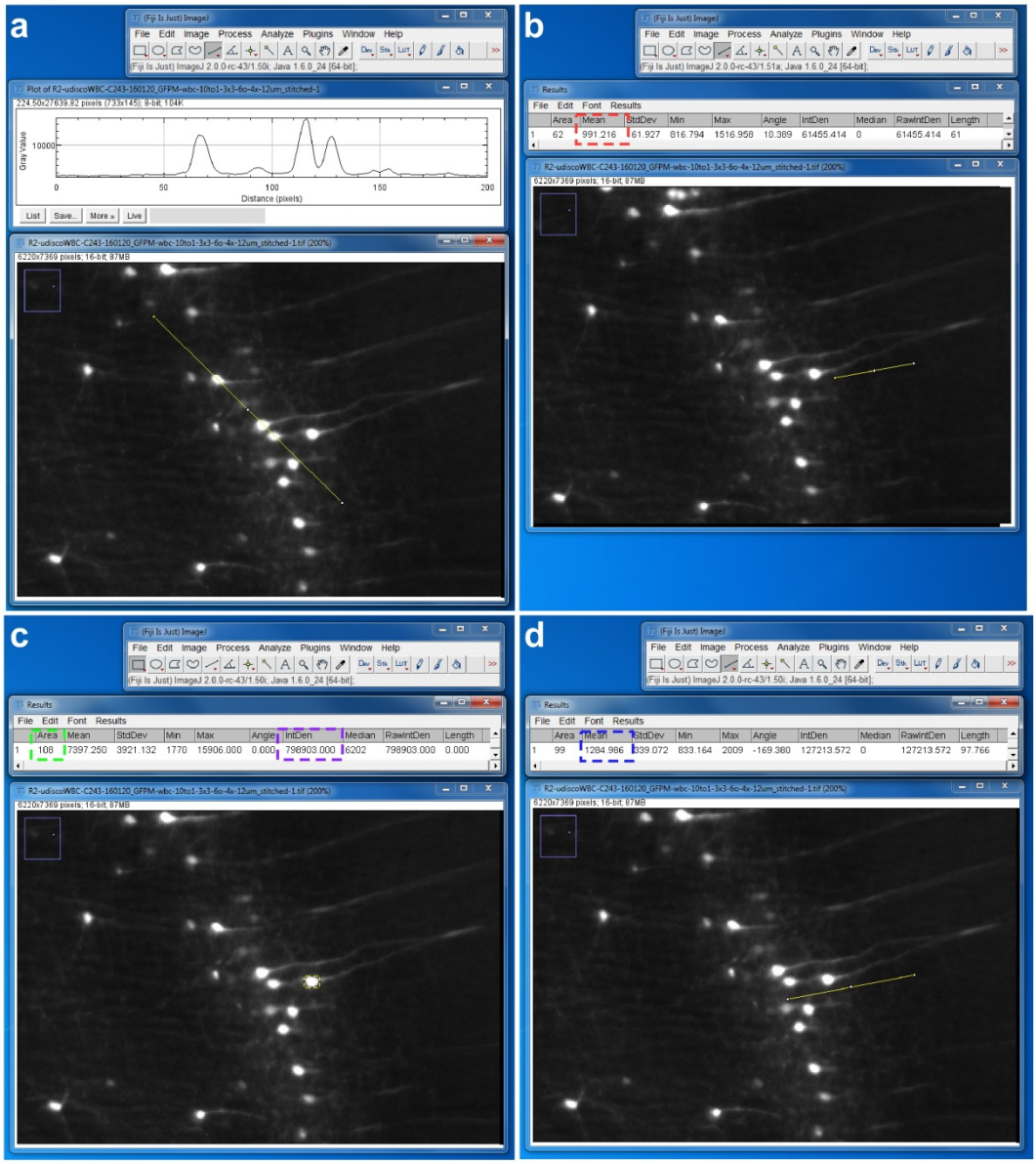


In Fiji (ImageJ2) software, a straight line was drawn across the specific signal spots and the plot profile of the signal was measured (**a**). Another straight line was drawn across the background area close to the specific signal spot to measure the mean value of the background (red box) (**b**). Next, the profile was divided by the selected background value and normalized profile of each sample was shown in the representative line chart (Supplementary Figs. 2, 5, 6, and 10). For signal intensity quantification, a rectangular selection covering the signal spot (a specific cellular structure) was made within the defined region and the integrated density of the signal was recorded (purple box) (**c**). A straight line was drawn across the background area close to the signal spot and the mean gray value of the background was measured (blue box) (**d**). (**e**) Formula for the signal intensity: 1) the total mean value of the background of the rectangular selection was subtracted from the integrated density of the signal to get the total signal density in the rectangular selection, and 2) the average intensity of the signal without background was calculated by dividing the total signal density with the pixel number of the rectangular selection (green box) (Supplementary Figs. 2, 5, 6, 9 and 10).

**Supplementary Protocol**

## Perfusion and tissue preparation

Before intracardial perfusion, anesthetize the animals deeply with a combination of anesthetics, such as midazolam/medetomidine/fentanyl (MMF) (1ml/100g of body mass for mice).

1. Transcardially perfuse the animals (e.g. using Leica perfusion one system at 100-125 mmHg pressure) first with heparinized (10U/ml of Heparin, ratiopharm GmbH, N68542.03) 0.1 M PBS for 5-10 minutes then with 4% paraformaldehyde (PFA, Morphisto, 11762.01000) in 0.1 M PBS for 20 minutes at room temperature.
   **TIP:** Skipping the Heparin when vasculature is labeled can increase the quality of labeling. For all perfusion steps, the needle should be placed and kept in the left ventricle of the heart and should not cross to the right side of the heart.
2. For whole-body clearing, remove the skin and carefully open the skull and vertebra without damaging the CNS tissue. At this point, the whole body clearing can be performed immediately, or the mouse body can be stored in 0.1M PBS at 4 °C up to 4 weeks. For clearing dissected organ, collect the tissues directly and post-fix them in 4% PFA for 1-2 days at 4°C. Wash the samples once in 0.1M PBS for 5 min before clearing.

## Preparation of uDISCO solutions

1. Prepare *tert*-butanol (Sigma, 360538) solutions with distilled water at 30 Vol%, 50 Vol%, 70 Vol%, 80 Vol%, 90 Vol%, 96 Vol% and 100 Vol% for gradient dehydration.
2. Use Dichloromethane (DCM) (Sigma, 270997) as a pure solution, for delipidation step.
3. Prepare refractive index matching solutions by mixing BABB (benzyl alcohol + benzyl benzoate 1:2, Sigma, 24122 and Sigma, W213802, respectively) and diphenyl ether (DPE) (Alfa Aesar, A15791) at following ratio: BABB-D4, BABB:DPE at a ratio 4:1 (Vol/Vol); BABB-D10, BABB:DPE at a ratio 10:1 (Vol/Vol); BABB-D15, BABB:DPE at a ratio 15:1 (Vol/Vol). Add 0.4% Vol vitamin E (Alfa Aesar, A17039) into BABB-D solutions to scavenge the peroxides.

*Tert*-butanol is flammable, DCM is toxic and BABB-D components can cause skin irritation, therefore they should be handled carefully. Waste should be treated and discarded accordingly.

## uDISCO passive clearing procedure for dissected organs

All incubation steps are performed in a fume hood with gentle rotation or shaking using 5 ml tubes (Eppendorf, 0030 119.401) for whole mouse brain or smaller samples, or using 80 ml glass chambers (omnilab, 5163279) for bigger samples such as rat tissues or whole brain + spinal cord. The samples are covered with aluminum foil to keep them in dark.

1. Incubate the fixed samples in 30 Vol%, 50 Vol%, 70 Vol%, 80 Vol%, 90 Vol%, 96 Vol% and 100% *tert*-butanol for 2-12 hours at 34-35°C (**Supplementary Table 1**).
2. Incubate in DCM for 45-60 minutes at room temperature (small tissues such as mouse spinal cord or 1 mm thick coronal slices can skip this step).
3. Incubate in BABB-D for 2-6 hours until the samples become optically transparent.

**TIP:** The higher amount of DPE in BABB yields better signal preservation (e.g. BABB-D15), while the lower amount of DPE in BABB results in higher transparency (e.g. BABB-D4). We recommend to use BABB-D4 for small tissues e.g. spinal cord or tissue slices, and BABB-D15 for large tissues e.g. for rat brain clearing. For whole-body clearing with perfusion system, use BABB-D10.

4. Samples can be stored in BABB-D at room temperature in the dark for several weeks. **TIP:** It is recommended to image sample as soon as possible to yield the best outcome.

**uDISCO whole-body clearing procedure with perfusion system**

Establish the transcardial-circulatory system as in **Supplementary Fig. 28**. Here, we used a peristaltic pump (Gilson, Peristaltic Pump MINIPULS 3) with one pumping channel (green dash line) and one recirculating channel (yellow dash line). All steps should be performed in a fume hood.

1. Connect the Viton reference tubing to the peristaltic pump.
   **TIP**: As the clearing solutions can be corrosive to various tubing material, we recommend usage of Viton tubing (Gilson, F1817745).
2. Insert the tubing connectors (Omnilab, 5434482) (red arrow) at each end of the Viton tubing (blue arrow).
3. Connect the tubing connectors (red arrow) with additional PVC tubing (Omnilab, 5437920) for extension (orange arrow).
   **TIP:** Transparent PVC tubing, which is compatible with clearing solutions, helps for checking unwanted air bubbles in the tubing system.
4. Cut the head part of the 1 ml syringe (Braun, 9166017V) as a connector (black arrow) and insert it into the outflow tubing of the pumping channel (orange arrow).
5. Connect the transcardiac perfusion needle (Leica, 39471024) (green arrow) for mouse or the thinnest perfusion needle (Leica, 39471022) without rubber head for rat with this connector. Subsequently, fix the inflow tubing of the recirculating channel in the glass chamber containing animal body ready for clearing.
   **TIP:** Fix the tubing with tapes (any kind). Keep a certain height between the inflow tubing head and bottom of the glass chamber to ensure that the sample is covered by clearing solutions during clearing at all times.
6. Keep the inflow tubing of the pumping channel beneath the surface of the clearing solution and start the circulation until air bubbles are pushed out from the tubing system.
   **TIP:** Avoid pumping air bubbles by keeping the tubing always immersed into solution while pumping.
7. Set the perfusion needle into the heart of the animal through the same pinhole made during perfusion and circulate the clearing solutions one by one as indicated in **Supplementary Table 1**.
   **TIP 1:** When starting the circulation, it might be visible that some ripples occur beside the right atrial appendage because the PBS in the sample is pushed into 30 Vol% *tert*-butanol solutions. This would be a good signal that the pumping is working appropriately. If not, try to change the angle of the perfusion needle to reach the best position and fix it with tapes. Because of the shrinkage during dehydration, the needle should stay in the heart without slipping out.
   **TIP 2:** Stop the pump temporarily when changing the clearing solutions between steps. Collect the last solution back to the bottle by using a serological pipette and fill the glass chamber with the next solution quickly to minimize exposure to air. Because serological pipettes are not stable in BABB-D, use them only in the prior steps. Hold the inflow tubing ending of the pumping channel carefully to avoid any air

bubble and put it beneath the surface of next solution. If there are large air bubbles within the tubing, they can be eliminated by a brief run of the pump in the reverse direction.

**TIP 3:** As the melting point of *tert*-butanol is between 23 and 26 °C (close to room temperature), use a heating plate at 35-40 °C for 100% *tert*-butanol circulation steps to prevent the solution from solidification.

**TIP 4:** The amount of solutions for circulation depends on the capacity of the clearing chamber and the size of the animal that is being cleared. For example, for mice, a 400 ml capacity glass chamber with 300 ml working clearing solution and for rats, a 1000 ml capacity glass chamber with 800 ml working clearing solution would be sufficient.

**TIP 5:** For rat clearing, because PVC tubing is not resistant to DCM, the DCM step can be performed with gentle shaking to increase the efficiency.

**TIP 6:** The flowing rate was set at 8-10 ml/min for mouse clearing and 15-20 ml/min for rat clearing.

8. At the final step, circulate BABB-D10 until full transparency is achieved (about 6-12 hours for mouse and ~24 hours for rat).

   **TIP:** It is recommended to image sample as soon as possible to yield the best outcome.

**Supplementary Table 1: Notes for clearing steps**

steps

| Tissue type / reagents temperature | half brain from adult animals | whole organs from adult animals such as brain, brain + intact spinal cord, kidney liver, bones | rat brain + spinal cord | Tissue type / reagents temperature | small tissues such as spinal cord, hippocampus, cerebellum | 1 mm slices | whole body with perfusion system (mouse) | whole body with perfusion system (rat) |
|---|---|---|---|---|---|---|---|---|
| **30% *tert*-but at 35°C** | ON | ON | 1 day | **30% *tert*-but at RT** | 4 hr | 2 hr | 12 hr | 1 day |
| **50% *tert*-but at 35°C** | 4 hr | 10 hr | 1 day | **50% *tert*-but at RT** | 4 hr | 2 hr | 12 hr | 1 day |
| **70% *tert*-but at 35°C** | 4 hr | ON | 1 day | **70% *tert*-but at RT** | ON | 2 hr | 12 hr | 1 day |
| **80% *tert*-but at 35°C** | ON | 10 hr | 1 day | **80% *tert*-but at RT** | 4 hr | 2 hr | – | – |
| **90% *tert*-but at 35°C** | 4 hr | ON | 1 day | **90% *tert*-but at RT** | 4 hr | 2 hr | 12 hr | 1 day |
| **96% *tert*-but at 35°C** | 4 hr | 10 hr | 1 day | **96% *tert*-but at RT** | ON | ON | – | – |
| **100% *tert*-but at 35°C** | ON | ON | 1 day x 2 | **100% *tert*-but at RT** | – | 2 hr | 12 hr x 2 | 1 day x 2 |
| **DCM at RT** | 40-50 min | 50-70 min | 2 hr | **DCM at RT** | – | – | – | 6-8 hr |
| **BABB-D4 or BABB-D15** | > 2 hr | > 3 hr | > 5 hr | **BABB-D4 or BABB-D15** | > 2 hr | > 1 hr | NA | NA |
| | | | | **BABB-D10** | | | > 6 hr | > 24 hr |

*tert*-but : *tert*-butanol, ON : overnight, hr : hour(s), min : minute(s), RT : room temperature, DCM : dichloromethane, BABB : benzyl alcohol + benzyl benzoate (1:2 in volume), BABB-D4 : BABB + diphenyl ether (4:1 in volume), BABB-D10 : BABB + diphenyl ether (10:1 in volume), BABB-D14 : BABB + diphenyl ether (14:1 in volume), –: skip the step

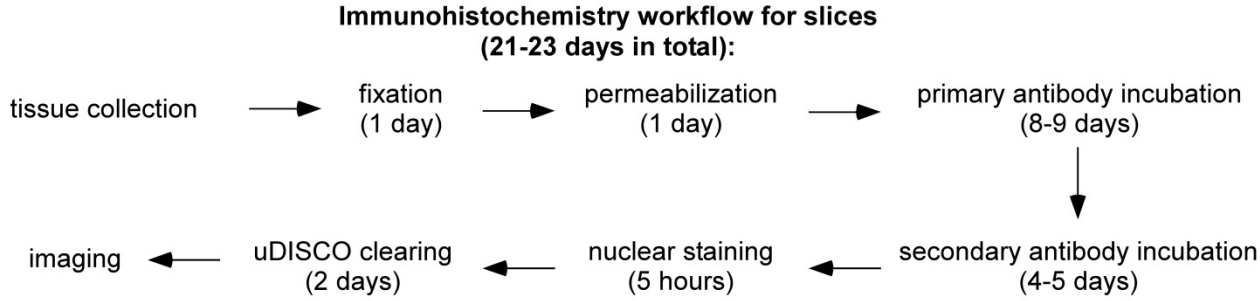


Times for each experiment step can be shortened (e.g to half) or extended (e.g. to double) depending on tissue size to improve antibody penetration or clearing performance. To preserve the signal better in low fluorescence conditions, dehydration can be ceased at 90% or 96% and proceed to the BABB-D step. We found that active (perfusion mediated) whole-body clearing provided superior transparency compared to passive clearing of dissected organs e.g. the brain.

Nature Methods: doi:10.1038/nmeth.3964

# Supplementary Table 2: Imaging specifications

| FIGURES | | SYSTEM | OBJECTIVE SPECIFICATIONS | | | | ACQUISITION PARAMETERS | | | |
|---|---|---|---|---|---|---|---|---|---|---|
| | | | Magnification | NA | RI | WD | Zoom | Image pixel size | z-step | imaging depth |
| Figures | | | | | | | | | | |
| | | | | | | | | | | |
| 1 | a | UM II | 4X corr. | 0.28 | 1.56 | 10mm | | 1.625µmx1.625µm | 8µm | 1mm |
| | g | UM II | 4X corr. | 0.28 | 1.56 | 10mm | | 1.625µmx1.625µm | 2µm | 2.0-2.2mm |
| | | | | | | | | | | |
| 2 | c | AxioZoom | Zeiss 1X | 0.25 | 1.0 | 56mm | | 6.49µmx6.49µm | n.a. | n.a. |
| | d | UM II -MVX10 | Oly. 2X | 0.5 | 1.33/1.56 | 6mm | 0.63 | 5.16µmx5.16µm | 8µm | 3D reconstruction |
| | e | UM II -MVX10 | Oly. 2X | 0.5 | 1.33/1.56 | 6mm | 0.63 | 5.16µmx5.16µm | 8µm | 1mm |
| | f | UM II -MVX10 | Oly. 2X | 0.5 | 1.33/1.56 | 6mm | 0.63 | 5.16µmx5.16µm | 8µm | 3mm |
| | g | UM II -MVX10 | Oly. 2X | 0.5 | 1.33/1.56 | 6mm | 0.63 | 5.16µmx5.16µm | 8µm | 5mm |
| | h | UM II -MVX10 | Oly. 2X | 0.5 | 1.33/1.56 | 6mm | 0.63 | 5.16µmx5.16µm | 10µm | projection of 8mm scan |
| | i,j | UM II -MVX10 | Oly. 2X | 0.5 | 1.33/1.56 | 6mm | 3.2 | 1.015µmx1.015µm | 4µm | projection of 8mm scan |
| | | | | | | | | | | |
| 3 | c | AxioZoom | Zeiss 1X | 0.25 | 1.0 | 56mm | | 6.49µmx6.49µm | n.a. | n.a. |
| | d,e,f | AxioZoom | Zeiss 1X | 0.25 | 1.0 | 56mm | | 1.42µmx1,42µm | n.a. | n.a. |
| | j,k,l,m | UM II | 4X corr. | 0.28 | 1.56 | 10mm | | 1.625µmx1.625µm | 20µm | projection of 10mm scan |
| | | | | | | | | | | |
| 4 | a,c | UM II | 4X corr. | 0.28 | 1.56 | 10mm | | 1.625µmx1.625µm | 4µm | entire scan projection |
| | d | UM II | 4X corr. | 0.28 | 1.56 | 10mm | | 1.625µmx1.625µm | 4µm | 1.8mm |
| | e | UM II | 4X corr. | 0.28 | 1.56 | 10mm | | 1.625µmx1.625µm | 4µm | 2.0mm |
| | f | UM II | 4X corr. | 0.28 | 1.56 | 10mm | | 1.625µmx1.625µm | 4µm | 3.0mm |
| | g | UM II | Zeiss 20x | 1.0 | 1.45 | 5.6mm | 2 | 0.1625µmx0.1625µm | 2µm | 500µm |
| | | | | | | | | | | |
| 5 | b | UM II | 4X corr. | 0.28 | 1.56 | 10mm | 0.63 | 2.56µmx2.56µm | 16µm | 1.5-3mm |
| | | UM II -MVX10 | Oly. 2X | 0.5 | 1.33/1.56 | 6mm | 0.63 | 5.16µmx5.16µm | 16µm | 3D reconstruction |
| | | | | | | | | | | |
| 6 | virus b,c,d,e,f | UM II | 4X corr. | 0.28 | 1.56 | 10mm | | 1.625µmx1.625µm | 12µm | entire scan projection |
| | mouse l,m | LSM880 | Leica 25x | 0.95 | 1.33 | 2.5mm | | 0.2µmx0.2µm | 3µm | 450-480µm, 600-630µm |
| | human u | LSM880 | Leica 25x | 0.95 | 1.33 | 2.5mm | | 0.2µmx0.2µm | 3µm | 270-282µm |
| | | | | | | | | | | |
| Sup. Figures | | | | | | | | | | |
| | | | | | | | | | | |
| S1 | c | AxioZoom | Zeiss 1X | 0.25 | 1.0 | 56mm | | 6.49µmx6.49µm | n.a. | n.a. |
| | d,e,f,g | UM II | 4X corr. | 0.28 | 1.56 | 10mm | | 1.625µmx1.625µm | n.a. | n.a. |
| | | | | | | | | | | |
| S2 | | UM II | 4X corr. | 0.28 | 1.56 | 10mm | | 1.625µmx1.625µm | 12µm | 2.5mm |
| | | | | | | | | | | |
| S5 | | UM II | 2X corr. | 0.14 | 1.56 | 10mm | | 3.25µmx3.25µm | 8µm | 0.5mm, 2.5mm |
| | | | | | | | | | | |
| S6 | | UM II | 2X corr. | 0.14 | 1.56 | 10mm | | 3.25µmx3.25µm | 8µm | 0.5mm, 2.5mm |
| | | | | | | | | | | |
| S8 | | AxioZoom | Zeiss 1X | 0.25 | 1.0 | 56mm | | 5.68µmx5.68µm | n.a. | n.a. |
| | | | | | | | | | | |
| S9 | a,c,e | UM II | 4X corr. | 0.28 | 1.56 | 10mm | | 1.625µmx1.625µm | 4µm | 0.44mm |
| | b,d,f | UM II | 4X corr. | 0.28 | 1.56 | 10mm | | 1.625µmx1.625µm | 4µm | 0.66mm |
| | | | | | | | | | | |
| S10 | a-f | UM II -MVX10 | Oly. 2X | 0.5 | 1.33/1.56 | 6mm | 0.63 | 5.16µmx5.16µm | 4µm | 0.66mm |
| | | | | | | | | | | |
| S11 | a,c | UM II -MVX10 | Oly. 2X | 0.5 | 1.33/1.56 | 6mm | 0.63 | 5.16µmx5.16µm | 4µm | 3D reconstruction |
| | | | | | | | | | | |
| S12 | | AxioZoom | Zeiss 1X | 0.25 | 1.0 | 56mm | | 5.68µmx5.68µm | n.a. | n.a. |
| | | | | | | | | | | |
| S13 | | LSM880 | Leica 25x | 0.95 | 1.33 | 2.5mm | | 0.183µmx0.183µm | 3-4µm | 0-100µm |
| | | | | | | | | | | |
| S14 | | LSM880 | Leica 25x | 0,95 | 1.33 | 2.5mm | | 0.183µmx0.183µm | 3-4µm | 0-100µm |
| | | | | | | | | | | |
| S17 | a | UM II | 2X corr. | 0.14 | 1.56 | 10mm | | 3.25µmx3.25µm | 6µm | 10mm |
| | b,c,d,e | UM II | 4X corr. | 0.28 | 1.56 | 10mm | | 1.625µmx1.625µm | 6µm | 10mm |
| | | | | | | | | | | |
| S19 | h | LSM880 | Leica 25x | 0.95 | 1.33 | 2.5mm | | 0.67µmx0.67µm | 2µm | 18-62µm |
| | i | LSM880 | Leica 25x | 0.95 | 1.33 | 2.5mm | | 0.43µmx0.43µm | 1µm | 6-45µm |
| | small boxes in figS4h | LSM880 | Leica 25x | 0.95 | 1.33 | 2.5mm | | 0.16µmx0.16µm | 1µm | |
| | small boxes in figS4i | LSM880 | Leica 25x | 0.95 | 1.33 | 2.5mm | | 0.10µmx0.10µm | 1µm | |
| | | | | | | | | | | |
| S20 | | AxioZoom | Zeiss 1X | 0.25 | 1.0 | 56mm | | 5.68µmx5.68µm | n.a. | n.a. |
| | | | | | | | | | | |
| S21 | | UM II -MVX10 | Oly. 2X | 0.5 | 1.33/1.56 | 10mm | 0.63 | 5.16µmx5.16µm | 8µm | 2.35mm |
| | | UM II -MVX10 | Oly. 2X | 0.5 | 1.33/1.56 | 10mm | 0.63 | 5.16µmx5.16µm | 8µm | 1.4mm |
| | | UM II -MVX10 | Oly. 2X | 0.5 | 1.33/1.56 | 10mm | 0.63 | 5.16µmx5.16µm | 8µm | 2.9mm |
| | | | | | | | | | | |
| S22 | | UM II | 4X corr. | 0.28 | 1.56 | 10mm | | 1.625µmx1.625µm | 6µm | 1.9mm |
| | | | | | | | | | | |
| S23 | | UM II | 4X corr. | 0.28 | 1.56 | 10mm | | 1.625µmx1.625µm | 12µm | entire scan projection |
| | | | | | | | | | | |
| S24 | d | LSM880 | Leica 25x | 0.95 | 1.33 | 2.5mm | | 0.2µmx0.2µm | 3µm | 24-30µm |
| | e | LSM880 | Leica 25x | 0.95 | 1.33 | 2.5mm | | 0.2µmx0.2µm | 3µm | 237-246µm |
| | | | | | | | | | | |
| S25 | d | LSM880 | Leica 25x | 0,95 | 1,33 | 2.5mm | | 0.2µmx0.2µm | 3µm | 327-387µm |
| | h | LSM880 | Leica 25x | 0,95 | 1,33 | 2.5mm | | 0.2µmx0.2µm | 4µm | 276-292µm |
| | | | | | | | | | | |
| S27 | a | UM II | Oly. 25X | 0,95 | 1.31-1.52 | 4mm | | 0.26µmx0.26µm | 4µm | 0.8-1.2mm |
| | b | UM II | Zeiss 20x | 1 | 1,45 | 5.6mm | | 0.325µmx0.325µm | 4µm | 0.4-0.8mm |
| | c | UM II | 20X corr. | 0,45 | 1,56 | 5mm | | 0.325µmx0.325µm | 4µm | 0.5-1.0mm |
| | d | UM II | Leica 20X | 0,95 | 1,56 | 1.8mm | | 0.325µmx0.325µm | 2µm | 0.65-1.05mm |

**Legend of abbreviations**

Imaging Systems

| | |
|---|---|
| UM II | LaVision BioTec - UltraMicroscope II |
| UM II -MVX | LaVision BioTec - UltramicroscopeM II -MVX10 |
| LSM880 | Zeiss confocal LSM880 with Airyscan |
| AxioZoom | Zeiss AxioZoom EMS3/SyCoP3 |

| | |
|---|---|
| NA | Numerical aperture |
| RI | Refractive Index |
| WD | Working distance |
| n.a. | not applicable |

Objectives

| | |
|---|---|
| Oly. 2X | Olympus MVPLAPO2XC |
| 2X corr. | Olympus XLFLUOR2x corrected |
| 4X corr. | Olympus XLFLUOR4x corrected |
| 20X corr. | Olympus LUCPLFLN20x corrected |

Oly. 25X Olympus XLPLN25X

Zeiss 1X Zeiss PlanNEOFLUAR Z 1x

Zeiss 20X Zeiss Clr Plan-Neofluar 20x

Leica 20X Leica HCX APO L20×

Leica 25X Leica HCX IRAPO L 25x

## 4.2 Panoptic imaging of transparent mice reveals whole-body neuronal projections and skull-meninges connections

The possibility to clear and analyze entire transparent rodent bodies would allow the study of physiological and pathological events with a holistic approach.

Recent papers (including our uDISCO paper) have already introduced the clearing and imaging of whole organisms, yet, reliable detection and quantification of the fluorescence signal in such thick tissues have remained a challenge because of several reasons: (i) most of the applications of tissue clearing are based on the detection of endogenous fluorescent proteins whose signal is often strongly reduced by the clearing process, (ii) these proteins are generally less bright than synthetic fluorescent dyes (for examples the ones conjugated to secondary antibodies), (iii) they emit light in the visible spectrum, a range where muscles and tissues are characterized by an obstructive autofluorescence.

To overcome the above mentioned limitations, in this article we developed a new method called vDISCO. vDISCO is the first method achieving whole-body immunolabeling and clearing, exploiting the small size of nanobodies- variable domain of heavy chain antibodies- (instead of using conventional antibodies) and boosting the signal of fluorescent proteins up to 2 orders of magnitude while maintaining it for years. In this way vDISCO allows light-sheet imaging of whole transparent bodies (panoptic imaging) through tissues, bones and skin, and the quantification of subcellular details. With vDISCO, we visualized and reconstructed the first map of neuronal projections embedded in muscles and bones of an adult mouse at subcellular resolution. Thanks to panoptic imaging, we were able to detect whole-body neuronal changes triggered by traumatic brain injury, to observe inflammatory events after stroke in the whole head and also to reveal short vascular connections –named short skull-meninges connections (SMCs)– between the skull marrow and brain meninges which represent a possible new route of immune cell invasion under pathological conditions such as stroke.

Taken together, vDISCO opens a new way to study the biological phenomena in an unbiased and comprehensive manner.

*Contribution of R.C. to this work: equal contribution to the development of the method with C.P.; moreover, I performed: characterization of the method: preservation of the fluorescent signal, fluorescent signal analysis, imaging penetration, deep tissue staining efficiency, comparison with other immunostaining methods (passive and active), pressure experiment; performing the experiments, analyzing the data and interpretation of the results for the followings: whole-body neuronal map experiments, skin cleared Thy1-GFPM animal, TBI experiments, NeuroGPS-Tree experiments, whole-body and whole-brain CX3CR1-GFP experiments, ClearMap experiments, vimentin nanobody experiments, SCI preliminary experiments; writing the manuscript with equal contribution from C.P. (please see section 12 for further details)*

nature neuroscience

TECHNICAL REPORT

https://doi.org/10.1038/s41593-018-0301-3

# Panoptic imaging of transparent mice reveals whole-body neuronal projections and skull–meninges connections

Ruiyao Cai[1,2,10], Chenchen Pan[1,2,10], Alireza Ghasemigharagoz[1], Mihail Ivilinov Todorov[1,2], Benjamin Förstera[1], Shan Zhao[1], Harsharan S. Bhatia[1], Arnaldo Parra-Damas[1], Leander Mrowka[1], Delphine Theodorou[3,4], Markus Rempfler[5], Anna L. R. Xavier[6], Benjamin T. Kress[6,7], Corinne Benakis[1], Hanno Steinke[8], Sabine Liebscher[3,4,9], Ingo Bechmann[8], Arthur Liesz[1,2,9], Bjoern Menze[5], Martin Kerschensteiner[3,4,9], Maiken Nedergaard[6,7] and Ali Ertürk[1,2,9]*

**Analysis of entire transparent rodent bodies after clearing could provide holistic biological information in health and disease, but reliable imaging and quantification of fluorescent protein signals deep inside the tissues has remained a challenge. Here, we developed vDISCO, a pressure-driven, nanobody-based whole-body immunolabeling technology to enhance the signal of fluorescent proteins by up to two orders of magnitude. This allowed us to image and quantify subcellular details through bones, skin and highly autofluorescent tissues of intact transparent mice. For the first time, we visualized whole-body neuronal projections in adult mice. We assessed CNS trauma effects in the whole body and found degeneration of peripheral nerve terminals in the torso. Furthermore, vDISCO revealed short vascular connections between skull marrow and brain meninges, which were filled with immune cells upon stroke. Thus, our new approach enables unbiased comprehensive studies of the interactions between the nervous system and the rest of the body.**

Most diseases, even when arising in a specific site, eventually affect the entire organism. Histological techniques developed in the last century have been the standard procedure for charting pathology, yet a more complete understanding of biological mechanisms requires an unbiased exploration of the whole organism, not just pre-defined tissues.

However, mammalian tissues are naturally opaque, hindering high-resolution imaging in any tissue deeper than a few hundred micrometers, a major reason why sectioning is needed for histological examination of target organs[1]. Recent innovations in tissue clearing technology now allow three-dimensional (3D) histological examination of intact organs[2–12]. Tissue clearing is a chemical process aiming to match refractive indices throughout intact tissues, thus rendering them transparent and allowing deep-tissue fluorescent microscope imaging. Most initial applications of tissue clearing relied on the assessment of endogenous fluorescent proteins expressed in the mouse CNS. More recently, deep-tissue immunolabeling methods have enhanced the quality of imaging for whole rodent organs as well as human embryos thanks to the conjugation of bright fluorescent dyes with secondary antibodies[4,13,14]. A few studies have even rendered entire adult mouse bodies transparent after removal of the skin[3,15–18] and allowed head-to-toe light-sheet microscopy imaging of intact adult mice[17,18]. All whole-body clearing and imaging methods to date rely on transgenic expression of fluorescent proteins such as enhanced green fluorescent protein (EGFP), enhanced yellow fluorescent protein (EYFP) and mCherry[17,18]. While these fluorescent proteins emit light in the visible spectrum, skeletal muscles and other bodily tissues possess obstructive autofluorescence in this range[19]. In addition, fluorescent proteins are often less bright compared with many synthetic fluorophores, and their signal intensity is further attenuated during the clearing and imaging procedure. Together, these bottlenecks hinder reliable detection and quantification of subcellular details in centimeters-thick transparent mice and therefore require reliance on imaging of dissected organs for quantifications, compromising the benefits of whole-body transparency.

Here we developed a whole-body immunolabeling method, named vDISCO (nanobody($V_HH$)-boosted 3D imaging of solvent-cleared organs), to boost the signal of fluorescent proteins using nanobodies, which consist of the variable domain of heavy chain antibodies ($V_HH$)[20]. This technology can enhance fluorescent signals more than 100 times and thereby allows head-to-toe light sheet microscopy scanning of transparent mice (panoptic imaging) and quantification of subcellular details. We used this technology to construct the first neuronal projection map of an adult mouse and to reveal far-reaching changes in neuronal projections and inflammatory processes following acute CNS injuries. Panoptic imaging also revealed short vascular connections between the skull marrow

[1]Institute for Stroke and Dementia Research, Klinikum der Universität München, Ludwig-Maximilians University Munich, Munich, Germany. [2]Graduate School of Systemic Neurosciences Munich, Munich, Germany. [3]Institute of Clinical Neuroimmunology, Klinikum der Universität München, Ludwig-Maximilians University Munich, Munich, Germany. [4]Biomedical Center, Ludwig-Maximilians University Munich, Munich, Germany. [5]Department of Computer Science and Institute for Advanced Study, Technical University of Munich, Munich, Germany. [6]Center for Translational Neuromedicine, Faculties of Health and Medical Sciences, University of Copenhagen, Copenhagen, Denmark. [7]Center for Translational Neuromedicine, University of Rochester, New York, NY, USA. [8]Anatomy Institute, University of Leipzig, Leipzig, Germany. [9]Munich Cluster for Systems Neurology (SyNergy), Munich, Germany. [10]These authors contributed equally: Ruiyao Cai, Chenchen Pan. *e-mail: ali.ertuerk@med.uni-muenchen.de

and meninges (both at the brain surface and sagittal sinus), which may serve as immune gateways following stroke.

## Results

**vDISCO principles and signal enhancement.** Quantitative assessments of intact transparent mouse bodies remained a major challenge impeding the study of neurological diseases at the whole-body scale. We reasoned that fluorescent proteins such as EGFP and red fluorescent protein (RFP) are relatively dim compared with bright fluorochromes (for example, Alexa and Atto dyes) after tissue clearing, making them difficult to detect in centimeters-thick mouse bodies, especially through intact thick bones (for example, skull and vertebrae) and skin. Therefore, we set out to enhance the signal of fluorescent proteins via whole-body immunolabeling with brighter and more stable fluorescent dyes to provide a much higher contrast (signal-to-background ratio) in cleared mice. Furthermore, using fluorescent dyes in the far-red spectrum could help to overcome tissue autofluorescence, thus allowing reliable detection of subcellular details in all tissues[4,19] (Supplementary Fig. 1). We reasoned that nanobodies are particularly suited to achieve thorough immunolabeling throughout entire adult mouse bodies because of their small molecular weight (12–15 kDa) compared with that of conventional antibodies (~150 kDa)[3,20]. Indeed, nanobodies were more efficient for labeling large tissues compared with conventional antibodies (Supplementary Figs. 2 and 3).

First, we tested the signal quality of nanobody labeling in dissected mouse brains from *Thy1*-GFP-M mice, in which a subset of neurons express EGFP[21]. Following the nanoboosting, the tissues were cleared using organic solvents[6,7]. We found that nanoboosting enhanced the signal intensity by one to two orders of magnitude compared with direct imaging of fluorescent proteins (Fig. 1a–i). In the nanoboosted samples, fine details of neurons were evident even in the deep brain regions of *Thy1*-GFP-M mice (compare Fig. 1b,c with Fig. 1e,f). We also obtained a similar signal intensity increase in the cerebellum of *Thy1*-GFP-M brains (compare Fig. 1g with Fig. 1h), which is notoriously difficult to clear due to the high lipid content.

A major aim of tissue clearing approaches is to perform automated quantifications in large imaging datasets in an unbiased and timely way. Towards this goal, we used the NeuroGPS-Tree algorithm, a robust, automated neuron-tracing tool that was recently developed for tracing neurons in scans of cortical regions obtained by high-resolution confocal microscopy[22]. We found that virtually all of the neuronal cell bodies and neurites were detected and linked to each other as complete neurons upon vDISCO nanoboosting in light-sheet microscopy scans (Supplementary Figs. 4 and 5). In contrast, in unboosted samples or in standard immunoglobulin G antibody-boosted samples, many fine extensions of neurons were not identified or not connected to somas and neuronal trees (Supplementary Fig. 4). Nanoboosting allowed imaging not only of neuronal details but also of smaller individual cells such as microglia cells and immune cells (Fig. 1j–m and Supplementary Fig. 6). Compared with unboosted samples, we could resolve fine details of microglia cells in intact transparent brains of CX3CR1$^{GFP/+}$ mice using light-sheet microscopy (Fig. 1j–m and Supplementary Video 1). Nanoboosting also enabled automated quantification of CX3CR1 GFP$^{+}$ cells using the ClearMap algorithms[23]: we found approximately 2.3 million microglia cells in the adult mouse brain (Supplementary Fig. 7a). We also automatically quantified microglia in all brain regions annotated by the Allen Brain Atlas. Thereby we found, for example, ~150,000 microglia in the hippocampus and ~50,000 in the thalamus of adult mice (Supplementary Fig. 7b–k). Furthermore, we found no significant decrease in signal intensity over time of the same samples, suggesting that vDISCO nanoboosting stabilizes the fluorescent signal (Fig. 1n,o), allowing long-term preservation and re-imaging of the samples. Thus, owing to the enormous enhancement and stabilization of fluorescent signals using nanobodies, we could use available computational tools to automatically trace neurons and count cell numbers in images acquired by light-sheet microscopy.

**vDISCO allows panoptic imaging of intact adult mouse bodies.** To apply whole-body clearing technology at the systems level, it is critical to obtain information not only from dissected organs but also from intact transparent bodies. Towards this goal, we aimed at establishing an approach to achieve nanoboosting in the entire mouse body. We reasoned that vDISCO amplification of the fluorescent signals would allow reliable quantification of cells through intact thick bones and highly autofluorescent muscles. To ensure homogeneous delivery of nanobodies into all body regions, we used high-pressure cardiac perfusion with two- to three-fold increased pressure compared with standard perfusion protocols (160–230 mmHg compared with 70–110 mmHg (ref. [24])). We also illustrated the effect of high-pressure delivery compared with standard pressure using methylene blue. This novel high-pressure delivery approach facilitated a consistent distribution of the dye into deep tissues (Supplementary Fig. 8). Assessing the tissue integrity upon high-pressure delivery, we did not observe any structural changes (Supplementary Fig. 9). Furthermore, we used a permeabilization solution containing Triton X-100, methyl-β-cyclodextrin (to extract the cholesterol from membranes) and *trans*-1-acetyl-4-hydroxy-L-proline (to loosen the collagen network)[12]. To further reduce the background signal caused by the residual blood and to decalcify the bones, we treated whole mouse bodies with aminoalcohols[5,15] and EDTA[25] before the whole-body immunolabeling step. Combination of these diverse improvements allowed us to achieve whole-body immunolabeling in adult mice with a high degree of transparency (Fig. 2a and Supplementary Fig. 10) and to obtain quantitative information on single cells in deep brain regions through the intact skull[3,15–18,23] (Supplementary Figs. 11 and 12). Here, we used anti-XFP nanobodies conjugated with bright Atto dyes (called nanoboosters) to boost the fluorescent protein signal in transparent mice. Moreover, we used anti-vimentin nanobodies to label activated glia cells in the brain upon trauma, demonstrating that our approach also works with nanobodies targeting endogenously expressed proteins (Supplementary Fig. 13).

In addition to the specific boosted signal, we also visualized and segmented other major tissues in the transparent body: muscles by their autofluorescence within the blue–green spectrum, and bones and internal organs by propidium iodide (PI) labeling (Fig. 2b,c and Supplementary Fig. 14a–d). Usage of organic solvents, which induce isotropic tissue shrinkage[17], allowed us to perform head-to-toe panoptic imaging of entire mice by light-sheet microscopy.

Being able to image subcellular details of neurons through intact bones and highly autofluorescent muscles in the whole mouse body using vDISCO panoptic imaging, we constructed the first whole-body neuronal projection map of a *Thy1*-GFP-M transgenic mouse (Fig. 2d,e, Supplementary Fig. 14 and Supplementary Video 2). We noticed that in the peripheral nervous system, mainly axons innervating muscles were labeled in this mouse line, which enabled us to investigate the neuromuscular junctions in greater detail. We also observed fluorescent labeling of the internal organs, such as kidneys of *Thy1*-YFP-H mice[21] (Supplementary Fig. 15). Owing to the great increase in signal-to-background ratio by vDISCO, we could readily visualize axonal projections from the spinal cord through intact vertebrae to their terminals into the muscles, even in very remote locations such as toes (Fig. 2f–i and Supplementary Videos 3 and 4). Panoptic imaging of individual neuronal projections through intact bones can now provide more details on neuroanatomy. For example, how axons coming from consecutive roots enter the spinal cord—that is, in an overlapping or non-overlapping manner—has been unclear[26]. Using our technology, we observed that in mice, the

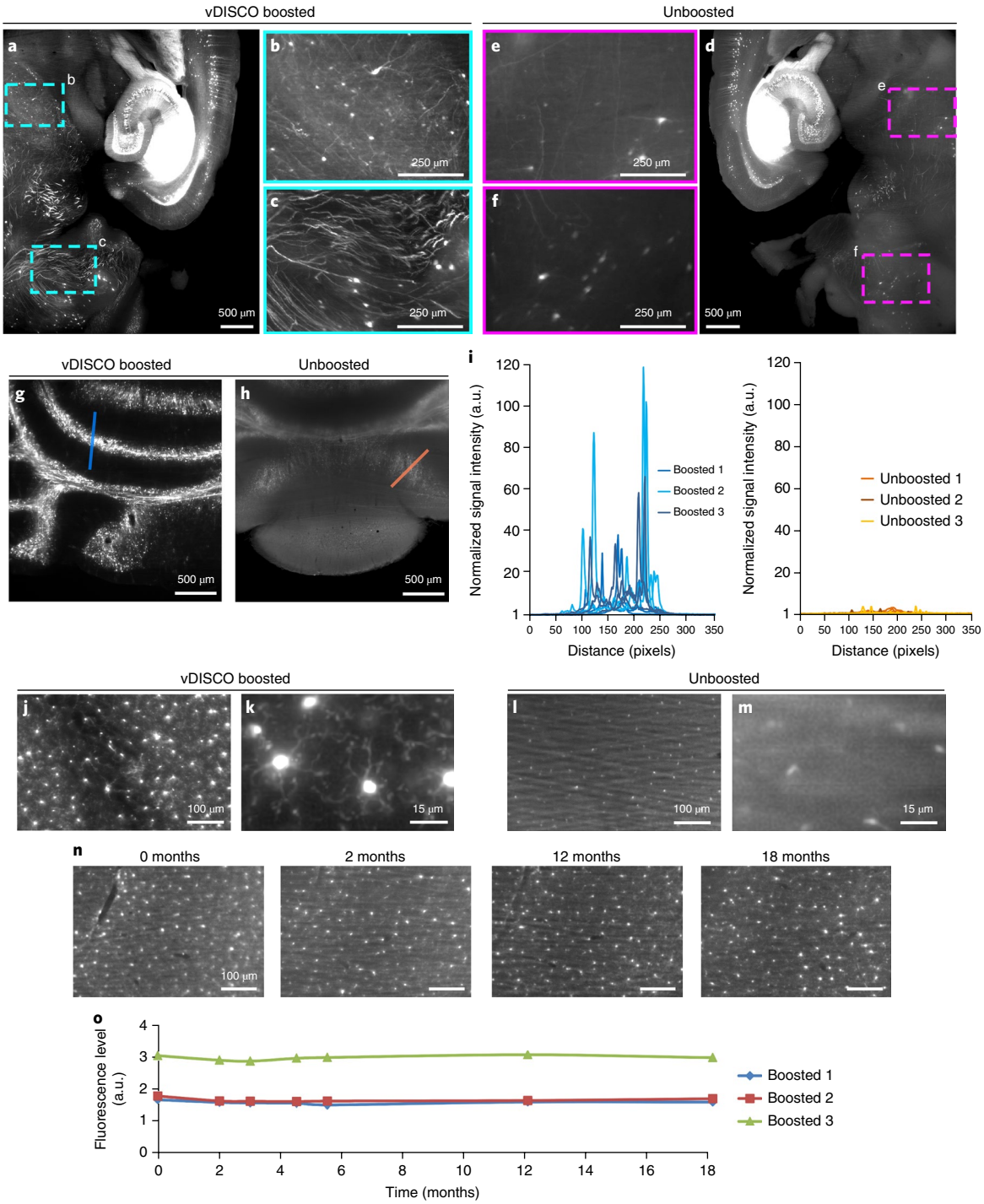


**Fig. 1 | Enhancement and permanent preservation of the fluorescence signal with vDISCO. a**–**f**, Signal quality comparison between vDISCO-boosted (**a**) and unboosted (**d**) half-brain samples coming from the same 11-month-old *Thy1*-GFP-M mouse. To achieve the best comparison between the two procedures, we divided the mouse brains in two halves for light-sheet microscopy imaging (one hemisphere boosted and imaged in the far-red channel, the other hemisphere unboosted and imaged in the green channel for endogenous EGFP). The boosted hemisphere showed highly distinguishable cellular details (**b**,**c**) such as axonal projections not visible in the unboosted hemisphere (**e**,**f**), especially in the regions with dim GFP labeling in *Thy1*-GFP-M mice, such as mid-brain (**b**,**e**) and cerebellum (**c**,**f**) (representative images, repeated at least on 3 different samples). **g**,**h**, Comparison of signal quality in cerebellum from the boosted (**g**) and unboosted (**h**) samples (repeated with at least 3 mice per group). **i**, Plots of signal intensity profiles from boosted samples (left) versus unboosted samples (right) along the blue and orange lines in **g** and **h**, respectively; $n = 3$ brains for each group (2- to 6-month-old *Thy1*-GFP-M mice). **j**–**m**, Light-sheet microscopy images (×4 and ×25 magnification) of the microglia from CX3CR1$^{GFP/+}$ mice in boosted (**j**,**k**) versus unboosted samples (**l**,**m**) showing the fine details of microglia ramifications obtained with vDISCO boosting (similar results repeated with at least 3 mice per group). **n**, Representative light-sheet microscopy images of 1 of 3 CX3CR1$^{GFP/+}$ mouse brains at 0, 2, 12 and 18 months after boosting, showing the preservation of the fluorescence signal over 18 months. **o**, Fluorescence level quantifications, in arbitrary units (a.u.), in CX3CR1$^{GFP/+}$ brains after boosting at different time points postclearing ($n = 3$ mice, 2–6 months old).

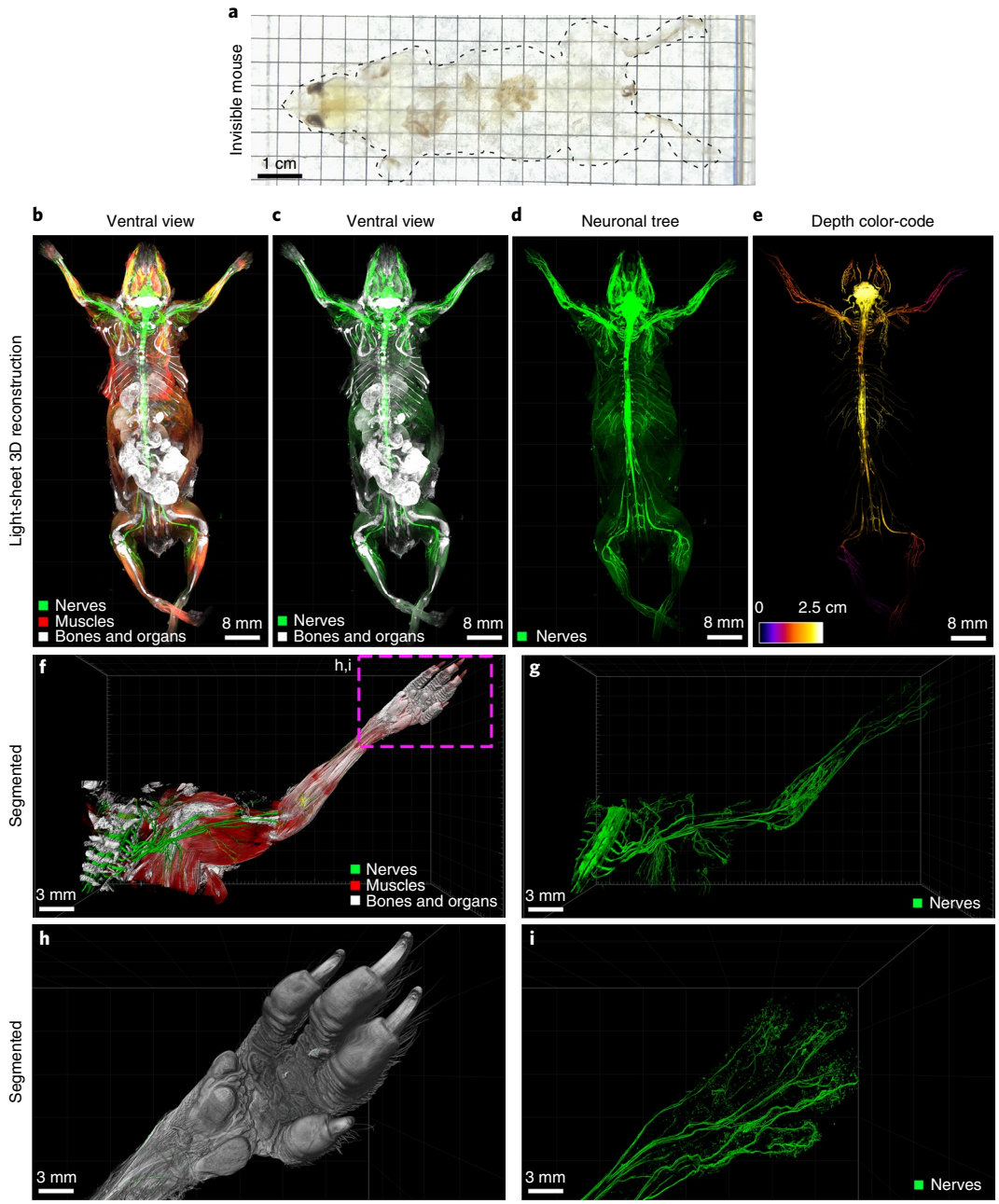


**Fig. 2 | vDISCO panoptic imaging uncovers neuronal projections in intact mice. a**, An example of a transparent 6-week-old mouse generated by vDISCO (similar results were observed from at least 20 independent mice). **b**–**e**, Three-dimensional reconstruction of complete neuronal projections of a 6-week-old *Thy1*-GFP-M mouse obtained by light-sheet microscopy imaging (similar labeling and imaging results were achieved at least in 5 different mice; whole-body reconstruction was performed on 2 mice). vDISCO boosted GFP$^+$ neuronal structures are shown in green, bones and internal organs are prominent with PI labeling in white, and the muscles visualized by autofluorescence background imaging are in red (**b**–**d**). The depth color-coding shows the neuronal projections at different *z* levels in the 2.5-cm-thick whole mouse body (**e**). **f**,**g**, High-resolution 3D reconstruction views of the left torso and forelimb from the same animal as in **b**–**e**. Details of innervation throughout muscles and bones are evident. **h**,**i**, Surface reconstruction of the paw (**h**) and its nerves (**i**) from the boxed region in **f**. See also Supplementary Videos 2–4.

axonal bundles coming from different roots enter the spinal cord at non-overlapping territories (Supplementary Fig. 16). Thus, the vDISCO approach provides a holistic view of the intact mouse, which should lead to novel discoveries on how interconnected organ systems function in health and what happens during their perturbation in disease.

**Clearing of the whole body without removal of the skin.** The skin is the largest organ, forming ~15–20% of the body. Among many other components, it consists of nerve endings, glands, immune cells, blood and lymphatic vessels, signifying its diverse biological roles in addition to being a physical barrier against the external environment[27]. However, clearing and imaging whole mice with skin has not been reported. Towards this goal, we adopted the vDISCO protocol to clear and image mice with skin. We observed that vDISCO could efficiently clear whole nude mice without removal of the skin (Fig. 3a,b). In addition, we cleared C57BL/6J (BL6) background mice after shaving the fur. In CX3CR1$^{GFP/+}$ mice, we could readily image

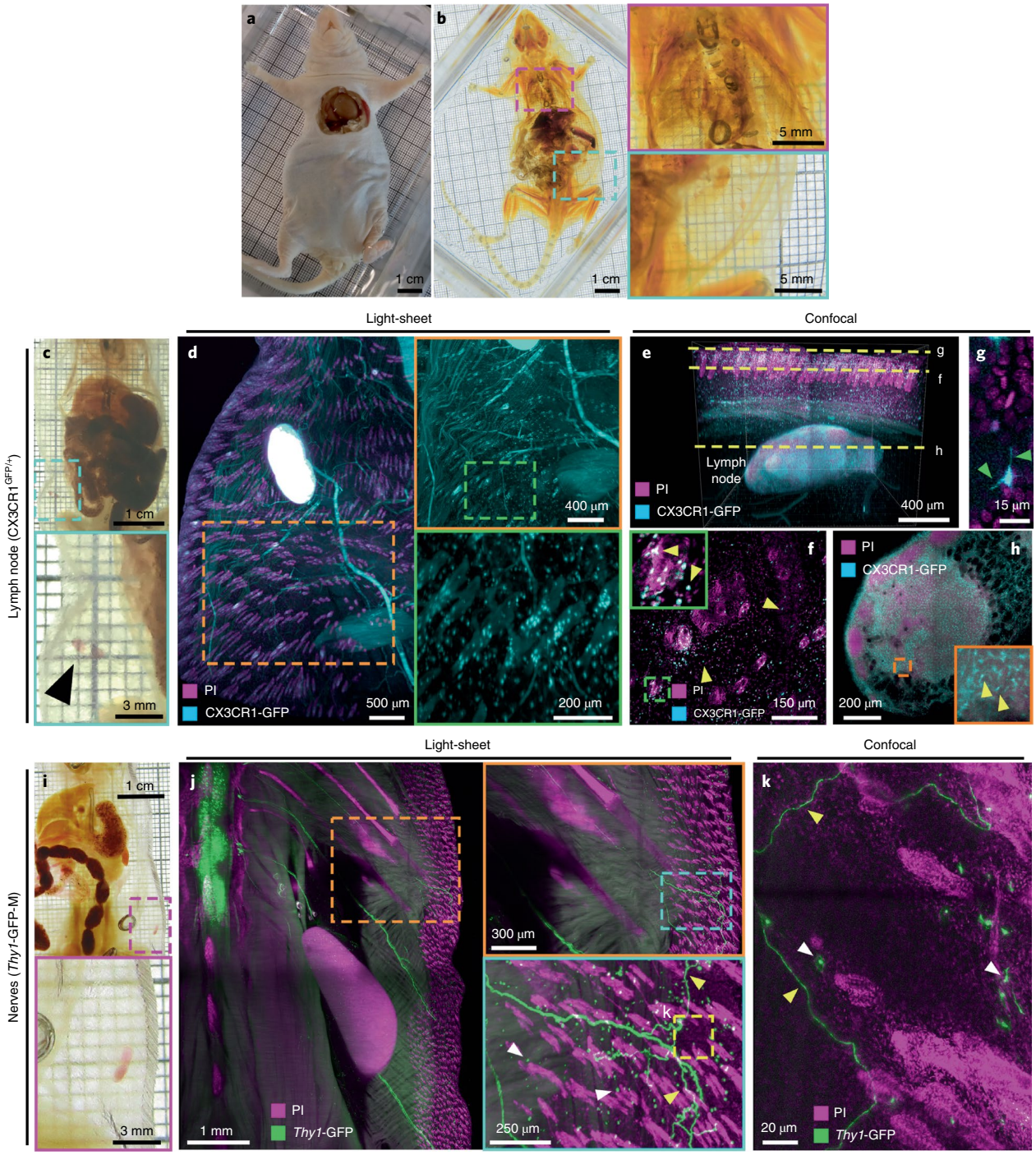


**Fig. 3 | vDISCO panoptic imaging on mice with the intact skin. a**,**b**, Adult NMRI nu/nu nude mouse, 3–4 months old (**a**), cleared with the vDISCO method (**b**): the insets show close-up views of the cleared lungs (magenta) and skin (cyan) in **b** (similar results were observed from 3 independent NMRI nu/nu mice). **c**–**h**, vDISCO on 6-week-old CX3CR1$^{GFP/+}$ mouse with intact skin. **c**, Cleared body, with the inset (cyan) showing visible inguinal lymph nodes (black arrowhead) through the transparent skin. **d**, Light-sheet images of CX3CR1$^{GFP/+}$ mouse boosted with anti-GFP 647-nanobooster (cyan) and labeled with PI (magenta), showing CX3CR1 GFP$^+$ cells (cyan) densely located in the lymph node and sparsely located in and under the skin, such as around hair follicles (magenta). **e**–**h**, Confocal 1-mm *z*-scan of the skin and lymph node in **d** with visible CX3CR1 GFP$^+$ cells (cyan) and nuclei (magenta). **e**, Three-dimensional rendering of the stack showing the skin and the lymph node beneath. **f**, Two-dimensional image at the level of the skin with individual CX3CR1 GFP$^+$ cells in the tissue and in the hair follicles (yellow arrowheads). **g**, The fine details of the ramifications of the immune cells at the surface of the skin are visible (green arrowheads). **h**, Two-dimensional image of the lymph node with visible immune cells (yellow arrowheads) in the organ. See also Supplementary Video 5. **i**–**k**, vDISCO on 2-month-old *Thy1*-GFP-M mouse with intact skin. **i**, Cleared body, with the inset (magenta) showing a visible inguinal lymph node through the skin. **j**, Light-sheet images of *Thy1*-GFP-M mouse boosted with anti-GFP 647-nanobooster (green) and labeled with PI (magenta), showing *Thy1*-GFP-expressing immune cells (white arrowheads) and neuronal projections coming from the spinal cord and projecting to the rest of the body, including the skin (green); the insets show close-up details of a neuronal projection (green fibers and yellow arrowheads) projecting into the skin. **k**, High-magnification confocal image of the region in **j** (yellow dashed rectangle) showing details of the immune cells (white arrowheads) and neuronal projections (green and yellow arrowheads) into the skin of the animal. All the results from **c** to **k** were similarly observed in 2 independent mice for each mouse line.

immune cells through the intact skin owing to the increase of fluorescent signal by vDISCO (Fig. 3c–h and Supplementary Video 5). In *Thy1*-GFP-M mice, we observed the axonal innervations in the skin in addition to *Thy1* GFP$^+$ immune cells[28] located under the skin (Fig. 3i–k). These results demonstrate that vDISCO allows detailed imaging of intact mice with skin, which may be of great value for studying skin-related pathologies.

**Degeneration of peripheral nerve terminals after brain injury.** Traumatic brain injury (TBI) is a major cause of death and disability, and currently there is no disease-modifying treatment available to combat especially chronic sequelae. In addition to its acute consequences, TBI often leads to chronic focal and global neurological impairments, such as dementia, epilepsy, progressive motor decline, peripheral neuropathy and dystonia[29,30]. These impairments could be due to degeneration of the corresponding brain regions and/or the dysfunction of nerves outside of the brain. However, so far, the impact of TBI on long-range neuronal projections outside of the brain has not been assessed. For example, while TBI-induced sensory-motor dysfunction has been observed in both animal models and human pathologies[31–34], the underlying mechanisms remain unknown, hampering the development of effective therapeutic approaches. Here, imaging the whole CNS, we found extensive neurodegeneration of the descending motor axons in the brainstem and spinal cord upon TBI over the right somatosensory and motor cortices (Supplementary Fig. 17). However, how TBI alters neuronal projections in the peripheral nervous system remains elusive. We used panoptic imaging to examine neuronal changes throughout the body more than a month after the brain injury (chronic stage) in comparison with control animals. As mainly axons innervating muscles are labelled in *Thy1*-GFP-M mice, we primarily focused on these nerve terminals. Our quantifications conducted in intact cleared mouse bodies demonstrated that the complexity of nerve terminals at the neuromuscular junctions was reduced after TBI, especially in the upper torso, compared with unlesioned control mice (Fig. 4a–d). We observed that nerve endings were reduced in complexity at the contralateral body regions, with fewer axonal ramifications left, implying partial degeneration of these axon terminals (Fig. 4e,f). Interestingly, we also observed changes at the ipsilateral axons, albeit to a smaller degree with respect to the contralateral body region (Fig. 4e). Overall, these data demonstrate that light-sheet microscopy imaging of entire transparent mouse bodies by vDISCO holds great promise for discovering hitherto unknown biological and pathophysiological processes.

**Visualizing new routes for immune cell trafficking in the brain and spinal cord.** The lymphatic system, which connects various lymphatic organs in the body, is crucial for immune responses. Until recently, the brain was considered to be devoid of any lymphatic vessels. In recent years, brain lymphatic vessels were re-discovered and are considered to play critical roles in brain pathologies[35–38]. As these lymphatic vessels are located between the brain and the skull[39], their connections are largely destroyed when the brain is harvested for standard histology.

We utilized panoptic imaging to overcome this hurdle and imaged details of meningeal vessels in intact transparent mice. We used *Prox1*-EGFP reporter mice, in which lymphatic endothelial cells express EGFP[40]. We readily observed previously described brain lymphatic structures, particularly along the sagittal sinus, pterygopalatine artery and transverse sinus (Fig. 5a–e and Supplementary Fig. 18) in addition to many other body regions (Supplementary Fig. 19 and Supplementary Video 6). Next, we imaged multiple subtypes of immune cells within and outside the meningeal vessels using the CX3CR1$^{GFP/+}$ × CCR2$^{RFP/+}$ mice by multiplexing with two different nanoboosters (anti-GFP conjugated to Atto-647N and anti-RFP conjugated to Atto-594N). The CX3CR1 GFP$^+$ microglia cells in the brain parenchyma (Fig. 5f,g) and CCR2 RFP$^+$ peripheral immune cells in the meningeal vessels were clearly identifiable (Fig. 5g,h and Supplementary Video 7). As expected, we also observed CX3CR1 GFP$^+$ immune cells in meningeal vessels, which likely represent meningeal monocytes and macrophages (Fig. 5h). It remains unclear how the immune cells within meningeal vessels contribute to the pathology of acute brain injuries, as they may be in an advantageous position to invade the brain. To start addressing this query, we used the middle cerebral artery occlusion (MCAO) model of stroke, which was performed in *LysM*-EGFP mice, a transgenic mouse line expressing EGFP in myeloid cells (mainly in neutrophils and monocytes) but not in microglial cells[41]. The mice with MCAO showed an invasion of LysM GFP$^+$ cells into the brain parenchyma, especially in the peri-infarct region, compared with sham-operated controls (Fig. 5i,j). Numbers of LysM GFP$^+$ cells also increased in the meningeal structures after MCAO (Fig. 5i), suggesting that the meninges might play a role as entry and/or exit routes of the brain in addition to the disrupted blood–brain barrier and the choroid plexus[42]. Thus, vDISCO panoptic imaging of transparent mice is a powerful tool to study the anatomy and cellular repertoire of meningeal vessels in health and disease.

Next, we aimed at investigating vascular connections between the skull and the meninges in greater detail. Towards this goal, we injected a cerebrospinal fluid (CSF) tracer (fluorophore-conjugated ovalbumin) into the cisterna magna in *VEGFR3*-YFP mice, another commonly used reporter line for meningeal vessels. We observed that the CSF tracer was quickly transported into the VEGFR3$^+$ meningeal vessels (Fig. 6a–d). Interestingly, we also observed that the tracer-labeled vessels extended into the skull (Fig. 6b,c). We further investigated the details of these new connections using lectin, another vessel tracer binding to endothelial cells. We found that these vascular connections are mostly located between the skull marrow and the outer surface of the meninges (both at the brain and sagittal sinus interfaces; Fig. 6e,f, Supplementary Fig. 20 and Supplementary Videos 8 and 9). We measured that they have an average size of 46.9 ± 5.8 µm in length and 19.2 ± 2.5 µm in width at the brain interface and of 83.7 ± 0.3 µm in length and 28.5 ± 1.8 µm in width at the sagittal sinus interface (mean ± s.e.m., $n = 3$ mice; Supplementary Fig. 20); therefore, we named them as short skull–meninges connections (SMCs). They also occasionally contain cells (Fig. 6e,f and Supplementary Fig. 20). To address whether the SMCs might play a role in neuropathological conditions, we studied the distribution of LysM GFP$^+$ immune cells in these connections after MCAO. The mice with MCAO showed significantly more LysM GFP$^+$ cells in the SMCs compared with sham-operated controls (Fig. 6g–i and Supplementary Video 10), suggesting that they might represent an entry route for myeloid cells from the skull marrow to the meningeal compartments after brain injury. Thus, vDISCO imaging revealed connections between skull and meninges, which might be important for immune cell trafficking, especially during brain pathologies.

Finally, we explored the immune cell trafficking after spinal cord injury using vDISCO panoptic imaging. To this end, we induced a spinal cord injury in *CD68*-EGFP transgenic mice expressing EGFP in monocytes and macrophages[43]. Upon spinal cord injury, we observed an influx of CD68 GFP$^+$ cells at the lesion site as well as a rather widespread increase in CD68 GFP$^+$ cells around the spinal cord (Supplementary Fig. 21 and Supplementary Video 11). Indeed, only 3.5% of these phagocytes were seen in the injured spinal cord, while ~96.5% of the CD68 GFP$^+$ cells were located in the surrounding tissues of the spinal cord including adjacent muscles, spinal cord roots and meningeal vessels, similar to sham mice (Supplementary Fig. 22). Thus, vDISCO is a powerful tool to image and quantify the trafficking of immune cells to and within the injured CNS.

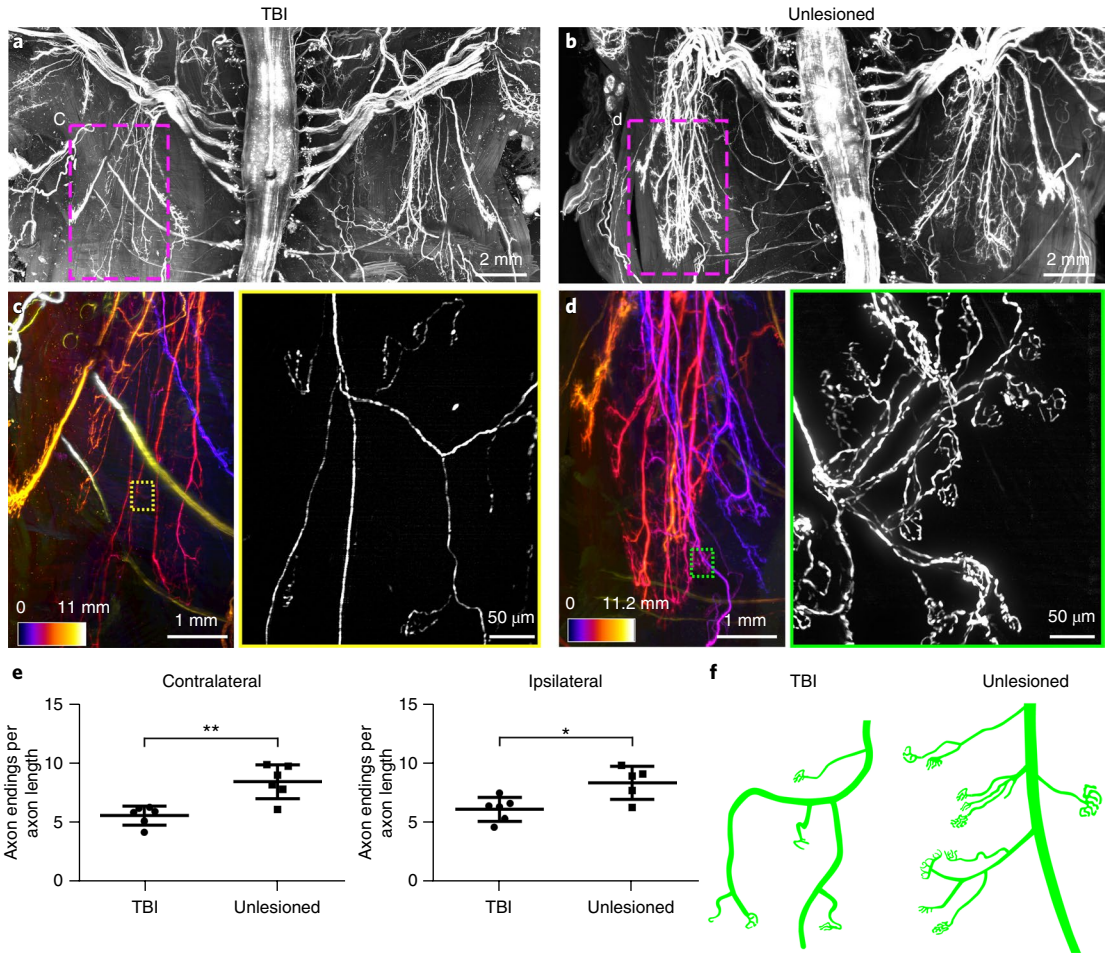


**Fig. 4 | TBI-induced peripheral nerve degeneration revealed by vDISCO panoptic imaging. a**,**b**, Background-equalized light-sheet microscopy maximum intensity projections of the torso from TBI-induced (**a**) vs. unlesioned control (**b**) *Thy1*-GFP-M mice. **c**,**d**, High-magnification views of marked regions in **a** and **b**, showing the left thoracic peripheral nerve projections in the TBI (**c**) vs. control animal (**d**); the color-code indicates the *z*-depth of anatomical regions as given in the scale bars. The colored rectangles show the high-magnification images of the marked regions in **c** and **d**, respectively, demonstrating fewer intact peripheral nerve endings in TBI mice compared with controls (similar results were observed from 6 independent mice per group). **e**, Quantification of axonal projection complexity expressed as number of peripheral nerve endings over length of axonal ramifications in TBI versus control mice (3–5 months old) at the level of the contralateral side (left) and ipsilateral side (right) (mean ± s.d.; for the contralateral side, $n = 6$ animals per group; for the ipsilateral side, $n = 6$ mice for the TBI group and 5 mice for the unlesioned group, respectively; statistical significance (**$P = 0.003$, *$P = 0.03$) was assessed by two-tailed $t$ test). **f**, Representative illustration showing the peripheral nerve ending morphology in TBI versus control mice.

## Discussion

Panoptic imaging of transparent adult mouse bodies from head to toe holds the promise of providing an unbiased and highly resolved view of entire organ systems in health and disease. Here, we developed a new whole-body nanobody labeling method in conjunction with whole-body tissue clearing, enabling a reliable visualization and quantification of subcellular details throughout centimeters-thick tissues of intact mouse bodies. This new panoptic imaging technology is straightforward in application and is suitable for systemic analysis of a vast range of biomedical inquires, as demonstrated here in visualization of the neuronal projections in whole mouse bodies, the description of vascular pathways between the skull and meninges, and the visualization of remote neuronal and immune consequences of acute CNS injury models. While we developed vDISCO for panoptic imaging of the whole mouse body, it is readily applicable for individual organs, using a simplified protocol to drastically increase and stabilize the signal contrast, as we show for mouse brains imaged more than a year after boosting and clearing (Supplementary Video 12 and Supplementary Table 1).

The panoptic imaging of nervous and immune systems in intact mouse bodies was achieved owing to the massive enhancement of the signal intensity by one to two orders of magnitude via whole-body immunolabeling employing nanobodies conjugated to bright dyes in the far-red spectrum. Therefore, the strong autofluorescence of tissues in shorter-wavelength spectra, in which traditional fluorescent proteins such as GFP are excited and imaged, is avoided. Here, we primarily used Atto dyes at 647 nm, and additional Atto 594 nm for multiplexing two different cell types. In the future, usage of nanobodies conjugated to dyes that emit in the near-infrared range[44] can further facilitate multiplexed detection of more than two targets. While the number of commercially available nanobodies is still limited, the nanoboosters used in this study can stain a broad selection of 21 different fluorescent proteins including EGFP, YFP, Venus, mCherry, and mRFP. Our method can also be used with nanobodies against endogenous proteins, as we demonstrated using anti-vimentin nanobodies labeling activated glia cells in the brain upon trauma[45,46]. Currently, nanobodies are developed mainly for *in vivo* applications due to their small size (for example, for crossing the blood–brain barrier)[47]; therefore, they are mostly selected for

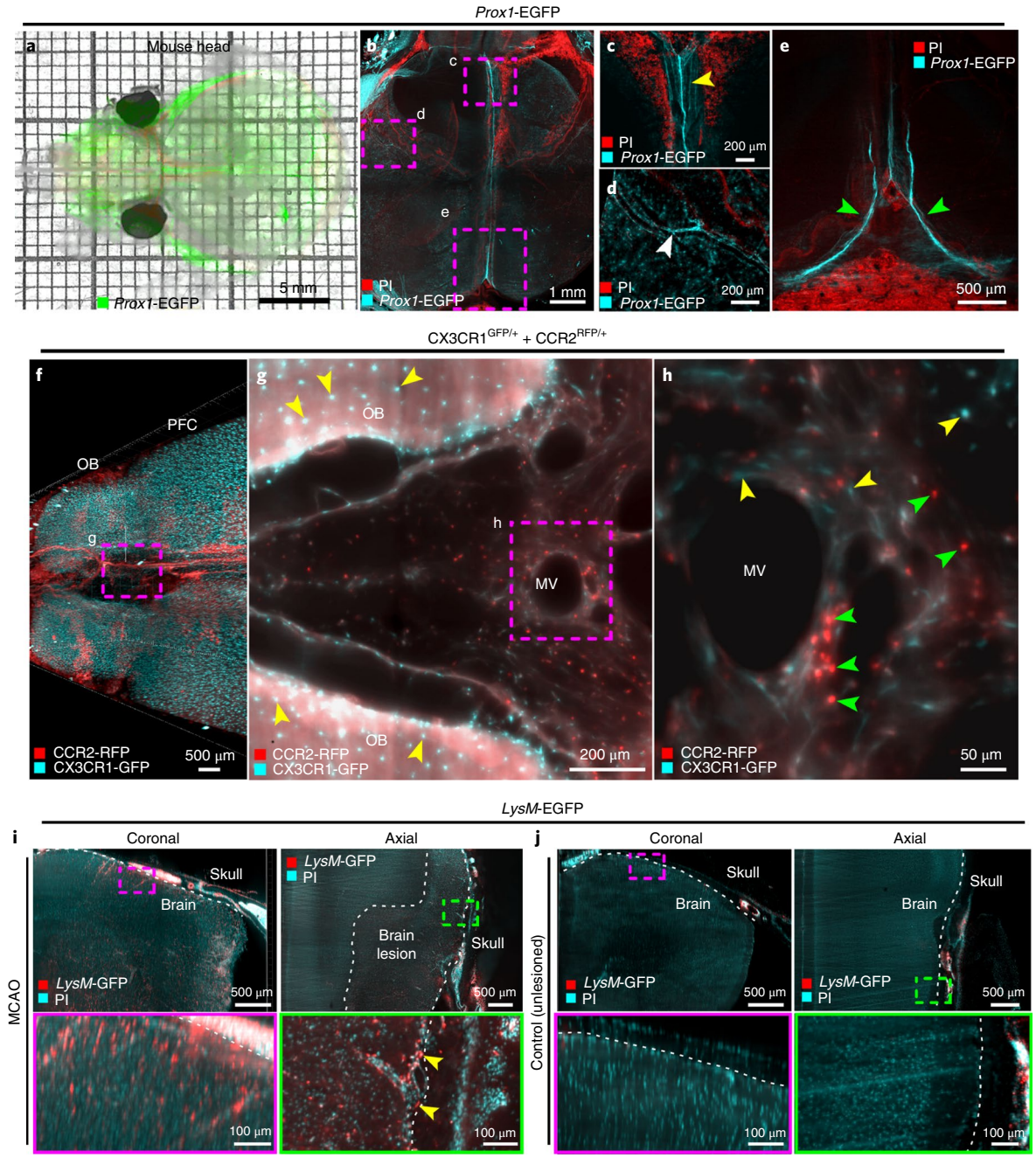


**Fig. 5 | Visualizing meningeal vessels through intact skull by vDISCO panoptic imaging. a**, A representative 4-week-old transparent *Prox1*-EGFP mouse head from 5 independent animals, showing the labeled vessels underneath the skull. **b**–**e**, The *Prox1*-EGFP mouse head, showing the brain lymphatic vessels along the sagittal sinus, pterygopalatine artery and transverse sinus (yellow, white and green arrowheads in **c**, **d** and **e**, respectively). Bone structures become prominent with PI labeling (red). Single experiment. **f**, Three-dimensional visualization of prefrontal cortex (PFC) and olfactory bulb (OB) in a 2-month-old CX3CR1$^{GFP/+}$ (cyan) and CCR2$^{RFP/+}$ (red) double-transgenic mouse (similar results were observed from 3 independent double-transgenic mice). **g**,**h**, High-magnification image of marked region in **f**, showing CCR2 RFP$^+$ cells (green arrowheads) and CX3CR1 GFP$^+$ cells (yellow arrowheads) in meningeal vessels (MV). See also Supplementary Video 7. **i**,**j**, *LysM*-EGFP transgenic mice (6 months old) with MCAO versus unlesioned control, showing the infiltration of immune cells in MCAO (similar results were observed from 4 independent mice per group). LysM GFP$^+$ cells are shown in red and nucleus labeling by PI in cyan. Immune cells in the meningeal vessels of the injured mice were observed (yellow arrowheads). All images were obtained by light-sheet microscopy.

*in vivo* epitopes but not for fixed tissues. We believe that our study will encourage the production of diverse nanobodies for deep-tissue immunolabeling.

Here, we used transgenic mice endogenously expressing fluorescent proteins; however, the labeling can also be achieved by rabies virus retrograde tracing, systemic adeno-associated virus injections[48] or transplantation of genetically engineered cells (such as stem cells or adoptive transfer of immune cells). Another key advantage of vDISCO panoptic imaging is that upon staining with Atto dyes through nanoboosting, the signal becomes permanent, permitting long-term imaging sessions and future re-analysis of the same sample if needed. This also enables high-resolution imaging

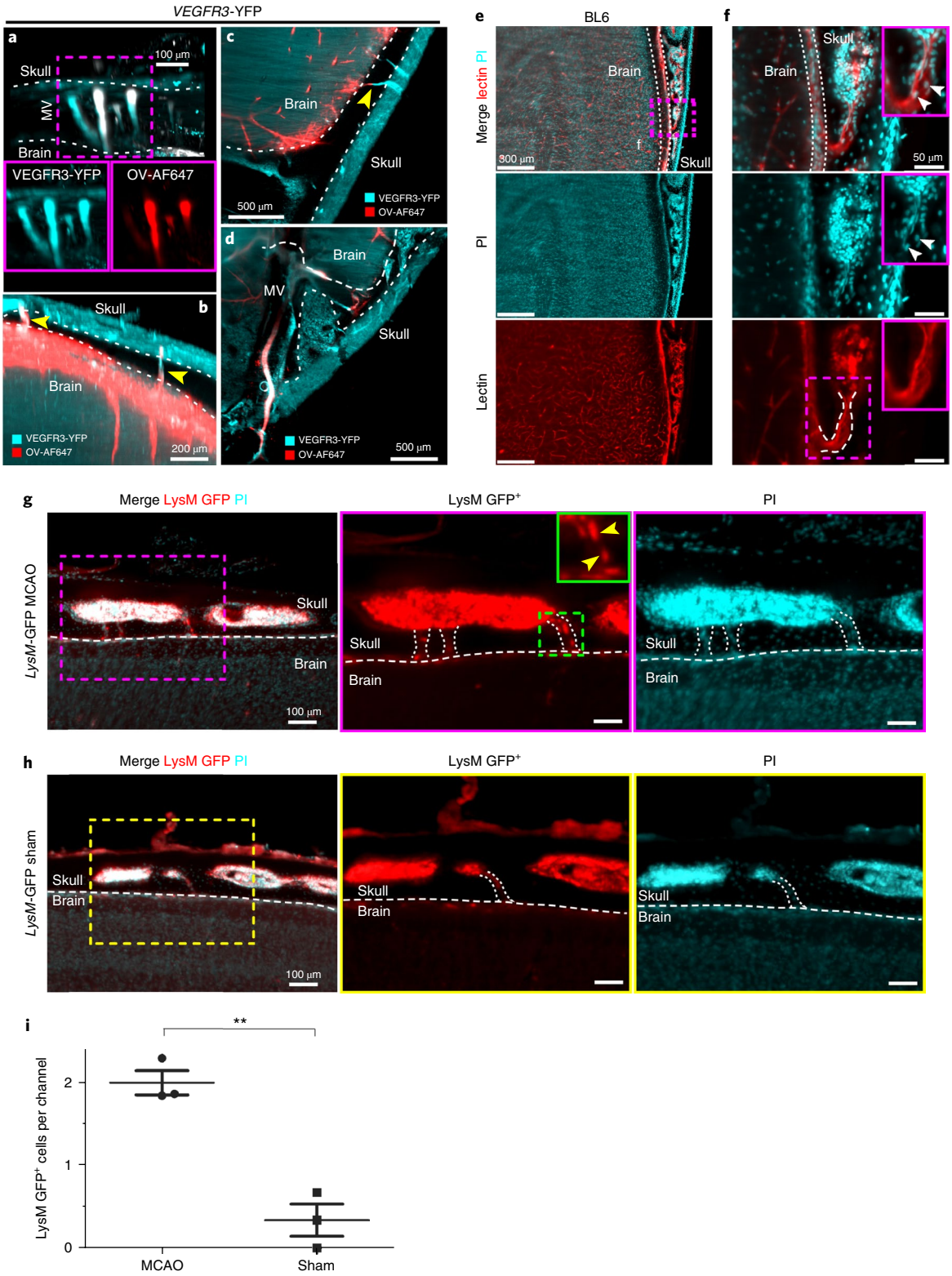


**Fig. 6 | Uncovering SMCs through intact skull by vDISCO panoptic imaging. a–d**, A 6-month-old *VEGFR3*-YFP mouse head in sagittal (**a**,**b**) and axial (**c**,**d**) views, showing that injected CSF tracer (ovalbumin–Alexa647 (OV-AF647); red) fills not only meningeal vessels but also some short SMCs between skull marrow and brain surface (**b**,**c**; yellow arrowheads). Representative images, single experiment. **e**,**f**, Details of SMCs after whole mouse body PI and lectin labeling of a 3-week-old BL6 mouse processed by vDISCO: the SMCs from skull marrow to brain surface with a funnel-shaped opening are marked with dashed lines in **f**. Cells in the channel are indicated by white arrowheads. Similar results were observed from 5 independent mice. **g**,**h**, *LysM*-EGFP transgenic mice (6 months old) after MCAO (**g**) versus sham control (**h**), showing increased numbers of LysM GFP$^+$ cells (yellow arrowheads) in the SMCs (marked with dashed lines) in MCAO. Similar results were observed from 3 independent mice per group. LysM GFP$^+$ cells are shown in red and nucleus labeling by PI in cyan. See also Supplementary Video 10. **i**, Quantification of LysM GFP$^+$ cells in the SMCs in MCAO versus sham mice (mean ± s.e.m., $n = 3$ animals per group; statistical significance ($^{**}P = 0.003$) was assessed by two-tailed $t$ test).

of desired body parts by confocal or two-photon microscopy. Indeed, the samples from this study are available to the scientific community upon request for further studies. We believe making vDISCO-treated samples accessible to other labs for further studies can save time and resources, reduce the number of mice used in experimental research and create more powerful datasets by allowing direct correlation of various inquiries by multiple studies from the same animals.

A current limitation is the absence of light-sheet microscope systems that could image the entire body of a mouse in one session without any displacement and turning of the sample. Construction of such new light-sheet microscopes should further decrease the time needed for data acquisition and simplify data processing for 3D reconstruction. In fact, as shown here, optics and light sources of current commercial light-sheet microscopes are sufficient to image intact mouse bodies at subcellular resolution, although the whole body has to be manually moved in the imaging chamber to achieve the scanning of different body regions. In addition, development of machine learning-based (artificial intelligence) algorithms to automatically identify and quantify cellular changes on the whole-organism scale will be important to further scale up this technology in the future.

Using panoptic imaging, we constructed a neuronal projection map for the *Thy1*-GFP-M transgenic line, showing subcellular details of long-range neuronal connections from the CNS to the distal extremities. Here, we visualized neuronal details in *Thy1*-GFP-M mice, in which only a subset of CNS neurons and peripheral nervous system neurons innervating skeletal muscles are labeled. In the future, panoptic imaging of other transgenic lines labeling a greater and more diverse subset of neurons will allow the exploration of other biological systems such as the autonomic innervation of internal organs.

In recent years, researchers have been providing more evidence on post-TBI changes that seem to form the basis of chronic complications, such as epilepsy, neuropsychiatric disorders, dementia and progressive motor decline[29]. However, the effects of a localized brain lesion on the rest of the body have been poorly understood, mainly due to the technical challenges in studying long-range neuronal projections. Because vDISCO fluorescent signal boosting allows both imaging and quantifications of light-sheet microscopy images of transparent mouse bodies, we identified TBI-induced changes at the peripheral axonal projections innervating the skeletal musculature of the torso. These data are in line with recent work by others and us demonstrating the functional deficits in fine motor movements in mice and the presence of sensory-motor dysfunctions in TBI patients[29,30,33]. Our data provide a possible cellular mechanism for these functional impairments, suggesting that they could arise due to degeneration of long-range axons throughout the spinal cord and peripheral nervous system. This discovery opens alternate avenues for the identification of therapeutic targets. For instance, recent literature showed that microtubule stabilization is a powerful way to block degeneration of axons in spinal cord injury[49]. In this regard, it would be important to assess whether microtubule stabilization would also counteract axon degeneration outside of the brain and circumvent the development of chronic sensory-motor dysfunctions. Here, we also demonstrated that meningeal vessels extending between the cranium and CNS tissue and their cellular content can readily be imaged by vDISCO panoptic imaging in naïve animals and acute CNS injury models. Importantly, we observed short vascular connections between the skull and meninges both at the brain interface (recently seen also by others[50]) and at the sagittal sinus, which were filled with immune cells following ischemic stroke injury. Most of the SMCs seem to be open both at the skull marrow and meningeal ends without being connected to the vascular system of the brain/head (Supplementary Video 9). In the future, it will be important to identify to which meningeal compartment or compartments (subdura, subarachnoid or subpial) the SMCs are connected. In addition, due to the present lack of appropriate reporter mice, it was not possible to distinguish the type of SMCs (blood or lymphatic vessels) with increased LysM$^+$ cells after stroke. In the future, vDISCO imaging of immune cells in a lymphatic vessel reporter mouse line with different fluorescent proteins (for example, *LysM*-EGFP + *Prox1*-RFP double reporter) could reveal more details of this new route for immune cell infiltration. As neuroinflammation is a major determinant of neuronal function and survival following CNS injuries of various etiologies, our technology should accelerate investigation of these novel immune cell infiltration routes in various CNS pathologies.

In conclusion, vDISCO enhancement and stabilization of fluorescent proteins combined with signal acquisition in far-red spectra should facilitate discovery of previously inaccessible biological information. For example, imaging and quantification of neuronal projections, vascular organizations and immune cell populations in the entire mouse body should contribute to a more comprehensive understanding of the initiation, progression and extent of neurological conditions.

## Online content

Any methods, additional references, Nature Research reporting summaries, source data, statements of data availability and associated accession codes are available at https://doi.org/10.1038/s41593-018-0301-3.

Received: 1 April 2018; Accepted: 21 November 2018;
Published online: 31 December 2018

## References

1. Tuchin, V. V. & Tuchin, V. *Tissue Optics: Light Scattering Methods and Instruments for Medical Diagnosis* (SPIE Press, Bellingham, 2007).
2. Chung, K. et al. Structural and molecular interrogation of intact biological systems. *Nature* **497**, 332–337 (2013).
3. Yang, B. et al. Single-cell phenotyping within transparent intact tissue through whole-body clearing. *Cell* **158**, 945–958 (2014).
4. Renier, N. et al. iDISCO: a simple, rapid method to immunolabel large tissue samples for volume imaging. *Cell* **159**, 896–910 (2014).
5. Susaki, E. A. et al. Whole-brain imaging with single-cell resolution using chemical cocktails and computational analysis. *Cell* **157**, 726–739 (2014).
6. Erturk, A. et al. Three-dimensional imaging of solvent-cleared organs using 3DISCO. *Nat. Protoc.* **7**, 1983–1995 (2012).
7. Erturk, A. et al. Three-dimensional imaging of the unsectioned adult spinal cord to assess axon regeneration and glial responses after injury. *Nat. Med.* **18**, 166–171 (2011).
8. Belle, M. et al. A simple method for 3D analysis of immunolabeled axonal tracts in a transparent nervous system. *Cell Rep.* **9**, 1191–1201 (2014).
9. Costantini, I. et al. A versatile clearing agent for multi-modal brain imaging. *Sci. Rep.* **5**, 9808 (2015).
10. Ke, M. T., Fujimoto, S. & Imai, T. SeeDB: a simple and morphology-preserving optical clearing agent for neuronal circuit reconstruction. *Nat. Neurosci.* **16**, 1154–1161 (2013).
11. Dodt, H. U. et al. Ultramicroscopy: three-dimensional visualization of neuronal networks in the whole mouse brain. *Nat. Methods* **4**, 331–336 (2007).
12. Hama, H. et al. ScaleS: an optical clearing palette for biological imaging. *Nat. Neurosci.* **18**, 1518–1529 (2015).
13. Belle, M. et al. Tridimensional visualization and analysis of early human development. *Cell* **169**, 161–173 (2017).
14. Murray, E. et al. Simple, scalable proteomic imaging for high-dimensional profiling of intact systems. *Cell* **163**, 1500–1514 (2015).
15. Tainaka, K. et al. Whole-body imaging with single-cell resolution by tissue decolorization. *Cell* **159**, 911–924 (2014).
16. Jing, D. et al. Tissue clearing of both hard and soft tissue organs with the PEGASOS method. *Cell Res.* **28**, 803–818 (2018).
17. Pan, C. et al. Shrinkage-mediated imaging of entire organs and organisms using uDISCO. *Nat. Methods* **13**, 859–867 (2016).
18. Kubota, S. I. et al. Whole-body profiling of cancer metastasis with single-cell resolution. *Cell Rep.* **20**, 236–250 (2017).
19. Tuchin, V. V. *Optical Methods for Biomedical Diagnosis* (SPIE Press, Bellingham, WA, USA, 2016).

20. Muyldermans, S. Nanobodies: natural single-domain antibodies. *Annu. Rev. Biochem.* **82**, 775–797 (2013).
21. Feng, G. et al. Imaging neuronal subsets in transgenic mice expressing multiple spectral variants of GFP. *Neuron* **28**, 41–51 (2000).
22. Quan, T. et al. NeuroGPS-Tree: automatic reconstruction of large-scale neuronal populations with dense neurites. *Nat. Methods* **13**, 51–54 (2016).
23. Renier, N. et al. Mapping of brain activity by automated volume analysis of immediate early genes. *Cell* **165**, 1789–1802 (2016).
24. GageG. J., KipkeD. R. & ShainW. Whole animal perfusion fixation for rodents. *J. Vis. Exp.* **65**, e3564 (2012).
25. Greenbaum, A. et al. Bone CLARITY: clearing, imaging, and computational analysis of osteoprogenitors within intact bone marrow. *Sci. Transl. Med.* **9**, eaah6518 (2017).
26. Leijnse, J. N. & D'Herde, K. Revisiting the segmental organization of the human spinal cord. *J. Anat.* **229**, 384–393 (2016).
27. Gimenez-Arnau, A. Standards for the protection of skin barrier function. *Curr. Probl. Dermatol.* **49**, 123–134 (2016).
28. Haeryfar, S. M. & Hoskin, D. W. Thy-1: more than a mouse pan-T cell marker. *J. Immunol.* **173**, 3581–3588 (2004).
29. Smith, D. H., Johnson, V. E. & Stewart, W. Chronic neuropathologies of single and repetitive TBI: substrates of dementia? *Nature Rev. Neurol.* **9**, 211–221 (2013).
30. Frei, K. Posttraumatic dystonia. *J. Neurol. Sci.* **379**, 183–191 (2017).
31. Williams, G., Schache, A. & Morris, M. E. Running abnormalities after traumatic brain injury. *Brain Inj.* **27**, 434–443 (2013).
32. Chen, Y., Constantini, S., Trembovler, V., Weinstock, M. & Shohami, E. An experimental model of closed head injury in mice: pathophysiology, histopathology, and cognitive deficits. *J. Neurotrauma* **13**, 557–568 (1996).
33. Erturk, A. et al. Interfering with the chronic immune response rescues chronic degeneration after traumatic brain injury. *J. Neurosci.* **36**, 9962–9975 (2016).
34. Evans, T. M. et al. The effect of mild traumatic brain injury on peripheral nervous system pathology in wild-type mice and the G93A mutant mouse model of motor neuron disease. *Neuroscience* **298**, 410–423 (2015).
35. Louveau, A. et al. Structural and functional features of central nervous system lymphatic vessels. *Nature* **523**, 337–341 (2015).
36. Nedergaard, M. Neuroscience. Garbage truck of the brain. *Science* **340**, 1529–1530 (2013).
37. Da Mesquita, S. et al. Functional aspects of meningeal lymphatics in ageing and Alzheimer's disease. *Nature* **560**, 185–181 (2018).
38. Andres, K. H., von During, M., Muszynski, K. & Schmidt, R. F. Nerve fibres and their terminals of the dura mater encephali of the rat. *Anat. Embryol.* **175**, 289–301 (1987).
39. Louveau, A. et al. Understanding the functions and relationships of the glymphatic system and meningeal lymphatics. *J. Clin. Investig.* **127**, 3210–3219 (2017).
40. Choi, I. et al. Visualization of lymphatic vessels by *Prox1*-promoter directed GFP reporter in a bacterial artificial chromosome-based transgenic mouse. *Blood* **117**, 362–365 (2011).
41. Faust, N., Varas, F., Kelly, L. M., Heck, S. & Graf, T. Insertion of enhanced green fluorescent protein into the lysozyme gene creates mice with green fluorescent granulocytes and macrophages. *Blood* **96**, 719–726 (2000).
42. Llovera, G. et al. The choroid plexus is a key cerebral invasion route for T cells after stroke. *Acta Neuropathol.* **134**, 851–868 (2017).
43. Iqbal, A. J. et al. Human CD68 promoter GFP transgenic mice allow analysis of monocyte to macrophage differentiation in vivo. *Blood* **124**, e33–e44 (2014).
44. Hong, G., Antaris, A. L. & Dai, H. Near-infrared fluorophores for biomedical imaging. *Nat. Biomed. Eng.* **1**, 0010 (2017).
45. Noristani, H. N. et al. RNA-Seq analysis of microglia reveals time-dependent activation of specific genetic programs following spinal cord injury. *Front. Mol. Neurosci.* **10**, 90 (2017).
46. Villapol, S., Byrnes, K. R. & Symes, A. J. Temporal dynamics of cerebral blood flow, cortical damage, apoptosis, astrocyte-vasculature interaction and astrogliosis in the pericontusional region after traumatic brain injury. *Front. Neurol.* **5**, 82 (2014).
47. Leslie, M. Small but mighty. *Science* **360**, 594–597 (2018).
48. Deverman, B. E. et al. Cre-dependent selection yields AAV variants for widespread gene transfer to the adult brain. *Nat. Biotechnol.* **34**, 204–209 (2016).
49. Hellal, F. et al. Microtubule stabilization reduces scarring and causes axon regeneration after spinal cord injury. *Science* **331**, 928–931 (2011).
50. Herisson, F. et al. Direct vascular channels connect skull bone marrow and the brain surface enabling myeloid cell migration. *Nat. Neurosci.* **21**, 1209–1217 (2018).


## Acknowledgements

This work was supported by the Vascular Dementia Research Foundation, Synergy Excellence Cluster Munich (SyNergy; EXC 1010), ERA-Net Neuron (01EW1501A; A.E.), Fritz Thyssen Stiftung (reference 10.17.1.019MN; A.E.), DFG (reference ER 810/2-1; A.E.), National Institutes of Health (A.E. and M.N.), Helmholtz ICEMED Alliance (A.E.), the Novo Nordisk Foundation (M.N.), the Howard Hughes Medical Institute (B.T.K.) and the Lundbeck Foundation (A.L.R.X. and M.N.). We thank A. Weingart for illustrations, F. Hellal for technical advice and critical reading of the manuscript, and F. P. Quacquarelli and G. Locatelli for help during initial optimization. A.E, C.P., R.C., A.L. and M.I.T. are members of the Graduate School of Systemic Neurosciences at the Ludwig Maximilian University of Munich.

## Author contributions

A.E. initiated and led all aspects of the project. R.C. and C.P. developed the method and conducted most of the experiments. R.C. A.G., C.P., H.S.B., M.R., and B.M. analyzed data. M.I.T. stitched and analyzed the whole mouse body scans. A.P.D., B.F., S.Z. and L.M. helped to optimize the protocols. I.B., H.S.B., and S.L. helped to investigate skull–meninges connections. D.T. and M.K. contributed spinal cord injury experiments; C.B. and A.L., MCAO experiments; and A.X., B.K. and M.N., cisterna magna injection experiments. A.E., R.C. and C.P. wrote the paper. All the authors edited the manuscript.

## Competing interests

A.E. filed a patent on some of the technologies presented in this work.

## Additional information

**Supplementary information** is available for this paper at https://doi.org/10.1038/s41593-018-0301-3.

**Reprints and permissions information** is available at www.nature.com/reprints.

**Correspondence and requests for materials** should be addressed to A.E.

**Publisher's note:** Springer Nature remains neutral with regard to jurisdictional claims in published maps and institutional affiliations.

## Methods

**Animals.** We used the following mixed-gender animals in the study: CX3CR1$^{GFP/+}$ (B6.129P-Cx3cr1tm1Litt/J; Jackson Laboratory strain code 005582)[51], *Thy1*-GFP-M and *Thy1*-YFP-H[21], *Prox1*-EGFP (Tg(Prox1-EGFP)KY221Gsat/Mmucd; Mutant Mouse Resource and Research Centers strain code 031006-UCD), *VEGFR3*-YFP, CX3CR1$^{GFP/+}$ × CCR2$^{RFP/+}$ (B6.129(Cg)-Ccr2tm2.1Ifc/J; Jackson Laboratory strain code 017586), *LysM*-EGFP (Lyz2tm1.1$^{Graf}$, Mouse Genome Informatics strain code 2654931), *CD68*-EGFP (C57BL/6-Tg(CD68-EGFP)1Drg/j; Jackson Laboratory strain code 026827), C57BL/6J, and NMRI nu/nu mice. The animals were housed under a 12/12 h light/dark cycle. The animal experiments were conducted according to institutional guidelines (Klinikum der Universität München/Ludwig Maximilian University of Munich), after approval of the ethical review board of the government of Upper Bavaria (Regierung von Oberbayern, Munich, Germany) and the Animal Experiments Council under the Danish Ministry of Environment and Food (2015-15-0201-00535), and in accordance with the European directive 2010/63/EU for animal research. Ages of the animals are indicated in the figure legends. All data are reported according to the Animal Research: Reporting of In Vivo Experiments (ARRIVE) criteria. Sample sizes were chosen on the basis of prior experience with similar models and are specified in figure legends. Within each strain, animals were randomly selected. Animals that resulted negative for the expression of fluorescent proteins by genotyping were excluded from the study. No statistical methods were used to pre-determine sample sizes, but our sample sizes are similar to those reported in previous publications[17].

**TBI.** TBI was performed using a controlled cortical impact device (Leica Benchmark Stereotaxic Impactor, 39463923). At 30 min before surgery, we administered carprofen (4 mg per kg body weight) and buprenorphin (0.05 mg per kg) to the animals via subcutaneous injection. Then, anesthesia was induced in animals with 4% isoflurane in a $N_2O/O_2$ (70%/30%) mixture and afterwards maintained with 1.5% isoflurane in the same mixture for the whole surgery. As soon as the animals did not show any pedal reflex, they were placed in the associated stereotaxic apparatus, and their body temperature was kept at 37 °C using a heating pad for the whole surgery procedure. Next, the scalp of the animals was shaved, aseptically prepared by wiping with Octenisept (Schülke, 22580-A) as disinfectant and the skin of the scalp was incised longitudinally between the occiput and forehead. We identified the target area of the injury, which was the right somatosensory cortex extending to the motor cortex, using the stereotaxic frame (bregma coordinates: 2 mm posterior, 5 mm right lateral). The injury was then triggered via controlled cortical impact machine using the following parameters: impact speed, 6.9 m s$^{-1}$; impact duration, 400 ms; impact depth, 2 mm. With these parameters, the resulting injury was severe, with cracks in the skull, bleeding and exposed brain tissue. After the impact, the skin was sutured with metallic wound closure clips (VWR, 203-1000), and the animals were kept at 31 °C in a recovery chamber (Mediheat, 34-0516) for at least 30 min until they recovered from the anesthesia. In the following days, animals were subcutaneously injected with carprofen (4 mg per kg) once per day for 4 d and sacrificed at >1 month post-injury by transcardial perfusion according to the 'Perfusion and tissue preparation' section below.

**MCAO model.** Experimental stroke was induced using the intraluminal filament model of MCAO (fMCAO) for transient, focal brain ischemia. Mice were anesthetized with isoflurane delivered in a mixture of 30% $O_2$ and 70% $N_2O$. A heat-blunted nylon suture (6/0) was inserted into the external carotid artery and advanced until it obstructed the middle cerebral artery together with the ligation of the common carotid artery for 30 min. Regional cerebral blood flow (bregma coordinates: 2 mm posterior, 5 mm lateral) was continuously recorded by transcranial laser Doppler flowmetry from the induction of ischemia until 10 min after reperfusion. Following fMCAO, mice were placed in temperature-controlled recovery cages for 2 h to prevent post-surgery hypothermia. For the survival period (3 d), the mice were kept in their home cage with facilitated access to water and food. Sham-operated mice received the same surgical procedure without insertion of the filament. Body temperature was maintained throughout surgery using a feedback-controlled heating pad and kept constant (37.0 ± 0.5 °C). Exclusion criteria were as follows: insufficient MCAO (a reduction in blood flow to 15% of the baseline value) and blood flow recovery >80% within 10 min of reperfusion. Mice were sacrificed at 3 d post-injury by transcardial perfusion according to the 'Perfusion and tissue preparation' section below.

**Cisterna magna injection for meningeal vessel labeling.** For the cisterna magna injections, mice (*VEGFR3*-YFP; 6 months old) were anesthetized with a mixture of ketamine and xylazine (100 mg per kg and 10 mg per kg, respectively) via intraperitoneal injection. After toe pinch reflexes ceased, mice were fixed in a stereotaxic frame by the zygomatic arch, with the head slightly tilted to form an angle of 120° in relation to the body. The head and neck regions were shaved to expose the neck muscles, which were bluntly dissected to expose the cisterna magna. Cannulas composed of a dental needle (SOPIRA Carpule 30 G 0.3 × 12 mm; Kulzer, AA001) and polyethylene tubing (0.024 in OD (outside diameter) × 0.011 in ID (interior diameter); Scandidact, PE10-CL-500) were used to perform the cisterna magna injections. A cannula filled with CSF tracer (2% ovalbumin 45 kDa conjugated to Alexa Fluor 647 (Thermo Fisher Scientific, O34784), diluted in artificial CSF (126 mM NaCl, 2.5 mM KCl, 1.25 mM $NaH_2PO_4$, 2 mM $Mg_2SO_4$, 2 mM $CaCl_2$, 10 mM glucose, 26 mM $NaHCO_3$; pH 7.4 when gassed with 95% $O_2$ and 5% $CO_2$)) was inserted into the cisterna magna. With the aid of an injection pump (LEGATO 130 Syringe pump; KD Scientific, 788130), 10 µl of CSF tracer was injected into the cisterna magna at a rate of 1 µl min$^{-1}$. At the end of the injection, CSF tracer was allowed to circulate in the subarachnoid and paravascular spaces for 1 h. Mice were then transcardially perfused according to the 'Perfusion and tissue preparation' section below.

**Spinal cord injury model.** Mice were deeply anesthetized by intraperitoneal injection of a combination of midazolam (5 mg per kg), medetomidine (0.5 mg per kg) and fentanyl (0.05 mg per kg). The mid-thoracic spinal cord of anesthetized *CD68*-EGFP mice was surgically exposed by a dorsal laminectomy as previously described[52]. A hemisection of the spinal cord was performed using fine-tip surgical scissors (Fine Science Tools 15000-08 spring scissor, 2.5 mm cutting edge). For sham surgery, the dorsal laminae of mid-thoracic vertebrae were surgically exposed in anesthetized *CD68*-EGFP mice. After spinal cord injury or sham surgery, muscle tissue and skin were sutured with a surgical thread (Ethilon suture 6-0, 667 H) and animals were allowed to recover on a heating pad. After 48 h, mice were transcardially perfused according to the 'Perfusion and tissue preparation' section below.

**Perfusion and tissue preparation.** Mice were deeply anesthetized using a combination of midazolam, medetomidine and fentanyl (MMF; 1 ml per 100 g body mass for mice; intraperitoneal). As soon as the animals did not show any pedal reflex, they were intracardially perfused with heparinized 0.1 M PBS (10 U ml$^{-1}$ of heparin, Ratiopharm; ~110 mmHg pressure using a Leica Perfusion One system) for 5–10 min at room temperature until the blood was washed out, followed by 4% paraformaldehyde (PFA) in 0.1 M PBS (pH 7.4; Morphisto, 11762.01000) for 10–20 min. Next, optionally, skin and eyes as well as premaxilla and maxilla bones were carefully removed, the palate of the animal was opened (without damaging the tissue beneath), and the feces were gently washed out from the intestine with 0.1 M PBS through small cuts using a syringe. For the animals cleared with skin, the skin was not removed from the bodies, and in case of BL6 background animals, the fur was shaved off using a razor blade (Personna, 604305-001001). Then, the bodies were post-fixed in 4% PFA for 1 d at 4 °C and later washed with 0.1 M PBS for 10 min 3 times at room temperature. Either the whole-body nanoboosting procedure was started immediately or whole mouse bodies were stored in PBS at 4 °C for up to 4 weeks or in PBS containing 0.05% sodium azide (Sigma-Aldrich, 71290) for up to 6 months.

For the collection of dissected tissues such as brains, mice were perfused with PBS and PFA as described above. Subsequently, the organs of interest were dissected out and post-fixed in 4% PFA overnight at 4 °C, washed with 0.1 M PBS for 10 min 3 times at room temperature and kept in PBS plus 0.05% sodium azide for up to 3 weeks.

**Clearing of unboosted samples.** For the quantification of fluorescence signal after clearing, without boosting, we followed the uDISCO passive clearing protocol as described by Pan et al.[17]. In brief, dissected brains were placed in 5 ml tubes (Eppendorf, 0030 119.401) and covered with 4.5 ml of clearing solution. All incubation steps were performed in a fume hood with gentle shaking or rotation, with the samples covered with aluminum foil to keep them in dark. To clear the samples, we incubated them in a gradient of *tert*-butanol (Sigma-Aldrich, 360538): 30 vol%, 50 vol%, 70 vol%, 80 vol%, 90 vol%, 96 vol% (in distilled water), and 100 vol% twice at 35 °C for 12 h each step followed by immersion in dichloromethane (Sigma-Aldrich, 270997) for 45–60 min at room temperature and finally incubation with the refractive index matching solution BABB-D15, containing 15 parts BABB (benzyl alcohol + benzyl benzoate 1:2; Sigma-Aldrich, 24122 and W213802), 1 part diphenyl ether (Alfa Aesar, A15791) and 0.4 vol% vitamin E (DL-α-tocopherol; Alfa Aesar, A17039), for at least 6 h at room temperature until transparency was achieved.

**Nanobodies, antibodies and fluorescent dyes used in this study.** The nanobodies, antibodies and fluorescent dyes used in this study are as follows: Atto594-conjugated anti-RFP nanobooster (Chromotek, rba594-100), Atto647N-conjugated anti-GFP nanobooster (Chromotek, gba647n-100), Atto488-conjugated anti-GFP nanobooster (Chromotek, gba488-100), Atto488-conjugated anti-vimentin nanobooster (Vimentin-Label_Atto488; Chromotek, vba488-100), Alexa647-conjugated anti-GFP antibody (Invitrogen, A31852), and PI (Sigma-Aldrich, P4864). For the nanobody and antibody validation information, see the Life Sciences Reporting Summary.

*Validation of nanoboosters for vDISCO.* Post-fixed brains from fluorescent protein-expressing mice (for example, *Thy1*-GFP-M) were cut into 400 µm slices using a vibratome (Leica, VT1200S). The slices were imaged before staining with a Zeiss AxioZoom EMS3/SyCoP3 fluorescence stereomicroscope to make sure that the samples have fluorescent protein expression. All the following steps were done with gentle shaking. The slices were first incubated for 3 h in a 24 multiwell (Falcon,

353504) at 37 °C with 1 ml of permeabilization solution containing 1.5% goat serum (Gibco, 16210072), 0.5% Triton X-100 (AppliChem, A4975,1000), 0.5 mM of methyl-β-cyclodextrin (Sigma-Aldrich, 332615), 0.2% *trans*-1-acetyl-4-hydroxy-L-proline (Sigma-Aldrich, 441562) and 0.05% sodium azide (Sigma-Aldrich, 71290) in 0.1 M PBS. Subsequently, they were incubated overnight at 37 °C with the same permeabilization solution, and the nanobooster of interest was added with dilution 1:500 considering final volume = 500 µl. The multiwell was covered with aluminium foil to keep the slices in dark and was sealed well with parafilm (Bemis, PM-992) to prevent the solution from drying out. One slice was kept as negative control where there was no adding of nanobooster. After the incubation, slices were washed with the washing solution (1.5% goat serum, 0.5% Triton X-100, 0.05% sodium azide in 0.1 M PBS) at room temperature for 15 min 4 times and then washed with 0.1 M PBS at room temperature for 10 min 3 times. Then the slices were imaged again after staining with the AxioZoom microscope to check whether the staining worked. In the end, slices were moved to 5 ml Eppendorf tubes wrapped with aluminium foil to keep them in dark and cleared with 3DISCO protocol: first they were incubated at room temperature in the following gradient of tetrahydrofuran (THF; Sigma-Aldrich, 186562) in distilled water (45 min for each step): 50 vol% THF, 70 vol% THF, 80 vol% THF, 100 vol% THF and 1 h 100 vol% THF; after dehydration, samples were incubated for 15 min in dichloromethane, and finally in BABB until transparency. Finally, the slices were imaged again with the AxioZoom microscope to make sure that the staining worked even after clearing. For more details of the AxioZoom imaging setup, see the 'Fluorescence stereomicroscopy imaging' section below.

**vDISCO whole-body immunostaining, PI labeling and clearing.** In order to remove remaining blood and heme after PFA perfusion, and to decalcify the bones, the animals were subjected to perfusion with decolorization solution and decalcification solution before immunostaining. The decolorization solution was made with 25–30 vol% dilution of CUBIC reagent 1[5] in 0.1 M PBS. CUBIC reagent 1 was prepared with 25 wt% urea (Carl Roth, 3941.3), 25 wt% *N,N,N′,N′*-tetrakis (2-hydroxypropyl)ethylenediamine (Sigma-Aldrich, 122262) and 15 wt% Triton X-100 in 0.1 M PBS. The decalcification solution consisted of 10 wt/vol% EDTA (Carl Roth, 1702922685) in 0.1 M PBS, adjusting the pH to 8–9 with sodium hydroxide (Sigma-Aldrich, 71687).

The solutions for the immunolabeling pipeline were pumped inside the body of the animal by transcardial-circulatory perfusion, exploiting the same entry point hole into the heart created during the PBS and PFA perfusion step (see above) and following the procedure described by Pan et al.[17]. In brief, the mouse body was placed in a 300 ml glass chamber (Omnilab, 5163279) filled with 250–300 ml of appropriate solution, which covered the body completely. Next, the transcardial-circulatory system was established involving a peristaltic pump (ISMATEC, REGLO Digital MS-4/8 ISM 834; reference tubing, SC0266), keeping the pressure at 160–230 mmHg (45–60 r.p.m.). One channel from the pump, made by a single reference tube, was set for circulation of the solution through the heart into the vasculature: one ending of the tube was connected to the tip of a syringe (cut from a 1 ml syringe; Braun, 9166017V) which held the perfusion needle (Leica, 39471024), and the other ending was immersed in the solution chamber where the animal was placed. The perfusion needle pumped the appropriate solution into the mouse body, and the other ending collected the solution exiting the mouse body to recirculate the solution, pumping it back into the animal. To fix the needle tip in place and to ensure extensive perfusion, we put a drop of superglue (Pattex, PSK1C) at the level of the hole where the needle was inserted inside the heart. Using the setting explained above, after post-fixation and PBS washing, the mice were first perfused with 0.1 M PBS overnight at room temperature; then, the animals were perfused with 250 ml of decolorization solution for 2 d at room temperature, exchanging with fresh decolorization solution every 6–12 h until the solution turned from yellowish to clear and the spleen became lighter in color (indicating that the blood heme was extracted). Then, they were perfused with 0.1 M PBS, washing for 3 h 3 times, followed by perfusion with 250 ml of decalcification solution for 2 d at room temperature and again perfusion/washing with 0.1 M PBS for 3 h 3 times. After this, the animals were perfused with 250 ml of permeabilization solution containing 1.5% goat serum, 0.5% Triton X-100, 0.5 mM of methyl-β-cyclodextrin, 0.2% *trans*-1-acetyl-4-hydroxy-L-proline and 0.05% sodium azide in 0.1 M PBS for half a day at room temperature. Subsequently, the perfusion proceeded further, through connection of a 0.20 µm syringe filter (Sartorius, 16532) to the ending of the tube not holding the needle to efficiently prevent accumulation of dye aggregates into the sample. At the same time, from this step we used an infrared lamp (Beuer, IL21) directed to the chamber to heat up the solution to 26–28 °C. With this setting, the animals were perfused for 6 d with 250 ml of the same permeabilization solution containing 35 µl of nanobooster, which is 20–35 µg in 250 ml (0.08–0.14 µg ml$^{-1}$), 1:7,000 in dilution (stock concentration 0.5–1 mg ml$^{-1}$; the amount of nanobody was adjusted depending on the expected presence of fluorescent protein in the mouse body) and 290 µl of PI (stock concentration 1 mg ml$^{-1}$). Next, we removed the animals from the chamber, and with fine scissors we removed a tiny piece from the back of the skull (above the cerebellum) at the level of the occipital bone; we then placed the bodies in a 50 ml tube (Falcon, 352070) filled with the same permeabilization solution containing an extra 5 µl of nanobooster and incubated the tubes at 37 °C with gentle shaking for an additional 2–3 d of labeling. After that, the mice were placed back in the perfusion system, and labeling solution was washed out by perfusing with washing solution (1.5% goat serum, 0.5% Triton X-100, 0.05% of sodium azide in 0.1 M PBS) for 3 h 3 times at room temperature and 0.1 M PBS for 3 h 3 times at room temperature.

After the staining, the animals were cleared using a 3DISCO-based passive whole-body clearing protocol optimized for big samples. The mice were incubated at room temperature in dehydration and clearing solutions inside a 300 ml glass chamber, kept with gentle rotation on top of a shaking rocker (IKA, 2D digital) inside a fume hood. For dehydration, mice bodies were incubated in 200 ml of the following gradient of THF in distilled water (12 h for each step): 50 vol% THF, 70 vol% THF, 80 vol% THF, 100 vol% THF and again 100 vol% THF, followed by 3 h in dichloromethane and finally in BABB. During all incubation steps, the glass chamber was sealed with parafilm and covered with aluminum foil. See Supplementary Table 1 and http://www.discotechnologies.org/vDISCO/.

**vDISCO whole-mount immunolabeling of individual organs.** vDISCO was performed on dissected organs as well: dissected brains were stained using the immunolabeling protocol for dissected organs. First, the post-fixed brains were pretreated, incubating them for 2 d at 37 °C with gentle shaking in 4.5 ml of same solution used at the permeabilization step (see above). Subsequently, the brains were incubated in 4.5 ml of this same permeabilization solution plus the nanobooster of interest with the concentration adjusted to expression of the target (for example, Atto647N-conjugated anti-GFP nanobooster dilution 1:600, which is ~5–8 µg of nanobooster in 4.5 ml (1.1–1.8 µg ml$^{-1}$; stock concentration, 0.5–1 mg ml$^{-1}$) for *Thy1*-GFP-M brains) for 12–14 d at 37 °C with gentle shaking, then brains were washed for 2 h 3 times and once overnight with the washing solution (1.5% goat serum, 0.5% Triton X-100, 0.05% of sodium azide in 0.1 M PBS) at room temperature and in the end washed for 2 h 4 times with 0.1 M PBS at room temperature. The immunostained brains were cleared with 3DISCO clearing: first they were put in the Eppendorf 5 ml tubes, and then they were incubated at room temperature with gentle shaking in 4.5 ml of the following gradient of THF in distilled water (2 h for each step): 50 vol% THF, 70 vol% THF, 80 vol% THF, 100 vol% THF and overnight ;vol% THF; after dehydration, the samples were incubated for 1 h in dichloromethane and finally in BABB until transparency. During all the clearing steps, the tubes were wrapped with aluminum foil to keep them in dark. See Supplementary Table 1.

For the comparison of deep-tissue staining efficiency in terms of penetration of the staining of nanobody versus conventional antibody (Supplementary Fig. 2), we followed the same protocol described above in this section for both nanobody and antibody experimental groups. The only exception was that for the antibody group, in the immunostaining step, we replaced the nanobooster with Alexa647-conjugated anti-GFP antibody (Invitrogen, A31852) with the same concentration (see above).

**Pumping pressure measurement.** A KKmoon Digital Manometer Pressure Gauge Manometer (HT-1891) was used to measure the pressure. To achieve one additional measuring channel to connect with the manometer, a two-head connector (B.Braun Discofix C Dreiwegehahn, 16494C) was inserted into the pumping channel, and the second head was further connected to the manometer with extended PVC tubing. The pumping channel was set in the standard way as described including a transcardiac perfusion needle. First, the switch on the two-head connector was set without connecting the measuring tubing, and pumping was started until all the air bubbles were excluded from the pumping channel. Subsequently, the switch was set to connect the measuring tubing while pumping was continued, and the pressure was measured when the manometer readouts stabilized. Three measurements were made at different time points including morning, afternoon and evening to exclude the variation of room temperature, and the data were quantified by averaging.

**Comparison of high-pressure versus low-pressure perfusion with methylene blue.** The diffusion of methylene blue (Sigma-Aldrich, M9140), perfused into the body of the animals, was used to compare the efficiency of high-pressure versus low-pressure perfusion (Supplementary Fig. 8). For this purpose, we used 3 BL6 animals (4 months old) per experimental group: post-fixed whole bodies were perfused for 15 min with 0.05% methylene blue in 0.1 M PBS, at either 50 r.p.m. (~180 mmHg) for the high-pressure group or 25 r.p.m. (~70 mmHg) for the low-pressure group. The same pump setting explained in the section 'vDISCO whole-body immunostaining, PI labeling and clearing' was used, including the usage of superglue to fix the needle in place inside the hole in the heart.

**iDISCO+.** *Antibody validation: methanol compatibility test.* Before performing the comparison of the efficiency between vDISCO nanobody staining and iDISCO+ antibody staining on whole brains, we verified the compatibility of the chosen antibody with the iDISCO+ protocol (Supplementary Fig. 3a–d). This was done performing the antibody validation step, which tested the compatibility of the antibody with the methanol pretreatment required by iDISCO+. To do so, we followed the original iDISCO+ publication[23] and the latest protocol updates from https://idisco.info. Briefly, post-fixed brains from *Thy1*-GFP-M and CX3CR1$^{GFP/+}$

mice (2–3 months old) were cut into 600 µm slices with a vibratome. First, the slices were incubated overnight in 100% methanol (Roth, 4627.6) at room temperature; then, after rehydrating and washing with 0.1 M PBS, the iDISCO+ immunostaining protocol was done as normally using 3 h as permeabilization time, 6 h as blocking time and overnight as immunolabeling time, adding 1:850 of Alexa647-conjugated anti-GFP antibody (already used in the previous section) in 500 µl of incubation solution. Non-methanol-treated slices were used as positive controls. In the end, the slices were imaged using the Zeiss AxioZoom stereomicroscope (see 'Fluorescence stereomicroscopy imaging' section below).

*iDISCO+ on dissected brains.* After having verified that the previously mentioned conventional anti-GFP antibody is compatible with iDISCO+, we performed comparison of staining efficiency between vDISCO with nanobody and iDISCO+ with conventional antibody (Supplementary Fig. 3e–i). For this purpose, 3 CX3CR1$^{GFP/+}$ post-fixed brains (6–7 months old) were used per experimental group. The brains allocated into the vDISCO group were processed following the vDISCO protocol for dissected brains (see 'vDISCO whole-mount immunolabeling of individual organs' section), while the brains allocated into the iDISCO+ group were processed using 1:730 of the above-mentioned Alexa647-conjugated anti-GFP antibody following the iDISCO+ protocol and its updates from https://idisco.info (ref. [23]).

**Different whole-body labeling protocols comparison.** To show that vDISCO with nanobody is the only method that can efficiently boost the GFP signal in mouse whole bodies, we performed the following comparison using 3 GFP-M animals (2–3 months old) per experimental group: (1) high-pressure active perfusion vDISCO with nanobody, (2) passive incubation vDISCO with nanobody, (3) high-pressure active perfusion vDISCO with conventional antibody, (4) high-pressure active perfusion iDISCO+ with conventional antibody, and (5) high-pressure active perfusion iDISCO+ with nanobody. Group 1 was processed using the above-described vDISCO whole-body immunostaining and clearing method; the group 2 was processed following all the steps of the vDISCO whole-body immunostaining and clearing protocol described above, but replacing all the original steps done in perfusion with passive incubation; group 3 was processed using the same vDISCO whole-body immunostaining and clearing protocol, but replacing the nanobooster with Alexa647-conjugated anti-GFP antibody at the same concentration as the nanobooster during the staining step; groups 4 and 5 were processed performing the iDISCO+ methanol pretreatment on the animals followed by sequential perfusion of all the iDISCO+ solutions[23] (except that the clearing was done with passive incubation): the timing of each iDISCO+ step was adjusted considering the size of a whole body compared with a dissected brain (for example, during the methanol dehydration, each step was increased to 5 h versus 1 h for dissected brains). The antibody used for group 4 is the Alexa647-conjugated anti-GFP antibody mentioned above.

**Previously published whole-body clearing methods for comparison.** For PARS clearing, 10% EDTA adopted from Bone-CLARITY[25] was transcardially perfused through the whole mouse bodies after PFA fixation for 5–7 d to decalcify the bones. Then, the standard PARS procedure was followed[53]. CUBIC[18], uDISCO[17] and PEGASOS[16] were conducted based on the original publications. It is worth noting that among all the clearing methods tested, PARS, PEGASOS and vDISCO were characterized by a decalcification step using EDTA solutions.

**Light-sheet microscopy imaging.** Single-plane illuminated (light-sheet) image stacks were acquired using an Ultramicroscope II (LaVision BioTec), featuring an axial resolution of 4 µm with the following filter sets: ex 470/40 nm, em 535/50 nm; ex 545/25 nm, em 605/70 nm; ex 560/30 nm, em 609/54 nm; ex 580/25 nm, em 625/30 nm; ex 640/40 nm, em 690/50 nm. For low-magnification whole-body imaging of the *Thy1*-GFP-M mouse, we used a ×1 Olympus air objective (Olympus MV PLAPO ×1/0.25 NA (WD = 65 mm)) coupled to an Olympus MVX10 zoom body, which provided zoom-out and zoom-in ranging from ×0.63 up to ×6.3. Using ×1 objective and ×0.63 of zoom, we imaged a field of view of 2 × 2.5 cm, covering the entire width of the mouse body. Tile scans with 60% overlap along the longitudinal *y* axis of the mouse body were obtained from ventral and dorsal surfaces up to 13 mm in depth, covering the entire volume of the body using a *z*-step of 8 µm. Exposure time was 120 ms, laser power was adjusted depending on the intensity of the fluorescent signal (in order to never reach the saturation) and the light-sheet width was kept at maximum. After tile imaging of the sample within the entire field of view, already scanned regions were cut using a thin motorized dental blade (0.2 mm; Dremel 8200) for further imaging. After low-magnification imaging of the whole body, a forelimb of the *Thy1*-GFP-M animal was imaged with a ×2 objective (Olympus MVPLAPO2XC/0.5 NA (WD = 6 mm)) coupled with the same Olympus MVX10 zoom body at zoom magnification ×1.6. Moreover, the same ×2 objective with different zooms was used to perform high-magnification imaging of specific body regions (for example, the back of the animal at the level of lumbar vertebra, the inguinal lymph node area or the head). Individual organs (including brain, lungs, intestine and thymus) were imaged individually using high-magnification objectives: ×2 objective (Olympus MVPLAPO2XC/0.5 NA (WD = 6 mm)) coupled with the same Olympus MVX10 zoom body, ×4 objective (Olympus XLFLUOR ×4 corrected/0.28 NA (WD = 10 mm)), ×25 objective (Olympus XLPLN ×25/0.95 NA (WD = 4 mm)) and ×20 objective (Zeiss ×20 Clr Plan-Neofluar/0.1 NA (WD 5.6 = mm)) coupled to an Olympus revolving zoom body unit (U-TVCAC) kept at ×1. High-magnification tile scans were acquired using 8–30% overlap, and the light-sheet width was reduced to obtain maximum illumination in the field. For the specific imaging settings used in each figure panel, see Supplementary Table 2.

**Fluorescence stereomicroscopy imaging.** For images in Supplementary Fig. 3, brain slices were kept immersed in PBS. For nanobody validation, cleared slices were put on a glass lid and kept immersed in BABB. The imaging was performed with Zeiss AxioZoom EMS3/SyCoP3 fluorescence stereomicroscope using Zen 2 software (v.2.0.0.0; Carl Zeiss AG) using a ×1 long-working-distance air objective lens (Plan Z ×1, 0.25 NA, WD = 56 mm; Supplementary Table 2). For the comparison of YFP-H mouse tissues after high-pressure pumping versus low-pressure pumping in Supplementary Fig. 9, the mouse brains were cut into 1 mm slices using a vibratome and imaged with magnification ×7 for overview and with magnification ×112 in GFP channel for their detailed cell structures. See Supplementary Table 2.

**Laser-scanning confocal microscopy imaging.** After imaging with light-sheet microscopy, areas of interest from the cleared specimens, such as whole heads and body parts, were imaged with an inverted laser-scanning confocal microscope (Zeiss, LSM 880) using Zen 2 software (v.10.0.4.910; Carl Zeiss AG). Before imaging, samples were mounted by placing them onto the glass surface of a 35 mm glass-bottom petri dishes (MatTek, P35G-0-14-C) and adding a few drops of BABB to make sure that the imaging region was immersed in BABB. Closing or sealing of the petri dish was not necessary because BABB has a high evaporation point and doesn't dry out for several days. The only precaution taken was to check the resistance of the dish against BABB, by testing that the glue sealing the glass to the dish and the plastic parts were not dissolved after several hours of exposure to BABB.

The imaging was done using a ×40 oil-immersion objective lens (Zeiss, ECPlan-NeoFluar ×40/1.30 oil DIC M27, 1.3 NA, WD = 0.21 mm) and a ×25 water-immersion long-working-distance objective lens (Leica, 0.95 NA, WD = 2.5 mm) mounted on a custom mounting thread. See Supplementary Table 2.

**Reconstructions of whole-mouse body scans.** We acquired light-sheet microscope stacks using ImSpector (v.5.295, LaVision BioTec) as 16-bit grayscale TIFF images for each channel separately. In each pair of neighboring stacks, alignment was done by manually selecting 3 to 4 anatomic landmarks from the overlapping regions, and then the stitching was done sequentially with the Scope Fusion module of the Vision4D (v.2.12.6 × 64, Arivis) software. Landmarks were mainly chosen from the skeletal bones or occasionally from the neuronal structures on the basis of visual inspection of the anatomical features. After completing the 3D reconstructions, the data visualization was done with Amira (v.6.3.0, FEI Visualization Sciences Group), Imaris (v.9.1, Bitplane) and Vision4D in both volumetric and maximum-intensity projection color mapping. Depth coding was done using the Temporal-Color Code plugin in Fiji (ImageJ2, v.1.51, https://fiji.sc/).

**Image processing.** Processing, data analysis, 3D rendering and video generation for the rest of the data were done on an HP workstation Z840, with 8 core Xeon processor, 196 GB RAM, and Nvidia Quadro k5000 graphics card and HP workstation Z840 dual Xeon 256 GB DDR4 RAM, nVidia Quadro M5000 8GB graphic card. We used Imaris, Amira and Fiji (ImageJ2) for 3D and 2D image visualization. Tile scans were stitched by Fiji's stitching plugin49. Stitched images were saved in TIFF format and optionally compressed in LZW format to enable fast processing. We removed tiles with acquisition errors using Fiji's TrakEM2 plugin and Imglib2library. In case of tiling errors in the *z* dimension, we used TeraStitcher (v.1.10; https://abria.github.io/TeraStitcher/) with its default settings to globally optimize the tiled volumes and reconstruct the entire dataset. To increase the quality of the images, we used the following functions in Fiji: to enhance the contrast of microglia cells (Fig. 1n and Supplementary Fig. 2a–f), we used 'Enhance Local Contrast (CLAHE)'; to equalize the images (Fig. 4a,b and Supplementary Fig. 2a–f), we used 'Pseudo Flat-Field Correction'; to enhance the contrast over the background of the axonal terminals in Fig. 4c,d, we used the custom-made macro for Fiji that we utilized to generate the pre-processed data for NeuroGPS-Tree (see the section 'Neuron tracing' below).

**Neuron tracing.** For automated neuron tracing in our light-sheet datasets obtained with Zeiss ×20 Clr Plan-Neofluar/0.1 NA (WD = 5.6 mm) objective, we used the NeuroGPS-Tree algorithm[22]. NeuroGPS-Tree was developed for tracing relatively small volumes of confocal microscopy data; therefore, we initially reduced the file size to under 1 GB (approximate maximum data size for NeuroGPS-Tree computation) by using the Fiji scale function. Due to high signal intensity discrepancy between soma and neurites, we next pre-processed the data with a custom-made macro in Fiji (available upon request), which consisted of background removal, pseudo-background correction, noise filtering

and sharpening. Next, the pre-processed data were loaded and analyzed first in NeuroGPS for soma detection and later in NeuroGPS-Tree for neurite detection (both steps are part of the same algorithm package). The best parameters for soma and neurite detection were chosen following the original publication. To quantify the features (such as the number of neurites per cell and the number of somas with at least one neurite) of these detected neuronal cells, we used Amira software: we chose the 10 neurons with the biggest file size per group and analyzed them using the Spatial Graph Statistics function of the software.

**Quantifications.** All the details of imaging settings used to acquire the data for the quantifications described in this section are available in Supplementary Table 2.

*Analysis of fluorescence signal profiles from light-sheet images.* The fluorescence signal profiles from each channel (excitation 470 nm, 560 nm and 647 nm) were plotted in the same *z*-stack and normalized as percentage over the maximum peak using Fiji (Supplementary Fig. 1).

To compare vDISCO boosted and unboosted protocols and consequently the reduction of the background and the improvement of the signal over background ratio in the far-red channel, we analyzed neurons and axonal bundles expressing GFP imaged with excitation at 470 nm, and neurons and axonal bundles labeled with anti-GFP nanobody conjugated with Atto647N imaged with excitation at 640 nm at the same anatomic region. First, the scans were taken with the light-sheet microscope using the ×4 objective (Olympus XLFLUOR ×4 corrected/0.28 NA (WD = 10 mm)). Then, the signal profiles were analyzed in Fiji and measured from a defined straight line covering the neuronal structure and surrounding tissue background, and the normalized plots of the signal profile (Fig. 1i) were calculated by normalizing the plots of neuronal structures obtained as described above over the average signal intensity of the respective surrounding background. Each experimental group consisted of 3 animals, and for each animal at the same anatomic region we plotted 3 profiles.

The same analysis of signal profile was used to compare the labeling efficiency of vDISCO with nanobody and iDISCO+ with antibody (Supplementary Fig. 3g–i): in this case the signal of interest was the one coming from microglia. Each experimental group consisted of 3 animals, and for each animal at the same anatomic region we plotted 3 profiles from 3 different microglia. The same analysis of signal profile was used to compare different clearing methods in Supplementary Fig. 12.

*Fluorescence level.* Fluorescence level quantification was expressed as a signal-to-background ratio and was calculated using Fiji[17] at the following time points: 0, 2, 3, 4.5, 5.5, 12 and 18 months after nanoboosting (Fig. 1n,o). Each ×4 light-sheet microscopy brain scan was taken with the same imaging parameters, and an image in TIFF format of the same anatomic region for all the samples was quantified. The mean value of the background for each image was obtained by averaging the background values of 12–40 regions from equally sized areas of the image in regions of the sample without signal. To calculate the mean value of the signal for each image, we used the threshold function of the software: the threshold was adjusted to consider the fluorescence signal visible in the image. After adjusting the threshold, only the sharp signal from specific cellular structures was analyzed per image. To this end, we used Fiji's 'analyze particles' function to measure the signal intensity only of particles sized between 5–10 and 100–150 pixels (visible fluorescent cells) and calculated the average value from all the particles. Next, this value was divided by the mean value of the background of the respective image, obtaining the fluorescence level over the background. The corresponding images, visually showing the preservation of signal over time in relation to the respective fluorescence levels, were processed using the Enhance Local Contrast (CLAHE) function in Fiji to increase the contrast of fluorescent cells in the tissue.

*Quantification of deep-tissue staining efficiency of nanobody versus antibody.* To quantify the depth of staining and therefore to compare whole-organ staining efficiency of nanobody versus antibody labeling (Supplementary Fig. 2), we used CX3CR1$^{GFP/+}$ animals (3–7 months old), 3 whole brains per experimental group. The tile scans of the brains were taken with light-sheet microscopy in axial view using the ×4 objective (Olympus XLFLUOR ×4 corrected/0.28 NA (WD = 10 mm)). After stitching we chose the *z*-plane showing the same anatomic structures from all brains for comparison. These axial-view 2D images of whole brains were analyzed in Fiji; the distance of staining depth was quantified using the 'line' function in the *z*-plane at the greatest width of the brain, measuring from the surface until the last visible boosted microglia. Then, for each image, this staining depth value was normalized over the total thickness of the brain at the considered *z*-level, measuring a line drawn from the same point of the surface until the axial middle line of the brains.

*Quantification of whole-body labeling efficiency of different whole-body labeling protocols.* To quantify the rate of staining of the different whole-body labeling protocols in Supplementary Fig. 11, the tile scans of 3 whole heads per method were taken with light-sheet microscopy in axial view using the ×2 objective described in the 'Light-sheet microscopy imaging' section above with a total magnification of ×1.26. For the analysis, we used Fiji to choose 3 regions in *z* in the 2D visualization, to have comparative data in 3 different depths (see Supplementary Fig. 2a,b). For each region, we chose the *z*-plane displaying the same anatomic structures in each sample. Next, the 2D images were opened in Fiji and, after adjusting the threshold to the fluorescence signal visible in the image, the stained area in the brain in each image was quantified using the 'freehand selections' function. Next, this stained area value was normalized over the total area of the brain visible in that 2D image. This total area was quantified using the same 'freehand selections' function in Fiji, following the brain outline. Statistical comparison was performed considering each set of corresponding regions from the different samples separately.

*ClearMap.* To quantify microglia distribution, we used ClearMap[23]. Since the script was originally developed for quantification of the cFos$^+$ cells, to comply with the offered method, we did the following pre-processing steps on our microglia data using Fiji before ClearMap:

- Background equalization to homogenize intensity distribution and appearance of the microglia cells over different regions of the brain, using pseudo-flat-field correction function from Bio-Voxxel toolbox.
- Convoluted background removal, to remove all particles bigger than relevant cells. This was done with the median option in the Bio-Voxxel toolbox.
- Two-dimensional median filter to remove remaining noise after background removal. The filter radius was chosen to ensure the removal of all particles smaller than microglia cells.
- Unshapen mask to amplify the high-frequency components of a signal and increase overall accuracy of the cell detection algorithm of ClearMap.

After pre-processing, ClearMap was applied by following the original publication and considering the threshold levels that we obtained from the pre-processing steps. As soon as the quantification was completed, the data was exported as an Excel file for further analysis. For example, the cellular density per brain region was obtained considering the absolute number of cells detected by ClearMap and the volume of that specific brain region, which was calculated using a custom script (available upon request) based on ClearMap (Elastix registration).

*Quantification of peripheral neuronal degeneration in acute brain injury.* Peripheral neuronal degeneration in TBI animals versus unlesioned control animals was done in the *Thy1*-GFP-M line and was assessed considering the complexity of axonal ramifications that projected from the left (left = contralateral side) cervical and thoracic vertebra to the left muscles of the back at the level of the torso of the mouse, including the left spinotrapezius and latissimus dorsi. The complexity was expressed as number of axonal endpoints (nerve terminals that appear as a button-like shape; see Fig. 4) over the total length of axonal ramifications that were protruding from a main branch. To calculate this index, first a 3 × 3 tile of *z*-stacks of this anatomic region was taken from the animals by light-sheet microscopy using the ×2 objective described in the 'Light-sheet microscopy imaging' section with a total magnification of ×5, to have enough resolution to manually trace the axonal ramifications and axonal end-feet. Then, the analysis was done over the maximum intensity projections of the tile scans with Fiji software. To measure the length of the ramifications, we used the 'free hand line' function and the 'ROI manager tool' of Fiji to record all the traced axonal ramifications of interest, which were coming from a main branch; later, we calculated the sum of the length of all of the recorded ramifications with the 'measure' function of Fiji. To count the nerve terminals, we used the 'point tool' function and the same 'ROI manager tool' to record all the visible axonal endpoints protruding from the traced ramifications. The analysis was performed over 2–4 branches from the same anatomic region for each animal, in 6 animals (3–6 months old) per experimental group. The same quantification procedure was followed to analyze the complexity at the equivalent ipsilateral (right side from dorsal view) side of the animals, in 6 and 5 animals for the TBI and unlesioned groups, respectively.

*Quantification of CD68 GFP$^+$ cells with spinal cord injury.* The spine areas of interest from *CD68*-EGFP line mice with spinal cord injury or sham surgery and from naïve animals were imaged with light-sheet microscopy using the ×2 objective described in the 'Light-sheet microscopy imaging' section with a total magnification of ×3.2 and with 2 × 3 tile *z*-stacks. After stitching, the entire *z*-stacks of scans were loaded in Fiji software with the 'use virtual stack' mode. To segment the spinal cord tissue from surrounding tissue, including bone and muscles, and count the cell numbers separately, the border of the spinal cord was marked by using the 'free hand line' function in Fiji as a manual selection. These manual selections were done in every 6–9 image slices and were recorded by the 'ROI manager tool' function. The complete selections for the entire *z*-stacks were then achieved by using the 'interpolate ROIs' function and were saved as .zip files. Then, the entire *z*-stacks of scans were loaded in Fiji software again, without selecting the 'use virtual stack' mode. By loading the complete selections generated from former steps respectively, each spinal cord was segmented by using a custom-made macro with the 'clear outside' function and saved as a new 'image sequence'. To maintain the integrity of the raw data, one should not save the changes when closing the window after running the macro. Then, the intact original *z*-stacks and complete selections were loaded again in the same way, and surrounding tissues including bone and muscles were segmented by using another custom-made macro with

the 'clear' function. All the custom-made macros are available upon request. Next, the segmented image stacks of spinal cord or surrounding tissue were loaded with Imaris respectively, and the 'surface' function was used to segment the CD68 $GFP^+$ cells. By generating the 'surface' selection, the 'statistic' function was available to count the number of cells in the region of interest.

*Quantification of short SMCs with MCAO.* The transparent skulls from *LysM*-EGFP line mice with MCAO or sham were imaged with intact heads from the sagittal view with light-sheet microscopy using the ×2 objective described in the 'Light-sheet microscopy imaging' section with a total magnification of ×3.2 and with 2×4 tile *z*-stacks. After stitching, the entire *z*-stacks of scans were loaded in Imaris, and the length, width and cell numbers in the SMCs were manually calculated by using the 'measure-line' function. Then, the length and width of the channels were corrected by a shrinkage rate of DISCO clearing[17].

**Statistical analysis.** Data collection and analysis were not performed blind to the conditions of the experiments. Data distribution was assumed to be normal, but this was not formally tested. Data are presented as mean ± s.d. except for in Fig. 6 and Supplementary Fig. 22, where they are presented as mean ± s.e.m. Sample sizes are indicated in the figure legends. Statistical analysis was performed using Prism GraphPad software v.6 with 95% confidence interval. *P* values were calculated using two-tailed unpaired *t* test to compare data between two groups. *P* values were calculated using one-way ANOVA followed by Dunnett's *post hoc* test to compare data in Supplementary Figs. 4 and 11. For *CD68*-EGFP quantification in Supplementary Fig. 22, *P* values were calculated using one-way ANOVA followed by Tukey multiple comparison test to compare data between SCI (spinal cord injury), sham and naïve groups. A *P* value of $<0.05$ was considered statistically significant. In ANOVA analysis the reported *P* values are adjusted in GraphPad prism to account for multiple comparisons. The protocols described in this study were replicated successfully more than five times in independent experiments, and they were also reproduced at least by three different operators. See also the Life Sciences Reporting Summary.

**Reporting Summary.** Further information on research design is available in the Nature Research Reporting Summary linked to this article.

**Code availability.** The custom codes used to analyze the data in this study are available from the corresponding author upon request.

## Data availability

The data that support the findings of this study are available from the corresponding author upon reasonable request.

## References

51. Niess, J. H. et al. CX3CR1-mediated dendritic cell access to the intestinal lumen and bacterial clearance. *Science* **307**, 254–258 (2005).
52. Nikic, I. et al. A reversible form of axon damage in experimental autoimmune encephalomyelitis and multiple sclerosis. *Nat. Med.* **17**, 495–499 (2011).
53. Treweek, J. B. et al. Whole-body tissue stabilization and selective extractions via tissue-hydrogel hybrids for high-resolution intact circuit mapping and phenotyping. *Nat. Protoc.* **10**, 1860–1896 (2015).

nature research

Corresponding author(s): Ali Ertürk

# Reporting Summary

Nature Research wishes to improve the reproducibility of the work that we publish. This form provides structure for consistency and transparency in reporting. For further information on Nature Research policies, see Authors & Referees and the Editorial Policy Checklist.

## Statistical parameters

When statistical analyses are reported, confirm that the following items are present in the relevant location (e.g. figure legend, table legend, main text, or Methods section).

| n/a | Confirmed | |
|---|---|---|
| ☐ | ☒ | The exact sample size (*n*) for each experimental group/condition, given as a discrete number and unit of measurement |
| ☐ | ☒ | An indication of whether measurements were taken from distinct samples or whether the same sample was measured repeatedly |
| ☐ | ☒ | The statistical test(s) used AND whether they are one- or two-sided<br>*Only common tests should be described solely by name; describe more complex techniques in the Methods section.* |
| ☒ | ☐ | A description of all covariates tested |
| ☐ | ☒ | A description of any assumptions or corrections, such as tests of normality and adjustment for multiple comparisons |
| ☐ | ☒ | A full description of the statistics including central tendency (e.g. means) or other basic estimates (e.g. regression coefficient) AND variation (e.g. standard deviation) or associated estimates of uncertainty (e.g. confidence intervals) |
| ☐ | ☒ | For null hypothesis testing, the test statistic (e.g. *F*, *t*, *r*) with confidence intervals, effect sizes, degrees of freedom and *P* value noted<br>*Give P values as exact values whenever suitable.* |
| ☒ | ☐ | For Bayesian analysis, information on the choice of priors and Markov chain Monte Carlo settings |
| ☒ | ☐ | For hierarchical and complex designs, identification of the appropriate level for tests and full reporting of outcomes |
| ☒ | ☐ | Estimates of effect sizes (e.g. Cohen's *d*, Pearson's *r*), indicating how they were calculated |
| ☐ | ☒ | Clearly defined error bars<br>*State explicitly what error bars represent (e.g. SD, SE, CI)* |

*Our web collection on statistics for biologists may be useful.*

## Software and code

Policy information about availability of computer code

| | |
|---|---|
| Data collection | The commercially available softwares used in this study to collect, stitch and visualize the data are: ImSpector (Version 5.295, LaVision BioTec GmbH), Vision4D (Version 2.12.6 x64, Arivis AG), Amira (Version 6.3.0, FEI Visualization Sciences Group), Imaris (Version 9.1, Bitplane AG), Zen 2 (Version 10.0.4.910, Carl Zeiss AG), Zen 2 (Version 2.0.0.0, Carl Zeiss AG). |
| Data analysis | The commercially available softwares used in this study to analyze the data are: Amira (Version 6.3.0, FEI Visualization Sciences Group), Imaris (Version 9.1, Bitplane AG), GraphPad Prism (Version 6, GraphPad Software Inc.).<br>The already publicly or published codes/softwares used in this study to stitch and analyze the data are: Fiji (Version 1.51, https://fiji.sc/), TeraStitcher (Version 1.10, https://abria.github.io/TeraStitcher/), NeuroGPS-Tree (https://www.nature.com/articles/nmeth.3662), ClearMap (https://www.sciencedirect.com/science/article/pii/S0092867416305554).<br>All the custom-made codes: the code to pre-process the data for NeuroGPS-Tree in Fiji, the custom-made macros for Fiji to remove region of interests in images, the custom-script to calculate the volume of specific brain regions for the cellular density are available upon request. |

For manuscripts utilizing custom algorithms or software that are central to the research but not yet described in published literature, software must be made available to editors/reviewers upon request. We strongly encourage code deposition in a community repository (e.g. GitHub). See the Nature Research guidelines for submitting code & software for further information.

## Data

Policy information about availability of data

All manuscripts must include a data availability statement. This statement should provide the following information, where applicable:

- Accession codes, unique identifiers, or web links for publicly available datasets
- A list of figures that have associated raw data
- A description of any restrictions on data availability

The data of this study are available from the corresponding author upon reasonable request.

# Field-specific reporting

Please select the best fit for your research. If you are not sure, read the appropriate sections before making your selection.

☒ Life sciences ☐ Behavioural & social sciences ☐ Ecological, evolutionary & environmental sciences

For a reference copy of the document with all sections, see nature.com/authors/policies/ReportingSummary-flat.pdf

# Life sciences study design

All studies must disclose on these points even when the disclosure is negative.

| | |
|---|---|
| Sample size | Sample sizes were chosen based on prior experience with similar models. Sample sizes are specified in figure legends. |
| Data exclusions | Exclusion criteria were pre-established.<br>Animals that resulted negative for the expression of fluorescent proteins by genotyping were excluded from the study.<br>For MCAO experiments, exclusion criteria were as follows: insufficient MCA occlusion (a reduction in blood flow to 15% of the baseline value) and blood flow recovery >80% within 10 min of reperfusion. |
| Replication | The indication of how many times each experiment was repeated independently showing similar results is written in the corresponding figure legend. Overall, the protocols described in this study were replicated successfully more than 5 times in independent experiments and they were also reproduced at least by 3 different operators. |
| Randomization | The animals used in this study were selected for each experiment based on their genetic background (wt or fluorescent transgenes). Within each strain, animals were randomly selected. |
| Blinding | Littermates were housed in the same cage. The investigator was not blinded to group allocation for data analysis as this was obvious during the experiments (e.g. stroke vs sham or TBI vs unlesioned). |

# Reporting for specific materials, systems and methods

### Materials & experimental systems

| n/a | Involved in the study |
|---|---|
| ☒ | ☐ Unique biological materials |
| ☐ | ☒ Antibodies |
| ☒ | ☐ Eukaryotic cell lines |
| ☒ | ☐ Palaeontology |
| ☐ | ☒ Animals and other organisms |
| ☒ | ☐ Human research participants |

### Methods

| n/a | Involved in the study |
|---|---|
| ☒ | ☐ ChIP-seq |
| ☒ | ☐ Flow cytometry |
| ☒ | ☐ MRI-based neuroimaging |

## Antibodies

| | |
|---|---|
| Antibodies used | Atto594 conjugated anti-RFP nanobooster (Chromotek, rba594-100), Atto647N conjugated anti-GFP nanobooster (Chromotek, gba647n-100), Atto488N conjugated anti-GFP nanobooster (Chromotek, gba488-100), Atto488 conjugated anti-Vimentin nanobooster (Vimentin-Label_Atto488, Chromotek, vba488-100), Alexa647 conjugated anti-GFP antibody (Invitrogen, A31852). All the nanoboosters were used in dilution 1:500 to label brain slices, 1:600 to label whole brains and 1:7000 to label whole bodies. The antibody was used in dilution 1:850 to label brain slices, 1:730 to label whole brains and 1:7000 to label whole bodies. |

| | |
|---|---|
| Validation | All the nanoboosters were coming from the same company which is the manufacturer: Chromotek https://www.chromotek.com/products/nano-boosters/. The manufacturer validated the nanoboosters and in its website (see link) they provide references, images of the validation from published papers and from validation experiments. We used nanobooster to label fluorescent proteins and vimentin expressed in mouse tissue, as indicated in example images from the manufacturer website. Before any deep tissue staining such as vDISCO whole body labeling, we further validated the compatibility of the nanoboosters with vDISCO in brain slices from transgenic animals as indicated in Method part of the manuscript.<br><br>The Alexa647 conjugated anti-GFP antibody (GFP Polyclonal Antibody Alexa Fluor 647, Invitrogen, A31852) has been validated by the manufacturer: Invitrogen https://www.thermofisher.com/antibody/product/GFP-Antibody-Polyclonal/A-31852. In the manufacturer website (see link) they provide references, images of the validation from published papers and from validation experiments. We used this antibody to label GFP expressed in mouse tissue, and this application has already been shown by references indicated in the manufacturer website. We further validated the compatibility of this antibody with iDISCO+ protocol in Supplementary Figure 3. |

## Animals and other organisms

Policy information about studies involving animals; ARRIVE guidelines recommended for reporting animal research

| | |
|---|---|
| Laboratory animals | We used the following mixed gender animals in the study: 6 weeks-12 months old CX3CR1GFP/+ (B6.129P-Cx3cr1tm1Litt/J, Jackson Laboratory strain code: 005582), 6 weeks-6 months old Thy1-GFPM , 3-7 months old Thy1-YFPH, 4 weeks old Prox1-EGFP (Tg(Prox1-EGFP)KY221Gsat/Mmucd, MMRRC strain code: 031006-UCD), 6 months old VEGFR3-YFP, 2 months old CX3CR1GFP/+ x CCR2RFP/+ (B6.129(Cg)-Ccr2tm2.1Ifc/J, Jackson Laboratory strain code: 017586), 6 months old LysM-EGFP (Lyz2tm1.1Graf, MGI: 2654931), 3 months old CD68-EGFP (C57BL/6-Tg(CD68-EGFP)1Drg/j, Jackson Laboratory strain code: 026827), 3 weeks-4 months old C57BL/6J, 3-4 months old NMRI nu/nu mice. |
| Wild animals | This study does not involve wild animals |
| Field-collected samples | This study does not involve Field-collected samples |

nature neuroscience

SUPPLEMENTARY INFORMATION

https://doi.org/10.1038/s41593-018-0301-3

In the format provided by the authors and unedited.

# Panoptic imaging of transparent mice reveals whole-body neuronal projections and skull–meninges connections

**Ruiyao Cai[1,2,10], Chenchen Pan[1,2,10], Alireza Ghasemigharagoz[1], Mihail Ivilinov Todorov[1,2], Benjamin Förstera[1], Shan Zhao[1], Harsharan S. Bhatia[1], Arnaldo Parra-Damas[1], Leander Mrowka[1], Delphine Theodorou[3,4], Markus Rempfler[5], Anna L. R. Xavier[6], Benjamin T. Kress[6,7], Corinne Benakis[1], Hanno Steinke[8], Sabine Liebscher[3,4,9], Ingo Bechmann[8], Arthur Liesz[1,2,9], Bjoern Menze[5], Martin Kerschensteiner[3,4,9], Maiken Nedergaard[6,7] and Ali Ertürk[1,2,9]***

[1]Institute for Stroke and Dementia Research, Klinikum der Universität München, Ludwig-Maximilians University Munich, Munich, Germany. [2]Graduate School of Systemic Neurosciences Munich, Munich, Germany. [3]Institute of Clinical Neuroimmunology, Klinikum der Universität München, Ludwig-Maximilians University Munich, Munich, Germany. [4]Biomedical Center, Ludwig-Maximilians University Munich, Munich, Germany. [5]Department of Computer Science and Institute for Advanced Study, Technical University of Munich, Munich, Germany. [6]Center for Translational Neuromedicine, Faculties of Health and Medical Sciences, University of Copenhagen, Copenhagen, Denmark. [7]Center for Translational Neuromedicine, University of Rochester, New York, NY, USA. [8]Anatomy Institute, University of Leipzig, Leipzig, Germany. [9]Munich Cluster for Systems Neurology (SyNergy), Munich, Germany. [10]These authors contributed equally: Ruiyao Cai, Chenchen Pan. *e-mail: ali.ertuerk@med.uni-muenchen.de

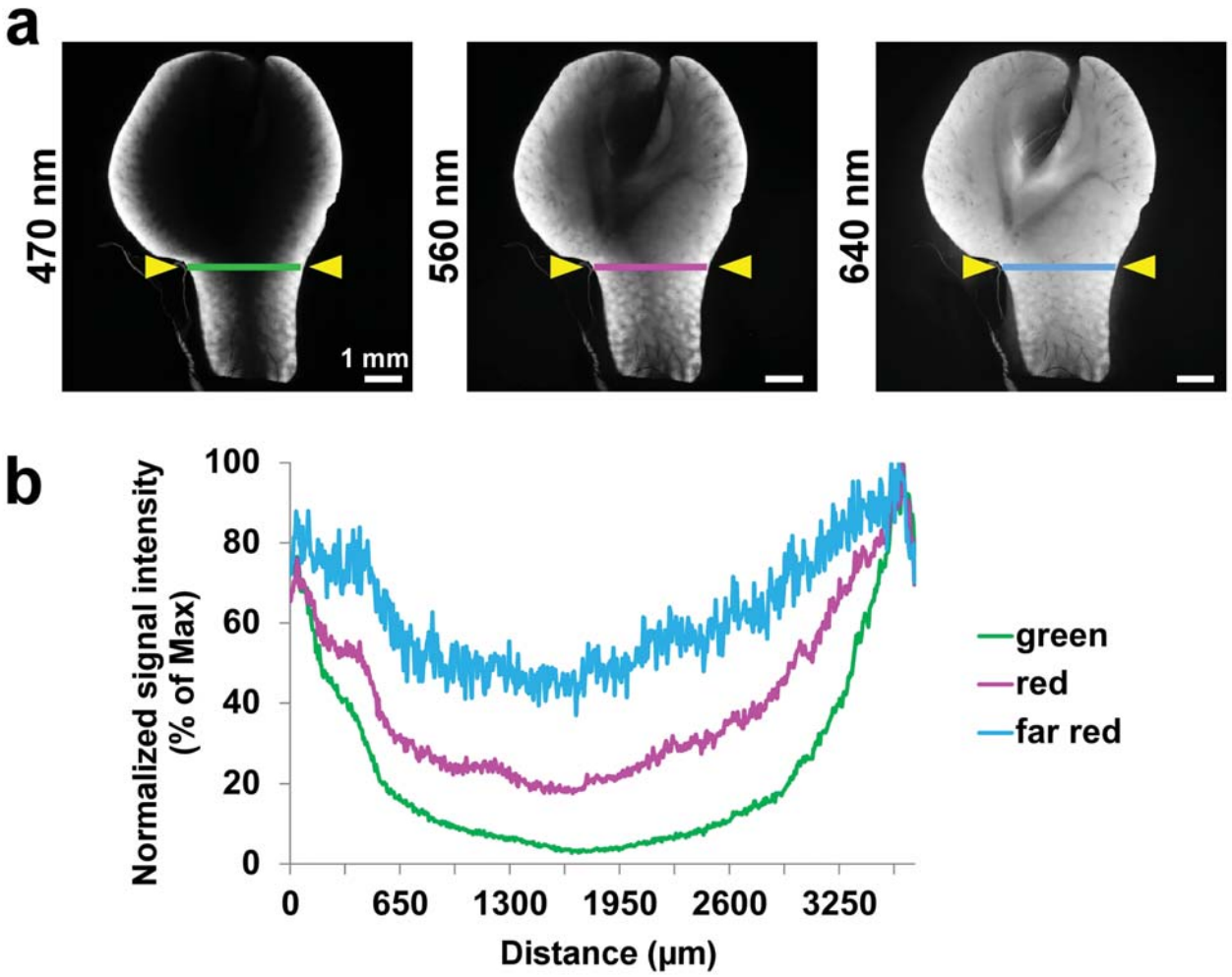


# Supplementary Figure 1

**Light penetration deep in tissue at different wavelengths**

(**a**) Demonstration of tissue penetration of the light at different imaging wavelengths. The same liver region (without any labeling) of a cleared mouse imaged in green (ex: 470 nm) (left), red (ex: 560 nm) (middle) and far-red channels (ex: 640 nm) (right) using light-sheet microscopy. (**b**) Fluorescence signal intensity profiles normalized over the maximum intensity of the regions indicated by the lines in a. Complete illumination of cleared liver at 640 nm compared to other wavelengths is evident. Similar results were observed in 10 independent animals.

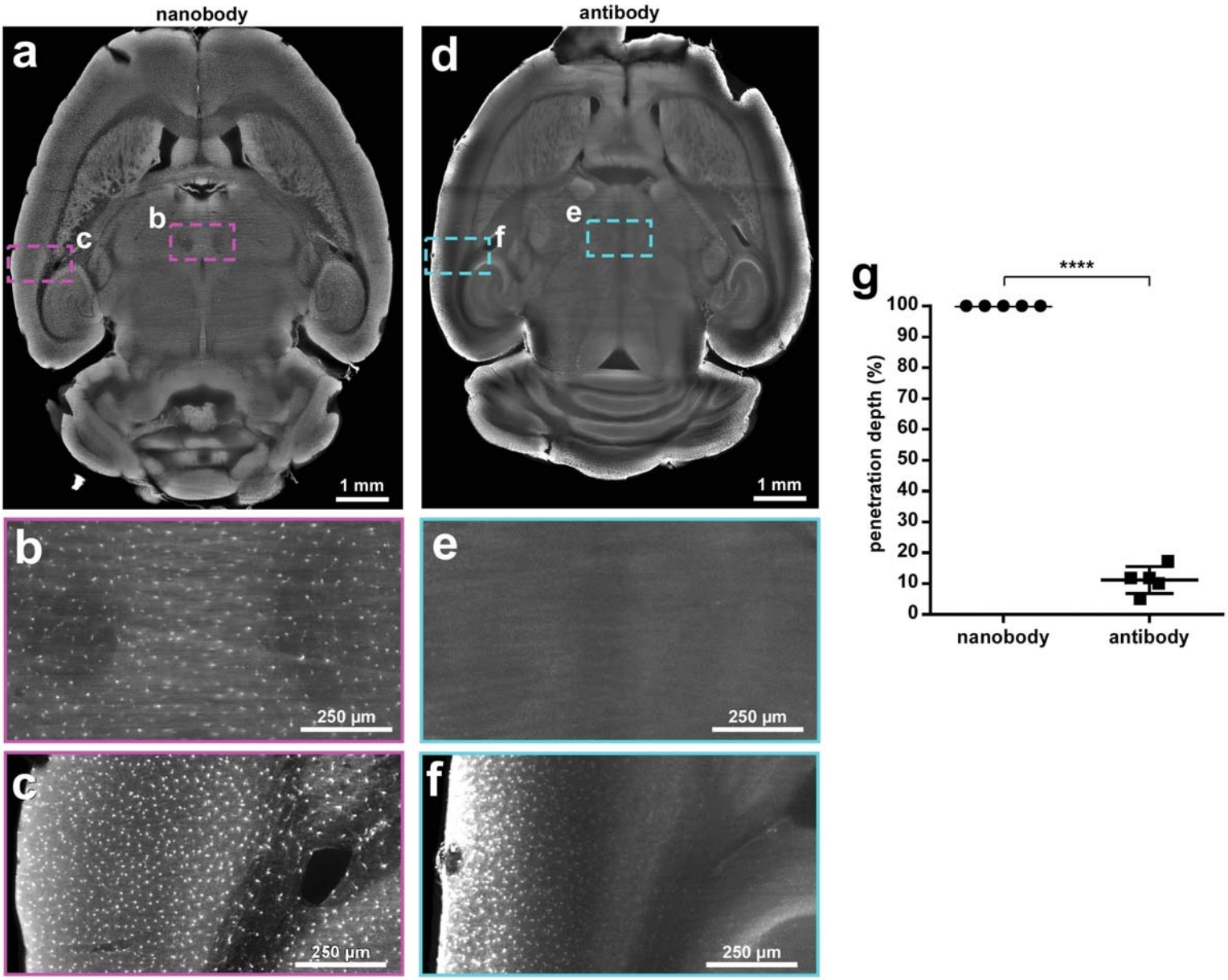


# Supplementary Figure 2

**Deep tissue staining efficiency of nanobody vs conventional antibody**

Penetration depth comparison between anti-GFP nanobody (**a**-**c**) vs. conventional anti-GFP antibody (**d**-**f**) from brains coming from CX3CR1$^{GFP/+}$ mice. Representative images of 1 brain from each group consisting of 5 independent animals. (**g**) Penetration depth quantifications of anti-GFP nanobody vs. conventional anti-GFP antibody stained brains from 5-12 months old CX3CR1$^{GFP/+}$ mice (mean ± s.d.; n=5 mice per group; statistical significance (****$p < 0.0001$) was assessed by two tailed *t*-test)

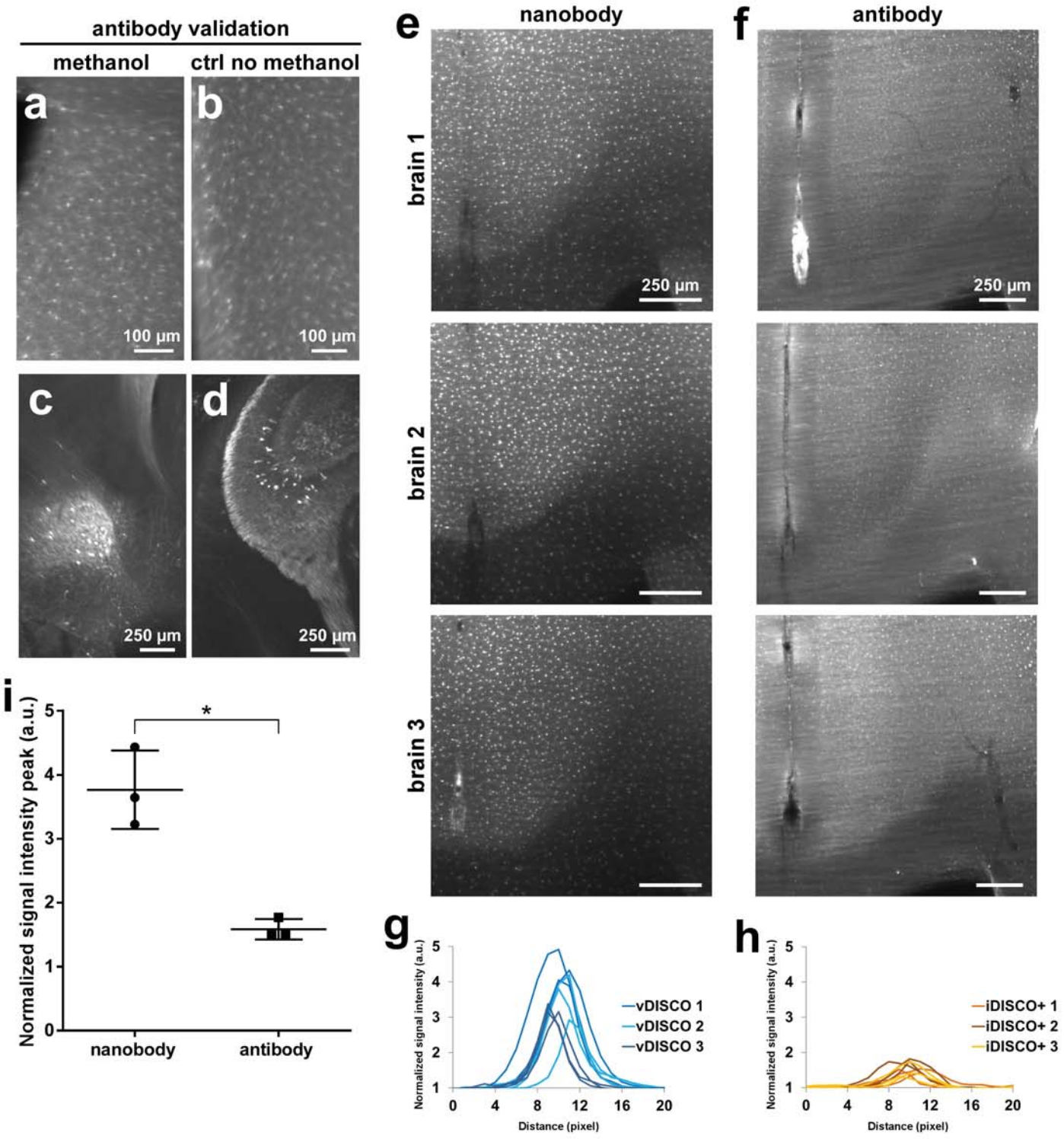


# Supplementary Figure 3

**Compatibility test of conventional anti-GFP antibody with iDISCO+ protocol and comparison between vDISCO passive boosting with anti-GFP nanobooster vs iDISCO+ passive labeling with conventional anti-GFP antibody on CX3CR1$^{GFP/+}$ brains**

(**a**-**d**) Fluorescent stereomicroscope images of 600 µm brain slices from CX3CR1$^{GFP/+}$ animal (**a**,**b**), and GFPM animal (both 2-3 months old) (**c**,**d**) showing the compatibility of a conventional anti-GFP antibody with methanol pretreatment: (**a**) slice from CX3CR1$^{GFP/+}$ brain and (**c**) slice from GFPM brain both pretreated with methanol and labeled with the conventional anti-GFP antibody showing the persistence of fluorescence signal compared with: (**b**) slice from the same CX3CR1 brain and (**d**) slice from the same GFPM brain labeled with the conventional anti-GFP antibody without methanol pretreatment as positive control. Similar results were observed in 2 independent animals. (**e**-**i**) Comparison between passive vDISCO boosting with anti-GFP nanobooster (conjugated with Atto-647N) vs. passive iDISCO+ labeling with the tested conventional anti-GFP antibody (conjugated with Alexa-647) on CX3CR1$^{GFP/+}$ whole brains from 5-7 months old mice: (**e**,**f**) light-sheet images showing the difference in labeling after vDISCO (**e**) vs. iDISCO+ (**f**) at the level of the same anatomical region (cortex and corpus callosum) in 3 different independent brains per each group; (**g**,**h**) plots of signal intensity profiles from vDISCO boosted brains in e (**g**) and iDISCO+ labeled brains in f (**h**); (**i**) Comparison of the peaks of the signal intensity profiles in g vs. h (mean ± s.d., n=3 animals per group, statistical significance (*$p$ = 0.02) was assessed by two tailed $t$-test).

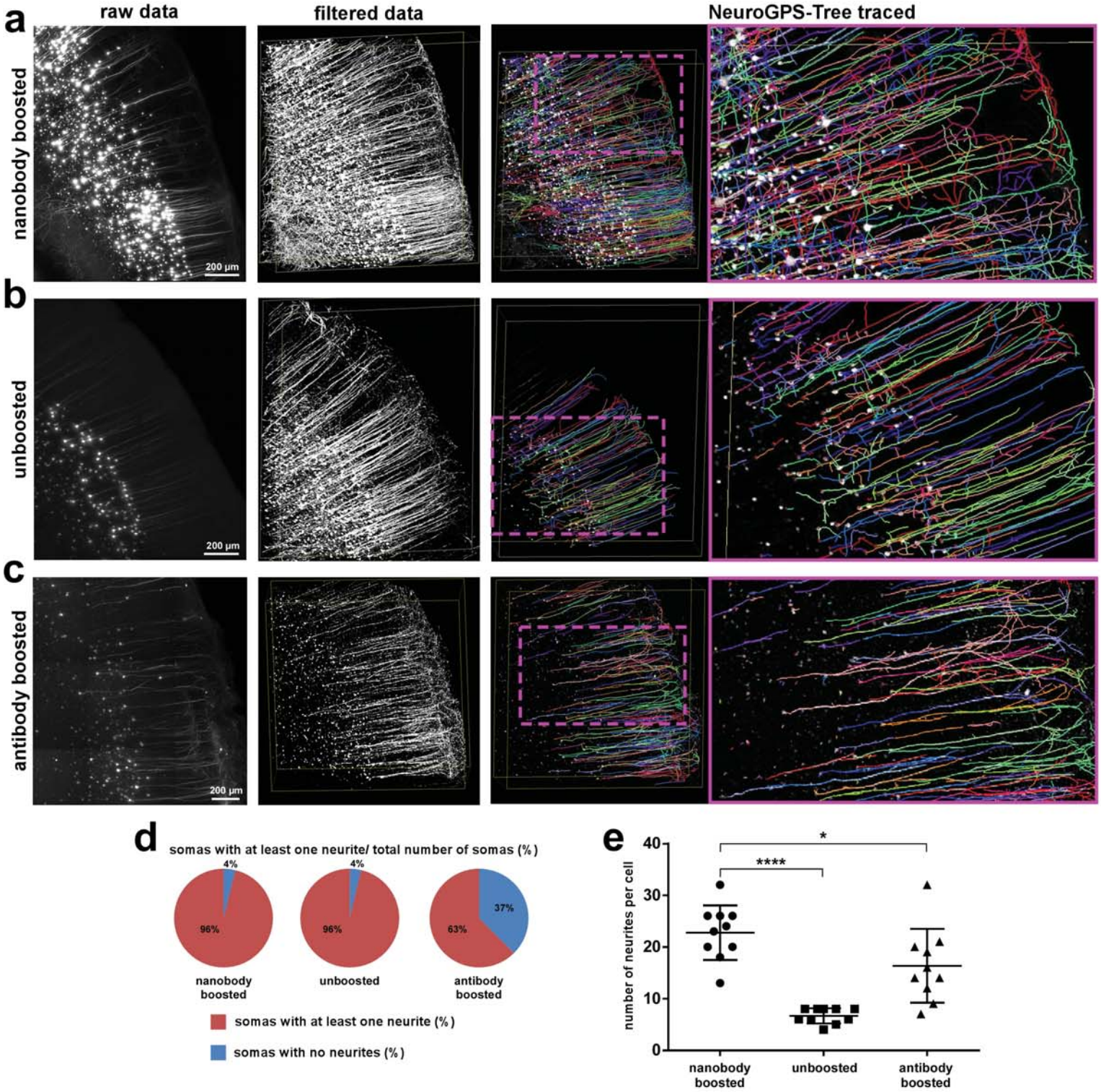


# Supplementary Figure 4

**Neuron tracing with NeuroGPS-Tree**

(**a**-**c**) Tracing of neurons in vDISCO nanobody boosted (**a**), unboosted (**b**) and iDISCO+ conventional anti-GFP antibody boosted (**c**) brains from 6-13 weeks old *Thy1*-GFPM mice using NeuroGPS-Tree algorithms. The scans were obtained with a commercial light-sheet microscope (Ultramicroscope II, LaVision Biotec), optimized for large cleared tissue imaging, thereby with lower resolution compared to standard confocal microscopes. From left to right: raw image, equalized & filtered images, and NeuroGPS-Tree traced neuronal structures are shown: all the neurites belonging to a neuron are represented by the same color. Neuronal soma identified by NeuroGPS-Tree are represented by red dots. Single experiment per each method. (**d**) Quantification of number of detected neurons characterized by their soma with at least one detected neurite over the total number of detected somas in vDISCO boosted vs unboosted and conventional antibody boosted samples. While in vDISCO boosted and unboosted cases almost all the neurons were detected with at least one neurite per soma, in the antibody boosted case only 63% was detected with neurites (**e**) Quantification of number of detected neurites per neuron in vDISCO boosted vs. unboosted and conventional antibody boosted samples, showing that only vDISCO allows the tracing of more neurites per cell (mean ± s.d; n=10 neurons per group; statistical significance ($F_{2,27}$=24.30, ****$p$ < 0.0001,*$p$ = 0.02) was assessed by one-way ANOVA followed by Dunnett´s *post hoc* test).

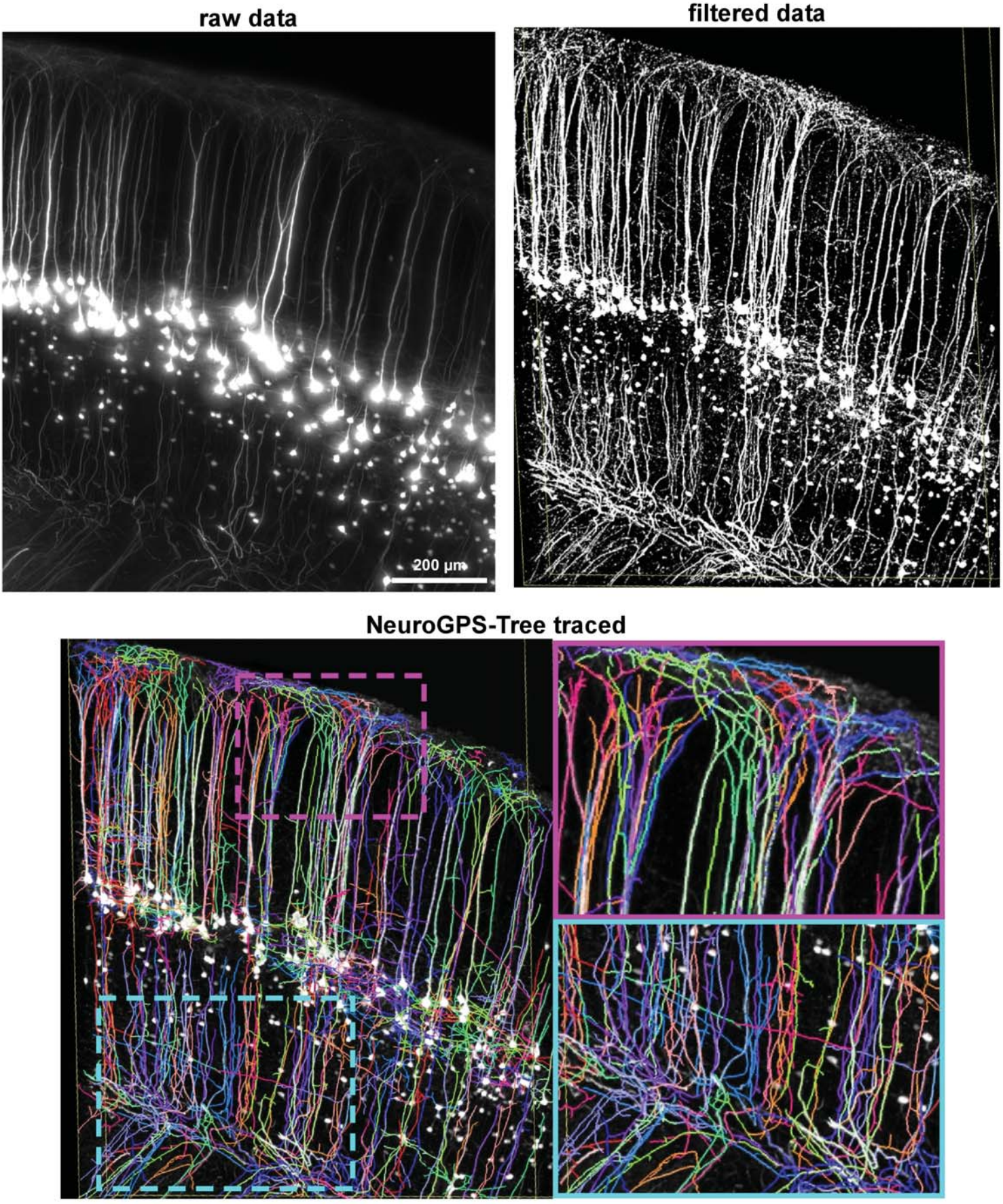


# Supplementary Figure 5

**Neuron tracing with NeuroGPS-Tree, secondary somatosensory cortex**

Tracing of neurons in vDISCO boosted brain from a 6 weeks old *Thy1*-GFPM mouse using NeuroGPS-Tree algorithms. The displayed region is around the secondary somatosensory cortex (Region S2 of the Figure 152 of the Franklin & Paxinos atlas, Bregma -2.80, Interaural 3.00). The scans were obtained with a commercial light-sheet microscope (Ultramicroscope II, LaVision Biotec), optimized for large cleared tissue imaging, thereby with lower resolution compared to standard confocal microscopes. From left, right to down: raw image, equalized & filtered images, and NeuroGPS-Tree traced neuronal structures are shown: all the neurites belonging to a neuron are represented by the same color. Axons projecting out from the somas to the corpus callosum are visible and traced. Single experiment.

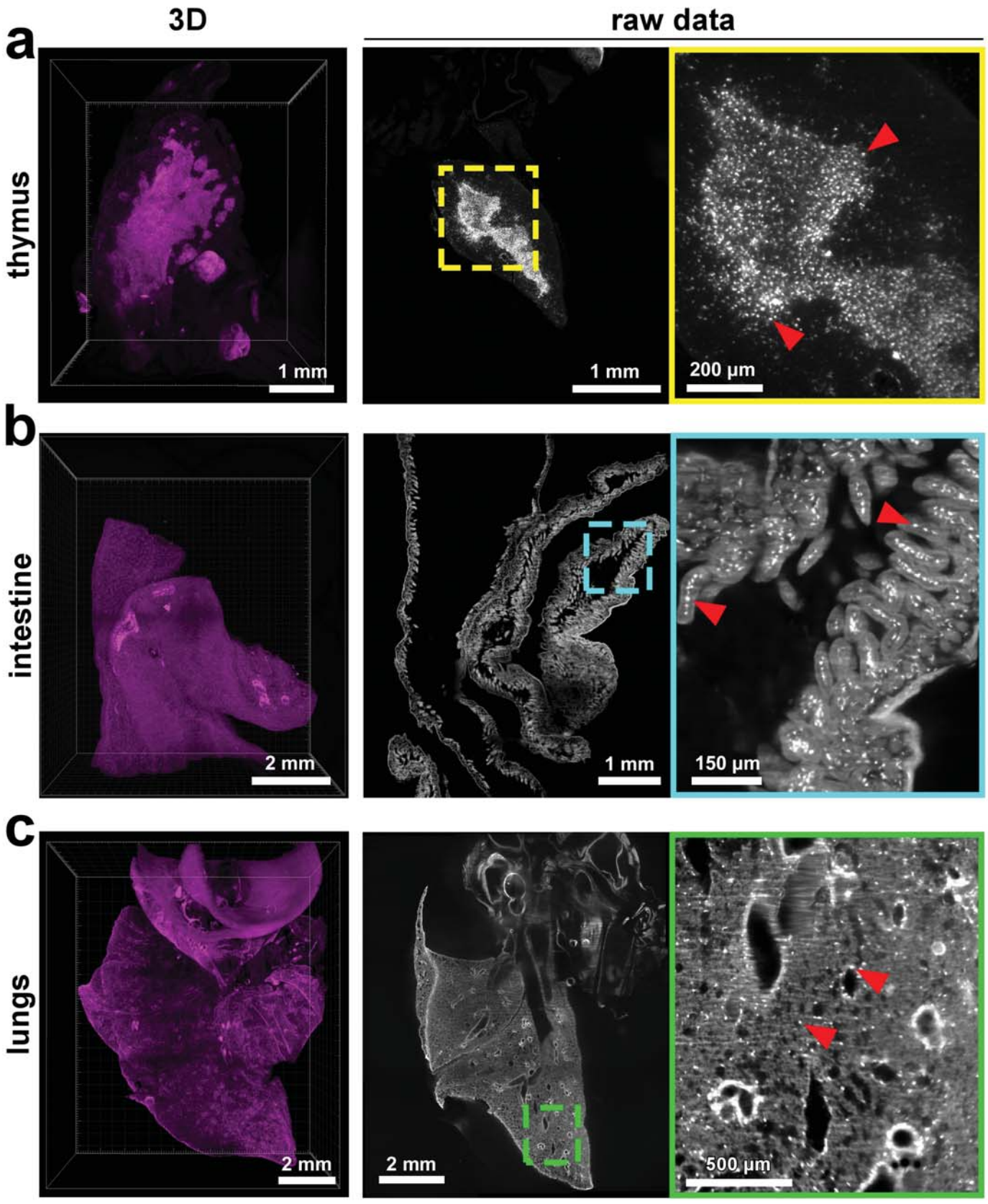


# Supplementary Figure 6

**Visualization of CX3CR1 GFP+ cells in individual organs**

(**a**-**c**) 3D visualization (magenta) and raw data images (grey) of individual organs including thymus (**a**), intestine (**b**), and lungs (**c**) from a 6 months old CX3CR1$^{GFP/+}$ mouse imaged by light-sheet microscopy. Individual CX3CR1 GFP+ cells are indicated by red arrow-heads in the zoomed images from the boxed regions. Similar results were observed in 3 independent animals.

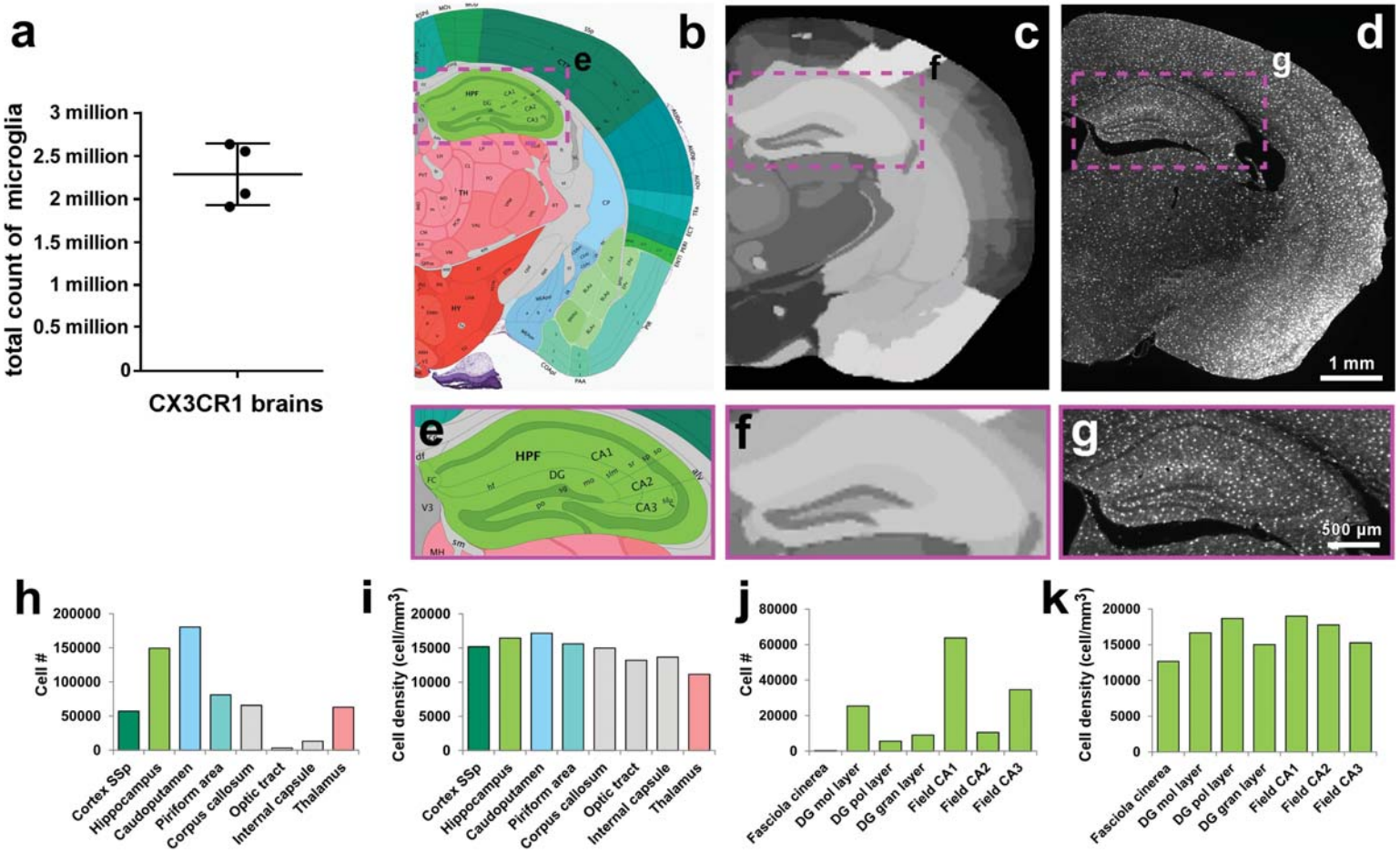


# Supplementary Figure 7

**Visualization and quantification of the signal from CX3CR1$^{GFP/+}$ mouse by vDISCO boosting**

(**a**-**k**) Automated analysis of fluorescent cells quantification and distribution in CX3CR1$^{GFP/+}$ mouse brain after vDISCO boosting (mean ± s.d.; n = 4 2-5 months old mice: 2.647, 2.553, 1.909, 2.061 millions respectively (**a**)): (**b**) reference image from the Allen brain atlas, (**c**) registered reference annotation image, (**d**) the corresponding region in raw data in coronal view. (**e**-**g**) High magnification images of the region indicated in b-d containing the hippocampus. Automated quantification of absolute cell numbers (**h**) and cell densities (**i**) of the anatomical regions visible in b-d. Absolute cell numbers (**j**) and cell densities (**k**) of sub-regions of hippocampus shown in e-g. The quantifications include the cells in both brain hemispheres.

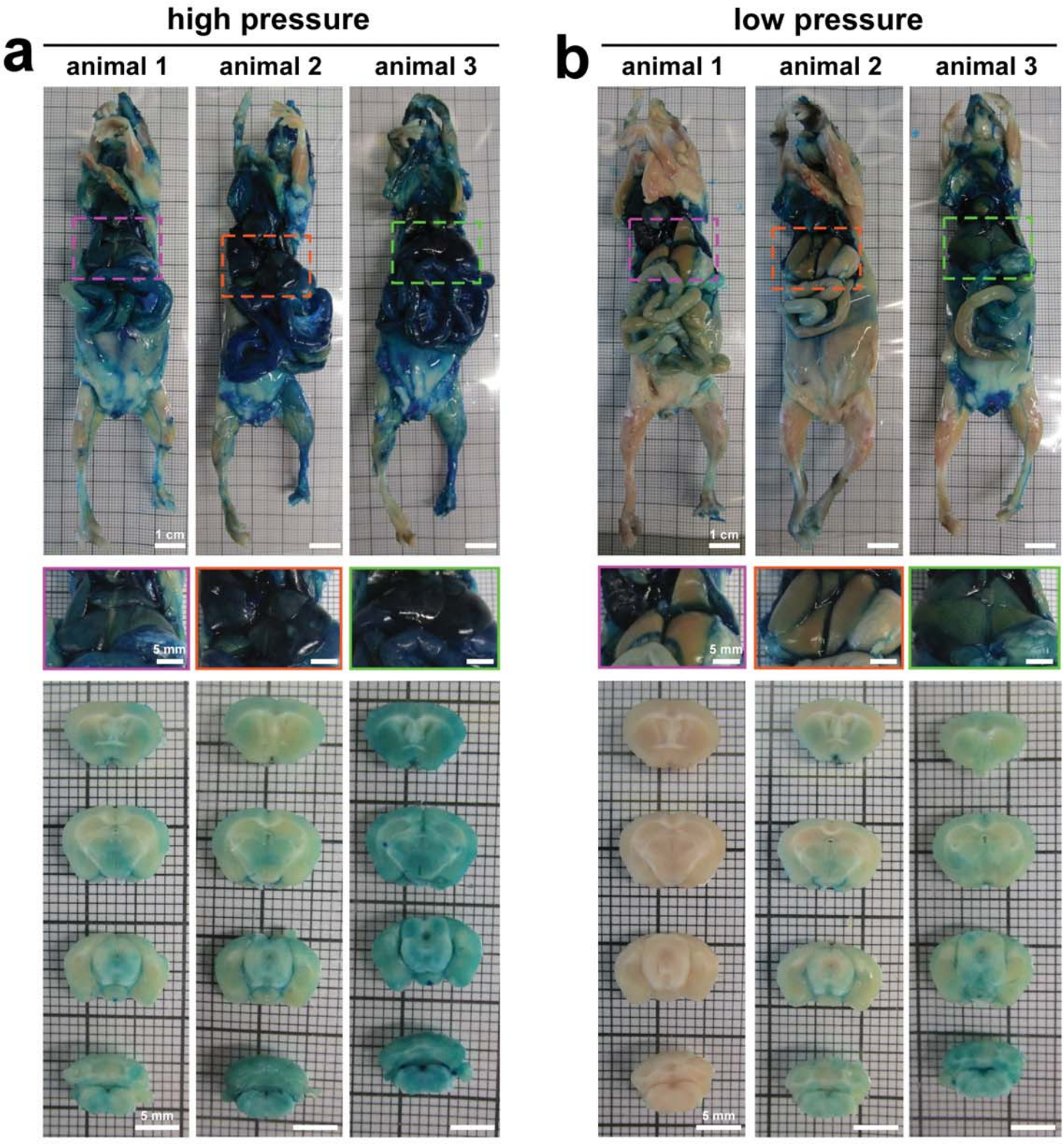


# Supplementary Figure 8

**Comparison between high vs low pressure transcardial perfusion**
Diffusion of blue dye in the body (up) and brain (down) of 4 months old C57BL/6J animals trascardially perfused for 15 minutes with methylene blue with high pressure (approx. 180 mmHg) (**a**) vs low pressure (approx. 70 mmHg) (**b**). The colored rectangles (middle) show the high magnification images of the dashed regions at the level of the liver.

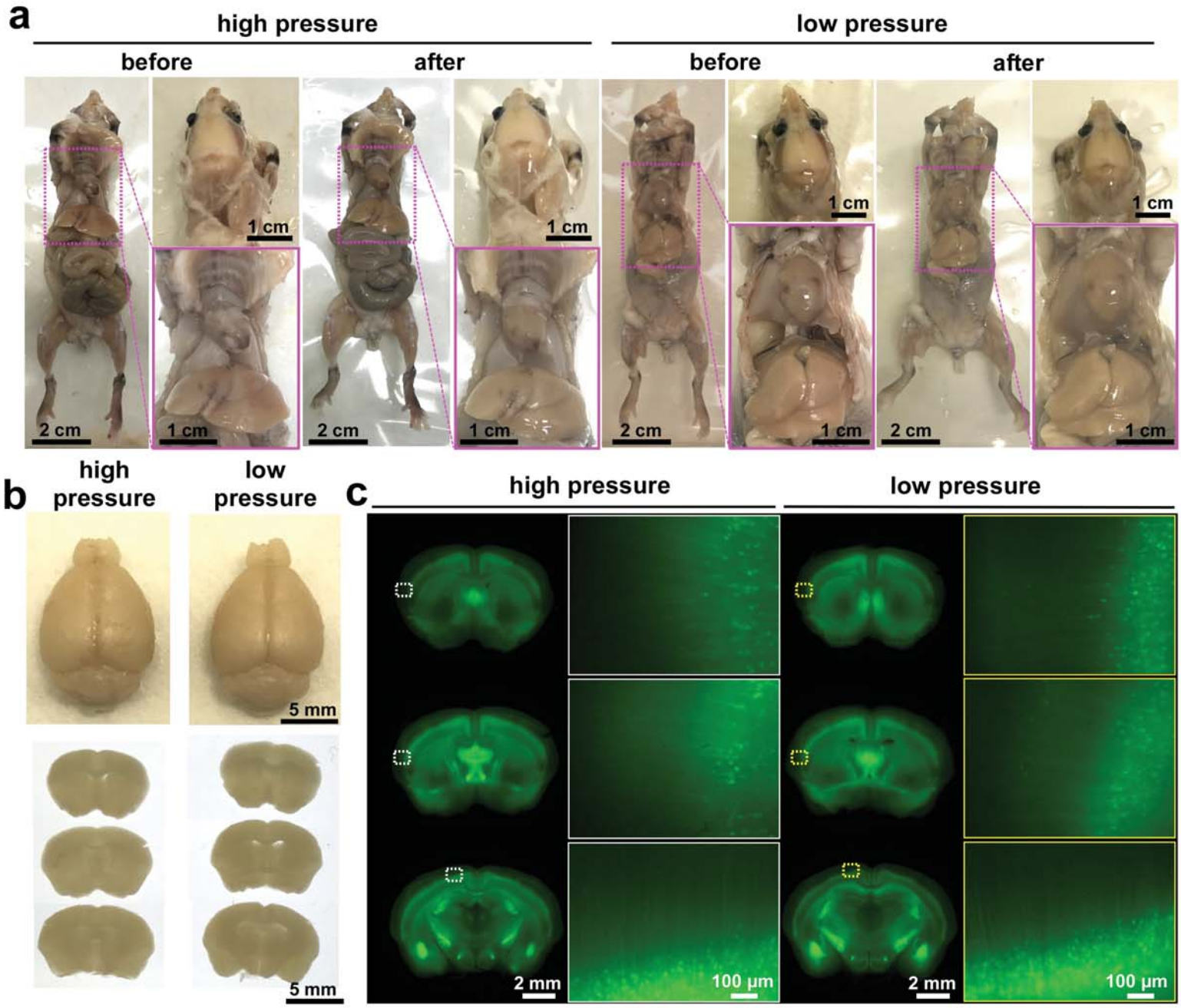


# Supplementary Figure 9

**Comparison between *Thy1*-YFPH line mice perfused with high (230 mmHg) or low pressure (110 mmHg)**

(**a**) Images of 3 months old mice taken before and after high or low pressure perfusion for 3 days, showing no morphological organ changes due to high pressure perfusion. (**b**) Comparison of dissected brains and brain slices from mice after high or low pressure perfusion, showing that the brain was not deformed or disrupted by high pressure perfusion at the macroscopic scale (similar results were observed from 2 independent mice per group) (**c**) Using a stereo-fluorescent microscope, the cortical neurons were imaged at single cell resolution. No morphology changes in neuronal structures were detected at the microscopic scale indicating that the high (230 mmHg) pressure perfusion in the vDISCO protocol does not damage the tissue (single experiment).

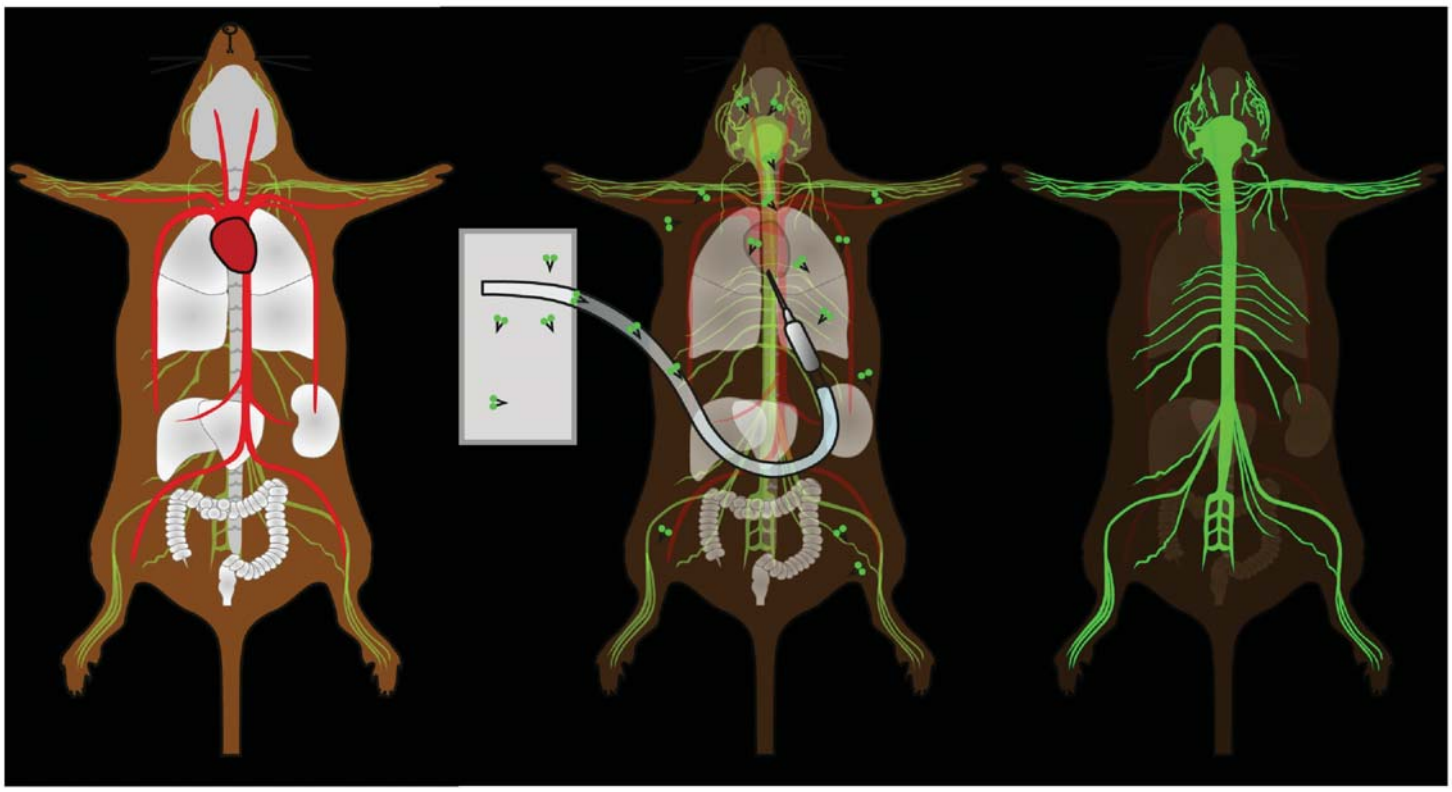

# Supplementary Figure 10

**Schematic illustration of whole-body vDISCO boosting method**

The decolorization, decalcification, and nanoboosting steps are performed via transcardiac perfusion. After boosting, the boosted fluorescence signal becomes highly visible over the reduced background in the intact transparent animals.

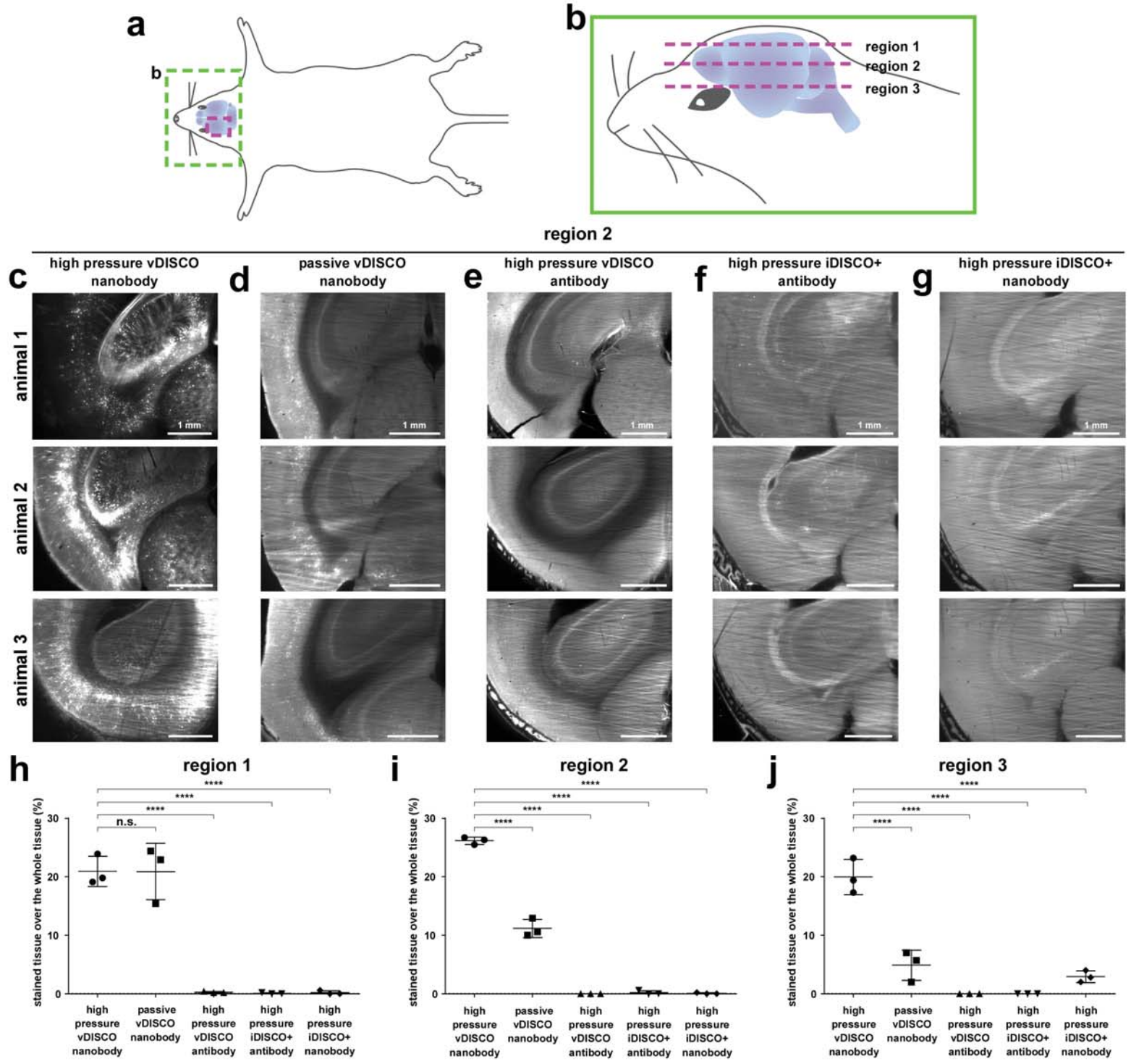


# Supplementary Figure 11

**Whole-body immunolabeling by vDISCO vs. other labeling methods**

(**a**) Illustration showing the anatomic region (dashed magenta rectangle) of the cleared mice imaged for the comparative analysis. (**b**) Zoom-in illustration at the level of the head of the representative animal showing the 3 different z regions of interest considered for the comparative analysis. (**c**-**g**) Light-sheet images of 3 brains from 3 independent cleared animals per each group at the level of region 2 indicated in a and b showing the complete penetration of the nanobody in animals processed with vDISCO method using active high pressure perfusion (**c**) vs. the partial labeling of the surface of the brain in animals processed with vDISCO with passive incubation of the nanobody (**d**) and vs. the limited labeling of the brain in animals processed with vDISCO using active high pressure pumping of conventional anti-GFP antibody (**e**), in animals processed with iDISCO+ using active high pressure pumping of conventional anti-GFP antibody (**f**) and in animals processed with iDISCO+ using active high pressure pumping of nanobody (**g**). (**h**-**j**) Quantification of the % of stained tissue from the described protocols at the level of region 1 (**h**), region 2 (**i**) and region 3 (**j**). mean ± s.d.; n=3 2-3 months old animals per group; statistical significance (n.s.=no significant, ****$p < 0.0001$, in h: $F_{4\text{-}10}$=64.26, in i $F_{4\text{-}10}$=693.0, in j $F_{4\text{-}10}$=62.19) was assessed by one-way ANOVA followed by Dunnett´s *post hoc* test).

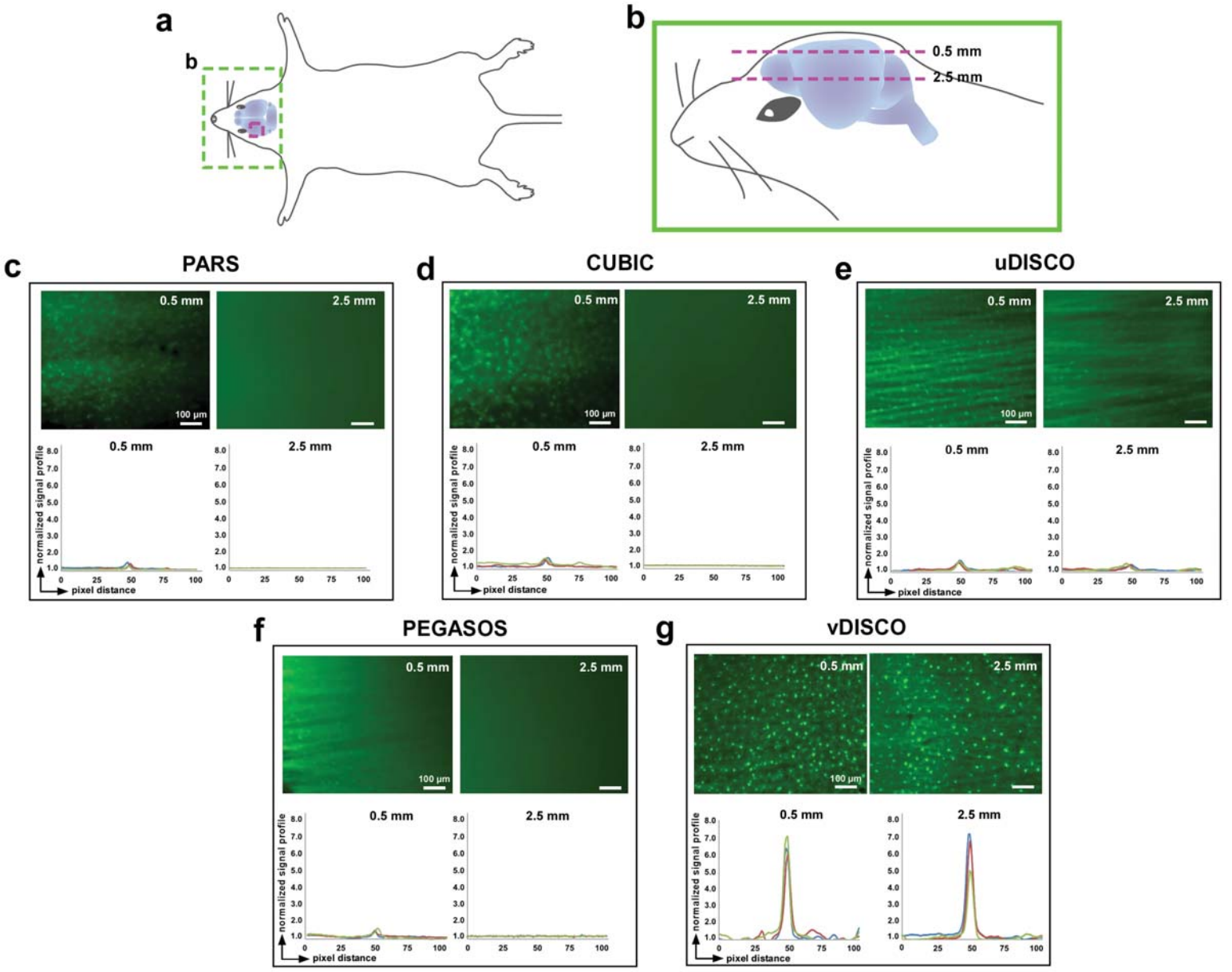


# Supplementary Figure 12

**Quality of imaging single cells deep in the brain through the skull by different whole-body clearing approaches**
(**a**) Illustration showing the anatomic region (dashed magenta rectangle) of the cleared mice imaged for the comparative analysis. (**b**) Zoom-in illustration at the level of the head of the representative animal showing the 2 different z regions (0.5 mm and 2.5 mm deep from the dorsal brain surface) considered for the comparative analysis. (**c**-**g**) To compare different clearing methods, whole-bodies of 2 months old CX3CR1$^{GFP/+}$ mice were cleared by PARS (**c**), CUBIC-R (**d**), uDISCO (**e**), PEGASOS (**f**) and vDISCO (**g**). After clearing, the whole-heads of mice with intact skull were taken for light-sheet microscopy for signal comparison. Representative images and normalized signal profiles at 0.5 mm and 2.5 mm depth indicate that vDISCO is the only method providing reliable detection of microglia cells through the intact skull. Similar results were observed from 3 independent mice per group. Among all the clearing methods tested, PARS, PEGASOS and vDISCO were characterized by a decalcification step using EDTA solutions.

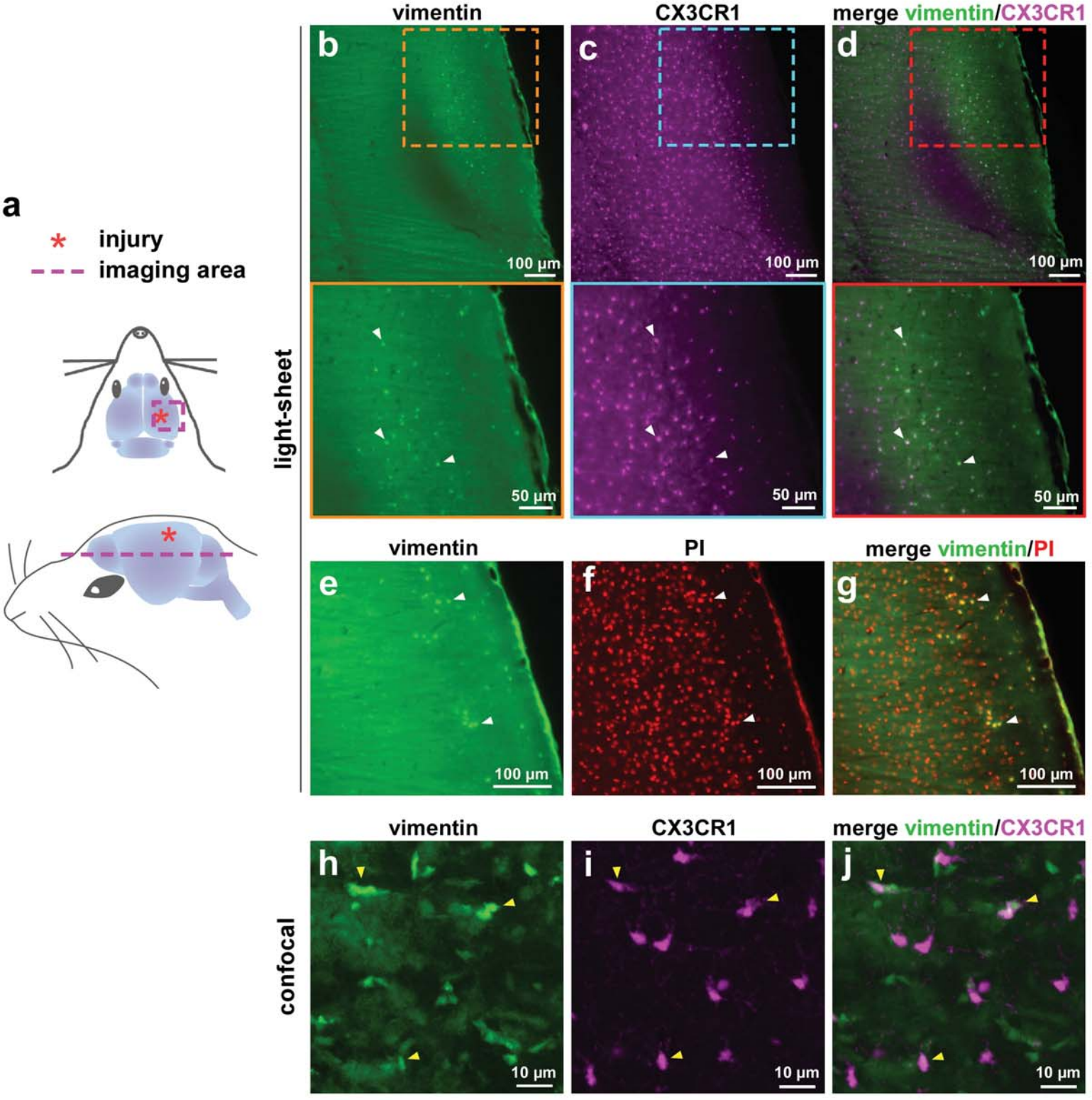


# Supplementary Figure 13

**vDISCO labeling of vimentin expressing cells using anti-vimentin nanobody**

(**a**) Illustration showing the injury location of the brain trauma (red asterisk) and the imaging area (magenta dashed line). (**b-d**) Light-sheet imaging of a mouse brain from traumatic brain injured 4 months old CX3CR1$^{GFP/+}$ animal 1 month after the injury: vimentin was labeled using anti-vimentin 488-nanobooster (green), in which the autofluorescence of the tissue is much higher than in the far-red spectrum. (**b**) CX3CR1 GFP+ cells were boosted using anti-GFP 647-nanobooster (magenta) (**c**), the colocalization of CX3CR1 GFP+ immune cells expressing vimentin is visible in white in the merge panel (**d**). The colored rectangles show zoom-in images of the dashed regions in b-d. White arrow-heads indicate examples of colocalizing signal in cells. (**e-g**) Light-sheet imaging of the same brain from the TBI CX3CR1$^{GFP/+}$ animal in b-d: vimentin is shown in green (**e**), while all nuclei of the cells were labeled using propidium iodide (PI) (red) (**f**), the colocalization of the signal in cells expressing vimentin and stained with PI is visible in yellow in the merge panel (**g**). White arrow-heads indicate examples of colocalizing signal in cells. (**h-j**) Confocal imaging of the mouse brain in b-d showing vimentin (green) (**h**) and CX3CR1 GFP+ cells (magenta) (**i**), the colocalization of CX3CR1 GFP+ immune cells expressing vimentin is visible in white and indicated by yellow arrow-heads in the merge panel (**j**). Single experiment.

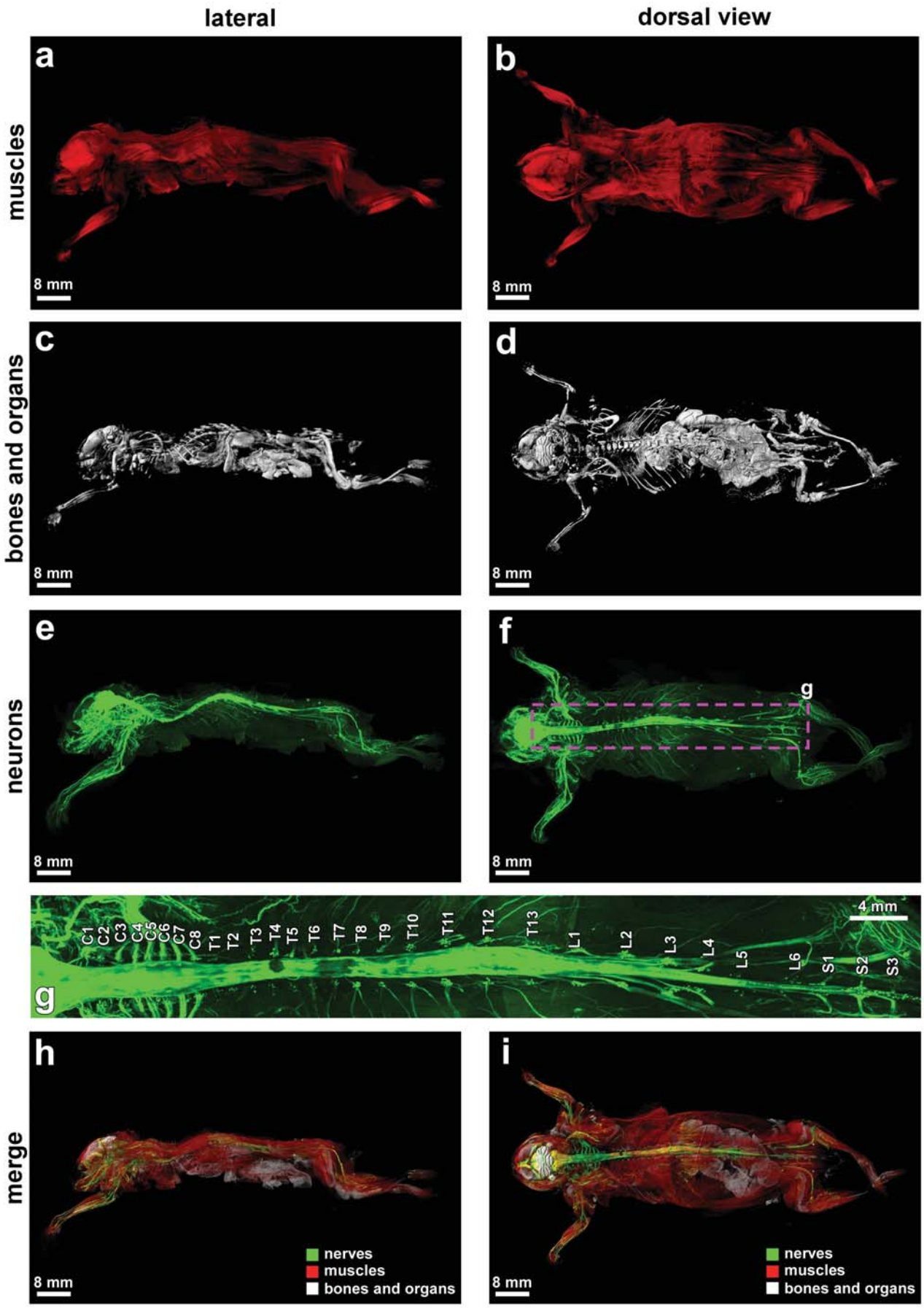


# Supplementary Figure 14

**Whole body neuronal projections of a *Thy1*-GFPM mouse by panoptic imaging** (**a-d**) The lateral and dorsal views of autofluorescence (muscles), and PI (bones and organs) channels. (**e**,**f**) Neuronal projections of the whole body in lateral and dorsal views. (**g**) High magnification view from the indicated region in **f** showing details of spinal cord segments. (**h**,**i**) The merge channels in lateral (**h**) and dorsal (**i**) views of neurons, bones and organs, and muscles are shown. Comparable labeling and imaging results were achieved in 5 independent animals, whole body reconstruction was done in one mouse.

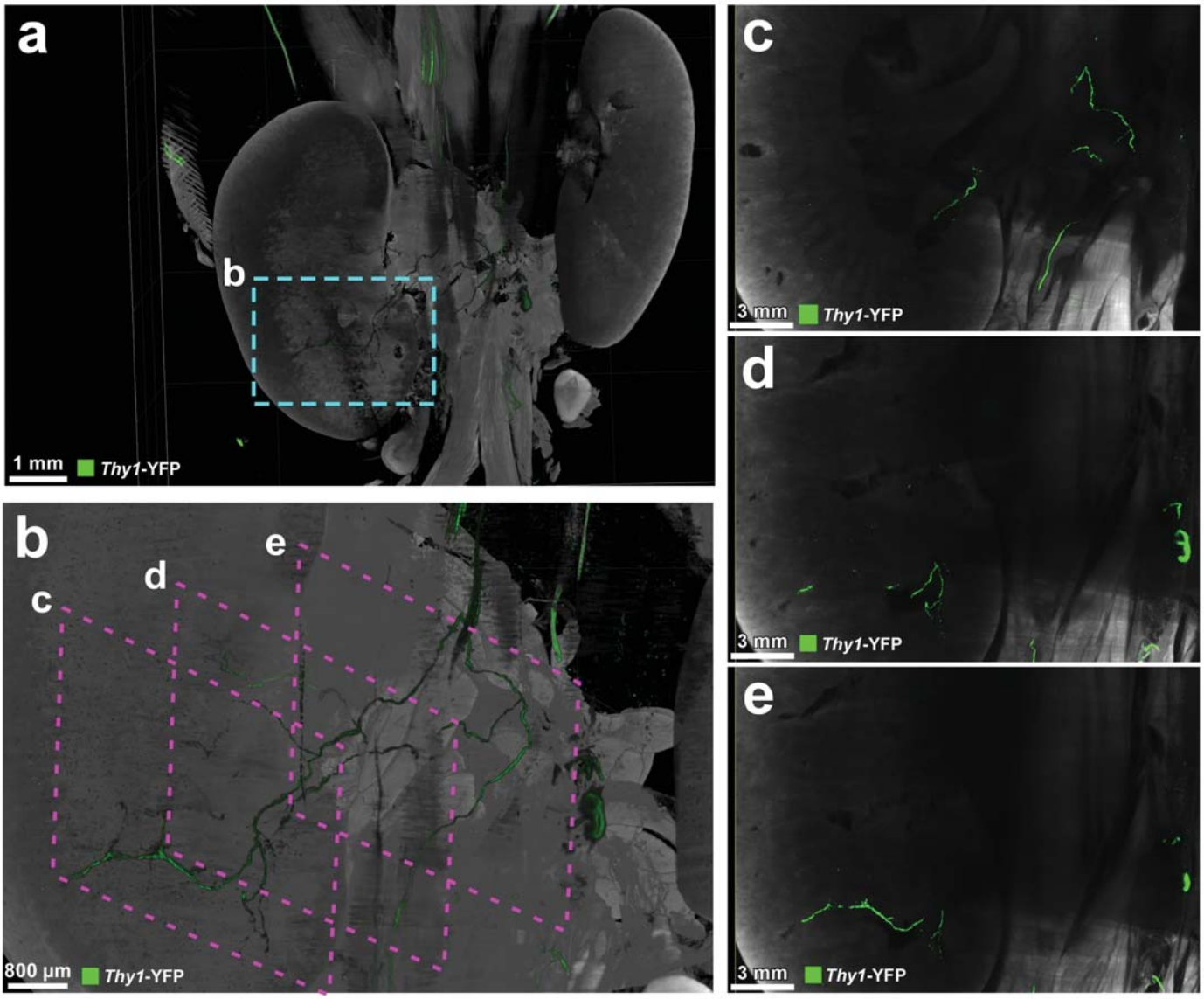


# Supplementary Figure 15

**Peripheral nerves innervating kidneys in *Thy1*-YFPH mouse**

(**a**) 3D visualization of nerves innervating the kidneys of a 7 months old *Thy1*-YFPH animal. (**b**) Zoom image from the marked region in **a**. (**c**-**e**) 2D projection images of the kidney at the indicated depths in **b**. Single experiment.

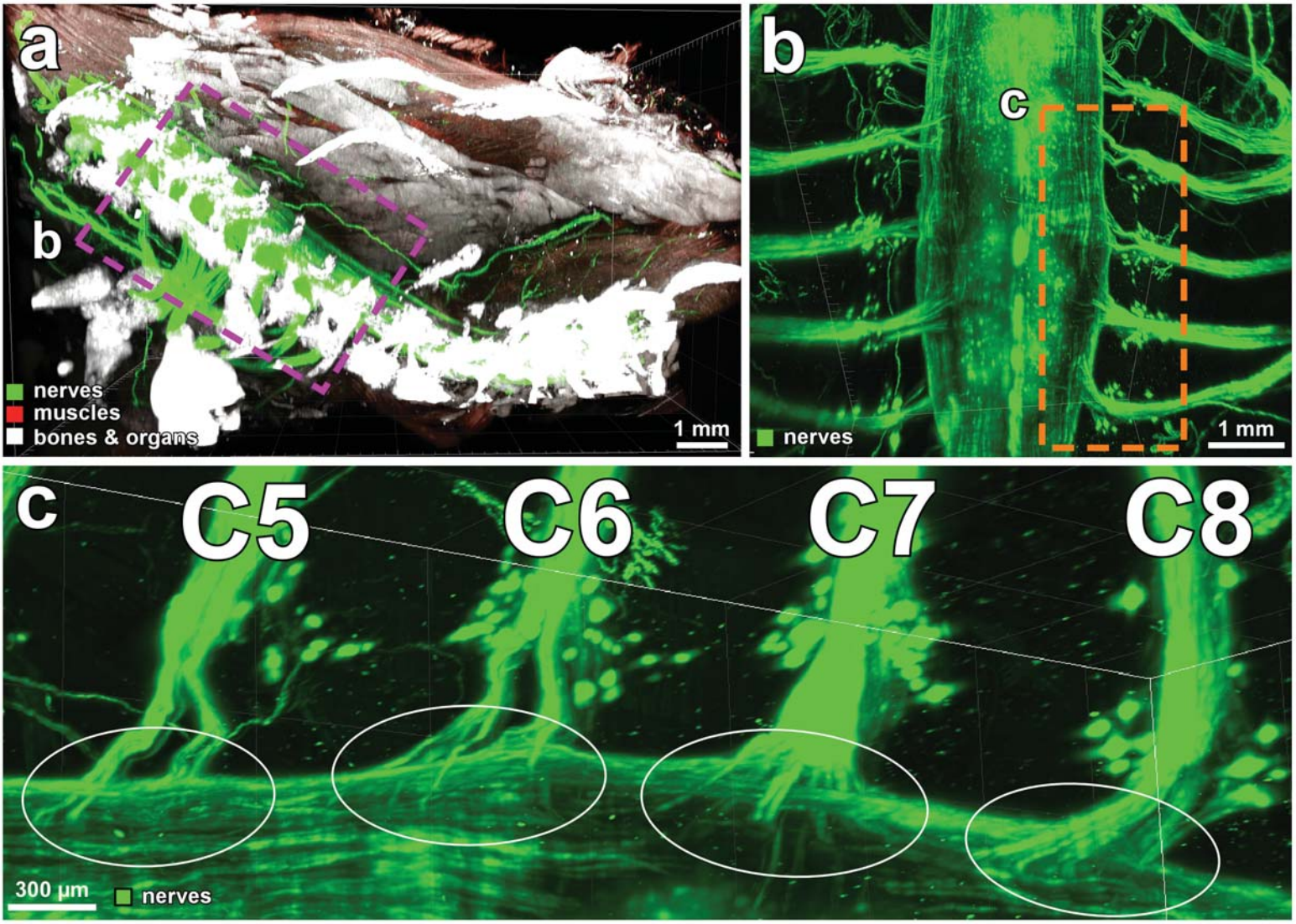


# Supplementary Figure 16

**Upper torso and individual spinal cord roots**

(**a**) Panoptic imaging of the upper torso of the 6 weeks old transparent mouse showing individual spinal cord roots. The bones and organs are in white, mostly the muscles are visible in autofluorescence channel and displayed in red, and the nerves are in green. (**b**) High magnification view from the region indicated in **a** showing only nerve signal (ventral roots). (**c**) High magnification view from the region indicated in **b** demonstrating non-overlapping entry of axons in C5-C8 ventral spinal cord segments (white circles). Comparable labeling and imaging results were achieved in 5 independent animals.

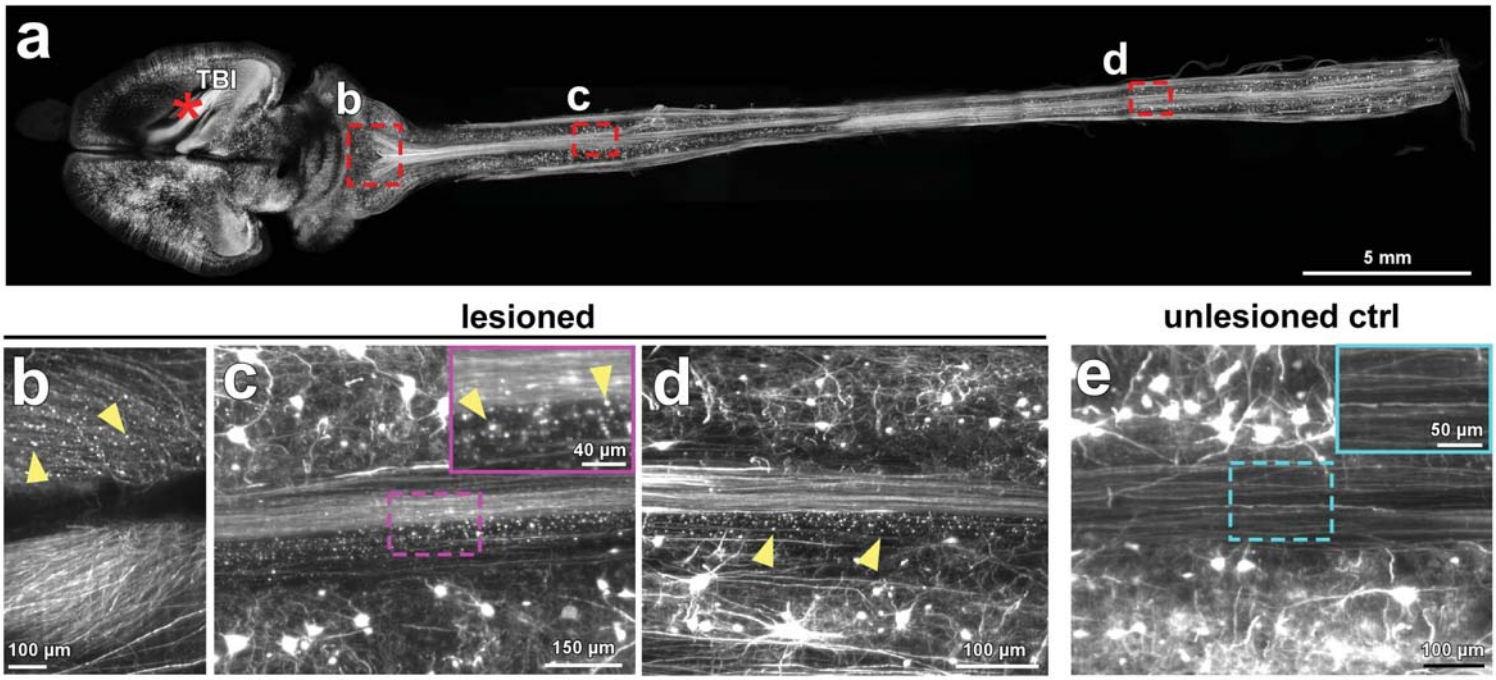


# Supplementary Figure 17

**TBI induces the degeneration of descending motor axons in the central nervous system**

(**a**) To investigate a potential degeneration of the descending motor axons upon TBI, we applied vDISCO on the intact CNS (brain and spinal cord) from *Thy1*-GFPM mice already 1 week after TBI. (**b-d**) High magnification images coming from the indicated spinal cord regions marked in a. The fragmentation (yellow arrow-heads) of the descending motor axons ipsilaterally in the brainstem before the decussation (**b**), and contra-laterally after decussation is evident throughout the spinal cord (**c,d**). (**e**) An unlesioned spinal cord view at the same region shown in the lesioned animal in d. Similar results were observed from 2 independent animals.

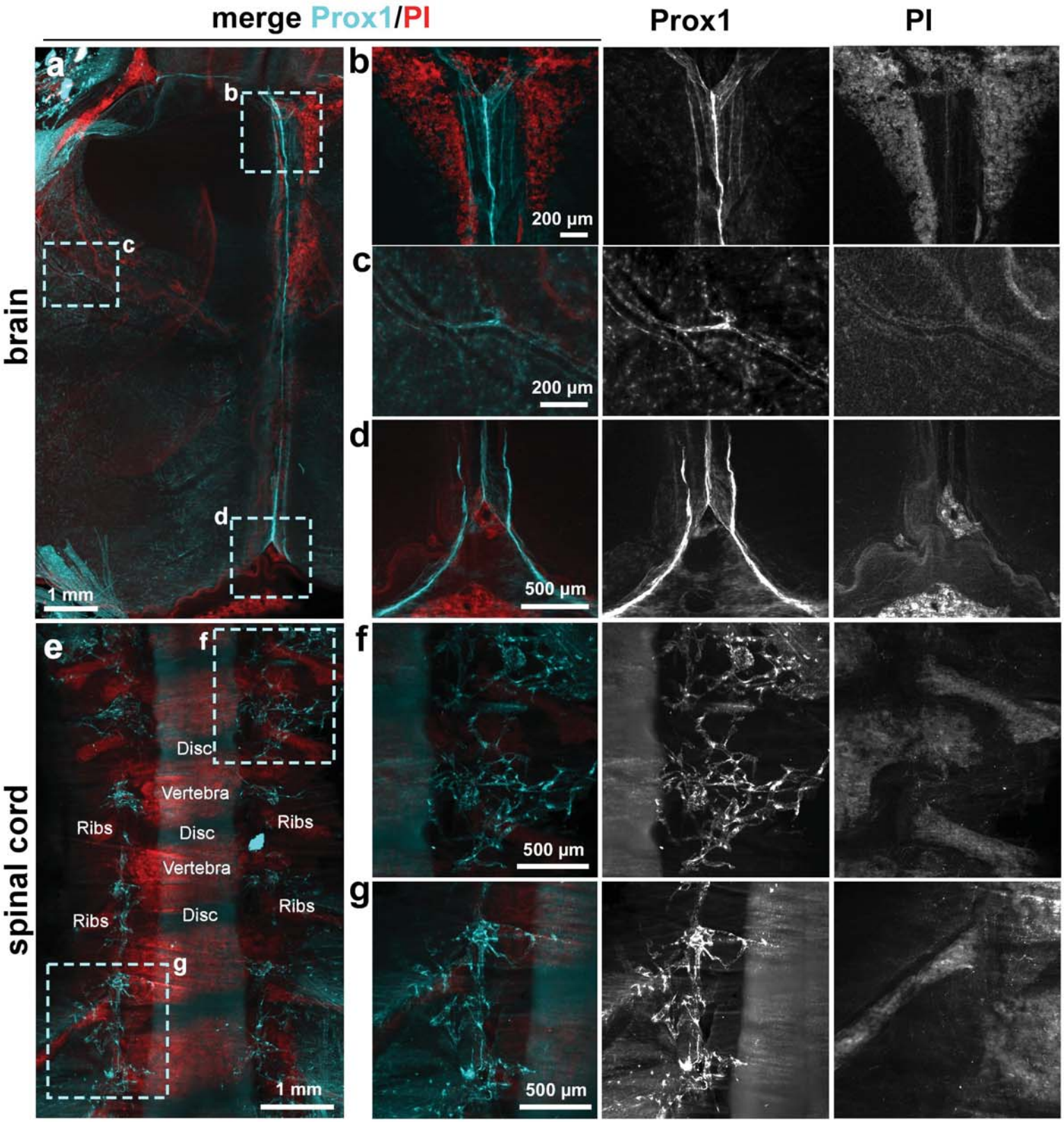


# Supplementary Figure 18

**Meningeal lymphatic vessels through transparent skull and vertebra by vDISCO**

After applying vDISCO pipeline, the 4 weeks old *Prox1*-EGFP mouse was imaged with light-sheet microscopy. Prox1 and PI channels are shown in merge and separate views. (**a-d**) *Prox1*-EGFP mouse head showing the brain lymphatic vessels (cyan) along the sagittal sinus (**b**), pterygopalatine artery (**c**) and transverse sinus (**d**) (similar results were observe from 5 independent mice). (**e-g**) Images from the thoracic region of the spine show the lymphatic vessels (cyan) in the spine region (single experiment).

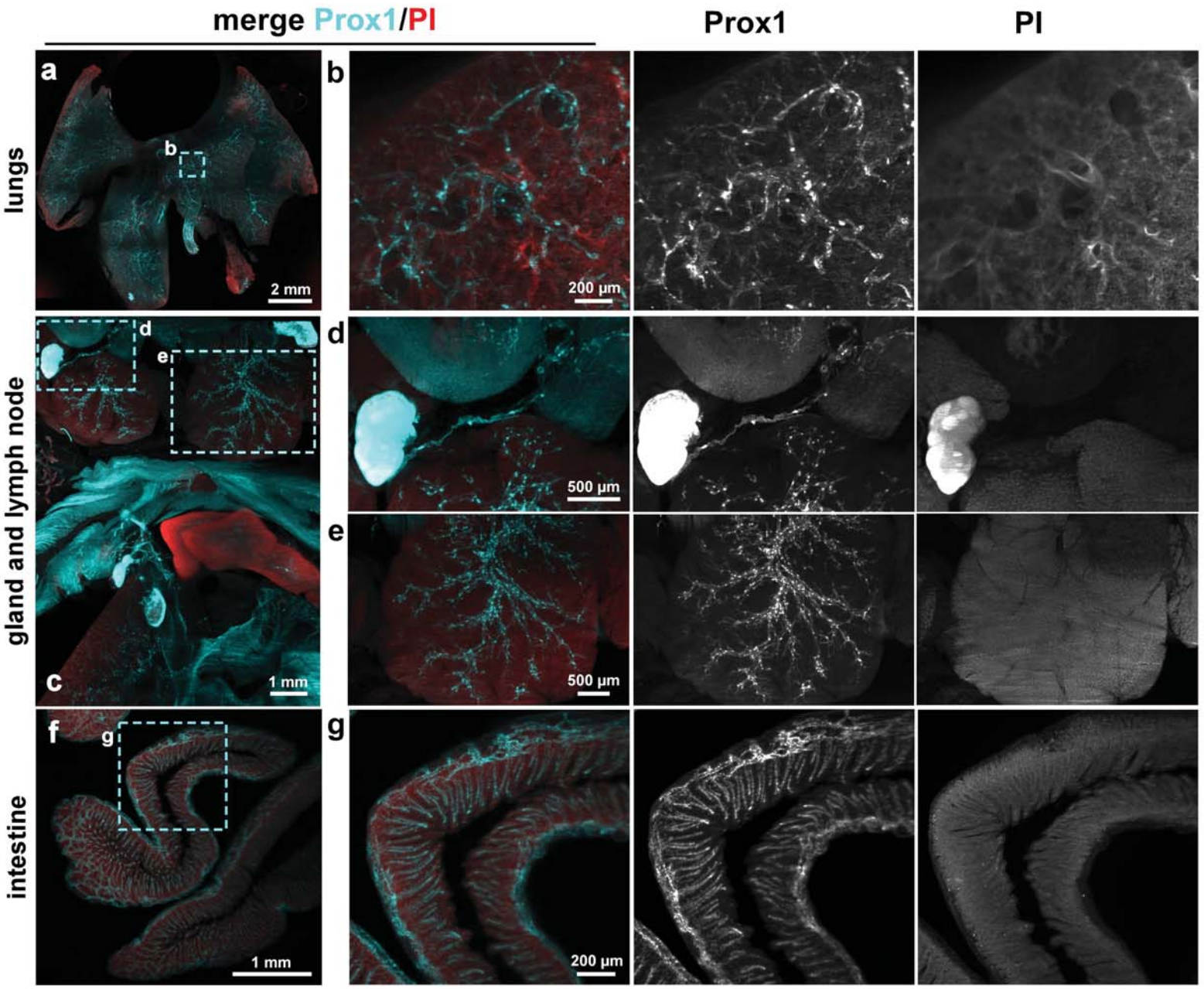


# Supplementary Figure 19

**Lymphatic vessels in internal organs by vDISCO**

After applying vDISCO pipeline, the 4 weeks old *Prox1*-EGFP mouse was imaged with light-sheet microscope (single experiment). Prox1 and PI channels are shown in merge and separate views. The lymphatic vessels (cyan) in lungs (**a-b**), in cervical lymph node (**c**,**d**), in salivery gland (**c**,**e**) and in intestine (**f**,**g**) are evident. See also Supplementary Video 6.

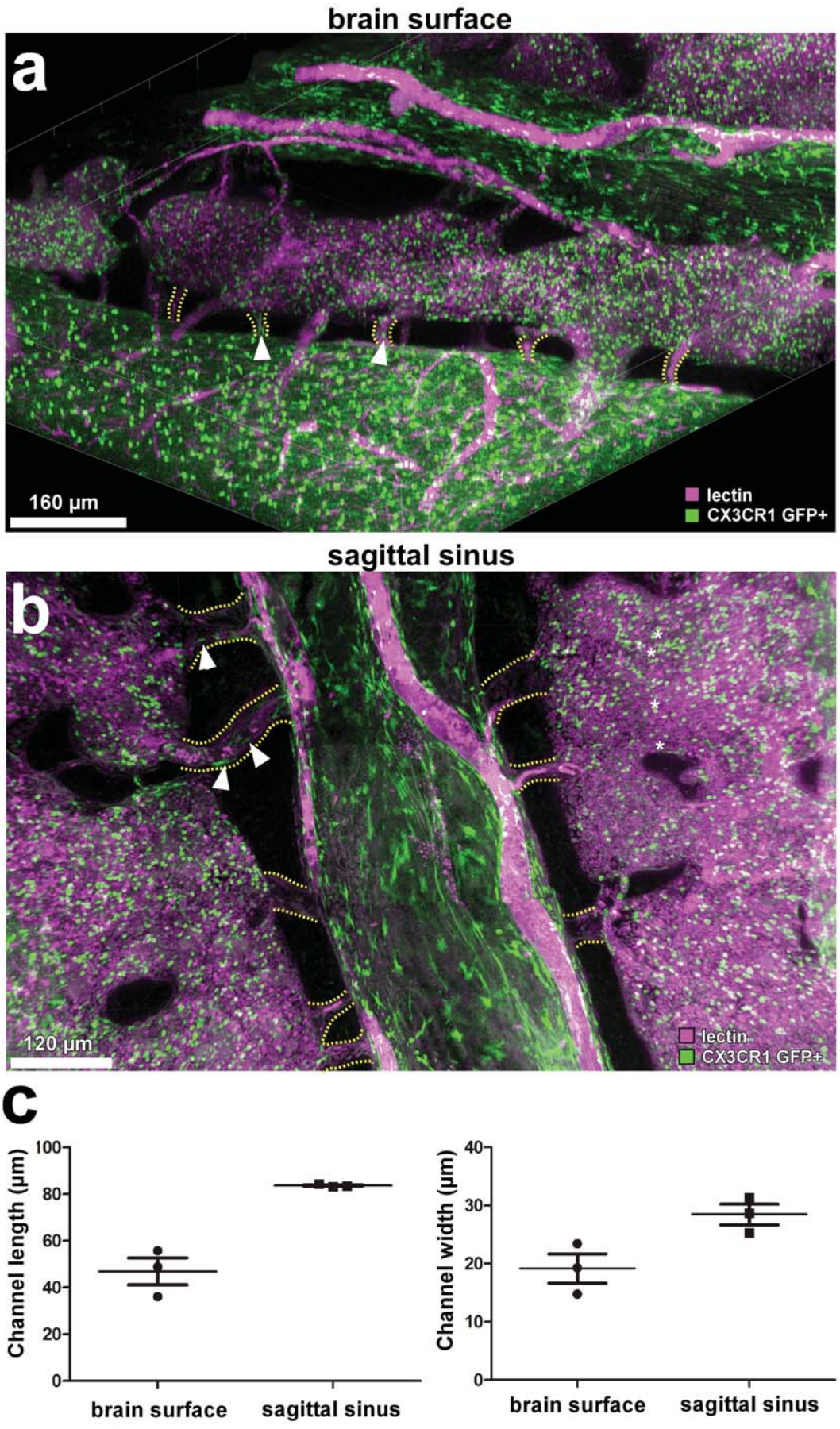


# Supplementary Figure 20

**Structural features of short skull-meninges connections (SMCs)**

(**a**,**b**) 3D confocal images of brain-skull interface. A 4 months old CX3CR1$^{GFP/+}$ mouse (CX3CR1 GFP+ cells in green) was injected with lectin dye (magenta). Vascular connections between the skull marrow and meninges at the brain surface (**a**) and sagittal sinus (**b**) are visible, including the CX3CR1 GFP+ cells (white-arrow heads) in the connections (similar results were observed from 3 independent mice). See also Supplementary Video 9. (**c**) Quantifications of length and width of the SMCs at sagittal sinus and brain surface (mean ± SEM; n=3 animals per group).

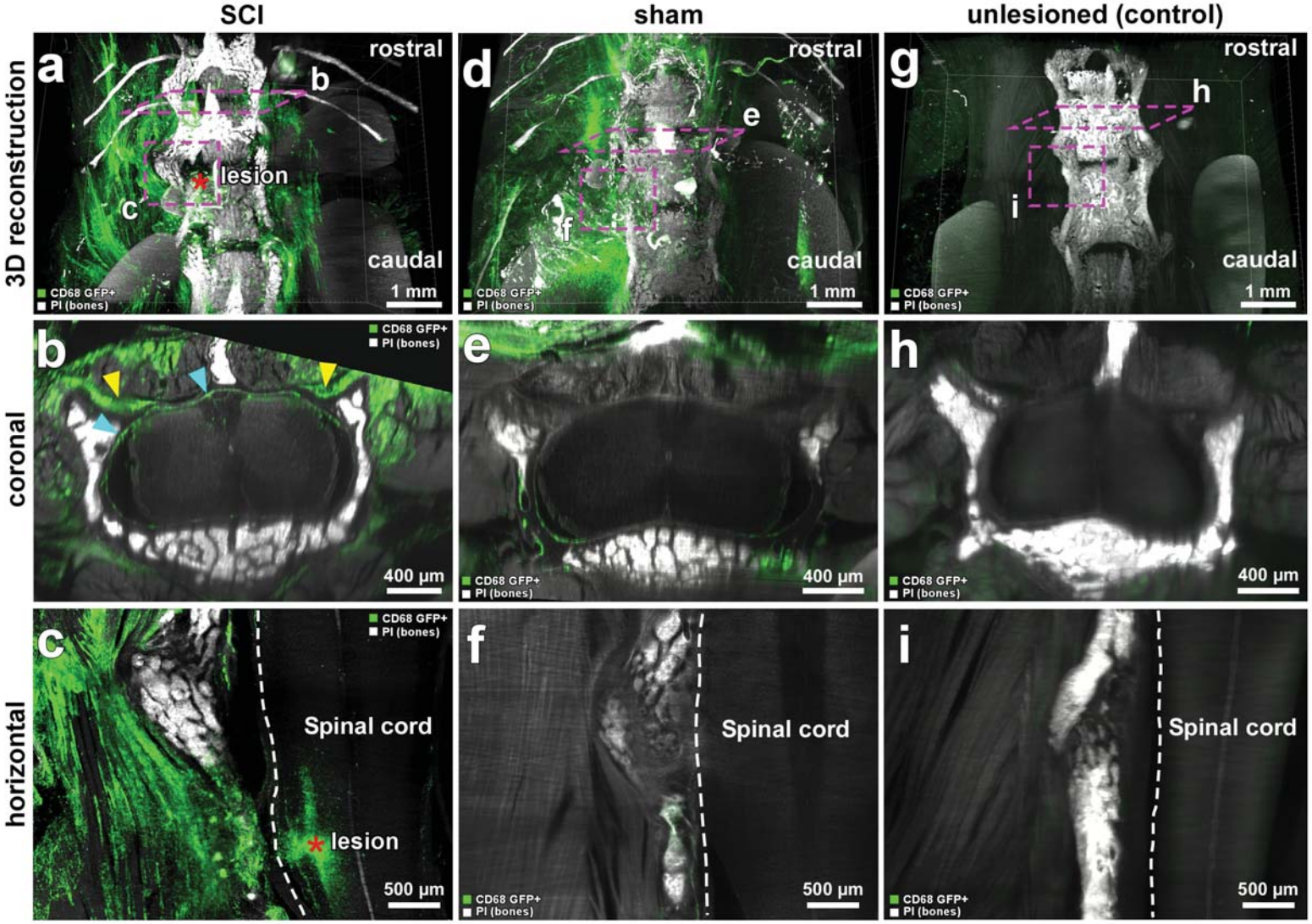


# Supplementary Figure 21

**Immune cell activation and invasion induced by spinal cord injury**

3D visualization of spinal cord from 3 months old *CD68*-EGFP transgenic mice with spinal cord injury (**a**-**c**) compared to mice with sham surgery (**d**-**f**) and unlesioned controls (**g**-**i**). CD68 GFP+ cells are shown in green and PI labeled bones in white. Red asterisks indicate the lesion site. Increased CD68 GFP+ cells throughout the muscles, spinal cord roots (yellow arrow-heads) and meninges (cyan arrow-heads) are evident in the injured spinal cord (**a**-**c**) compared to the controls (**g**-**i**). In the group with sham surgery, the CD68 GFP+ cells increased in the muscles but not in the spinal cord (similar results were observed from 3 independent mice per group). See also Supplementary Video 11.

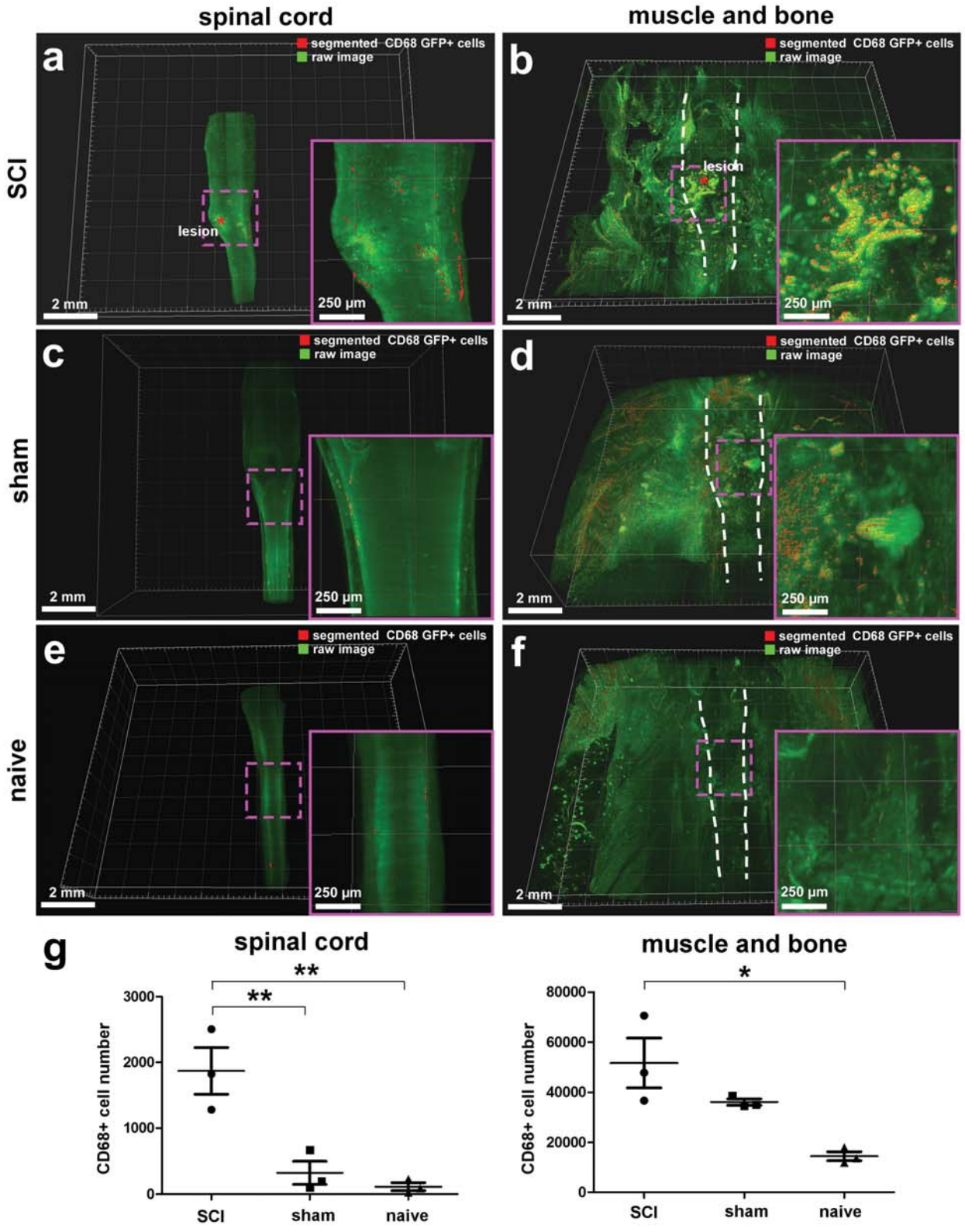


# Supplementary Figure 22

**CD68 GFP+ cell number increased significantly both in spinal cord and peripheral tissues after spinal cord injury (SCI)**

(**a**-**f**) 3D visualization of the spine region from 3 months old *CD68*-EGFP mice with SCI (**a**,**b**) vs. mice with sham surgery (**c**,**d**) and naive mice (**e**,**f**) cleared by vDISCO and imaged by light-sheet microscope. To better visualize the region, spinal cords (**a**,**c** and **e**) were segmented out from their locations in the surrounding tissues (muscle and bone) (**b**,**d** and **f**) using Fiji and afterwards CD68 GFP+ cells were segmented (red) and quantified by IMARIS (similar results were observed from 3 independent mice per group). (**g**) Quantification of CD68 GFP+ cells in spinal cord showing significant cell number increase after SCI compared to sham and naive animals. While CD68 GFP+ cell number increased significantly in surrounding tissue (muscle and bone) in SCI group compared to naive animals (mean ± SEM; n=3 animals per group; statistical significance (for spinal cord, $F_{2,6}$=17.22, SCI vs. sham ***p*=0.0077, SCI vs. naive ***p*=0.0041 and sham vs. naive ns=0.8049. For muscle and bone, $F_{2,6}$=10.05, SCI vs. sham ns=0.2273, SCI vs. naive **p*=0.0101 and sham vs. naive ns=0.0905) was assessed by one-way ANOVA followed by Tukey multiple comparison Test).

## DISSECTED ORGANS

steps

| tissue type / passive incubation (with shaking) | whole organs such as brain, heart or spleen | soft and porous organs such as gut, lungs or thymus | small organs such as adrenal glands, lymphnodes, organoids or 1 mm slices |
|---|---|---|---|
| pretreatment with permeabilization solution at 37°C | 1-2 days | overnight | 6 hours |
| incubation with immunostaining solution at 37°C | 10-14 days | 4-5 days | 3-4 days |
| washing with washing solution at room temperature | 2 hours x 4 times (optionally last step overnight) | 1.5 hours x 4 times | 1 hour x 4 times |
| PBS washing at room temperature | 2 hours x 4 times | 1.5 hours x 4 times | 1 hour x 4 times |
| DISCO clearing | | | |
| 50% THF at room temperature | 1-2 hours | 1 hour | 1 hour |
| 70% THF at room temperature | 1-2 hours | 1 hour | 1 hour |
| 80% THF at room temperature | 1-2 hours | 1 hour | 1 hour |
| 100% THF at room temperature | 1 hour and overnight | 1 hour and overnight | 1 hour and 5 hours |
| 100% DCM at room temperature | 1 hour | 45 minutes | 30 minutes |
| BABB at room temperature | overnight | > 6 hours | > 4 hours |
| cost per sample | ~25-30 $ | ~15-20 $ | ~6-8 $ |
| imaging time (light-sheet microscopy) | ~1.5-3 hours | ~3-6 hours | ~0.5-1.5 hours |

## WHOLE BODY

steps

| | modality | timing | temperature |
|---|---|---|---|
| PBS washing | active perfusion | overnight | at room temperature |
| decolorization with 25% CUBIC#1 in PBS | active perfusion | 12 hours x 4 times | at room temperature |
| PBS washing | active perfusion | 3 hours x 3 times | at room temperature |
| decalcification with 10% of EDTA in PBS pH8-9 | active perfusion | 2 days | at room temperature |
| PBS washing | active perfusion | 3 hours x 3 times | at room temperature |
| pretreatment with permeabilization solution | active perfusion | 12 hours | at room temperature |
| boosting with immunostaining solution | active perfusion | 6 days | with infrared lamp (up to 30°C) |
| boosting with immunostaining solution | passive shaking | 2 days | at 37°C |
| wash with washing solution | active perfusion | 3 hours x 3 times | at room temperature |
| PBS washing | active perfusion | 3 hours x 3 times | at room temperature |
| DISCO clearing | | | |
| 50% THF in distilled water | passive shaking | 12 hours | at room temperature |
| 70% THF in distilled water | passive shaking | 12 hours | at room temperature |
| 80% THF in distilled water | passive shaking | 12 hours | at room temperature |
| 100% THF | passive shaking | 12 hours x 2 times | at room temperature |
| 100% DCM | passive shaking | 3 hours | at room temperature |
| BABB | passive shaking | > 12 hours | at room temperature |
| cost per animal | ~180-200 $ | | |
| imaging time (light-sheet microscopy) | ~3-5 days | | |

**permeabilization solution**: 1.5% goat serum , 0.5% Triton X-100, 0.5 mM Methyl-beta-cyclodextrin, 0.2% trans-1-Acetyl-4-hydroxy-L-proline, 0.05% Sodium Azide in 0.1 M PBS

**washing solution**: 1.5% goat serum , 0.5% Triton X-100, 0.05% Sodium Azide in 0.1 M PBS

**immunostaining solution**: permeabilization solution + nanobooster

**THF**: tetrahydrofuran
**DCM** : dichloromethane
**BABB**: benzyl alcohol + benzyl benzoate (1:2) in volume
**CUBIC#1**: 25 wt% urea , 25 wt% N,N,N´,N´-tetrakis (2-hydroxypropyl)ethylenediamine, 15 wt% Triton X-100 in 0.1 M PBS

# Supplementary Table 1

### Notes for vDISCO protocol

The timing for each experimental step can be shortened or extended based on tissue size to improve nanobooster penetration or clearing performance. We found that active (perfusion mediated) whole-body boosting provides more homogeneous and even nanobooster staining compared to passive staining of dissected organs e.g. the brain, if the perfusion is done properly. The costs were estimated only based on the reagents and considering organs from transgenic mouse lines that highly express GFP, such as *Thy1*-GFPM. If other lines (which express less GFP) are used, the amount of nanobooster needed for the protocol can be reduced and the cost might reduce significantly as well. The imaging time has been estimated considering the imaging only with one channel using the Ultramicroscope II (LaVision BioTec) with a 4x objective and it can significantly vary based on many factors: z-step, magnification, different microscope version etc. More information available at www.discotechnologies.org/vDISCO.

| FIGURES | | SYSTEM | OBJECTIVE SPECIFICATIONS | | | | | ACQUISITION PARAMETERS | | | DATA SIZE |
|---|---|---|---|---|---|---|---|---|---|---|---|
| | | | Magnification | NA | RI | WD | Zoom | Image pixel size | z-step | type | |
| **Figures** | | | | | | | | | | | |
| 1 | a-f | UM II | 4X corr. | 0.28 | 1.56 | 10mm | | 1.625µmx1.625µm | 4µm | single slice | (a)24.8GB, (e)34.7GB |
| | g,h | UM II | 4X corr. | 0.28 | 1.56 | 10mm | | 1.625µmx1.625µm | (i)8µm, (j)12µm | single slice | (i)29.5GB, (j)9.90GB |
| | i | UM II | 4X corr. | 0.28 | 1.56 | 10mm | | 1.625µmx1.625µm | 4-12µm | quantification on single slice | 67GB |
| | j,l,n | UM II | 4X corr. | 0.28 | 1.56 | 10mm | | 1.625µmx1.625µm | 8-10 µm | single slice | (j,l)12.8GB, (n)6.94GB |
| | k,m | UM II | Oly. 25X | 0.95 | 1.31-1.52 | 4mm | | 0.26µmx0.26µm | 4µm | single slice | (m)1.37GB, (o)222MB |
| | o | UM II | 4X corr. | 0.28 | 1.56 | 10mm | | 1.625µmx1.625µm | 8µm | single slice | 456GB |
| 2 | b-d | UM II -MVX10 | Oly. 1X | 0.25 | 1.0 | 65mm | 0.63x | 10.32µmx10.32µm | 8µm | 3D reconstruction | 3.27TB |
| | f-i | UM II -MVX10 | Oly. 2X | 0.5 | 1.33/1.56 | 6mm | 1.6x | 2.03µmx2.03µm | 6µm | 3D reconstruction | 1.5TB |
| 3 | d | UM II | 4X corr. | 0.28 | 1.56 | 10mm | | 1.625µmx1.625µm | 8µm | 3D reconstruction | 140GB |
| | e,g | LSM880 | Leica 25x | 0.95 | 1.33 | 2.5mm | | 0.67µmx0.67µm | 4µm | (e) 3D reconstr., (g) single slice | 3.89GB |
| | f,h | LSM880 | Leica 25x | 0.95 | 1.33 | 2.5mm | | 0.67µmx0.67µm | 4µm | 96µm thick projection | same data from Fig.6e,g |
| | j | UM II -MVX10 | Oly. 2X | 0.5 | 1.33/1.56 | 6mm | 0.8x | 4.06µmx4.06µm | 8µm | 1440µm thick projection | 117GB |
| | k | LSM880 | Leica 25x | 0.95 | 1.33 | 2.5mm | | 0.4µmx0.4µm | 2.50 µm | 180µm thick projection | 2.45GB |
| 4 | a-d | UM II -MVX10 | Oly. 1X | 0.25 | 1.0 | 65mm | (a,c)1.25x, (b,d)0.63x | (a,c)5.2µmx5.2µm, (b,d)10.32µmx10.32µm | 8µm | entire scan projection | (a,c)52.2GB, (b,d)16.8GB |
| | c,d (yellow, green rectangles) | UM II | Zeiss 20x | 1 | 1.45 | 5.6mm | | 0.325µmx0.325µm | 2µm | (c)824µm, (d)430µm thick projections | (c)64.8GB, (d)62.7GB |
| | e | UM II -MVX10 | Oly. 2X | 0.5 | 1.33/1.56 | 6mm | 2.5x | 1.3µmx1.3µm | 8µm | quantification entire scan projection | 1TB |
| 5 | b | UM II -MVX10 | Oly. 2X | 0.5 | 1.33/1.56 | 6mm | 1x | 3.25µmx3.25µm | 8µm | 1.6mm thick projection | 105GB |
| | c-e | UM II -MVX10 | Oly. 2X | 0.5 | 1.33/1.56 | 6mm | 2x | 1.625µmx1.625µm | 10µm | (c)600µm, (d) 500µm, (e)400µm thick projections | (c,e) 42.5GB, (d) 28.4GB |
| | f | UM II -MVX10 | Oly. 2X | 0.5 | 1.33/1.56 | 6mm | 2x | 1.625µmx1.625µm | 7µm | 3D reconstruction | 87GB |
| | g,h | UM II | Zeiss 20x | 1 | 1.45 | 5.6mm | | 0.325µmx0.325µm | 3µm | 15µm thick projections | 552GB |
| | i,j | UM II -MVX10 | Oly. 2X | 0.5 | 1.33/1.56 | 6mm | 2x | 1.625µmx1.625µm | 10µm | single slices | (i)102GB, (j)86.5GB |
| 6 | a | UM II | 4X corr. | 0.28 | 1.56 | 10mm | 2x | 0.8µmx0.8µm | 6µm | 3D reconstruction | 5.8GB |
| | b-d | UM II -MVX10 | Oly. 1X | 0.25 | 1.0 | 65mm | 3.2x | 2µmx2µm | 8µm | 80µm thick projections | 5.5GB |
| | e,f | UM II -MVX10 | Oly. 1X | 0.25 | 1.0 | 65mm | 0.63x | 8µmx8µm | 3µm | single slices | 77.9GB |
| | g,h | UM II -MVX10 | Oly. 2X | 0.5 | 1.33/1.56 | 6mm | 1.6x | 2µmx2µm | 8µm | 40µm thick projections | (g)349GB, (h)550GB |
| | i | UM II -MVX10 | Oly. 2X | 0.5 | 1.33/1.56 | 6mm | 1.6x | 2µmx2µm | 8µm | quantification 40µm projection | 1.38 TB for 6 samples |
| **Sup. Figures** | | | | | | | | | | | |
| S1 | a | UM II -MVX10 | Oly. 1X | 0.25 | 1.0 | 65mm | 1x | 6.5µmx6.5µm | 10µm | single slice | 9.37GB |
| S2 | a-f | UM II | 4X corr. | 0.28 | 1.56 | 10mm | | 1.625µmx1.625µm | 10-12 µm | 40-48µm thick projection | (a,b,c)30.2GB, (d,e,f) 31.7 GB |
| | g | UM II | 4X corr. | 0.28 | 1.56 | 10mm | | 1.625µmx1.625µm | 8-16 µm | quantification single slide | 71.31GB |
| S3 | a-d | AxioZoom | Zeiss 1X | 0.25 | 1.0 | 56mm | | (a,b)1.14µmx1.14µm, (c,d) 1.82µmx1.82µm | n.a. | single slice | 5.46MB x 4= 21.84MB |
| | e,f | UM II | 4X corr. | 0.28 | 1.56 | 10mm | | 1.625µmx1.625µm | 10µm | 50µm thick projection | (e)43.01GB, (f)5.93GB |
| | g-i | UM II | 4X corr. | 0.28 | 1.56 | 10mm | | 1.625µmx1.625µm | 10µm | quantification single slice | same data from Fig.S3e,f |
| S4 | a-e | UM II | Zeiss 20x | 1 | 1.45 | 5.6mm | | 0.325µmx0.325µm | 2µm | 800 µm thick projection, 3D reconstr. | 193.1GB |
| S5 | | UM II | Zeiss 20x | 1 | 1.45 | 5.6mm | | 0.325µmx0.325µm | 2µm | 800 µm thick projection, 3D reconstr. | same data as Fig.S4 |
| S6 | a-c | UM II | 4X corr. | 0.28 | 1.56 | 10mm | | 1.625µmx1.625µm | 4µm | 3D reconstr. 8µm, thick projection | 2.1GB |
| S7 | a,h-k | UM II | 4X corr. | 0.28 | 1.56 | 10mm | | 1.625µmx1.625µm | 10µm | | 118.1 GB |
| | d,g | UM II | 4X corr. | 0.28 | 1.56 | 10mm | | 1.625µmx1.625µm | 3µm | single slice | 32 GB |
| S9 | c | AxioZoom | Zeiss 1X | 0.25 | 1.0 | 56mm | | 6.49µmx6.49µm, zoom in 0.405µmx0.405µm | n.a. | single slice | 106MB |
| S11 | c-j | UM II -MVX10 | Oly. 2X | 0.5 | 1.33/1.56 | 6mm | 0.63x | 5.16µmx5.16µm | 8-20µm | quantification on single slice | 117.1GB |
| S12 | c-g | UM II | 4X corr. | 0.28 | 1.56 | 10mm | | 1.625µmx1.625µm | 8µm | single slices | 10-50GB for each sample |
| S13 | b-g | UM II -MVX10 | Oly. 2X | 0.5 | 1.33/1.56 | 6mm | 4x | 0.81µmx0.81µm | 6µm | single slice | 10.6GB |
| | h-j | LSM880 | Leica 25x | 0.95 | 1.33 | 2.5mm | | 0.10µmx0.10µm | 2.5µm | single slice | 120MB |
| S14 | a-i | UM II -MVX10 | Oly. 1X | 0.25 | 1 | 65mm | 0.63x | 10.32µmx10.32µm | 8µm | 3D reconstruction | same data from Fig. 2b-d |
| S15 | a-e | UM II -MVX10 | Oly. 1X | 0.25 | 1 | 65mm | 1x | 6.5µmx6.5µm | 10µm | 3D reconstruction | 24GB |
| S16 | a-c | UM II -MVX10 | Oly. 2X | 0.5 | 1.33/1.56 | 6mm | 1.25x | 2.6µmx2.6µm | 4µm | 3D reconstruction | 39GB |
| S17 | a | UM II | 4X corr. | 0.28 | 1.56 | 10mm | | 1.625µmx1.625µm | 8µm | entire scan projection | 57.8GB |
| | b-d | UM II | 4X corr. | 0.28 | 1.56 | 10mm | | 1.625µmx1.625µm | 8µm | 80µm thick projection | same data from Fig S17a |
| | e | UM II | 4X corr. | 0.29 | 1.57 | 10mm | | 1.625µmx1.625µm | 8µm | 80µm thick projection | 42.1 GB |
| S18 | a | UM II -MVX10 | Oly. 2X | 0.5 | 1.33/1.56 | 6mm | 1x | 3.25µmx3.25µm | 8µm | 1.6mm thick projection | same data from Fig. 5b |
| | b-d | UM II -MVX10 | Oly. 2X | 0.5 | 1.33/1.56 | 6mm | 2x | 1.625µmx1.625µm | 10µm | (b)600µm, (c) 500µm, (d)400µm thick projections | same data from Fig. 5c-e |
| | e-g | UM II -MVX10 | Oly. 2X | 0.5 | 1.33/1.56 | 6mm | 2x | 1.625µmx1.625µm | 6µm | 1.6mm thick projection | 61GB |
| S19 | a,b | UM II | 4X corr. | 0.29 | 1.57 | 10mm | | 1.625µmx1.625µm | 8µm | (a) 1.92mm, (b)640µm thick projections | 474GB |
| | c-e | UM II -MVX10 | Oly. 1X | 0.25 | 1 | 65mm | 2x | 3.25µmx3.25µm | 10µm | 800 µm thick projections | 103GB |
| | f-g | UM II -MVX10 | Oly. 1X | 0.25 | 1 | 65mm | 3.2x | 2µmx2µm | 8µm | 240µm thick projections | 18GB |
| S20 | a,b | LSM880 | Zeiss 40X | 1.3 | 1.518 | 0.21mm | 1x | 0.21µmx0.21µm | 4µm | 3D reconstruction | 13GB |
| S21 | a,d,g | UM II -MVX10 | Oly. 2X | 0.5 | 1.33/1.56 | 6mm | 1.6x | 2µmx2µm | 6µm | 3D reconstructions | (a)232GB, (d)114GB, (g)199GB |
| | b,e,h | UM II -MVX10 | Oly. 2X | 0.5 | 1.33/1.56 | 6mm | 1.6x | 2µmx2µm | 6µm | 30µm thick projections | (b)232GB, (e)114GB, (h)199GB |
| | c,f,i | UM II -MVX10 | Oly. 2X | 0.5 | 1.33/1.56 | 6mm | 1.6x | 2µmx2µm | 6µm | single slices | (c)232GB, (f)114GB, (i)199GB |
| S22 | a,b | UM II -MVX10 | Oly. 2X | 0.5 | 1.33/1.56 | 6mm | 1.6x | 2µmx2µm | 6µm | 3D reconstructions | 18GB |
| | c,d | UM II -MVX10 | Oly. 2X | 0.5 | 1.33/1.56 | 6mm | 1.6x | 2µmx2µm | 6µm | 3D reconstructions | 62GB |
| | e,f | UM II -MVX10 | Oly. 2X | 0.5 | 1.33/1.56 | 6mm | 1.6x | 2µmx2µm | 6µm | 3D reconstructions | 73GB |
| | g | UM II -MVX10 | Oly. 2X | 0.5 | 1.33/1.56 | 6mm | 1.6x | 2µmx2µm | 6µm | quantification on 3d reconstructions | 3.35TB for 9 samples |

**Legend of abbreviations**

Imaging Systems

| | |
|---|---|
| UM II | LaVision BioTec - UltraMicroscope II |
| UM II -MVX10 | LaVision BioTec - UltramicroscopeM II -MVX10 |
| LSM880 | Zeiss confocal LSM880 with Airyscan |
| AxioZoom | Zeiss AxioZoom EMS3/SyCoP3 |

| | |
|---|---|
| NA | Numerical aperture |
| RI | Refractive Index |
| WD | Working distance |
| n.a. | not applicable |

Objectives

| | |
|---|---|
| Oly. 1X | Olympus MV PLAPO 1x/0.25 NA |
| Oly. 2X | Olympus MVPLAPO2XC |
| 4X corr. | Olympus XLFLUOR4x corrected |
| Oly. 25X | Olympus XLPLN25X |
| Zeiss 20X | Zeiss Clr Plan-Neofluar 20x |
| Zeiss 40X | Zeiss ECPlan-NeoFluar 40x/1.30 Oil DIC M27 |
| Leica 25X | Leica HCX IRAPO L 25x |

# Supplementary Table 2

## Imaging specifications

## SUPPLEMENTARY VIDEO LEGENDS

### Supplementary Video 1
### vDISCO reveals individual microglia in CX3CR1$^{GFP/+}$ mouse brain

3D brain reconstruction of a vDISCO boosted CX3CR1$^{GFP/+}$ mouse brain, in which microglia express GFP, imaged with 4x objective by light-sheet microscopy. After vDISCO, all labelled microglia became evident, allowing quantification of their numbers in each brain region and assessment of the details of the microglia ramifications. Similar results were observed in 2 independent animals.

### Supplementary Video 2
### vDISCO reveals whole body neuronal projections in *Thy1*-GFPM mouse

3D reconstruction of neuronal projections in a *Thy1*-GFPM mouse scanned by light-sheet microscopy. The muscles (red) are visualized in autofluorescent channel (blue-green spectra). The bones and internal organs (white) are prominent with PI labeling. The GFP expressing neurons are boosted with nanobody conjugated with Atto 647N and imaged in far-red channel. The overall view of the entire labeled nervous system in the *Thy1*-GFPM mouse and fine details of neuronal connections are evident throughout the whole body. Comparable labeling and imaging results were achieved in 5 independent animals, whole body reconstruction was done in 2 mice.

### Supplementary Video 3
### Neuronal projections from spinal cord to right forelimb in *Thy1*-GFPM mouse

3D visualization obtained by light-sheet microscopy of neuronal projections from spinal cord to right forelimb of a *Thy1*-GFPM mouse. The muscles are shown in red, bones in white and the neurons in green. The fine details of axonal extensions and their endings at neuromuscular junctions are visible. Similar results were observed in 2 independent animals.

### Supplementary Video 4
### vDISCO imaging of neuronal projections in the spinal cord and muscles

The first part of the video is the 2D orthoslicing of the spinal cord of an intact *Thy*1-GFPM mouse in dorso-ventral orientation. The muscles are shown in red, bones in white and the neurons in green. The details of neuronal cell bodies in ganglia embedded in the spinal cord vertebra and their axonal extensions into the CNS and PNS are visible. In the second part, neuronal connections (green) from spinal cord to muscles are shown in 3D and 2D. Similar results were observed in 2 independent animals.

### Supplementary Video 5
### vDISCO imaging of CX3CR1$^{GFP/+}$ mouse with intact skin

The first part of the video is the 3D reconstruction of the inguinal area from a CX3CR1$^{GFP/+}$ mouse cleared with intact skin, showing inguinal lymph nodes and surrounding tissues (skin

and muscles). CX3CR1 GFP+ immune cells are shown in cyan and cell nuclei labeled by PI are shown in magenta. The second part is the 2D orthoslicing visualization of a confocal scan of the same area, showing the subcellular details of CX3CR1 GFP+ cells in the lymph node and around the hair follicles. Similar results were observed in 2 independent animals.

**Supplementary Video 6**
**vDISCO reveals lymphatic vessels of different organs in *Prox1*-EGFP mouse**
After applying vDISCO whole-body labeling of a *Prox1*-EGFP line mouse, the lungs and intestine were further imaged using high-magnification light-sheet microscopy. *Prox1*-EGFP lymphatic vessels (green) are evident throughout the tissues. Single experiment.

**Supplementary Video 7**
**Microglia and peripheral immune cells in CX3CR1$^{GFP/+}$ x CCR2$^{RFP/+}$ mouse**
Multiplexed visualization of CX3CR1$^{GFP/+}$ x CCR2$^{RFP/+}$ transgenic mouse head after panoptic imaging with two different nanoboosters (anti-GFP conjugated to Atto647N and anti-RFP conjugated to Atto594N). The CX3CR1 GFP+ microglia cells in the brain parenchyma vs. CCR2 RFP+ peripheral immune cells in the meningeal vessels were clearly visible in 3D reconstruction and 2D orthoslicing. Similar results were observed from 3 independent double transgenic mice.

**Supplementary Video 8**
**Revealing short skull meninges connections (SMCs) in intact CX3CR1$^{GFP/+}$ mouse heads**
2D orthoslicing of transparent head from the sagittal view of a CX3CR1$^{GFP/+}$ line mouse imaged by light-sheet microscope. The vasculature was labelled by Lectin (red) and CX3CR1 GFP+ immune cells and microglia cells (green) were boosted by vDISCO. Short skull-meninges connections (SMCs) containing CX3CR1 GFP+ immune cells are evident. Similar results were observed in 3 independent animals.

**Supplementary Video 9**
**Cellular details of SMCs in intact mouse heads**
3D visualization of skull and brain interface in a CX3CR1$^{GFP/+}$ line mouse imaged by confocal microscope. Vasculature was labelled with lectin (magenta) and CX3CR1 GFP+ cells (green) were boosted by vDISCO. Short vascular connections between skull marrow and meninges at the sagittal sinus and brain interfaces are clearly visualized. We also observed occasional connections between neighbouring skull marrow regions. Note that lectin dye is taken up by phagocytic cells in the skull marrow similar to dextran[54]. Similar results were observed in 3 independent animals.

**Supplementary Video 10**
**LysM GFP+ immune cells observed in SMCs upon ischemic stroke lesion**

2D orthoslicing of *LysM*-EGFP mouse head with MCAO. LysM GFP+ neutrophils and monocytes are shown in red and cell nuclei labelled by PI are shown in green. LysM GFP+ cells increased in the lesion site indicating the infiltration of immune cells after MCAO. In addition, many LysM GFP+ cells are observed in the vascular connections to the meninges suggesting that SMCs can be a potential cell trafficking route and play a role in the neuroinflammatory process. Similar results were observed from 4 independent mice per group.

**Supplementary Video 11**
**Widespread inflammation upon SCI assessed by panoptic vDISCO imaging**
Panoptic imaging of *CD68*-EGFP transgenic mouse upon SCI. 2D orthoslicing in horizontal and sagittal views clearly shows the activated immune cells (green) in the muscles, spinal cord roots and meningeal compartments. Vertebra, which become prominent with PI labelling, are shown in white. Similar results were observed from 3 independent mice per group.

**Supplementary Video 12**
**Extensive details of neuronal connections in the mouse brain revealed by vDISCO**
A *Thy1*-GFPM mouse brain was imaged by light-sheet microscopy more than a year after vDISCO. The details of the neuronal structures down to the subcellular level were imaged by Zeiss 20x objective on the light-sheet microscope. Similar results were observed in 2 independent animals.

# 5 Discussion

## 5.1 Comprehensive and reasoned summary of the results

In this project, I have developed new technologies with the aim to study biological events with the consideration for the whole complexity of an organism and to elucidate body-wide changes in neuronal pathologies. In particular, my work focused on establishing whole body tissue clearing and imaging methods that are able to overcome the limitations of traditional 2D histology (such as the sectioning of the samples and the reconstruction of 3D information from fragments), to provide quantitative data about physiological and pathological phenomena from a big perspective, and to discover new biological information.

First, by an extensive chemical screen and an optimization of the protocol conditions, we established uDISCO, a new whole-body tissue clearing method that is able to clear in a fast and easy way whole rodent bodies with the highest level of transparency[10]. uDISCO is based on the chemical properties of *tert*-butanol and diphenyl ether to dehydrate and match the refractive indexes of biological tissues respectively. Since these two reagents are more chemically stable compared with previous organic-solvent-based chemicals used in tissue clearing, uDISCO preserves the fluorescence signal from endogenous fluorescent proteins for months (while previous organic-solvent-based clearings used to quench the signal in few days). Furthermore, uDISCO shrinks the samples (including whole rodent bodies) up to 65% in their volume; therefore, it is the first tissue clearing method that allowed the high resolution imaging with light-sheet microscopy of unsectioned whole adult rodent bodies.

As mentioned in the introduction, the alteration of the tissue size after chemical procedures has been already exploited as a way to improve the imaging performance: for example, the expansion of sample sizes has been the basis for super-resolution imaging from expansion microscopy[37,60,62,177]. With uDISCO we applied this concept but in the other direction: we exploited the shrinkage, in order to be able to achieve the imaging of big samples without apparent loss of resolution.

In fact, using uDISCO we accomplished the following results:

- The first whole-body light-sheet imaging of a cleared adult *Thy1*-GFPM mouse, of which subsets of neurons express GFP.
- The first light-sheet imaging at subcellular resolution of intact brain and spinal cord dissected from a *Thy1*-GFPM mouse, where we resolved dendrites, axons and dendritic spines.

- Imaging of the complete vasculature of the CNS and of the whole body of an adult rat for the first time.
- Deep tissue staining of 1 mm thick fresh-fixed mouse and over-fixed human brain slices, showing the compatibility of uDISCO with standard immunohistochemistry.
- Compatibility of uDISCO with virus tracing.
- Application of uDISCO for unbiased detection of transplanted fluorescent stem cells at single-cell resolution in whole mouse bodies. We showed that our method allowed the fast screening and the accurate assessment of the distribution of transplanted cells. Similar results were not achievable with previous methods such as bioluminescence or standard histology which provides much poorer resolution or is very time-consuming respectively.

Moreover, we used uDISCO as a tool that contributed to the discovery of new immune cell infiltration routes into the brain under pathological conditions after visualizing in 3D the specific T-cell distribution pattern in the brain upon stroke. With uDISCO, we could quickly assess the accumulation of lymphocytes in specific areas of the brain: between the lateral ventricle and the lesion site. From this first observation we discovered that the choroid plexus represents an important route for T-cell invasion into the infarcted brain[178].

uDISCO clearing belongs to the group of organic-solvent-based clearing methods, thereby it possesses all the advantages of this category: as already mentioned, it achieves a high grade of transparency, it is simple to perform and it physically reduces the sample size. Moreover, the cleared specimens are easy to handle: due to the dehydration and the chemical steps, the tissue becomes hard but flexible and easier to position in the imaging apparatus. In contrast, aqueous clearing methods such as the ones based on high concentration of sugar or the ones relying on the creation of a hydrogel scaffold are more difficult to adopt because of the jelly and fragile texture of the cleared brains, the high viscosity of the clearing solutions or because they are time consuming, requiring weeks to months to a clear whole organ [49].

Therefore, in our research we focused on the optimization and the application of the organic-solvent-based methods.

With uDISCO we paved the way for a new approach to study biological events by imaging at high resolution: without focusing on selected body areas only, but providing a global view of the investigated system instead. However, uDISCO still had many limitations: (i) the weakness of endogenous fluorescent proteins in clearing solutions, (ii) the strong tissue autofluorescence which can reduce the signal over background ratio[6], (iii) the incomplete clearing of calcified tissues such as bones which limits the imaging penetration. All these factors prevented the possibility to reliably obtain quantitative data, especially from complex structures like neuronal projections, without the opening of hard tissues such as the bones enclosing the CNS.

Recent methods[19-22] have combined immunostaining with organic-solvent-based clearing procedures, thus providing different advantages: the long-term stabilization of the signal and the usage of very bright fluorescent dyes like Alexa- or Atto-dyes to increase the signal to background ratio.

Taken all these aspects in consideration, we next implemented a new method called "vDISCO". Using a unique combination of different chemicals, we managed to develop a protocol that is able to: (i) reduce the autofluorescence of the tissue by removing residual heme pigment from the body, (ii) decalcify the bones to make them transparent for imaging, and (iii) enhance the fluorescence signal/background ratio by up to two orders of magnitude. Thanks to these achievements, vDISCO also gives superior imaging quality compared with other methods. These results were accomplished by exploiting a "high-pressure" delivery approach to achieve whole-body immunostaining using nanobodies—variable domain of heavy chain antibodies—which are ten times smaller than conventional antibodies[179]. Owing to their small size, the nanobodies can extensively reach all the epitopes in a mouse body. Moreover, since the nanobodies are conjugated to synthetic dyes, the fluorescent signal is (i) bright, (ii) can be shifted to the far-red spectrum, range where the light penetrates deeper and the autofluorescence is reduced, and (iii) can be maintained for years allowing repeated imaging of the same sample. This last aspect, together with the reduction of the time needed for the whole experimental procedure and the possibility to create high fidelity atlases and databases, also represents an important factor to decrease the resources and the number of animals needed in research in the future.

Using vDISCO we achieved the following results in intact samples:

- We obtained the imaging of cellular structures under hard tissues such as bones. In this way, it is no longer necessary to remove bones such as skull and vertebra from the body.
- We created the first high resolution neuronal map of a whole adult mouse body from the *Thy1*-GFPM line, giving the possibility to trace all axonal projections in the entire body of this transgenic line.
- We cleared mice with intact skin and imaged the cellular content of the skin beyond its surface.
- Owing to the great enhancement of signal/background ratio of the cellular structures, we could obtain quantitative data about the neurodegenerative and neuroinflammatory effects of acute CNS injuries onto remote body parts.
- We could image anatomic structures such as meningeal lymphatic vessels that would be normally damaged by conventional dissection in standard histology.
- We also revealed short vascular connections named SMCs between the skull marrow and the meninges. Since we quantified an increase of the presence of immune cells in these structures in disease (e.g. stroke), these channels are hypothesized to be an important factor in the inflammatory processes involving the brain. For instance, they could work as a new route of immune cell trafficking.

Overall, we showed that the panoptic imaging of cleared whole mouse bodies represents a promising tool to provide an unbiased and highly resolved view of the entire organism in health and disease.

## 5.2 Considerations and future perspectives about the technical aspects

Both uDISCO and vDISCO are easily implementable for dissected organs: in fact, we have shown that both of them can be applied to process dissected brains with simplified passive versions of the protocols. Moreover, both methods are compatible with other staining strategies including virus labeling or fluorescent transplanted cells. They are also compatible with higher resolution imaging systems such as confocal and two-photon microscopy: for instance, we demonstrated that it is possible to dissect out parts of the body from the cleared animal for more detailed investigation with other microscope set-ups.

It is noteworthy to say that since DISCO methods require steps of delipidation, the retention of the lipids and lipid-associated proteins in the tissue after clearing should be carefully assessed. In addition, the usage of organic solvents might raise concerns in terms of laboratory safety. However, these chemicals can be safely handled with the proper equipment such as chemical hoods which are available in most of the laboratories.

Although causing the shrinkage, we have shown that our organic-solvent-based methods do not alter the proportions of the samples and their structural integrity, at least for the cerebral tissue. Further evaluation of other tissues is needed to confirm that the shrinkage is isotropic throughout the entire organism.

Despite achieving 3D reconstruction of whole mouse bodies, we currently cannot perform the imaging in only one session due to the still big size of whole adult intact rodents. In order to image all body parts, we have to displace and flip the intact animal in the microscope chamber and stitch the imaged volumes together afterwards. In the future, the development of larger microscopes together with longer working distance objectives will overcome the need for manual displacement so that the whole-body information can be obtained in an even faster and less work intensive way.

At the moment, the approach of panoptic imaging generates an extraordinary amount of raw data (e.g. 2-3 terabytes for a single animal): clearly, there is need for a parallel development of more powerful hardware and computer tools that are able to automatically analyze this information with drastically reduced supervision and workload for the human operator. Efforts in this direction already resulted in informatics tools to automatically process big imaging datasets. For example, for one of the most popular image processing softwares called “ImageJ” computer scientists have written plug-ins which provide automated segmentation, visualization, enhancement and reconstruction of biological structures[180-182]. Apart from ImageJ, several

groups implemented their own platforms for automated data processing: Renier *et al*. developed "Clearmap" which is an algorithm that provides automatic quantification, annotation and registration of cells in whole cleared brains[22], while Quan *et al*. developed "NeuroGPS-Tree" which is an algorithm that automatically traces neurons from confocal microscopy data of up to 1 gigabyte in size[183]. However, the methods available so far rely on traditional data analysis approaches that are based on explicit preprocessing (such as thresholding or normalization) and filter-based detections. This means that the parameters for the preprocessing and for the filters used in data analysis are hand-crafted features that need to be tailored by a human expert to the specifics of each individual data set, strongly limiting the flexibility of these traditional computer tools. For instance, if the signal intensity of a scan varies the parameters of such filter-based approaches, then a re-calibration of the parameters would be necessary. The rising interest in deep learning is promising for fully automated data analysis: in contrast to traditional detection approaches, all features are learnt from the data and do not need to be explicitly defined by a human expert. In addition, deep learning tools can process terabyte-size data and perform tasks significantly faster and with more accuracy and precision than a traditional method or even a human can[184]. In the computer vision and image analysis field, deep learning has been used to improve microscopy images[185] or for feature and cell detection in biomedical images, performing significantly better than traditional methods[186-188]. It has been also shown that deep learning could work on enormous image databanks from online servers[189,190] and could provide decisive contribution in medical assessment: for instance, Liang *et al*. employed deep learning to analyze massive electronic health records (hundreds of millions of data points from more than one million of patients) from entire hospital databanks to outperform the diagnosis of pediatric diseases in new patients compared with a single expert physician[191]. Thus, artificial intelligent represents a powerful solution to process whole organism datasets.

As mentioned before, our latest method vDISCO has been mainly applied for the enhancement and the detection of transgenically expressed fluorescent proteins (putatively 21 types including cerulean fluorescent protein (CFP), Venus among others). This is due to the fact that there are not many commercially available nanobodies to be used in histology because the research efforts so far have mainly focused on the *in vivo* application of nanobodies such as therapeutic agents[192]. However, in this work we also demonstrated that it is possible to use vDISCO with other nanobodies targeting antigens of endogenous proteins (e.g vimentin). We believe that our data will encourage the future development of new nanobodies for immunostaining of fixed thick samples. For this purpose, it will be advantageous to conjugate the nanobodies with synthetic dyes that emit in the near-infrared spectrum in order to combine more targets and imaging channels in multiplexing studies and to further improve the imaging depth.

## 5.3 Considerations about the biological findings, future directions and applications in biomedical research

In this project, we demonstrated that our technology represents a powerful tool for biomedical investigations.

The phenomenon of neurodegeneration is not limited to the neurons directly harmed[193]. In fact, it has been reported that patients that have undergone different grades of brain ablation can develop diaschisis[194] which is a change or loss of the functionality of a region of the brain connected to a distant and damaged brain area. Furthermore, other papers have shown that in both patients and animal models cerebral ischemia can trigger the atrophy of distal brain regions that are functionally connected to the ischemic site[195,196]. These remote effects of brain insults result from the transneuronal degeneration: a biological process that describes the degeneration of neurons which are functionally connected with a damaged neuron and it is characterized by shrinkage of the cells, swelling of the mitochondria and detaching of nucleus membrane[197]. This kind of degeneration can happen retrogradely and/or anterogradely[198-200] and it is caused by the fact that the loss of neurons creates an imbalance in the whole neuronal network[193,197,201]. The evaluation of the transneuronal degeneration has been mostly restricted to the CNS using methods such as electrophysiological recording[194], standard histology[196] or MRI[202]. Other studies employing optical coherence tomography focused on analyzing the spread of the neurodegeneration through connected synapses into the periphery, including the ones showing degeneration of retinal ganglion cells after visual cortex lesion[203-205] or the reduction of retinal nerve fiber layer thickness after cerebral infarction[206]. However, while it has been demonstrated that stroke do not cause degeneration of lower motor neurons which are connected to the damaged upper motor neurons[207], little is known about the exact locations of transneuronal changes in the PNS triggered by TBI. Through our vDISCO method, we have shown for the first time that TBI triggered axonal degeneration in the spinal cord and peripheral neurodegeneration in distal regions (in particular in the torso) of the body. This reduction of axonal complexity was observed more than one month after the initial injury, in the chronic stage of the pathology. In particular, the degeneration of axons in the spinal cord, visible as fragmentation of axonal fibers, was detected along the cortico-spinal tract of the animal, that is along the dorsal spinal tract which relays control of voluntary movements. These findings are in accordance with the disruption and degeneration of the descending (efferent) motor pathways that start from the injured right somato-motor cortex, and with our observation of the reduction of axonal complexity of the nerves innervating voluntary muscles (including the left spinotrapezius and latissimus dorsi) of the animals. Since the axonal tract involved belongs to the descending pathways we can plausibly deduce that it is anterograde transneuronal degeneration. Moreover, these results also account for the motor impairments evaluated by rotarod test in mice in the chronic stage of TBI[67]. However, owing to the fact that our model of TBI does not cause a focal injury, we cannot exclude that other pathways might be involved in the degeneration, as well. Nevertheless, vDISCO gives the possibility to

quickly screen for these alternative pathways of degeneration and to follow them from the very beginning (brain) to the very end (peripheral nerve endfeet) along the connectivity in a whole organism. Before, this kind of systemic analysis on the effects of brain lesions could not be performed in an efficient way, as sectioning all the body parts would have been excessively time-consuming. Our TBI findings represent the first visualization of the alteration of the neuronal connectivity outside the CNS which may explain behavioral alterations which could not be explained by the CNS lesion itself (e.g. neuropathies) and present a cellular basis for the clinical observations of peripheral symptoms after TBI[97-99]. Future research efforts could be addressed for the followings:

- Track in detail all the CNS and PNS regions affected by degeneration also in other TBI models.
- Elucidate all the molecular mechanisms involved.
- Understand the contribution of retrograde and anterograde transneuronal degeneration.
- Evaluate if there are mechanisms of physiological regeneration occurring as well such as the one following Wallerian degeneration.
- Identify new therapeutic strategies to limit the spreading of the pathology in distal sites.

We showed that CNS injuries such as spinal cord injury also triggered a massive extended inflammation not only limited to the neuronal tissue. In fact, besides the activation of the microglia we observed that peripheral macrophages were also recruited from distal muscle tissues to accumulate around the lesion area, putatively invading the CNS through the meninges, as indicated by the presence of immune cells in the spinal meningeal compartment at the level of the lesion. Previously, the assessment of the inflammatory level after spinal cord injury has never been focused on investigating the spinal meningeal spaces in detail including their cellular content. In addition, the analysis of the injured tissue was done either in dissected spinal cords[17], performed observing small areas by intravital microscopy[125] or done with low resolution MRI[141]. Our findings show that it is possible to investigate (neuronal)inflammation from a broader perspective, by taking into account not only the CNS but also all the surrounding tissues such as muscles, bones and meninges. Future research will better elucidate the mechanisms behind this inflammatory process and its extent in the whole-body. Moreover, the fate of these recruited macrophages needs to be determined. For example, it would be interesting to investigate: (i) to which extent these peripheral cells infiltrate into the spinal cord and through which routes, (ii) if they possess a clearance activity phagocytizing cellular debris and dead cells, and (iii) whether these inflammatory cells belong to the myeloid-derived suppressor cell population that has been previously shown to prevent the autoimmune response after CNS trauma[130] or whether they play a detrimental role by worsening the injury outcome through enhanced inflammation.

In the last years, tissue clearing technology has also been used to discover new anatomical structures because it delivers 3D information of body regions which were not accessible before by other techniques. For example, using a clearing method called "SimpleCLEAR"[53] Gunzer´s group discovered a dense network of previously unknown trans-cortical blood capillaries in long bones that is connected to the cardiovascular system[208]. In our work, we demonstrated that our technology can be used to study and explore the meningeal content located between CNS tissue and the skull/vertebra. The investigation of this anatomic area has often been limited by the fact that it can either be damaged after brain harvesting or it has to be dissected out during histological preparations[168,173]. Only vDISCO could permit us to study this region in its "native" state inside the head of the animal. In particular, we revealed the presence of newly discovered short vascular connections –named SMCs– which are not part of the vascular system of the brain/head, but they directly link the skull marrow to the meninges. These structures might represent a direct and quick way for the brain to transfer information (soluble molecules, signaling factors etc…) about its state to a close hematopoietic organ and influence its hematopoietic activity (e.g. locally decreasing leukocyte retaining factors such as SDF-1), and to trigger the recruitment of spatially close skull marrow immune cells via chemokines upon pathological conditions. In fact, we observed that the immune cellular content of the SMCs increases in stroke and this can be an indication that the inflammatory signaling from the brain can directly reach the skull bone marrow and that these connections might work as an alternative route for cells to enter and exit the brain after cerebral ischemia. Interestingly, the presence of short vascular connections in the inside of the skull has also been recently supported by Herisson *et al.*[209]. Besides, the researchers showed that most of the peripheral immune cells migrating towards the dura after stroke were preferentially recruited from the skull, particularly the calvaria bone marrow, compared with the tibia, indicating that the access to the ischemic brain might be open through alternative ways which are independent from the systemic circulation. After analysing craniectomy specimens, they also proved in humans the existence of these short vascular structures connecting the brain cortex surface with skull marrow cavities. Their findings together with ours support the fact that the SMCs might play an important role in healthy and especially inflammatory conditions during diseases. In fact, as said in the introduction, the involvement of the meninges in inflammatory responses and pathological conditions such as multiple sclerosis[173] and Alzheimer´s disease has recently been reported[175]. In light of these results, immune cells and soluble factors which are able to exploit the SMCs as transfer channels could contribute to the pathogenesis of chronic neurodegenerative diseases. Future research using *in vivo* animal models and intravital microscopy or 2-photon microscopy might focus on (i) how the immune cells can traffick between brain and bone marrow via SMCs, (ii) how manipulating or impairing the SMCs would affect the outcome of brain diseases (e.g. decreasing the inflammatory response) or (iii) how it would be possible to exploit them as a direct and a safer means to delivery therapeutic agents against brain disorders without extended systemic side effects of other drugs or invasive brain parenchyma interventions. Furthermore, this

direct connection between brain and skull marrow may open up new diagnostic opportunities by monitoring changes in the skull. However, owing to the current lack of specific lymphatic transgenic reporter mice, future investigations are needed not only to clarify whether SMCs are lined with blood or lymphatic endothelial cells, but also to further characterize their anatomic features such as which layer of meninges they connect to. It would be also important to perform their molecular characterization via proteomics and transcriptomics studies in order to elucidate in what extent the skull marrow immune population trafficking in these channels differs from the ones originating from more distal bones (e.g tibia). In the end, it would also be interesting to explore whether external biological entities such as bacteria or other pathogens can hijack the SMCs to access to the brain and whether the functionality of the SMCs change during aging or during neurological acute and chronic conditions.

There are extensive findings that suggest that the pathological effects of a cerebral ischemic stroke are not confined to the brain but also significantly affect other organs. In fact, it has been shown that brain ischemia can cause general immunodepression[210], global activation of peripheral immune system[211] or can induce CNS-specific antigens including immunomodulators such as alarmins and cytokines to enter into the systemic circulation[163,212]. These are released from the damaged brain tissue and can immunomodulate[213] the whole body by chemoattraction or interaction with various immune and no immune cell populations possibly leading to vascular inflammation[68]. At a more specific level it has been shown that stroke can deeply affect the other peripheral organs and viceversa: it can lead to multiple organ failure[214], including heart, lung, kidney, pancreas and spleen. DISCO methods will help to better understand the interactions of all these organs from a global perspective.

Recently, there has been an increasing interest in understanding how microbiota can affect the course of diseases[215], especially after discovering the close relationship between brain and gut (the gut-brain axis)[216,217]. The influence of the microbiota on the brain and other organs can be mediated by the dissemination of molecules, including biochemical signals in the host[218], and/or by the priming/activation/interaction with circulating cells such as immune cells. For example, it has been shown that gut microbiota can affect stroke outcome[219] and modulate anxiety[220,221]. By utilizing DISCO methods, the relationship between so many distant components would be easier and faster to assess. The task of tracking and detecting fluorescent circulating cells that are known to interact with intestine bacteria would become easier, for example.

Cancer research represents another possible application of our technology. An example would be to exploit vDISCO to study animal models of the dissemination of metastases (which are often the main cause of the death of cancer patients) from the primary fluorescent tumor into the whole organism[222]. So far, the screening of metastases has been performed using poor resolving systems such as bioluminescence imaging which are unable to detect isolated single metastatic cells[3]. The high resolution reached by our pipeline can overcome

this problem because it allows the detection and analysis of micrometastases in the whole-body. This will help to understand the distribution and the localization of each single metastatic cell in every part of the body and also to evaluate the performance of therapeutical agents in reaching these cells (e.g anti-tumor antibodies conjugated to fluorescent dyes).

# 6 Conclusion

With this PhD project I developed new technologies that allow the systemic assessment of whole bodies, laying the foundation of a new histological approach to study in an unbiased way biological phenomena: considering the high complexity of biological systems. Importantly, the findings reached by our technology demonstrate that using this approach we could uncover unknown biological information that was not accessible before. Thus, I discovered peripheral degeneration after TBI, extensive multi organ inflammation after spinal cord injury and the existence of SMCs between the skull and the brain. These results contribute to the better understanding of the physiology and pathology of biological phenomena and will pave the way for future research lines aiming to elucidate the mechanisms behind these events.

Taken together, we believe that our DISCO technology will greatly contribute not only to the study of neuronal pathological conditions, allowing the detection of whole-organisms changes, but also to investigate the systemic phenomena of known whole-body diseases such as metabolic diseases or diabetes and to uncover new distal effects of many other pathologies.

# 7 References


1 Justice, M. J. & Dhillon, P. Using the mouse to model human disease: increasing validity and reproducibility. *Disease models & mechanisms* 9, 101-103, doi:10.1242/dmm.024547 (2016).

2 Kirschner, M. W. The meaning of systems biology. *Cell* 121, 503-504, doi:10.1016/j.cell.2005.05.005 (2005).

3 James, M. L. & Gambhir, S. S. A molecular imaging primer: modalities, imaging agents, and applications. *Physiological reviews* 92, 897-965, doi:10.1152/physrev.00049.2010 (2012).

4 Alturkistani, H. A., Tashkandi, F. M. & Mohammedsaleh, Z. M. Histological Stains: A Literature Review and Case Study. *Global journal of health science* 8, 72-79, doi:10.5539/gjhs.v8n3p72 (2015).

5 Tuchin, V. V. Tissue optics: light scattering methods and instruments for medical diagnosis. *SPIE press Bellingham* 642 (2007).

6 Tuchin, V. V. Tissue optics and photonics: light-tissue interaction. *J. Biomed. Photonics Eng.* 1, 98-134, doi:10.18287/jbpe-2015-1-2-98 (2015).

7 Tuchin, V. V. *et al.* Light propagation in tissues with controlled optical properties *J. Biomed. Opt.* 2, 401-417, doi:https://doi.org/10.1117/12.281502 (1997).

8 Spalteholz, W. Über das Durchsichtigmachen von menschlichen und tierischen Präparaten. *Leipzig, Ger.: S. Hirzel* (1911).

9 Dodt, H. U. *et al.* Ultramicroscopy: three-dimensional visualization of neuronal networks in the whole mouse brain. *Nature methods* 4, 331-336, doi:10.1038/nmeth1036 (2007).

10 Wan, P. *et al.* Evaluation of seven optical clearing methods in mouse brain. *Neurophotonics* 5, 035007, doi:10.1117/1.NPh.5.3.035007 (2018).

11 Tainaka, K., Kuno, A., Kubota, S. I., Murakami, T. & Ueda, H. R. Chemical Principles in Tissue Clearing and Staining Protocols for Whole-Body Cell Profiling. *Annual review of cell and developmental biology* 32, 713-741, doi:10.1146/annurev-cellbio-111315-125001 (2016).

12 Becker, K., Jahrling, N., Saghafi, S., Weiler, R. & Dodt, H. U. Chemical clearing and dehydration of GFP expressing mouse brains. *PloS one* 7, e33916, doi:10.1371/journal.pone.0033916 (2012).

13 Espinosa-Medina, I. *et al.* Neurodevelopment. Parasympathetic ganglia derive from Schwann cell precursors. *Science* 345, 87-90, doi:10.1126/science.1253286 (2014).

14 Liu, Z. *et al.* Immune homeostasis enforced by co-localized effector and regulatory T cells. *Nature* 528, 225-230, doi:10.1038/nature16169 (2015).

15 Oshimori, N., Oristian, D. & Fuchs, E. TGF-beta promotes heterogeneity and drug resistance in squamous cell carcinoma. *Cell* 160, 963-976, doi:10.1016/j.cell.2015.01.043 (2015).

16 Erturk, A. *et al.* Three-dimensional imaging of solvent-cleared organs using 3DISCO. *Nature protocols* 7, 1983-1995, doi:10.1038/nprot.2012.119 (2012).

17 Erturk, A. *et al.* Three-dimensional imaging of the unsectioned adult spinal cord to assess axon regeneration and glial responses after injury. *Nature medicine* 18, 166-171, doi:10.1038/nm.2600 (2012).

18 Schwarz, M. K. *et al.* Fluorescent-protein stabilization and high-resolution imaging of cleared, intact mouse brains. *PloS one* 10, e0124650, doi:10.1371/journal.pone.0124650 (2015).

19 Belle, M. *et al.* A simple method for 3D analysis of immunolabeled axonal tracts in a transparent nervous system. *Cell reports* 9, 1191-1201, doi:10.1016/j.celrep.2014.10.037 (2014).

20 Belle, M. *et al.* Tridimensional Visualization and Analysis of Early Human Development. *Cell* 169, 161-173 e112, doi:10.1016/j.cell.2017.03.008 (2017).

21 Renier, N. *et al.* iDISCO: a simple, rapid method to immunolabel large tissue samples for volume imaging. *Cell* 159, 896-910, doi:10.1016/j.cell.2014.10.010 (2014).

22 Renier, N. *et al.* Mapping of Brain Activity by Automated Volume Analysis of Immediate Early Genes. *Cell* 165, 1789-1802, doi:10.1016/j.cell.2016.05.007 (2016).

23 Meglinski, I. V., Bashkatov, A. N., Genina, E. A., Churmakov, D. Y. & Tuchin, V. V. The enhancement of confocal images of tissues at bulk optical immersion. *Laser Phys* 13, 65-69 (2003).

24 Aoyagi, Y., Kawakami, R., Osanai, H., Hibi, T. & Nemoto, T. A Rapid Optical Clearing Protocol Using 2,2'-Thiodiethanol for Microscopic Observation of Fixed Mouse Brain. *PloS one* 10, doi:ARTN e011628010.1371/journal.pone.0116280 (2015).

25 Hou, B. *et al.* Scalable and Dil-compatible optical clearance of the mammalian brain. *Frontiers in neuroanatomy* 9, doi:Artn 1910.3389/Fnana.2015.00019 (2015).

26 Staudt, T., Lang, M. C., Medda, R., Engelhardt, J. & Hell, S. W. 2,2 '-thiodiethanol: A new water soluble mounting medium for high resolution optical microscopy. *Microsc Res Techniq* 70, 1-9, doi:10.1002/jemt.20396 (2007).

27 Costantini, I. *et al.* A versatile clearing agent for multi-modal brain imaging. *Scientific reports* 5, doi:Artn 980810.1038/Srep09808 (2015).

28 Ke, M. T., Fujimoto, S. & Imai, T. SeeDB: a simple and morphology-preserving optical clearing agent for neuronal circuit reconstruction. *Nature neuroscience* 16, 1154-1161, doi:10.1038/nn.3447 (2013).

29 Hama, H. *et al.* ScaleS: an optical clearing palette for biological imaging. *Nature neuroscience* 18, 1518-1529, doi:10.1038/nn.4107 (2015).

30 Hou, B. *et al.* Scalable and DiI-compatible optical clearance of the mammalian brain. *Frontiers in neuroanatomy* 9, 19, doi:10.3389/fnana.2015.00019 (2015).

31 Lai, H. M. *et al.* Next generation histology methods for three-dimensional imaging of fresh and archival human brain tissues. *Nature communications* 9, 1066, doi:10.1038/s41467-018-03359-w (2018).

32 Kurihara, D., Mizuta, Y., Sato, Y. & Higashiyama, T. ClearSee: a rapid optical clearing reagent for whole-plant fluorescence imaging. *Development* 142, 4168-4179, doi:10.1242/dev.127613 (2015).

33 Hama, H. *et al.* Scale: a chemical approach for fluorescence imaging and reconstruction of transparent mouse brain. *Nature neuroscience* 14, 1481-1488, doi:10.1038/nn.2928 (2011).

34 Chen, L. *et al.* UbasM: An effective balanced optical clearing method for intact biomedical imaging. *Scientific reports* 7, 12218, doi:10.1038/s41598-017-12484-3 (2017).

35 Susaki, E. A. *et al.* Whole-brain imaging with single-cell resolution using chemical cocktails and computational analysis. *Cell* 157, 726-739, doi:10.1016/j.cell.2014.03.042 (2014).

36 Tainaka, K. *et al.* Whole-body imaging with single-cell resolution by tissue decolorization. *Cell* 159, 911-924, doi:10.1016/j.cell.2014.10.034 (2014).

37 Murakami, T. C. *et al.* A three-dimensional single-cell-resolution whole-brain atlas using CUBIC-X expansion microscopy and tissue clearing. *Nature neuroscience* 21, 625-637, doi:10.1038/s41593-018-0109-1 (2018).

38 Nojima, S. *et al.* CUBIC pathology: three-dimensional imaging for pathological diagnosis. *Scientific reports* 7, 9269, doi:10.1038/s41598-017-09117-0 (2017).

39 Kubota, S. I. *et al.* Whole-Body Profiling of Cancer Metastasis with Single-Cell Resolution. *Cell reports* 20, 236-250, doi:10.1016/j.celrep.2017.06.010 (2017).

40 Chung, K. *et al.* Structural and molecular interrogation of intact biological systems. *Nature* 497, 332-337, doi:10.1038/nature12107 (2013).

41 Yang, B. *et al.* Single-cell phenotyping within transparent intact tissue through whole-body clearing. *Cell* 158, 945-958, doi:10.1016/j.cell.2014.07.017 (2014).

42 Treweek, J. B. *et al.* Whole-body tissue stabilization and selective extractions via tissue-hydrogel hybrids for high-resolution intact circuit mapping and phenotyping. *Nature protocols* 10, 1860-1896, doi:10.1038/nprot.2015.122 (2015).

43 Greenbaum, A. *et al.* Bone CLARITY: Clearing, imaging, and computational analysis of osteoprogenitors within intact bone marrow. *Science translational medicine* 9, doi:10.1126/scitranslmed.aah6518 (2017).

44 Murray, E. *et al.* Simple, Scalable Proteomic Imaging for High-Dimensional Profiling of Intact Systems. *Cell* 163, 1500-1514, doi:10.1016/j.cell.2015.11.025 (2015).

45 Park, Y. G. *et al.* Protection of tissue physicochemical properties using polyfunctional crosslinkers. *Nature biotechnology*, doi:10.1038/nbt.4281 (2018).

46 Sylwestrak, E. L., Rajasethupathy, P., Wright, M. A., Jaffe, A. & Deisseroth, K. Multiplexed Intact-Tissue Transcriptional Analysis at Cellular Resolution. *Cell* 164, 792-804, doi:10.1016/j.cell.2016.01.038 (2016).

47 Alnuami, A. A., Zeedi, B., Qadri, S. M. & Ashraf, S. S. Oxyradical-induced GFP damage and loss of fluorescence. *Int J Biol Macromol* 43, 182-186, doi:10.1016/j.ijbiomac.2008.05.002 (2008).

48 Alkaabi, K. M., Yafea, A. & Ashraf, S. S. Effect of pH on thermal- and chemical-induced denaturation of GFP. *Appl Biochem Biotech* 126, 149-156, doi:Doi 10.1385/Abab:126:2:149 (2005).

49 Richardson, D. S. & Lichtman, J. W. Clarifying Tissue Clearing. *Cell* 162, 246-257, doi:10.1016/j.cell.2015.06.067 (2015).

50 Jing, D. *et al.* Tissue clearing of both hard and soft tissue organs with the PEGASOS method. *Cell research* 28, 803-818, doi:10.1038/s41422-018-0049-z (2018).

51 Xu, N. *et al.* Fast free-of-acrylamide clearing tissue (FACT)-an optimized new protocol for rapid, high-resolution imaging of three-dimensional brain tissue. *Scientific reports* 7, 9895, doi:10.1038/s41598-017-10204-5 (2017).

52 Qi, Y. S. *et al.* FDISCO: Advanced solvent-based clearing method for imaging whole organs. *Sci Adv* 5, doi:ARTN eaau835510.1126/sciadv.aau8355 (2019).

53 Klingberg, A. *et al.* Fully Automated Evaluation of Total Glomerular Number and Capillary Tuft Size in Nephritic Kidneys Using Lightsheet Microscopy. *J Am Soc Nephrol* 28, 452-459, doi:10.1681/Asn.2016020232 (2017).

54 Rawat, S., Suri, C. R. & Sahoo, D. K. Molecular mechanism of polyethylene glycol mediated stabilization of protein. *Biochemical and biophysical research communications* 392, 561-566, doi:10.1016/j.bbrc.2010.01.067 (2010).

55 Kuwajima, T. *et al.* Clear(T): a detergent- and solvent-free clearing method for neuronal and non-neuronal tissue. *Development* 140, 1364-1368, doi:10.1242/dev.091844 (2013).

56 Tainaka, K., Kuno, A., Kubota, S. I., Murakami, T. & Ueda, H. R. Chemical Principles in Tissue Clearing and Staining Protocols for Whole-Body Cell Profiling. *Annu Rev Cell Dev Bi* 32, 713-741, doi:10.1146/annurev-cellbio-111315-125001 (2016).

57 Pende, M. *et al.* High-resolution ultramicroscopy of the developing and adult nervous system in optically cleared Drosophila melanogaster. *Nature communications* 9, doi:Artn 473110.1038/S41467-018-07192-Z (2018).

58 Proksch, E., Brandner, J. M. & Jensen, J. M. The skin: an indispensable barrier. *Experimental dermatology* 17, 1063-1072 (2008).

59 Gimenez-Arnau, A. Standards for the Protection of Skin Barrier Function. *Current problems in dermatology* 49, 123-134, doi:10.1159/000441588 (2016).

60 Chen, F., Tillberg, P. W. & Boyden, E. S. Optical imaging. Expansion microscopy. *Science* 347, 543-548, doi:10.1126/science.1260088 (2015).

61 Chen, F. *et al.* Nanoscale imaging of RNA with expansion microscopy. *Nature methods* 13, 679-684, doi:10.1038/nmeth.3899 (2016).

62 Tillberg, P. W. *et al.* Protein-retention expansion microscopy of cells and tissues labeled using standard fluorescent proteins and antibodies. *Nature biotechnology* 34, 987-992, doi:10.1038/nbt.3625 (2016).

63 Ku, T. *et al.* Multiplexed and scalable super-resolution imaging of three-dimensional protein localization in size-adjustable tissues. *Nature biotechnology* 34, 973-981, doi:10.1038/nbt.3641 (2016).

64 Langlois, J. A., Rutland-Brown, W. & Wald, M. M. The epidemiology and impact of traumatic brain injury: a brief overview. *The Journal of head trauma rehabilitation* 21, 375-378 (2006).

65 Mortality, G. B. D. & Causes of Death, C. Global, regional, and national life expectancy, all-cause mortality, and cause-specific mortality for 249 causes of death, 1980-2015: a systematic analysis for the Global Burden of Disease Study 2015. *Lancet* 388, 1459-1544, doi:10.1016/S0140-6736(16)31012-1 (2016).

66 Anthony, D. C. & Couch, Y. The systemic response to CNS injury. *Experimental neurology* 258, 105-111, doi:10.1016/j.expneurol.2014.03.013 (2014).

67 Erturk, A. *et al.* Interfering with the Chronic Immune Response Rescues Chronic Degeneration After Traumatic Brain Injury. *The Journal of neuroscience : the official journal of the Society for Neuroscience* 36, 9962-9975, doi:10.1523/JNEUROSCI.1898-15.2016 (2016).

68 Roth, S. *et al.* Brain-released alarmins and stress response synergize in accelerating atherosclerosis progression after stroke. *Science translational medicine* 10, doi:10.1126/scitranslmed.aao1313 (2018).

69 Newsome, M. R. *et al.* Chronic Effects of Blast-Related TBI on Subcortical Functional Connectivity in Veterans. *Journal of the International Neuropsychological Society : JINS* 22, 631-642, doi:10.1017/S1355617716000448 (2016).

70 Petraglia, A. L. *et al.* The spectrum of neurobehavioral sequelae after repetitive mild traumatic brain injury: a novel mouse model of chronic traumatic encephalopathy. *Journal of neurotrauma* 31, 1211-1224, doi:10.1089/neu.2013.3255 (2014).

71 Javouhey, E., Guerin, A. C. & Chiron, M. Incidence and risk factors of severe traumatic brain injury resulting from road accidents: a population-based study. *Accident; analysis and prevention* 38, 225-233, doi:10.1016/j.aap.2005.08.001 (2006).

72 Gardner, R. C. & Yaffe, K. Epidemiology of mild traumatic brain injury and neurodegenerative disease. *Molecular and cellular neurosciences* 66, 75-80, doi:10.1016/j.mcn.2015.03.001 (2015).

73 Maas, A. I., Roozenbeek, B. & Manley, G. T. Clinical trials in traumatic brain injury: past experience and current developments. *Neurotherapeutics : the journal of the American Society for Experimental NeuroTherapeutics* 7, 115-126, doi:10.1016/j.nurt.2009.10.022 (2010).

74 McConeghy, K. W., Hatton, J., Hughes, L. & Cook, A. M. A review of neuroprotection pharmacology and therapies in patients with acute traumatic brain injury. *CNS drugs* 26, 613-636, doi:10.2165/11634020-000000000-00000 (2012).

75 Kenzie, E. S. *et al.* Concussion As a Multi-Scale Complex System: An Interdisciplinary Synthesis of Current Knowledge. *Frontiers in neurology* 8, 513-513, doi:10.3389/fneur.2017.00513 (2017).

76 Hardman, J. M. & Manoukian, A. Pathology of head trauma. *Neuroimaging clinics of North America* 12, 175-187, vii (2002).

77 Xiong, Y., Mahmood, A. & Chopp, M. Animal models of traumatic brain injury. *Nature reviews. Neuroscience* 14, 128-142, doi:10.1038/nrn3407 (2013).

78 Gaetz, M. The neurophysiology of brain injury. *Clinical neurophysiology : official journal of the International Federation of Clinical Neurophysiology* 115, 4-18 (2004).

79 Roth, T. L. *et al.* Transcranial amelioration of inflammation and cell death after brain injury. *Nature* 505, 223-228, doi:10.1038/nature12808 (2014).

80 Prins, M., Greco, T., Alexander, D. & Giza, C. C. The pathophysiology of traumatic brain injury at a glance. *Disease models & mechanisms* 6, 1307-1315, doi:10.1242/dmm.011585 (2013).

81 Kurland, D., Hong, C., Aarabi, B., Gerzanich, V. & Simard, J. M. Hemorrhagic progression of a contusion after traumatic brain injury: a review. *Journal of neurotrauma* 29, 19-31, doi:10.1089/neu.2011.2122 (2012).

82 Bullock, R. *et al.* Evidence for prolonged release of excitatory amino acids in severe human head trauma. Relationship to clinical events. *Annals of the New York Academy of Sciences* 765, 290-297; discussion 298 (1995).

83 Young, W. Role of calcium in central nervous system injuries. *Journal of neurotrauma* 9 Suppl 1, S9-25 (1992).

84 Mazzeo, A. T., Beat, A., Singh, A. & Bullock, M. R. The role of mitochondrial transition pore, and its modulation, in traumatic brain injury and delayed neurodegeneration after TBI. *Experimental neurology* 218, 363-370, doi:10.1016/j.expneurol.2009.05.026 (2009).

85 Finnie, J. W. Neuroinflammation: beneficial and detrimental effects after traumatic brain injury. *Inflammopharmacology* 21, 309-320, doi:10.1007/s10787-012-0164-2 (2013).

86 Hickey, W. F., Hsu, B. L. & Kimura, H. Lymphocyte-T Entry into the Central-Nervous-System. *Journal of neuroscience research* 28, 254-260, doi:DOI 10.1002/jnr.490280213 (1991).

87 Morganti-Kossmann, M. C., Satgunaseelan, L., Bye, N. & Kossmann, T. Modulation of immune response by head injury. *Injury-International Journal of the Care of the Injured* 38, 1392-1400, doi:10.1016/j.injury.2007.10.005 (2007).

88 Raghupathi, R. Cell death mechanisms following traumatic brain injury. *Brain pathology* 14, 215-222 (2004).

89 Bramlett, H. M. & Dietrich, W. D. Progressive damage after brain and spinal cord injury: pathomechanisms and treatment strategies. *Progress in brain research* 161, 125-141, doi:10.1016/S0079-6123(06)61009-1 (2007).

90 Wilson, L. *et al.* The chronic and evolving neurological consequences of traumatic brain injury. *The Lancet. Neurology* 16, 813-825, doi:10.1016/S1474-4422(17)30279-X (2017).

91 Algattas, H. & Huang, J. H. Traumatic Brain Injury pathophysiology and treatments: early, intermediate, and late phases post-injury. *International journal of molecular sciences* 15, 309-341, doi:10.3390/ijms15010309 (2014).

92 Blennow, K., Hardy, J. & Zetterberg, H. The neuropathology and neurobiology of traumatic brain injury. *Neuron* 76, 886-899, doi:10.1016/j.neuron.2012.11.021 (2012).

93 Shively, S., Scher, A. I., Perl, D. P. & Diaz-Arrastia, R. Dementia resulting from traumatic brain injury: what is the pathology? *Archives of neurology* 69, 1245-1251, doi:10.1001/archneurol.2011.3747 (2012).

94 Ikonomovic, M. D. *et al.* Alzheimer's pathology in human temporal cortex surgically excised after severe brain injury. *Experimental neurology* 190, 192-203, doi:10.1016/j.expneurol.2004.06.011 (2004).

95 Gardner, R. C. *et al.* Traumatic brain injury in later life increases risk for Parkinson disease. *Annals of neurology* 77, 987-995, doi:10.1002/ana.24396 (2015).

96 Ding, K., Gupta, P. K. & Diaz-Arrastia, R. in *Translational Research in Traumatic Brain Injury Frontiers in Neuroscience* (eds D. Laskowitz & G. Grant) (2016).

97 Chen, H., Richard, M., Sandler, D. P., Umbach, D. M. & Kamel, F. Head injury and amyotrophic lateral sclerosis. *American journal of epidemiology* 166, 810-816, doi:10.1093/aje/kwm153 (2007).

98 Frei, K. Posttraumatic dystonia. *Journal of the neurological sciences* 379, 183-191, doi:10.1016/j.jns.2017.05.040 (2017).

99 Stone, L. & Keenan, M. A. Peripheral nerve injuries in the adult with traumatic brain injury. *Clinical orthopaedics and related research*, 136-144 (1988).

100 Johnson, V. E., Stewart, W. & Smith, D. H. Widespread tau and amyloid-beta pathology many years after a single traumatic brain injury in humans. *Brain pathology* 22, 142-149, doi:10.1111/j.1750-3639.2011.00513.x (2012).

101 Lu, P. *et al.* Prolonged human neural stem cell maturation supports recovery in injured rodent CNS. *The Journal of clinical investigation* 127, 3287-3299, doi:10.1172/JCI92955 (2017).

102 Kadoya, K. *et al.* Spinal cord reconstitution with homologous neural grafts enables robust corticospinal regeneration. *Nature medicine* 22, 479-487, doi:10.1038/nm.4066 (2016).

103 Hellal, F. *et al.* Microtubule stabilization reduces scarring and causes axon regeneration after spinal cord injury. *Science* 331, 928-931, doi:10.1126/science.1201148 (2011).

104 Ruschel, J. *et al.* Axonal regeneration. Systemic administration of epothilone B promotes axon regeneration after spinal cord injury. *Science* 348, 347-352, doi:10.1126/science.aaa2958 (2015).

105 David, S., Kroner, A., Greenhalgh, A. D., Zarruk, J. G. & Lopez-Vales, R. Myeloid cell responses after spinal cord injury. *Journal of neuroimmunology* 321, 97-108, doi:10.1016/j.jneuroim.2018.06.003 (2018).

106 Oyinbo, C. A. Secondary injury mechanisms in traumatic spinal cord injury: a nugget of this multiply cascade. *Acta neurobiologiae experimentalis* 71, 281-299 (2011).

107 Peng, W. *et al.* Systemic administration of an antagonist of the ATP-sensitive receptor P2X7 improves recovery after spinal cord injury. *Proceedings of the National Academy of Sciences of the United States of America* 106, 12489-12493, doi:10.1073/pnas.0902531106 (2009).

108 Simon, C. M., Sharif, S., Tan, R. P. & LaPlaca, M. C. Spinal cord contusion causes acute plasma membrane damage. *Journal of neurotrauma* 26, 563-574, doi:10.1089/neu.2008.0523 (2009).

109 Xu, G. Y., Hughes, M. G., Zhang, L. P., Cain, L. & McAdoo, D. J. Administration of glutamate into the spinal cord at extracellular concentrations reached post-injury causes functional impairments. *Neuroscience letters* 384, 271-276, doi:10.1016/j.neulet.2005.04.100 (2005).

110 Choo, A. M. *et al.* Contusion, dislocation, and distraction: primary hemorrhage and membrane permeability in distinct mechanisms of spinal cord injury. *J Neurosurg-Spine* 6, 255-266, doi:DOI 10.3171/spi.2007.6.3.255 (2007).

111 Liu, X. Z. *et al.* Neuronal and glial apoptosis after traumatic spinal cord injury. *Journal of Neuroscience* 17, 5395-5406 (1997).

112 Casha, S., Yu, W. R. & Fehlings, M. G. Oligodendroglial apoptosis occurs along degenerating axons and is associated with Fas and p75 expression following spinal cord injury in the rat. *Neuroscience* 103, 203-218, doi:Doi 10.1016/S0306-4522(00)00538-8 (2001).

113 Xiong, Y. Q., Rabchevsky, A. G. & Hall, E. D. Role of peroxynitrite in secondary oxidative damage after spinal cord injury. *J Neurochem* 100, 639-649, doi:10.1111/j.1471-4159.2006.04312.x (2007).

114 Sullivan, P. G., Krishnamurthy, S., Patel, S. P., Pandya, J. D. & Rabchevsky, A. G. Temporal characterization of mitochondrial bioenergetics after spinal cord injury. *Journal of neurotrauma* 24, 991-999, doi:10.1089/neu.2006.0242 (2007).

115 Fehlings, M. G. & Nguyen, D. H. Immunoglobulin G: A Potential Treatment to Attenuate Neuroinflammation Following Spinal Cord Injury. *J Clin Immunol* 30, S109-S112, doi:10.1007/s10875-010-9404-7 (2010).

116 Allan, S. M. & Rothwell, N. J. Inflammation in central nervous system injury. *Philos T R Soc B* 358, 1669-1677, doi:10.1098/rstb.2003.1358 (2003).

117 Hammarberg, H. *et al.* Neuroprotection by encephalomyelitis: rescue of mechanically injured neurons and neurotrophin production by CNS-infiltrating T and natural killer cells. *The Journal of neuroscience : the official journal of the Society for Neuroscience* 20, 5283-5291 (2000).

118 Tator, C. H. & Koyanagi, I. Vascular mechanisms in the pathophysiology of human spinal cord injury. *Journal of neurosurgery* 86, 483-492, doi:DOI 10.3171/jns.1997.86.3.0483 (1997).

119 Mabon, P. J., Weaver, L. C. & Dekaban, G. A. Inhibition of monocyte/macrophage migration to a spinal cord injury site by an antibody to the integrin alphaD: a potential new anti-inflammatory treatment. *Experimental neurology* 166, 52-64, doi:10.1006/exnr.2000.7488 (2000).

120 Wells, J. E., Hurlbert, R. J., Fehlings, M. G. & Yong, V. W. Neuroprotection by minocycline facilitates significant recovery from spinal cord injury in mice. *Brain : a journal of neurology* 126, 1628-1637, doi:10.1093/brain/awg178 (2003).

121 Gris, D. *et al.* Transient blockade of the CD11d/CD18 integrin reduces secondary damage after spinal cord injury, improving sensory, autonomic, and motor function. *The Journal of neuroscience : the official journal of the Society for Neuroscience* 24, 4043-4051, doi:10.1523/JNEUROSCI.5343-03.2004 (2004).

122 Fleming, J. C. *et al.* Alpha4beta1 integrin blockade after spinal cord injury decreases damage and improves neurological function. *Experimental neurology* 214, 147-159, doi:10.1016/j.expneurol.2008.04.024 (2008).

123 Kerr, B. J., Girolami, E. I., Ghasemlou, N., Jeong, S. Y. & David, S. The protective effects of 15-deoxy-delta-(12,14)-prostaglandin J2 in spinal cord injury. *Glia* 56, 436-448, doi:10.1002/glia.20630 (2008).

124 Lopez-Vales, R. *et al.* Phospholipase A2 superfamily members play divergent roles after spinal cord injury. *FASEB journal : official publication of the Federation of American Societies for Experimental Biology* 25, 4240-4252, doi:10.1096/fj.11-183186 (2011).

125 Evans, T. A., Barkauskas, D. S., Myers, J. T. & Huang, A. Y. Intravital Imaging of Axonal Interactions with Microglia and Macrophages in a Mouse Dorsal Column Crush Injury. *Jove-J Vis Exp*, doi:ARTN e5222810.3791/52228 (2014).

126 Kigerl, K. A. *et al.* Identification of Two Distinct Macrophage Subsets with Divergent Effects Causing either Neurotoxicity or Regeneration in the Injured Mouse Spinal Cord. *Journal of Neuroscience* 29, 13435-13444, doi:10.1523/Jneurosci.3257-09.2009 (2009).

127 Kroner, A. *et al.* TNF and Increased Intracellular Iron Alter Macrophage Polarization to a Detrimental M1 Phenotype in the Injured Spinal Cord. *Neuron* 83, 1098-1116, doi:10.1016/j.neuron.2014.07.027 (2014).

128 Ren, Y. & Young, W. Managing Inflammation after Spinal Cord Injury through Manipulation of Macrophage Function. *Neural Plast*, doi:Artn 94503410.1155/2013/945034 (2013).

129 Shechter, R. *et al.* Infiltrating Blood-Derived Macrophages Are Vital Cells Playing an Anti-inflammatory Role in Recovery from Spinal Cord Injury in Mice. *Plos Med* 6, doi:ARTN e100011310.1371/journal.pmed.1000113 (2009).

130 David, S. & Kroner, A. Repertoire of microglial and macrophage responses after spinal cord injury. *Nature reviews. Neuroscience* 12, 388-399, doi:10.1038/nrn3053 (2011).

131 Goldmann, T. *et al.* Origin, fate and dynamics of macrophages at central nervous system interfaces. *Nat Immunol* 17, 797-+, doi:10.1038/ni.3423 (2016).

132 Korin, B. *et al.* High-dimensional, single-cell characterization of the brain's immune compartment. *Nature neuroscience* 20, 1300-+, doi:10.1038/nn.4610 (2017).

133 Popovich, P. G. *et al.* Depletion of hematogenous macrophages promotes partial hindlimb recovery and neuroanatomical repair after experimental spinal cord injury. *Experimental neurology* 158, 351-365, doi:DOI 10.1006/exnr.1999.7118 (1999).

134 Popovich, P. G. & Hickey, W. F. Bone marrow chimeric rats reveal the unique distribution of resident and recruited macrophages in the contused rat spinal cord. *J Neuropathol Exp Neurol* 60, 676-685 (2001).

135 Keren-Shaul, H. *et al.* A Unique Microglia Type Associated with Restricting Development of Alzheimer's Disease. *Cell* 169, 1276-1290 e1217, doi:10.1016/j.cell.2017.05.018 (2017).

136 Popovich, P. G., Wei, P. & Stokes, B. T. Cellular inflammatory response after spinal cord injury in Sprague-Dawley and Lewis rats. *J Comp Neurol* 377, 443-464 (1997).

137 Imai, M. *et al.* Delayed accumulation of activated macrophages and inhibition of remyelination after spinal cord injury in an adult rodent model. *J Neurosurg-Spine* 8, 58-66, doi:10.3171/Spi-08/01/058 (2008).

138 Imamoto, K. & Leblond, C. P. Presence of Labeled Monocytes, Macrophages and Microglia in a Stab Wound of Brain Following an Injection of Bone-Marrow Cells Labeled with Uridine-H-3 into Rats. *J Comp Neurol* 174, 255-279, doi:DOI 10.1002/cne.901740205 (1977).

139 Pineau, I., Sun, L., Bastien, D. & Lacroix, S. Astrocytes initiate inflammation in the injured mouse spinal cord by promoting the entry of neutrophils and inflammatory monocytes in an IL-1 receptor/MyD88-dependent fashion. *Brain, behavior, and immunity* 24, 540-553, doi:10.1016/j.bbi.2009.11.007 (2010).

140 Horky, L. L., Galimi, F., Gage, F. H. & Horner, P. J. Fate of endogenous stem/progenitor cells following spinal cord injury. *J Comp Neurol* 498, 525-538, doi:10.1002/cne.21065 (2006).

141 Bendszus, M. & Stoll, G. Caught in the act: In vivo mapping of macrophage infiltration in nerve injury by magnetic resonance imaging. *Journal of Neuroscience* 23, 10892-10896 (2003).

142 Evans, T. A. *et al.* High-resolution intravital imaging reveals that blood-derived macrophages but not resident microglia facilitate secondary axonal dieback in traumatic spinal cord injury. *Experimental neurology* 254, 109-120, doi:10.1016/j.expneurol.2014.01.013 (2014).

143 Jassam, Y. N., Izzy, S., Whalen, M., McGavern, D. B. & El Khoury, J. Neuroimmunology of Traumatic Brain Injury: Time for a Paradigm Shift. *Neuron* 95, 1246-1265, doi:10.1016/j.neuron.2017.07.010 (2017).

144 Hatano, S. Experience from a multicentre stroke register: a preliminary report. *Bulletin of the World Health Organization* 54, 541-553 (1976).

145 Martin, R. L., Lloyd, H. G. & Cowan, A. I. The early events of oxygen and glucose deprivation: setting the scene for neuronal death? *Trends in neurosciences* 17, 251-257 (1994).

146 Katsura, K., Kristian, T. & Siesjo, B. K. Energy metabolism, ion homeostasis, and cell damage in the brain. *Biochemical Society transactions* 22, 991-996 (1994).

147 Moskowitz, M. A., Lo, E. H. & Iadecola, C. The science of stroke: mechanisms in search of treatments. *Neuron* 67, 181-198, doi:10.1016/j.neuron.2010.07.002 (2010).

148 Dirnagl, U., Iadecola, C. & Moskowitz, M. A. Pathobiology of ischaemic stroke: an integrated view. *Trends in neurosciences* 22, 391-397 (1999).

149 Yilmaz, G. & Granger, D. N. Cell adhesion molecules and ischemic stroke. *Neurological research* 30, 783-793, doi:10.1179/174313208X341085 (2008).

150 Schilling, M. *et al.* Microglial activation precedes and predominates over macrophage infiltration in transient focal cerebral ischemia: a study in green fluorescent protein transgenic bone marrow chimeric mice. *Experimental neurology* 183, 25-33 (2003).

151 Tanaka, R. *et al.* Migration of enhanced green fluorescent protein expressing bone marrow-derived microglia/macrophage into the mouse brain following permanent focal ischemia. *Neuroscience* 117, 531-539 (2003).

152 Price, C. J. *et al.* Cerebral neutrophil recruitment, histology, and outcome in acute ischemic stroke: an imaging-based study. *Stroke; a journal of cerebral circulation* 35, 1659-1664, doi:10.1161/01.STR.0000130592.71028.92 (2004).

153 Buck, B. H. *et al.* Early neutrophilia is associated with volume of ischemic tissue in acute stroke. *Stroke; a journal of cerebral circulation* 39, 355-360, doi:10.1161/STROKEAHA.107.490128 (2008).

154 Iadecola, C. & Anrather, J. The immunology of stroke: from mechanisms to translation. *Nature medicine* 17, 796-808, doi:10.1038/nm.2399 (2011).

155 Jin, R., Yang, G. & Li, G. Inflammatory mechanisms in ischemic stroke: role of inflammatory cells. *Journal of leukocyte biology* 87, 779-789, doi:10.1189/jlb.1109766 (2010).

156 Schilling, M. *et al.* Predominant phagocytic activity of resident microglia over hematogenous macrophages following transient focal cerebral ischemia: an investigation using green fluorescent protein transgenic bone marrow chimeric mice. *Experimental neurology* 196, 290-297, doi:10.1016/j.expneurol.2005.08.004 (2005).

157 Schilling, M., Strecker, J. K., Schabitz, W. R., Ringelstein, E. B. & Kiefer, R. Effects of monocyte chemoattractant protein 1 on blood-borne cell recruitment after transient focal cerebral ischemia in mice. *Neuroscience* 161, 806-812, doi:10.1016/j.neuroscience.2009.04.025 (2009).

158 Stevens, S. L. *et al.* The use of flow cytometry to evaluate temporal changes in inflammatory cells following focal cerebral ischemia in mice. *Brain research* 932, 110-119 (2002).

159 Kleinig, T. J. & Vink, R. Suppression of inflammation in ischemic and hemorrhagic stroke: therapeutic options. *Current opinion in neurology* 22, 294-301 (2009).

160 Macrez, R. *et al.* Stroke and the immune system: from pathophysiology to new therapeutic strategies. *The Lancet. Neurology* 10, 471-480, doi:10.1016/S1474-4422(11)70066-7 (2011).

161 Liesz, A. *et al.* Regulatory T cells are key cerebroprotective immunomodulators in acute experimental stroke. *Nature medicine* 15, 192-199, doi:10.1038/nm.1927 (2009).

162 Ito, M. *et al.* Brain regulatory T cells suppress astrogliosis and potentiate neurological recovery. *Nature* 565, 246-250, doi:10.1038/s41586-018-0824-5 (2019).

163 Urra, X., Miro, F., Chamorro, A. & Planas, A. M. Antigen-specific immune reactions to ischemic stroke. *Frontiers in cellular neuroscience* 8, 278, doi:10.3389/fncel.2014.00278 (2014).

164 Lopes Pinheiro, M. A. *et al.* Immune cell trafficking across the barriers of the central nervous system in multiple sclerosis and stroke. *Biochimica et biophysica acta* 1862, 461-471, doi:10.1016/j.bbadis.2015.10.018 (2016).

165 Zhou, W. *et al.* Postischemic Brain Infiltration of Leukocyte Subpopulations Differs among Murine Permanent and Transient Focal Cerebral Ischemia Models. *Brain pathology* 23, 34-44, doi:10.1111/j.1750-3639.2012.00614.x (2013).

166 Gelderblom, M. *et al.* Temporal and spatial dynamics of cerebral immune cell accumulation in stroke. *Stroke; a journal of cerebral circulation* 40, 1849-1857, doi:10.1161/STROKEAHA.108.534503 (2009).

167 Randolph, G. J., Ivanov, S., Zinselmeyer, B. H. & Scallan, J. P. The Lymphatic System: Integral Roles in Immunity. *Annual review of immunology* 35, 31-52, doi:10.1146/annurev-immunol-041015-055354 (2017).

168 Louveau, A. *et al.* Structural and functional features of central nervous system lymphatic vessels. *Nature* 523, 337-341, doi:10.1038/nature14432 (2015).

169 Ransohoff, R. M. & Engelhardt, B. The anatomical and cellular basis of immune surveillance in the central nervous system. *Nature reviews. Immunology* 12, 623-635, doi:10.1038/nri3265 (2012).

170 Kipnis, J. Multifaceted interactions between adaptive immunity and the central nervous system. *Science* 353, 766-771, doi:10.1126/science.aag2638 (2016).

171 Xie, L. *et al.* Sleep drives metabolite clearance from the adult brain. *Science* 342, 373-377, doi:10.1126/science.1241224 (2013).

172 Yang, L. *et al.* Evaluating glymphatic pathway function utilizing clinically relevant intrathecal infusion of CSF tracer. *Journal of translational medicine* 11, 107, doi:10.1186/1479-5876-11-107 (2013).

173 Louveau, A. *et al.* CNS lymphatic drainage and neuroinflammation are regulated by meningeal lymphatic vasculature. *Nature neuroscience* 21, 1380-+, doi:10.1038/s41593-018-0227-9 (2018).

174 Patel, T. K. *et al.* Dural lymphatics regulate clearance of extracellular tau from the CNS. *Molecular Neurodegeneration* 14, 11, doi:10.1186/s13024-019-0312-x (2019).

175 Da Mesquita, S. *et al.* Functional aspects of meningeal lymphatics in ageing and Alzheimer's disease. *Nature* 560, 185-191, doi:10.1038/s41586-018-0368-8 (2018).

176 Lohrberg, M. & Wilting, J. The lymphatic vascular system of the mouse head. *Cell and tissue research* 366, 667-677, doi:10.1007/s00441-016-2493-8 (2016).

177 Chozinski, T. J. *et al.* Expansion microscopy with conventional antibodies and fluorescent proteins. *Nature methods* 13, 485-488, doi:10.1038/nmeth.3833 (2016).

178 Llovera, G. *et al.* The choroid plexus is a key cerebral invasion route for T cells after stroke. *Acta neuropathologica* 134, 851-868, doi:10.1007/s00401-017-1758-y (2017).

179 Muyldermans, S. Nanobodies: natural single-domain antibodies. *Annual review of biochemistry* 82, 775-797, doi:10.1146/annurev-biochem-063011-092449 (2013).

180 Sato, Y. *et al.* 3D multi-scale line filter for segmentation and visualization of curvilinear structures in medical images. *Lect Notes Comput Sc* 1205, 213-222 (1997).

181 Frangi, A. F., Niessen, W. J., Vincken, K. L. & Viergever, M. A. Multiscale vessel enhancement filtering. *Medical Image Computing and Computer-Assisted Intervention - Miccai'98* 1496, 130-137 (1998).

182 Turetken, E., Benmansour, F. & Fua, P. Automated Reconstruction of Tree Structures using Path Classifiers and Mixed Integer Programming. *Proc Cvpr Ieee*, 566-573 (2012).

183 Quan, T. W. *et al.* NeuroGPS-Tree: automatic reconstruction of large-scale neuronal populations with dense neurites. *Nature methods* 13, 51-+, doi:10.1038/Nmeth.3662 (2016).

184 Litjens, G. *et al.* A survey on deep learning in medical image analysis. *Med Image Anal* 42, 60-88, doi:10.1016/j.media.2017.07.005 (2017).

185 Weigert, M. *et al.* Content-aware image restoration: pushing the limits of fluorescence microscopy. *Nature methods* 15, 1090-+, doi:10.1038/s41592-018-0216-7 (2018).

186 Eulenberg, P. *et al.* Reconstructing cell cycle and disease progression using deep learning. *Nature communications* 8, doi:ARTN 46310.1038/s41467-017-00623-3 (2017).

187 Dong, B., Shao, L., Da Costa, M., Bandmann, O. & Frangi, A. F. Deep Learning for Automatic Cell Detection in Wide-Field Microscopy Zebrafish Images. *I S Biomed Imaging*, 772-776 (2015).

188 Xing, F. & Yang, L. Robust Nucleus/Cell Detection and Segmentation in Digital Pathology and Microscopy Images: A Comprehensive Review. *IEEE reviews in biomedical engineering* 9, 234-263, doi:10.1109/RBME.2016.2515127 (2016).

189 Signaevsky, M. *et al.* Artificial intelligence in neuropathology: deep learning-based assessment of tauopathy. *Laboratory Investigation*, doi:10.1038/s41374-019-0202-4 (2019).

190 Coudray, N. *et al.* Classification and mutation prediction from non-small cell lung cancer histopathology images using deep learning. *Nature medicine* 24, 1559-+, doi:10.1038/s41591-018-0177-5 (2018).

191 Liang, H. *et al.* Evaluation and accurate diagnoses of pediatric diseases using artificial intelligence. *Nature medicine*, doi:10.1038/s41591-018-0335-9 (2019).

192 Leslie, M. Small but mighty. *Science* 360, 594-597, doi:10.1126/science.360.6389.594 (2018).

193 Fornito, A., Zalesky, A. & Breakspear, M. The connectomics of brain disorders. *Nature reviews. Neuroscience* 16, 159-172, doi:10.1038/nrn3901 (2015).

194 Zappoli, R. *et al.* Frontal and parieto-temporal cortical ablations and diaschisis-like effects on auditory neurocognitive potentials evocable from apparently intact ipsilateral association areas in humans: five case reports. *International journal of psychophysiology : official journal of the International Organization of Psychophysiology* 44, 117-142 (2002).

195 Schallert, T., Jones, T. A. & Lindner, M. D. Multilevel transneuronal degeneration after brain damage. Behavioral events and effects of anticonvulsant gamma-aminobutyric acid-related drugs. *Stroke; a journal of cerebral circulation* 21, III143-146 (1990).

196 Chang, S. J. *et al.* Transneuronal Degeneration of Thalamic Nuclei following Middle Cerebral Artery Occlusion in Rats. *BioMed research international* 2016, 3819052, doi:10.1155/2016/3819052 (2016).

197 Pinching, A. J. & Powell, T. P. Ultrastructural features of transneuronal cell degeneration in the olfactory system. *Journal of cell science* 8, 253-287 (1971).

198 Smith, M. C. Histological findings after hemicerebellectomy in man: anterograde, retrograde and transneuronal degeneration. *Brain research* 95, 423-442 (1975).

199 Beatty, R. M., Sadun, A. A., Smith, L., Vonsattel, J. P. & Richardson, E. P., Jr. Direct demonstration of transsynaptic degeneration in the human visual system: a comparison of retrograde and anterograde changes. *Journal of neurology, neurosurgery, and psychiatry* 45, 143-146 (1982).

200 Eisen, A. & Weber, M. The motor cortex and amyotrophic lateral sclerosis. *Muscle & nerve* 24, 564-573 (2001).

201 Heimer, L. & Kalil, R. Rapid transneuronal degeneration and death of cortical neurons following removal of the olfactory bulb in adult rats. *J Comp Neurol* 178, 559-609, doi:10.1002/cne.901780310 (1978).

202 Kodama, F. *et al.* Transneuronal degeneration in patients with temporal lobe epilepsy: evaluation by MR imaging. *European radiology* 13, 2180-2185, doi:10.1007/s00330-003-1875-y (2003).

203 Pearson, H. E., Labar, D. R., Payne, B. R., Cornwell, P. & Aggarwal, N. Transneuronal retrograde degeneration in the cat retina following neonatal ablation of visual cortex. *Brain research* 212, 470-475 (1981).

204 Park, H. Y., Park, Y. G., Cho, A. H. & Park, C. K. Transneuronal retrograde degeneration of the retinal ganglion cells in patients with cerebral infarction. *Ophthalmology* 120, 1292-1299, doi:10.1016/j.ophtha.2012.11.021 (2013).

205 Hendrickson, A. *et al.* Retrograde transneuronal degeneration in the retina and lateral geniculate nucleus of the V1-lesioned marmoset monkey. *Brain structure & function* 220, 351-360, doi:10.1007/s00429-013-0659-7 (2015).

206 Gunes, A. *et al.* Changes in retinal nerve fiber layer thickness in patients with cerebral infarction: evidence of transneuronal retrograde degeneration. *Acta neurologica Belgica* 116, 461-466, doi:10.1007/s13760-015-0592-z (2016).

207 Terao, S. *et al.* Upper motor neuron lesions in stroke patients do not induce anterograde transneuronal degeneration in spinal anterior horn cells. *Stroke; a journal of cerebral circulation* 28, 2553-2556 (1997).

208 Grüneboom, A. *et al.* A network of trans-cortical capillaries as mainstay for blood circulation in long bones. *Nature Metabolism* 1, 236-250, doi:10.1038/s42255-018-0016-5 (2019).

209 Herisson, F. *et al.* Direct vascular channels connect skull bone marrow and the brain surface enabling myeloid cell migration. *Nature neuroscience* 21, 1209-1217, doi:10.1038/s41593-018-0213-2 (2018).

210 Meisel, C., Schwab, J. M., Prass, K., Meisel, A. & Dirnagl, U. Central nervous system injury-induced immune deficiency syndrome. *Nature reviews. Neuroscience* 6, 775-786, doi:10.1038/nrn1765 (2005).

211 Offner, H. *et al.* Experimental stroke induces massive, rapid activation of the peripheral immune system. *Journal of cerebral blood flow and metabolism : official journal of the International Society of Cerebral Blood Flow and Metabolism* 26, 654-665, doi:10.1038/sj.jcbfm.9600217 (2006).

212 Brunkhorst, R., Pfeilschifter, W. & Foerch, C. Astroglial proteins as diagnostic markers of acute intracerebral hemorrhage-pathophysiological background and clinical findings. *Translational stroke research* 1, 246-251, doi:10.1007/s12975-010-0040-6 (2010).

213 Liesz, A. *et al.* DAMP signaling is a key pathway inducing immune modulation after brain injury. *The Journal of neuroscience : the official journal of the Society for Neuroscience* 35, 583-598, doi:10.1523/JNEUROSCI.2439-14.2015 (2015).

214 Ma, S., Zhao, H., Ji, X. & Luo, Y. Peripheral to central: Organ interactions in stroke pathophysiology. *Experimental neurology* 272, 41-49, doi:10.1016/j.expneurol.2015.05.014 (2015).

215 Wang, B. H., Yao, M. F., Lv, L. X., Ling, Z. X. & Li, L. J. The Human Microbiota in Health and Disease. *Engineering-Prc* 3, 71-82, doi:10.1016/J.Eng.2017.01.008 (2017).

216 Wang, Y. & Kasper, L. H. The role of microbiome in central nervous system disorders. *Brain, behavior, and immunity* 38, 1-12, doi:10.1016/j.bbi.2013.12.015 (2014).

217 Sudo, N. *et al.* Postnatal microbial colonization programs the hypothalamic-pituitary-adrenal system for stress response in mice. *The Journal of physiology* 558, 263-275, doi:10.1113/jphysiol.2004.063388 (2004).

218 Singh, V. *et al.* Microbiota Dysbiosis Controls the Neuroinflammatory Response after Stroke. *The Journal of neuroscience : the official journal of the Society for Neuroscience* 36, 7428-7440, doi:10.1523/JNEUROSCI.1114-16.2016 (2016).

219 Benakis, C. *et al.* Commensal microbiota affects ischemic stroke outcome by regulating intestinal gammadelta T cells. *Nature medicine* 22, 516-523, doi:10.1038/nm.4068 (2016).

220 Foster, J. & Neufeld, K. A. Gut-brain axis: How the microbiome influences anxiety and depression. *Int J Neuropsychoph* 17, 27-27 (2014).

221 Neufeld, K. M., Kang, N., Bienenstock, J. & Foster, J. A. Reduced anxiety-like behavior and central neurochemical change in germ-free mice. *Neurogastroent Motil* 23, doi:10.1111/j.1365-2982.2010.01620.x (2011).

222 de Jong, M., Essers, J. & van Weerden, W. M. Imaging preclinical tumour models: improving translational power. *Nature reviews. Cancer* 14, 481-493, doi:10.1038/nrc3751 (2014).

# 8 Publications

## 8.1 First authorship

- **Cai R***, Pan*C, Ghasemigharagoz A, Todorov MI, Förstera B, Zhao S, Bhatia HS, Mrowka L, Theodorou D, Rempfle M, Xavier A, Kress BT, Benakis C, Liebscher S, Liesz A, Menze B, Kerschensteiner M, Nedergaard M and Ertürk A. Panoptic imaging of transparent mice reveals whole-body neuronal projectome and skull-meninges connections. *Nat Neurosci* (2018). Cover of the issue. *equally contributed

- Pan C*, **Cai R***, Quacquarelli FP*, Ghasemigharagoz A, Lourbopoulos A, Matryba P, Presnila N, Dichgangs M, Hellal F and Ertürk A. Shrinkage mediated imaging of entire organs and organisms using uDISCO. *Nat Methods* 13, pp 859–867 (2016). Cover of the issue. *equally contributed

## 8.2 Co-authorship

- Pan C*, Schoppe O*, Parra-Damas A*, **Cai R**, Todorov MI, Gondi G, von Neubeck B, Ghasemigharagoz A, Reimer MA, Coronel J, Garvalov BK, Menze B, Zeidler and Erturk A. Deep learning reveals cancer metastasis and therapeutic antibody targeting in whole body. Submitted and available as preprint in Biorxiv https://doi.org/10.1101/541862. *equally contributed

- Llovera G, Benakis C, Enzmann G, **Cai R**, Arzberger T, Ghasemigharagoz A, Mao X, Malik R, Lazarevic I, Liebscher S, Ertürk A, Meissner L, Vivien D, Haffner C, Plenisla N, Montaner J, Engelhardt B, Liesz A. The choroid plexus is a key cerebral invasion route for T cells after stroke. *Acta Neuropathologica* 134, Issue 6, pp 851–868 (2017)

- Beretta S, Versace A, Carone D, Riva M, Dell´Era V, Cuccione E, **Cai R**, Monza L, Pirovano S, Padovano G, Stiro F, Presotto L, Paterno` G, Rossi E, Giussani C, Sganzerla EP, Ferrarese C. Cerebral collateral therapeutics in acute ischemic stroke: A randomized preclinical trial of four modulation strategies. *J Cereb Blood Flow Metab* 37, Issue 10 (2017)

- Cuccione E, Versace A, Cho TH, Carone D, Berner LP, Ong E, Rousseau D, **Cai R**, Monza L, Ferrarese C, Sganzerla EP, Berthezène Y, Nighoghossian N, Wiart M, Beretta S, Chauveau F. Multi-site laser Doppler flowmetry for assessing collateral flow in experimental ischemic stroke: validation of outcome prediction with acute MRI. *J Cereb Blood Flow Metab* 37, Issue 6 (2017)

- Carone D, Librizzi L, Cattalini A, Sala G, Conti E, Cuccione E, Versace A, **Cai R**, Monza L, de Curtis M, Ferrarese C, Beretta S. Pravastatin acute neuroprotective effects depend on blood brain barrier integrity in experimental cerebral ischemia, *Brain Res* 1615, pp 31-41 (2015)

- Beretta* S, Cuccione* E, Versace A, Carone D, Riva M, Padovano G, Dell'Era V, **Cai R**, Monza L, Presotto L, Rousseau D, Chaveau F, Paternò G, Pappadà GB, Giussani C, Sganzerla EP and Ferrarese C. Cerebral collateral flow defines topography and evolution of molecular penumbra in experimental ischemic stroke. *Neurobiol Dis* 74, pp 305-313 (2015). *equally contributed

- Neuhaus AA, Rabie T, Sutherland BA, Papadakis M, Hadley G, **Cai R** and Buchan AM. Importance of preclinical research in the development of neuroprotective strategies for ischemic stroke. *Jama Neurol* 71(5), pp 634-9 (2014)

# 9 Acknowledgements

This dissertation is not only mine.

In almost five years in Munich, several people have supported me to reach this important goal in my life. I would like to express my gratitude to all of you for your contributions and your help. I would not have achieved anything without you.

First of all, I would like to thank Ali for giving a chance to this young but bold girl to flourish. I would not have achieved the same results in any other places. With you, I learned how to push myself to limits that I would have never imagined. Here, in your lab and in Munich I could really experience an inspiring, multidisciplinary and innovative scientific environment. Thanks for having nurtured my ambitions and taken out the full potential from me.

Besides my supervisor Ali, I would like to thank the rest of my thesis advisor committee: Nick, Sabina and Thomas for your insightful suggestions and time.

Special thanks to Chenchen, my main science buddy. In these four and a half years we grew up professionally together, sharing tears and joy. It is even almost prosaic to say that my work would have not been anything without yours. It has been a great experience working together.

Thanks to all the past and present members of the e-lab: Jasmin, Leone, Lamia'a, Alireza, Francesca, Lina, Susanne, Lisa, Franzi, Josy, Ludwig, Arnaldo, Mike, Benjamin, Shan, Marin, Harsh, Doris, Madita, Muege, Zhouyi, Hongcheng, Ana, Chongyue, Oliver, Karen, Rupinder. Some of you actively contributed to this work, some of you became more than just colleagues, some of you became fundamental motivation guides, always ready to psychologically sustain me. However, each of you taught me something valuable during my studies and helped me so many times and made my PhD life more enjoyable. You were the thing that I appreciated the most in all these years. "When you are looking for a PhD position, don't focus on the project but focus on the team".

Thanks to all my students: Leander, Ilgin, Inés, Simge, Sam for the great time we had together and for having improved my supervision skills.

A big thanks to Farida. There are not enough words to describe how much you encouraged and helped me. I am deeply grateful for all the time that you dedicated to me.

My sincere thanks to Manu and the animal facility people, for their tremendous help.

During my PhD studies I could also collaborate with Thanasis, Arthur and Gemma. I would like to thank Thanasis for his great help in statistics and Arthur and Gemma for having given me the possibility to join their project.

Grazie ai miei genitori e a mio fratello: nonostante sapessero quanto fosse dura non avermi affianco, non mi hanno mai fatto pesare la lontananza in questi anni. Grazie per avermi lasciata libera nelle mie scelte e per avermi fatto spiccare il volo.

非常感谢我亲爱的父母和弟弟。感谢他们理解我不能常伴左右的愧疚，感谢这些年来他们孜孜不倦的支持。支持我自由选择和决定我的生活，支持我自由翱翔在远方。你们永远是我奋斗力量的源泉和坚实后盾！

Thanks to Evan, my patient and wise advisor that always had time to help me to improve myself and always knew the right thing to tell me at the right moment.

Grazie alla Vale, Sara, Laura, Alice, Nadia e Valerio per il loro supporto e apprezzamento e perché ho potuto sentire che veramente vi importava e grazie a tutti i miei amici a Milano e nel resto del mondo che quando c'è stato bisogno, non si sono tirati indietro a sostenermi. Grazie ad ogni singola persona su questo globo che ha tifato per me!

Thanks to all the CSD staff and this amazing scientific cluster in Munich. I can 100% say that this city is a wonderful place where to do scientific research.

# 10 Affidavit

Hiermit versichere ich an Eides statt, dass ich die vorliegende Dissertation “DISCO WHOLE BODY CLEARING AND IMAGING TO STUDY SYSTEMIC CHANGES IN NEURONAL PATHOLOGIES” selbstständig angefertigt habe, mich außer der angegebenen keiner weiteren Hilfsmittel bedient und alle Erkenntnisse, die aus dem
Schriftum ganz oder annähernd übernommen sind, als solche kenntlich gemacht und nach
ihrer Herkunft unter der Bezeichnung der Fundstelle einzeln nachgewiesen habe.

I hereby confirm that the dissertation “DISCO WHOLE BODY CLEARING AND IMAGING TO STUDY SYSTEMIC CHANGES IN NEURONAL PATHOLOGIES” is the result of my own work and that I have only used sources or materials listed and specified in the dissertation.

München, 14.03.2019

_____

Ruiyao Cai

# 11 Declaration of authors' contributions

Authors contributed to the Research Articles as follows:

1. Pan C*, **Cai R***, Quacquarelli FP*, Ghasemigharagoz A, Lourbopoulos A, Matryba P, Presnila N, Dichgangs M, Hellal F and Ertürk A. *equally contributed. **Shrinkage mediated imaging of entire organs and organisms using uDISCO.** A.E. designed and led all aspects of the project. C.P., **R.C**., and F.P.Q. performed most of the experiments. A.G. performed the image rendering and developed algorithms for data analysis. C.P., **R.C**., F.P.Q., and A.G. analyzed the data. A.L. interpreted data and performed the BMSC cultures, characterization, and transplantations; F.H. performed virus tracing; P.M. assisted first-clearing experiments; N.P. and M.D. supervised A.L. and F.H., respectively. A.E., C.P., **R.C**., F.P.Q., and A.G. wrote the paper. All authors edited the paper.

2. **Cai R***, Pan*C, Ghasemigharagoz A, Todorov MI, Förstera B, Zhao S, Bhatia HS, Mrowka L, Theodorou D, Rempfle M, Xavier A, Kress BT, Benakis C, Liebscher S, Liesz A, Menze B, Kerschensteiner M, Nedergaard M and Ertürk A. *equally contributed. **Panoptic imaging of transparent mice reveals whole-body neuronal projectome and skull-meninges connections.** A.E. initiated and led all aspects of the project. **R.C.** and C.P. developed the method and conducted most of the experiments. **R.C.**, A.G., C.P., H.S.B., M.R., and B.M. analyzed data. M.I.T. stitched and analyzed the whole mouse body scans. A.P.D., B.F., S.Z. and L.M. helped to optimize the protocols. I.B., H.S.B., and S.L. helped to investigate skull–meninges connections. D.T. and M.K. contributed spinal cord injury experiments; C.B. and A.L., MCAO experiments; and A.X., B.K. and M.N., cisterna magna injection experiments. A.E., **R.C.** and C.P. wrote the paper. All the authors edited the manuscript.

Herewith, I confirm the contributions to the manuscripts.

München, 14.03.2019

_____ _____

Ruiyao Cai

Dr. Ali Ertürk
(supervisor)

_____

Chenchen Pan
(shared first author for both Research Articles)

_____

Francesca P. Quacquarelli
(shared first author for Research Article 1)